African University of Science and Technology [AUST]

Knowledge is Freedom

ACTIVATED CARBON AND GRAPHENE OXIDE FOR SUPERCAPACITORS AND BATTERIES APPLICATION

A dissertation submitted to the Department of Materials Science and Engineering,

African University of Science and Technology,

In partial fulfilment of the requirements for the degree of

Doctor of Philosophy of Materials Science and Engineering (Energy)

By

Kigozi Moses

(70160)

JANUARY 2021

CERTIFICATION

This is to certify that the thesis titled “Activated carbon and graphene oxide for supercapacitors and batteries application” submitted to the school of postgraduate studies, African University of Science and Technology (AUST), Abuja, Nigeria for the award of Doctor of Philosophy is a record of original research carried out by Kigozi Moses in the Department of Materials Science and Engineering.

SIGNATURE PAGE

ACTIVATED CARBON AND GRAPHENE OXIDE FOR SUPERCAPACITORS AND BATTERIES APPLICATION

By

Kigozi Moses

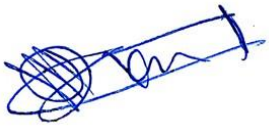

21st March 2021

A thesis approved by the Department of Materials Science and Engineering

RECOMMENDED:

Supervisor: Dr Nelson Yaw Dzade

Co-supervisor: Professor Peter Azikiwe Onwualu, FAS

Professor Peter Azikiwe Onwualu, FAS

Head, Department of Materials Science and Engineering

APPROVED: ……

Chief Academic Officer

Date: **10th March 2021**

ABSTRACT

Carbon-based materials are widely used for energy storage systems because of their unique properties, low cost, and availability. These include Graphite, graphene, activated carbon, graphene oxide, carbon nanotube, carbon forms, carbon aerogel etcetera. Graphite is a mineral mined from different parts of the world which includes Africa. It can be used or converted into different carbon materials such as exfoliated graphite, graphene, Graphene Oxide (GO), graphene nanoplatelets, carbon nanotubes, onions among others by chemical or mechanical methods. In this study, the locally mined graphite flakes were converted to GO using chemical methods known as Hummer's oxidation method (HM). This method was also compared with other modified Hummer's methods by altering the conditions and the materials used. The synthesized GO materials were characterized by different techniques such as UV-Vis spectroscopy, FTIR, SEM-EDX, XRD, and electrochemical analysis. The morphology, functional groups, different bonds, elemental percentage, crystallographic structure, and energy storage applicability were examined. The techniques confirmed the formation of functional groups like C-O, C=O, and the C/O ratio in the materials. The electrochemical characterization performance of materials produced the highest specific capacitance of 211.2 F/g with a current density of 0.5 A/g and the specific energy of 7.33 Wh/kg.

In this work, African Maize Cobs (AMC) was used as a rich biomass precursor in synthesizing carbon material through a chemical activation process for application in electrochemical energy storage devices. The carbonization and activation were carried out with concentrated sulphuric acid and potassium hydroxide. The activation was carried out using three different temperatures of 600, 700, and 800 ^{o}C. The activated carbon exhibited excellent microporous and mesoporous structures with a specific surface area that ranges between 30 - 254 m^2g^{-1} as measured by BET analysis. The morphology and structure of the produced materials are analyzed through Field Emission Scanning Electron Microscopy (FESEM), Fourier Transform Infrared Spectroscopy (FTIR), X-Ray Diffraction (XRD), Boehm titration, X-ray Photoelectron Spectroscopy (XPS), and Raman Spectroscopy. X-ray photoelectron spectroscopy indicates that a considerable amount of oxygen is present in the materials. The functional groups in the activated carbon enhanced the electrochemical performance and improved the double-layer capacitance of the material. The acid-activated material at 700°C exhibited excellent capacitance of 456 F g-1 at a specific current of 0.25 A g-1 in 6 M KOH electrolyte and show excellent stability after 10,000 cycles. The alkaline activated produced materials delivered a specific capacitance of 358.7 F/g with an energy density of 12.45 Wh/kg and a corresponding power density of 250 W/kg at 0.5 A/g. In addition to being low cost, the produced materials show excellent stability and electrochemical properties, thus suitable, as is a potential material for supercapacitor application. The hydrothermal method is used in heteroatomic metal oxide-graphene doping for improvement of the material properties. The $NaFe_2O_3$-GO composite was produced by batch hydrothermal method. The synthesised composite was tested for battery application. The material was characterized by FESEM/EDX, XRD, and electrochemical testing of the material which resulted in the performance of the discharge capacity approximated to be 720 mAh/g.

Keywords: Activated carbon; Carbon-based materials; Metal oxide composites; Cathode materials; High energy; Hydrothermal synthesis; Heteroatomic; Doping; Electrochemical analysis; Composite; Discharge capacity; Energy storage application.

DEDICATION

To the Almighty Allah for his guidance, care, and protection

To JARAR Family; my wife Nanyitti Annet Jamirah Kigozi and all my children for their continuous support, care, and love

To my mother Faridah Nambogga (deceased), my father Kangavve Umar Moses for all the toils you went through to make me who I am today.

ACKNOWLEDGMENTS

First and foremost, would like to acknowledge the management and the Department of Chemistry, Busitema University for allowing starting my study, I am grateful for your support and encouragement

I like to acknowledge the African Development Bank (AfDB) and Pan African Materials Institute (PAMI) under the African University of Science and Technology for financial support for studies. My humble thanks go to the entire management and staff of the African University of Science and Technology for the great welcome to Nigeria.

I would like to give my sincere appreciation to all the entities/centers of the International Advanced Research Centre for Powder Metallurgy and New Materials (ARCI) Hyderabad India for support during my research visit program. Firstly, I would like to thank the World Bank for availing of the opportunity for the exchange program in collaboration with Africa India Forum Summit III (INDO-AFRICA) under the Department of Science and Technology, Government of India through African Centre of Excellence (ACE's) strengthening projects. Secondly, I would like to thank and appreciate ARCI Hyderabad for accepting my application and the great support from DST at-large which helped in the facilitation of my entire stay for 6 months in India. Individually, I would like to thank Dr. P K Jain for the full support he has given me which included mentoring, training, support, encouragement among others which motivated my stay in India.

Dr Nelson Yaw Dzade and Professor Peter Azikiwe Onwualu the principal advisors for the extraordinaire guidance and mentorship, I am greatly for the training given to me. Your encouragement, scientific suggestions, and guidance are very much appreciated.

My special thanks go to my Ph.D. committee members: Dr. Pawan Kumar Jain, Prof Esidar Ntsoenzok, Prof Luke E K Achenie, and Dr Emmanuel Tebandeke.

I would like to thank all members of the Department of Materials Science and Engineering, especially the Energy section in African University Science and Technology (AUST), Abuja – Nigeria.

Last but not least, I would like to acknowledge JARAR Family and KV family to mention; Annet Nanyitti Jamirah Kigozi (my wife), Degeya Abdullah Kigozi, Nakimuli Janati Kigozi, Walusimbi Rayan Kigozi, Kigozi Alim Wasswa, Kigozi Rakib Kato, Kigozi Shanell A K, Nalumansi Jabirah Kigozi, Nakaweesa Amirah Kigozi, Kangavve Umar Moses and friends who needed me but due to academics I could not help in any way, thank you all.

LIST OF PUBLICATIONS

Kigozi, M., Kali, R., Bello, A., Padya, B., Kalu-uka, G. M., Wasswa, J., Jain, P. K., Onwualu, P. A., & Dzade, N. Y. (2020). Modified Activation Process for Supercapacitor Electrode Materials from African Maize Cob. Materials, 13(5412), 1–21. https://doi.org/10.3390/ma13235412

Kigozi, M., Koech, R. K., Kingsley, O., Ojeaga, I., Tebandeke, E., Kasozi, G., & Onwualu, P. A. (2020). Synthesis and characterization of graphene oxide from locally mined graphite flakes and its supercapacitor applications _ Elsevier Enhanced Reader.pdf. Results in Materials, 100113. https://doi.org/10.1016/j.rinma.2020.100113

Moses Kigozi, Blessing N Ezealigo, Azikiwe Peter Onwualu, Nelson Y Dzade (2020). Hydrothermal synthesis of metal oxide composite cathode materials for high energy application. **Accepted in Springer Nature** under Chemically deposited nanocrystalline metal oxide thin films, synthesis, characterizations, and their applications books

Moses Kigozi, Richard K Koech, Kingsley Orisekeh, Ravi Kali, Omar L M Kamoga, Balaji Padya, Abdulhakeem Bello, Pawan Kumar Jain, Azikiwe Peter Onwualu, Nelson Y Dzade, (2020). Porous carbon derived from Zea mays cobs as excellent electrodes for supercapacitor applications. Under review.

Orisekeh, K., Singh, B., Olanrewaju, Y., **Kigozi, M**., Ihekweme, G., Umar, S., Anye, V., Bello, A., Parida, S., & Soboyejo, W. O. (2020). Processing of α-Fe2O3 Nanoparticles on Activated Carbon Cloth as Binder-Free Electrode Material for Supercapacitor Energy Storage. Journal of Energy Storage, July, 102042. https://doi.org/10.1016/j.est.2020.102042

Bello, A., Sanni, D. M., Adeniji, S. A., Anye, V., Orisekeh, K., **Kigozi, M**., & Koech, R. (2020). Combustion synthesis of battery-type positive electrodes for robust aqueous hybrid supercapacitor. Journal of Energy Storage, 27(December 2019), 101160. https://doi.org/10.1016/j.est.2019.101160

Koech, R. K., **Kigozi, M**., Bello, A., Onwualu, P. A., & Soboyejo, W. O. (2019). Recent advances in solar energy harvesting materials with particular emphasis on photovoltaic materials. IEEE PES/IAS PowerAfrica Conference: Power Economics and Energy Innovation in Africa, PowerAfrica 2019, 627–632. https://doi.org/10.1109/PowerAfrica.2019.8928859

Table of Contents

CERTIFICATION i

SIGNATURE PAGE ii

ABSTRACT iv

DEDICATION v

ACKNOWLEDGMENTS vi

LIST OF PUBLICATIONS viii

LIST OF FIGURES xii

LIST OF TABLES xv

LIST OF ABBREVIATION xvi

CHAPTER ONE 1

1.0. INTRODUCTION 1

1.1. Background 1

1.2. Problem statement 3

1.3. Research objectives 4

1.4. Scope of the study 5

REFERENCES 1

CHAPTER TWO 2

2.0. LITERATURE REVIEW 2

2.1. Energy storage systems 2

2.2. Batteries Energy Storage System (BESS) 3

2.3. Supercapacitors (SCs) 4

2.4. Carbon-based electrode materials 11

2.5. Activated carbon (AC) 23

2.6. Synthesis approach for electrode materials 33

2.7. Concept of supercapacitor technology 40

2.8. Characteristics of supercapacitors 43

2.9. Applications of supercapacitors 48

REFERENCES 52

CHAPTER THREE 62

3.0. Synthesis and characterization of graphene oxide from locally mined graphite flakes and its supercapacitor applications 62

3.1. Introduction 62

3.2. Materials and methods 66

3.3. Conversion by oxidation of graphite flakes into Graphene Oxide (GO) 66

3.4. Electrode preparation and electrochemical measurements 68

3.5. Results and discussions 70

Conclusion 91

REFERENCES 93

CHAPTER FOUR 99

4.0. Modified Activation process for Supercapacitor Electrode Materials from African Maize Cob 99

4.1. Introduction 99

4.2. Experiments 104

4.3. Results and Discussion 107

Conclusion 126

REFERENCES 127

CHAPTER FIVE 135

5.0. Porous carbon derived from *Zea mays* cobs as excellent electrodes for supercapacitor applications 135

5.1. Introduction 135

5.2. Experiments 138

5.3. Results and discussion 142

Conclusion 158

REFERENCES 159

CHAPTER SIX 164

6.0. Hydrothermal synthesis of metal oxide composite cathode materials for high energy application: $NaFe_2O_3$-GO composite 164

6.1. Introduction 164

6.2. Hydrothermal Synthesis (HS) apparatus 167

6.3. Hydrothermal synthesis (HS) of metal oxide composite 168

6.4. Metal oxide composite cathode materials for high energy density storage 177

6.5. Solvents under hydrothermal synthesis (HS) 179

6.6. Hydrothermal synthesis of $NaFe_2O_3$-GO 181

6.7. The future of the hydrothermal synthesis method 187

Conclusions 187

REFERENCES 189

CONCLUSION AND RECOMMENDATIONS 197

CONTRIBUTION TO KNOWLEDGE 200

Appendices 201

Appendex 1 201

APPENDIX 2 211

LIST OF FIGURES

FIGURE 2.1: SCHEMATIC OPERATION PRINCIPLE OF A BATTERY CELL. 4

FIGURE 2.2: THE SUPERCAPACITOR TAXONOMY 5

FIGURE 2.3: EDCL DEVICE SET UP 6

FIGURE 2.4: GRAPHENE OXIDE SYNTHESIS BY CHEMICAL OXIDATION METHOD FROM GRAPHITE 20

FIGURE 3.1: IMAGES OF SAMPLE PREPARATION. 67

FIGURE 3.2: UV-VIS SPECTRA OF GRAPHITE AND SYNTHESIZED GO. 71

FIGURE 3.3: FTIR SPECTRA OF GO SYNTHESIZED WITH HM, MHM1, AND MHM2 METHODS. 73

FIGURE 3.4: SEM MICROGRAPHS OF GRAPHITE AND SYNTHESIZED GO. 74

FIGURE 3.6: XRD SPECTRA FOR GO MATERIALS. 79

FIGURE 3.7: RAMAN SPECTRA FOR GO-HM, GO-MHM1, GO-MHM2, AND GRAPHITE FLAKES. 80

FIGURE 3.8: GALVANOSTATIC CHARGE/DISCHARGE OF GO MATERIALS PREPARED WITH HM, MHM1, ... 81

FIGURE 3.9: CYCLIC VOLTAMMETRY OF GO MATERIALS PREPARED WITH HM, MHM1, AND MHM2 USING 6M KOH AS ELECTROLYTE AT DIFFERENT SCAN RATES. 84

FIGURE 3.10: NYQUIST EIS PLOT FOR GO MATERIALS AT DIFFERENT VOLTAGES FOR THE THREE METHODS USED 85

FIGURE 3.11: VOLTAGE HOLDING STABILITY OF GO MATERIALS PREPARED WITH HM, MHM 1, AND MHM 2 METHODS AND EC STABILITY DISPLAY IN THE INSERT. 86

FIGURE 3.12: CV FOR THE GO MATERIALS BEFORE AND AFTER THE VOLTAGE HOLDING STABILITY TEST. 88

FIGURE 3.13: SELF-DISCHARGE OF GO MATERIALS AFTER CHARGING THE DEVICE TO 1V AND HOLDING FOR 5 MINUTES IN AN OPEN CIRCUIT 89

FIGURE 3.14: THE PLOT OF COLUMBIC EFFICIENCY % VERSING STABILITY VOLTAGE HOLDING TIME IN HOURS 91

FIGURE 4.1: N_2 ADSORPTION-DESORPTION ISOTHERM AT 77K OF ACTIVATED CARBON SAMPLES. 109

FIGURE 4.2: FESEM MICROGRAPHS FOR AC-S SAMPLES TAKEN AT TWO DIFFERENT MAGNIFICATIONS AC-S-600 AT (A) 200NM, (B) 1µM, AC-S-700 AT (C) 20µM, (D) 2µM, AC-S-800 AT (E) 10µM, (F) 1µM. 111

FIGURE 4.3: (A) FTIR SPECTRA AND (B) X-RAY DIFFRACTION PEAKS FOR AC-S-600, AC-S-700, AND AC-S-800 AC MATERIALS. 112

FIGURE 4.4: XPS DECONVOLUTED SPECTRA OF AC-S-600 ACTIVATED CARBON MATERIAL (A) C 1S CARBON ATOM AT 283.7 EV, (B) O 1S OXYGEN ATOM AT 531.7 EV, (C) S 2P SULPHUR ATOM AT 168.7 EV. 116

FIGURE 4.5: CV CURVES OF AC-S-600, AC-S-700, AND AC-S-800 ELECTRODE MATERIALS AT DIFFERENT SCAN RATES WITH 6MKOH AND 1M Na_2SO_4 AS ELECTROLYTES..... 119

FIGURE 4.6: GALVANOSTATIC CHARGE-DISCHARGE CURVES FOR AC-S-600, AC-S-700, AND AC-S-800 ELECTRODES MATERIALS AT DIFFERENT CURRENT DENSITIES WITH (A) 6M KOH AND (B) 1M Na_2SO_4 AS ELECTROLYTES. 120

FIGURE 4.7: ELECTROCHEMICAL IMPEDANCE SPECTROSCOPY (EIS) NYQUIST PLOT FOR AC-S-600, AC-S-700, AND AC-S-800 FOR TWO DIFFERENT ELECTROLYTES (6M KOH AND 1M NA2SO4) AT THE POTENTIAL OF 10MV 123

FIGURE 5.1: FESEM/EDX MORPHOLOGY AND COMPOSITIONS FOR (A) ANN6, (B) ANN7, THE AND (C) ANN8 SAMPLES. 143

FIGURE 5.2: (A) XRD SPECTRA, (B) FTIR SPECTRA FOR ANN6, ANN7, AND ANN8 ACTIVATED CARBON. 145

FIGURE 5.3: XPS DECONVOLUTED SPECTRA FOR ANN8 ACTIVATED SAMPLE. 146

FIGURE 5.4: TGA/DSC PROFILE (A) ZEA MAYS COBS AND (B) ACTIVATED CARBON ANN6, ANN7, AND ANN8..... 147

FIGURE 5.5: (A) N_2 ADSORPTION-DESORPTION ISOTHERMS AND (B) PORE SIZE DISTRIBUTION OF THE ACTIVATED CARBON SAMPLES. 150

FIGURE 5.6: (A) CVS AT A SCAN RATE OF 10MV/S, (B) GCD CARRIED AT A CURRENT DENSITY OF 0.25A/G, (C) SPECIFIC CAPACITANCE WITH DIFFERENT CURRENT DENSITIES OF ANN6, ANN7, AND ANN8 ACTIVATED CARBON SAMPLES. 151

FIGURE 5.7: CV CURVES FOR (A) ANN6, (B) ANN7, AND (C) ANN8 CARBON SAMPLES AT DIFFERENT SCAN RATES. 152

FIGURE 5.8: GCD CURVES FOR (A) ANN6, (B) ANN7, AND (C) ANN8 CARBON SAMPLES AT DIFFERENT CURRENT DENSITIES..... 154

FIGURE 5.9: FIGURE EIS FOR ANN6, ANN7, AND ANN8 ACTIVATED CARBON SCANNED AT 10MV, INSERT IS THE ZOOMED HIGH FREQUENCY. 156

FIGURE 6.1: SET UP A BATCH REACTION SYSTEM ARRANGEMENT..... 168

FIGURE 6.2: FLOW CHART FOR THE FLOW REACTION SYSTEM..... 176

FIGURE 6.3: ILLUSTRATION OF PRESSURE-TEMPERATURE PHASE DIAGRAM OF PURE WATER SHOWING SUPERCRITICAL DOMAIN 181

FIGURE 6.4: FESEM MORPHOLOGY FOR $NaFe_2O_3$-GO. 183

FIGURE 6.5: EDX PROFILE FOR THE $NaFe_2O_3$-GO. 183

FIGURE 6.6: XRD PROFILE FOR $NaFe_2O_3$-GO. 184

FIGURE 6.7: GCD PROFILE FOR $NaFe_2O_3$-GO. 185

FIGURE 6.8: CV PROFILE FOR $NaFe_2O_3$-GO. 185

LIST OF TABLES

TABLE 2.1: GRAPHENE AND GO NANOMATERIALS IN EDLCS 22

TABLE 2.2: CARBON-BASED EDLC AS ELECTRODE MATERIALS 30

TABLE 3.1: EDX ELEMENTAL WEIGHT PERCENTAGE OF GRAPHITE AND SYNTHESIZED GO 75

TABLE 3.2: THE CURRENT DENSITY, SPECIFIC CAPACITANCE (F/G), SPECIFIC ENERGY (WH/KG), SPECIFIC POWER (W/KG), AND EFFICIENCY (%) OF GO PRODUCED BY HM, MHM1, AND MHM2 USING 6M KOH ELECTROLYTE AND POTENTIAL OF 1.0 V. 78

TABLE 4.1: PHYSICAL PROPERTIES OF AC SAMPLES FROM N_2 ADSORPTION AT 350^{o}C 110

TABLE 4.2: PERFORMANCE OF SUPERCAPACITORS WITH DIFFERENT ELECTRODE MATERIALS FROM DIFFERENT BIOMASS SOURCES CHEMICALLY TREATED WITH DIFFERENT IMPREGNATION FROM LITERATURE IN COMPARISON WITH THIS CURRENT STUDY. 125

TABLE 5.1: EDS ELEMENTAL COMPOSITION FOR ANN6, ANN7, AND ANN8 AC SAMPLES ... 143

TABLE 5.2: ATOMIC PERCENTAGES AS OBTAINED FROM XPS ANALYSIS 147

TABLE 5.3: TGA/DSC MATERIAL DECOMPOSITION OF THE RAW MATERIAL AND ACTIVATED CARBON SAMPLES 148

TABLE 5.4: THE PORE CHARACTERISTICS OF ANN6, ANN7, AND ANN8 ACTIVATED CARBON SAMPLES 149

TABLE 6.1: PHASE PRODUCT SYNTHESIS USING BATCH HYDROTHERMAL REACTION SYSTEMS 169

TABLE 6.2: PHASE PRODUCT SYNTHESIS USING FLOW HYDROTHERMAL REACTION SYSTEMS 173

TABLE 6.3: THE PROPERTIES OF WATER AT DIFFERENT TEMPERATURE AND PRESSURE (ADAPTED FROM (LOPPINET-SERANI ET AL., 2010) 180

LIST OF ABBREVIATION

GO - Graphene Oxide

AC – Activated carbon

EC – Electrochemical

GCD - Galvanostatic Charge/Discharge

CV - Cyclic Voltammetry

EIS - Electrochemical Impedance Spectroscopy

HM - Hummer's method

MHM - modified Hummer's method

H_2SO_4 - Sulphuric acid

$NaNO_3$ - Sodium nitrate

$KMnO_4$ - Potassium permanganate

H_2O_2 - Hydrogen peroxide

HCl - Hydrochloric acid

UV-Vis - Ultra-Violet- Visible Spectroscopy

FTIR - Fourier Transform Infrared Spectroscopy

SEM- Scanning Electron Microscopy

EDX - Energy Dispersive X-ray

XRD - X-ray Diffraction.

SC – Supercapacitor

EDLC – Electrochemical double-layer capacitor

ESS – Energy storage system

BESS – battery energy storage system

CHAPTER ONE

1.0. INTRODUCTION

1.1. Background

The ever-increasing demand and consumption of fossil fuels, their effects on the environment towards pollution and their sustainability causes serious concerns for the next generation. The utilization of fossil fuels causes greenhouse gas emissions and pollution of soil, water, and air in our environment. This is caused by the ever-growing demand for energy which is very vital for human development. This mainly depends on the combustion of fossil fuels depleted from the Earth underneath. This accelerates the alarming growth rate of carbon dioxide (CO_2) emission and other greenhouse gases hence an increase in global pollution (Dubey & Guruviah, 2019).

In considering the objective of decreasing emission of the greenhouse gases, there is a need to develop environmentally friendly sources of energy generation and modern storage technologies. The urge of developing clean and sustainable energy sources is in high gear for renewable energies like solar, hydrothermal, wind among other energy sources that are friendly to nature (Mohmmad et al., 2018; Poonam et al., 2019). The renewable energy systems also still facing several challenges which include efficiency, high cost of materials, and advanced technology. There is a need for technology and materials that can optimize energy usage but also minimize fuel consumption and greenhouse gas emission. Looking at the alternative to fossil fuel consumption are renewable energy sources and the use of electric vehicles (Mohmmad et al., 2018). The renewable energy sources may not show potential impact unless there are effective energy

storage systems to store the energy required at a given time. The energy storage systems are a major key step to handle the challenge of renewable energy impact. This is because there is increased transmission of power from solar, wind, tidal among others from mini-grids to main power grid systems. This benefits only the real-time online users due to lack of storage devices causing overloading of the power grid with low consumption in the off-peak hours (Muhammad Khalid, 2019).

Several improve technologies and excellent discoveries have been made for the energy storage systems which include batteries, supercapacitors, accumulators, hybrids mong other. The discovery in energy storage application introduced innovations like wireless power transfer, output power stabilization, peak-shifting pricing, grid frequency and voltage regulation, micro to main grid integration including recuperation of regenerative braking (Fiori et al., 2016; M Khalid et al., 2018; L. Li et al., 2016; Merei et al., 2016). Batteries and supercapacitors are very known in energy storage systems. These work on the principle of electrochemical energy conversion. Compared to batteries, supercapacitors have high performance and capable of producing 100 to 1000 times higher power density than batteries but have a low energy density of 3 to 30 times lower (Z. Yang et al., 2015). The supercapacitors are increasingly developing towards the solution which can combine high power and high energy in a single device. These supercapacitors have several applications in the industrial field which includes; electric vehicles, accelerating/braking of high-speed transportation systems, powering portable devices like mobile phones, digital cameras, notebooks among others (Najib & Erdem, 2019; Poonam et al., 2019). The new frontiers are being directed to the development of new materials and technologies for energy storage systems. Recently, porous carbon nanomaterials like graphene, carbon nanotubes, carbon nanosheets, activated carbon,

metal oxide composites, conducting polymers, carbon aerogels are playing an important role to improve the efficiency of the supercapacitors (Dulyaseree et al., 2016).

The amount of electric energy produced per mass depends on the chemical energy stored with in the electrode materials. This is governed by the properties of the materials used as electrode. The availability of energy depends on stored chemical energy and the polarisation of the electrodes. The materials basically have two types of polarisation which include activation polarisation to drive an electrochemical reaction and concentration polarisation caused by concentration difference between reactants and products at the electrode surface and electrolyte used due to mass transfer. Supercapacitors can be made from different materials depending on the type of energy storage required by the application at hand, and the capacitance ranges required. The electrode materials for supercapacitors can be classified into three types based on their usage - for EDLCs, pseudocapacitors, and hybrid supercapacitors respectively. There are a significant number of materials presently available for supercapacitors, the major commercial material being carbon, which is widely used and can be converted into many forms.

1.2. Problem statement

In the sector of energy, the conversion of different energy systems into electrical energy is getting a breakthrough. The technologies like solar conversion, thermometric, photo-electrochemical among others are used in the conversion to electric energy. The global challenge is the storage of electrical energy harvested from these different energy conversion technologies that can used at peak demand where production is low. This has created a big gap between conversion and storage since storage capacity and efficiency is still very low, high cost of materials used in the device fabrication. This research work

looked at the best experimental activities for producing activated carbon/graphene as electrode materials for batteries/supercapacitor applications which can have high efficiency, low cost but lightweight. This is in line with science and technology for development, clean and efficient energy storage, and sustainable consumption and production.

1.3. Research objectives

To rationally produce efficient and low cost activated carbon/graphene oxide from maize cobs biomass and locally mined graphite as electrode materials for batteries / supercapacitor applications.

1.3.1. Specific objectives

The specific objective of the study was as follows;

i. To Synthesize graphene oxide and activated carbon from locally mined graphite flakes and maize cob biomass respectively
ii. To characterize the structural, electronic, and mechanical properties of the synthesized porous carbons
iii. To use graphene oxide for hydrothermal synthesis with alkaline metal for battery application
iv. To determine the electrochemical properties of graphene oxide / activated carbon as electrode materials for batteries/supercapacitor applications

1.4. Scope of the study

The scope of the study was to verify the possibility of converting maize cobs biomass and locally mined graphite into materials that can be used as electrode materials for supercapacitors and batteries application.

REFERENCES

Dubey, R., & Guruviah, V. (2019). Review of carbon-based electrode materials for supercapacitor energy storage. *Ionics*, *25*(4), 1419–1445. https://doi.org/10.1007/s11581-019-02874-0

Dulyaseree, P., V, Y., & W, W. (2016). Effects of microwave and oxygen plasma treatments on capacitive characteristics of supercapacitor based onmultiwalled carbon nanotubes. *Jpn J Appl Phys*, *55*(2), 02BD05. https://doi.org/10.7567/JJAP.55. 02BD05

Fiori, C., Ahn, K., & Rakha, H. . (2016). Power-based electric vehicle energy consumption model: Model development and validation. *Appl. Energy*, *168*, 257–268.

Khalid, M, Aguilera, R. ., Savkin, A. ., & Agelidis, V. G. (2018). On maximizing profit of wind-battery supported power station based on wind power and energy price forecasting. *Appl. Energy*, *211*, 764–773.

Khalid, Muhammad. (2019). A review on the selected applications of battery-supercapacitor hybrid energy storage systems for microgrids. *Energies*, *12*(23). https://doi.org/10.3390/en12234559

Li, L., Li, X., Wang, X., Song, J., He, K., & Li, C. (2016). Analysis of downshift's improvement to energy efficiency of an electric vehicle during regenerative braking. *Appl. Energy*, *176*, 125–137.

Merei, G., Moshövel, J., Magnor, D., & Sauer, D. . (2016). Optimization of self-consumption and techno-economic analysis of PV-battery systems in commercial applications. *Appl. Energy*, *168*, 171–178.

Mohmmad, K., Bhardwaj, P., & Varela, H. (2018). Carbon-Based Composites for Supercapacitor. In *Science, Technology and Advanced Application of supercapacitors* (Issue tourism, p. 13). https://www.intechopen.com/books/advanced-biometric-technologies/liveness-detection-in-biometrics

Najib, S., & Erdem, E. (2019). Current progress achieved in novel materials for supercapacitor electrodes: Mini review. *Nanoscale Advances*, *1*(8), 2817–2827. https://doi.org/10.1039/c9na00345b

Poonam, Sharma, K., Arora, A., & Tripathi, S. K. (2019). Review of supercapacitors: Materials and devices. *Journal of Energy Storage*, *21*(January), 801–825. https://doi.org/10.1016/j.est.2019.01.010

Yang, Z., Ren, J., & Z, Z. (2015). Recent advancement of nanostructured carbon for energy applications. *Chem Rev*, *115*, 5159–223.

CHAPTER TWO

2.0. LITERATURE REVIEW

2.1. Energy storage systems

The energy storage system (ESS) is a process of converting harvested energy from a power source into a form of energy that can be stored which can later be converted back for electrical energy when needed. When the energy is generated at a time of either low generation cost or low demand from the source can be utilized at a later time when the demand is higher or when there is no generation or used for peak hours. This makes ESS useful with several applications which include portable devices, stationary energy applications, transportation etcetera (Faisal et al., 2018; Koohi-Fayegh & Rosen, 2020; Wong et al., 2019). The high demand for energy consumption with the rapid growth of CO_2 is due to the rising population growth rate, development demands, and urbanization. These demands require optimum use of energy hence depletion of fossil fuel and becoming the possible solution for the rapidly growing demands. The ESS is the main part of the renewable energy integration which helps to balance the power generation and consumption. This creates stability in the system with significant effects on the overall electric system to store the energy for peak time consumption (M. Di Somma, 2015; Sandoval et al., 2017). The stability challenge mostly due to fluctuation which is caused by the high penetration of renewable energy in the system.

Solar and wind energies are commonly used for electric power generation with the installation of wind and photovoltaics (PV) capacity increasing every year. These are widely used to reduce greenhouse gas emissions by generating electrical energy to meet the demand (H. Zhang et al., 2016). Several storage technologies are applied in the ESS

structure to store produced electrical energy (Chemali et al., 2016; Mahlia et al., 2014). Different categories of ESS and their energy conversion mechanism and efficiency have been studied (Cansiz', 2018). The electric energy can be stored electrochemically in batteries and capacitors. Several new electrode materials and electrolytes have been studied to improve the performance, lower costs, increase energy and power density, safety, cycle life, and stability.

2.1.1. Energy storage system components

The components of ESS one grouped according to the function of the store energy which includes battery storage components, reliable system operation components, grid connection components. The battery system consists of the following;

a) Battery pack with cells for a given voltage and capacity
b) Battery management system for protection from external effects
c) Thermal system to protect the cell from damaging operation like the voltage, current, and temperature. This controls the temperature of the cells to achieve absolute working conditions (ADB, 2018).

2.2. Batteries Energy Storage Systems (BESS)

The batteries energy storage system (BESS) is considered as one of the most important and efficient systems for stabilization of electricity network system (Cansiz', 2018). BESS are economical, low maintenance, compact, and easy to assemble in the network system. These are composed of several connected cells arranged in series or parallel which uses a chemical reaction process to convert electrical energy into chemical energy and vice versa. The lead-acid battery energy storage system (LBESS) is the most widely used technology for largescale. The advancement of technology has resulted in new BESS

which includes; Sodium-sulfur, lithium-ion, sodium-ion, lithium-sulfur, sodium-nickel chloride, nickel-cadmium, metal-air, magnesium ion, and other several technologies as secondary cells (Koohi-Fayegh & Rosen, 2020; Ogunniyi & Pienaar, 2017). A battery system consists of cells composed of two electrodes namely anode and cathode and the electrolyte. The assembly of electrodes and electrolytes is kept close in a sealed container to avoid interaction with the atmosphere. The electrolytic ion exchange between the electrode creates the flow of electrons through the system to the external circuit as shown in Figure 2.1.

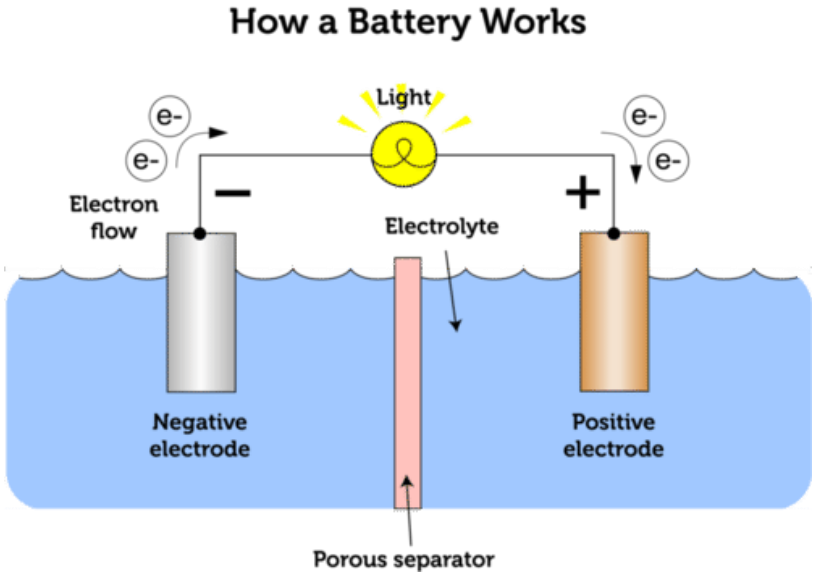

Figure 2.1: Schematic operation principle of a battery cell.

2.3. Supercapacitors (SCs)

The developing technology of SC showing improvement in energy density values and they tend to be closer as an alternative for conventional batteries (Genc et al., 2017). This is done by the use of multi-functional electrode materials with smart designs. The physical and chemical properties of the electrode materials lead to low cost and eco-friendly energy conversion and storage. The impact of SCs comes from the double layer where the capacitance is generated from pure electrostatic charge accumulated at the

electrode/electrolytic ion interface. The capacitance of SCs is defined by the electrochemical double-layer capacitor (EDLC) materials or pseudo-capacitor coming from reversible redox (Reduction and oxidation) reactions. When the SC combines both mechanisms it is called hybrid SC as shown in Figure 2.2 (Najib & Erdem, 2019). The electrode materials used in SC are the most important component of the SC (Iro Zaharaddeen et al., 2016). SCs have high power, long life, flexible packaging, low weight and low maintenance, friendly assembling technology, wide thermal range of -40 to 70^{o}C. the electrochemical performance of SCs electrode material depends on the properties of the materials such as specific surface area (SSA), electrical conductivity, pore-volume, the permeability of the electrolyte ions, and wetting of the electrode (Iro Zaharaddeen et al., 2016).

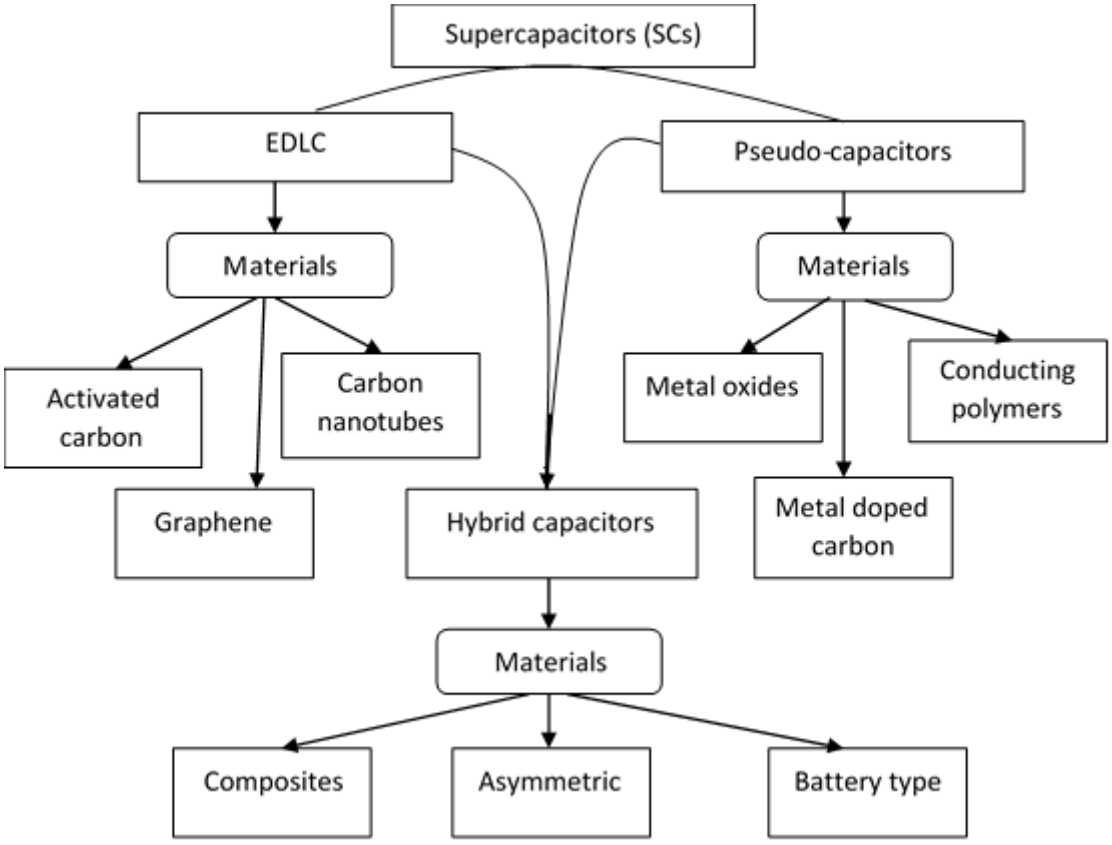

Figure 2.2: The supercapacitor taxonomy (Dubey & Guruviah, 2019)(Najib & Erdem, 2019)(Iro Zaharaddeen et al., 2016).

2.3.1. Electrochemical double-layer capacitors (EDLC)

The principle of EDLC is based on the electrostatic charge stored between the electrode material and the electrolyte solution interface or by a non-faradaic process that involves no transfer of charges between electrolyte and electrode (Figure 2.3). When a voltage is applied on an assembled SC, there is the acceleration of charges on the surface of the electrode caused by the difference in the potential creating an attraction of opposite charges which results in electrolytic ion diffusion over the separator to move to the oppositely charged electrode. A double layer of charges is formed at the surface of the electrode to avoid recombination of ions. This causes a decrease in the distance between electrodes due to increased surface area and allows the EDLC to attain a higher energy density (Najib & Erdem, 2019).

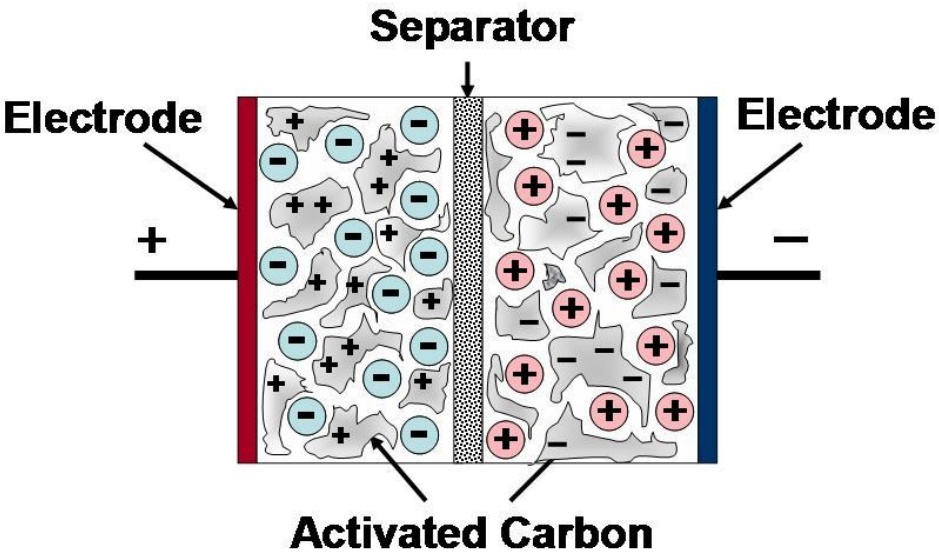

Figure 2.3: EDCL device set up (C, 2020).

The fundamental equation for all capacitors to determine the capacitance is shown in equation 1 (Mohmmad et al., 2018; Najib & Erdem, 2019)

$$C = \frac{(\varepsilon_o \varepsilon_r A)}{d} \tag{2.1}$$

Where A is the surface area of the used electrode, ε_o is the permittivity of free space, ε_r is the relative permittivity of the dielectric material and d is the distance between two electrodes.

Basing on the relationship from Eqn (2.1), the capacitance of a capacitor can be increased by an increase in the dielectric constant of the material, an increase in the surface area, and a decrease in the interplanar thickness. The change in capacitance can be increased by improving the properties of the materials like an increase in pore volume, specific surface area (SSA), particle size etcetera. The charge and discharge cycles of the EDCL are highly reversible because of the non-faradaic behavior of the electrical mechanism. This creates extremely stable cycling stability of more than 10^6 cycles, a high rate of charge-discharge with low degradation (Faisal et al., 2018). The EDLC storage principle allows a very fast energy uptake, better power performance, and delivery due to the non-faradaic process which causes no chemical reaction. The non-faradaic process prevents swelling and expansion of active materials which is common in batteries during the charge-discharge process. EDLC differs from the batteries in the charge storage mechanism and cycling life.

2.3.2. Pseudocapacitors

These store charge via a faradaic process that involves the transfer of charges between electrolyte and electrodes. When a potential is applied on an assembled device of pseudocapacitor, the reduction redox reaction takes place on the surface of the electrode materials that involve the transfer of charges across the double layer generating a faradaic current through the supercapacitor cell (Iro Zaharaddeen et al., 2016). The faradaic process allows the materials to achieve higher specific capacitance and higher energy density compared to EDLC materials, pseudocapacitors electrode materials are prepared

by redox, spinning, and intercalation methods. The electrode materials of pseudocapacitors include; metal-doped carbon, metal oxides, and conducting polymers. These materials lack stability during long cycles and lower power density (Najib & Erdem, 2019).

2.3.2.1. Conducting polymers

This type of SC can display a high capacitance and high conductivity at low electrical series resistance (ESR) and low cost compared to EDLC based carbon SC. They have high potential density with examples like polypyrrole, polythiophene, and polyaniline (Allagui et al., 2018). This is attributed to their conductivity and flexibility which are the parameter for improving capacitance (Faisal et al., 2018). The conducting polymers suffer from lower cycling stability than the carbon-based electrodes. The materials usually require doping to boost conductivity which in turn affects the volume hence causing swelling and increased thickness of the electrode creating failure in the device (Najib & Erdem, 2019).

2.3.2.2. Metal oxides pseudocapacitors

This type of SC provides a very high conductivity resulting in high specific capacitance but high cost. They still have low involvement in SC due to their processes of fabrication which include sol-gel, anodic deposition, insertion, intercalation, spray deposition, oxidation, hydrothermal synthesis etcetera (Faisal et al., 2018). These metal oxides improve capacitance at lower current density but they are said to cause cracks in the electrode which leads to short-term stability (Faisal et al., 2018). They are combined with carbon forming a composite to avoid cracks forming in the electrodes (Najib & Erdem, 2019).

2.3.3. Hybrid supercapacitors (HSC)

This type of SC offers a combination of both EDLC and pseudocapacitors performances. It combines the high energy and high power from the battery like electrode and capacitor like electrode respectively. The HSC has a combination of polarizable (carbon) electrode and non-polarizable (metal or conducting polymer) electrode to store the charges and also used both faradaic and non-faradaic processes to obtain high energy storage through the electrodes (Muhammad Khalid, 2019), exhibiting a low cost and better cycle stability than EDLC. The electrode combination is categorized into three which include; asymmetric, Battery-type, and composite (Iro Zaharaddeen et al., 2016; Najib & Erdem, 2019).

2.3.3.1. Asymmetric hybrid supercapacitors

This type of hybrid combines faradaic and non-faradaic processes by bringing the EDLC and pseudocapacitor behavior of electrodes together. In the asymmetric setup, carbon is mainly the negative electrode with either conducting polymer or metal oxide as the positive electrode (Iro Zaharaddeen et al., 2016). They are set to work simultaneously to reach high power and energy density requirements. One electrode will be a capacitive electrode and the other will be a faradaic electrode. The metal oxide electrodes have a high intrinsic volumetric capacity which leads to an increased energy density (Mathis et al., 2019). This type of setup can show higher energy density and excellent cycling stability compared to symmetric supercapacitors (Najib & Erdem, 2019). These capacitors face the challenge of short self-discharge which can be improved by introducing a simple rocking chair mechanism to ensure maximum potential at zero current (Poonam et al., 2019). There is also a possibility of electrolyte ion depletion of

the electrodes causing a decrease in conductivity with an increase in the internal resistance (Najib & Erdem, 2019).

2.3.3.2. Composite hybrid SC

These SC employ composite electrodes with a combination of carbon-based materials with either conducting polymer or metal oxides in a single electrode. The single electrode will contain both chemical and physical charge storage mechanism. The capacitive double layer of charges offered by carbon-based materials and improve the contact between the electrolyte and the pseudocapacitor materials. The composite electrode materials increase capacitance with faradaic reaction (Muhammad Khalid, 2019). The composite electrode materials include binary and ternary composite. The binary composites use two different electrode materials and the ternary composite uses three different electrode materials for a single electrode (Xuli Chen et al., 2017; Iro Zaharaddeen et al., 2016).

The objective of the composite hybrid is to have synergistic results of specific capacitance, excellent cycling stability, and high conductivity. The conductivity of composite is highly tuneable but it depends on carbon structure and the porosity (Dubey & Guruviah, 2019). This makes pore diameter and important factor that determines the ions' absorptivity on the surface of the electrode to define charge-discharge characteristics composite materials have a limitation when successive ion diffusion reduces to protruding nanowhiskers which grow on the carbon nanofibers even through the surface area of the metal oxide increases (Najib & Erdem, 2019).

2.3.3.3. Battery-type hybrid

These types of hybrids are on the diagonal center point of the Ragone plot with promising traits for higher specific capacitance, power density, and energy density. These materials

are still to be excelled in application compared to the present SCs. This type combines two different electrodes like asymmetric hybrids. They combine battery and supercapacitors electrodes to utilize the properties of both in a single cell (Najib & Erdem, 2019). The combination creates an electroactive nanoparticle which leads to faster reactions with the electrolyte hence leading to a redox faster reaction process. The electrode materials create a Helmholtz double layer where the charge is stored at the interface between electrolyte and carbon electrode (Dubey & Guruviah, 2019). This occurs due to like-charges being repelled from each other at the interface and attraction in the counter ions which causes a mechanism in physical charge storage (Najib & Erdem, 2019).

2.4. Carbon-based electrode materials

Different forms of carbon materials are mostly used in electrode materials in the fabrication of different SCs. These are used due to different properties which include; low cost, availability, high surface area, and electrode production technology. The storage mechanism involved in carbon materials is the electrochemical double layer occurring at the interface between the electrolyte and electrode. The capacitance of the material depends on the surface area, pore size distribution, surface functionality, pore shapes and structure, and electrical conductivity (Iro Zaharaddeen et al., 2016). The high specific surface area in carbon materials leads to a high capability for the accumulation of charges at the interface of the electrolyte and electrode. Several carbon materials are used as electrode materials which include; graphene/graphene oxide, activated carbon, carbon nanotubes, carbon aerogel etcetera (Xian Jian et al., 2016).

2.4.1. Graphene/graphene oxide

The flattish materials since its discovery by Novoselov and Geim in 2004, it has gained enormous attention. The graphene is a flat sheet thin layer with an sp^2-bond. The 2-dimensional honeycomb lattice of arranged carbon with fully conjugated structures of alternating C=C and C-C bonds. It has unique quasi-metal physical-chemical properties which makes it a suitable material for energy storage systems. The use of graphene as a material for an electronic application requires specific functionalization of the graphene sheets into their derivates at a molecular level. This makes surface functionalization of graphene sheets an important aspect using different covalent and non-covalent methods for making graphene materials with the bulk and surface properties required for potential application which include energy conversion and storage. The excellent electrical, high mechanical strength, thermal conductivity, and theoretical surface area ($2600 m^2/g$) make it suitable for energy storage devices (Mohmmad et al., 2018). The functionalized graphene is graphene oxide (GO) with functional groups on the surface and the allotropes like 3D-graphite, 1D carbon nanotubes all have hexagonal rings structure with different orientations in space (Borenstein et al., 2017).

In general, graphene activation properties can be attained by methods such as; exfoliation method, introducing spacers between its layers, templating technique, or forming hydrogel by reducing graphene oxide. For application purposes, graphene is not used as pristine but it has to be applied as reduced graphene oxide or doped graphene or activated graphene or graphene/polymer composites or graphene/metal oxide composites (Mohmmad et al., 2018). Literature reported new carbon material by chemical modification of one-atom-thick layer of graphene with specific surface area 705 m^2/g, which exhibited high specific capacitance of 135 F/g in aqueous electrolyte and 99 F/g in

organic electrolyte. Also, exhibited good retention ability over a wide range of voltage scan rates (Muhammad Khalid, 2019). Another literature reported the synthesis of graphene with thermal exfoliation of graphitic oxide at a very high temperature of 1050°C which showed a high surface area of 925 m^2/g and specific capacitance is 117 F/g in aqueous 2M H_2SO_4 electrolyte. Alternatively, functionalization of graphene can also be attained by controlled thermal exfoliation at low temperatures (Y. Liu et al., 2017) without compromising its capacitance performance. Chemical functionalization of graphene oxide platelets grown on highly porous, intrinsically flexible, and ordered carbon films by nitrogen doping (Mohmmad et al., 2018) has proven to increase its electrical as well as supercapacitive properties. The above-discussed activation methods have led to the production of materials with high capacitance but for actual practical application of these materials, the other important factor to be considered is energy density. The commercially accessible batteries have higher energy density than supercapacitors. This means that supercapacitors can provide a very high energy pulse when required but can store less energy per unit weight, as compared to batteries. The literature reported the synthesis of 1-layer graphene in a curved form which limited the face-to-face restacking of its sheets, hereafter, utilizing maximum possible electrode surface. This resulted in supercapacitor electrode material with a very high specific energy of 86 and 136 Wh/kg at room temperature and 80°C respectively at 1 A/g current density (Muhammad Khalid, 2019). There is also a description for the development of sponge-like graphene nanostructures that exhibited a high energy density of 48 kW/kg. There is a new approach to efficiently maximize the surface of each layer of graphene structure by using the “in-plane” strategy in place of stacking (Y. Liu et al., 2017). Lest of conventional (stacked) assembly, the entire electrochemical (specific) surface area cannot be used because some of the regions are unapproachable to the electrolyte ions.

Although, the new structural design assists the percolation of electrolyte ions between graphene layers to reach the current collector. Therefore, facilitating the high usage of available specific surface area (Y. Liu et al., 2017). This type of in-plane 2D graphene supercapacitor has shown a high specific capacitance of 250 F/g at current density 176 mA/g with good retention rate for 1500 cycles.

2.4.2. Graphene-Metal oxide composite

There are several carbon-based materials like carbon nanotubes, carbon quantum dots, graphene, and nitrogen-doped carbons that can be used as single electrode materials because of their unique electrical, structural, and mechanical properties. Yet, they demonstrate low volumetric capacitance performance and are hard to fabricate. Composing nanocarbon like graphene applied to supporting 3-D activated carbon matrices may create high-capacity composite electrodes (Sonawane et al., 2018). Furthermore, the nanoworld may be too far from practical realities. Nanomaterials that can display outstanding performance at low electrode loading in research testing may not fit heavily loaded electrodes which are necessary for practical devices. Composite materials may provide the right solution for active nanomaterials embedded in micrometric size carbonaceous matrices that can serve as a robust active mass with excellent inter-particles electronic contact and appropriate mechanical stability (Moyo et al., 2018). Embedding nanocarbon like graphene or nanotubes may create mesoporous structures with high specific surface area and excellent cycle stability. For SC applications, the porosity of the electrode material is a crucial factor and proved to be highly established when various nanocarbon are embedded in activated carbon matrices. This can help achieve materials an interesting synergy in which the carbonaceous matrix stabilizes the active nanoparticles, thus improving their charge storage capability, and the

latter moieties, in turn, stabilize meso-porosity of the composite matrices what enables to obtain high-rate capability (Borenstein et al., 2017).

The MnO_2/CNT composite was prepared using a simple hydrothermal treatment. The MnO_2/CNT nanocomposite electrode displayed a higher specific capacitance and rate capability compared to pure MnO_2 and CNT electrodes. High specific capacitance gotten in the composite can be attributed to the high specific surface area of MnO_2 and high porous structure (Iro Zaharaddeen et al., 2016). In literature, an asymmetric supercapacitor was assembled using MnO_2 and graphene. The prepared composite of MnO_2-coated/graphene was used as a cathode while pure graphene was used as an anode. The process of electro-activation was used on a graphene electrode where a capacitance of 245 F/g at a charging current of 1 mA was reported. When MnO_2 was deposited, the capacitance increased to 328 F/g at the same charging current resulting in an energy density of 11.4 Wh/kg and a power density of 25.8 kW/kg (Iro Zaharaddeen et al., 2016).

CNT and graphene can be surface functionalized by metal oxide, polymers, or oxidizing to be stunned by the presence of some impurities. In research carried CNT/MnO_2 composite, first, it was observed that there was a vertical alignment in CNTs resulting in a higher capacitance as compared to random ones. This indicates that morphology affects capacitance significantly. Secondly, when water plasma treatment was applied on the surface and it gave higher results due to the clearer and larger active surface of nanotubes. Lastly, the addition of MnO2 via the electrochemical deposition technique exhibited the highest specific capacitance of 475 F/g (Iro Zaharaddeen et al., 2016). When carried out using a composite of reduced graphene oxide (RGO) with molybdenum sulfide (MoS_2) synthesized by a simple process of one-pot hydrothermal. The resultant composite

exhibited a specific capacitance of 253 F/g at a current density of 1 A/g with excellent cycling stability (Najib & Erdem, 2019).

Activated carbon having good properties like large-good electrical properties, surface area, and the moderate cost was used in three different metal oxides Cobalt (Co), Nickle (Ni), and Manganese (Mn) for different combinations to produce the highest specific capacitance. The AC was used as anode and a combination of any two of the metal oxides as a cathode. The degree of inversion was diverse by a factor of 0.2 to study the effect on the performance. A combination of 12 different samples was organized and the highest specific capacitance was 78 F/g from ($Mn_{0.6}Co_{0.4}$) which was due to large pores that were examined from the SEM images that allowed easy diffusion of electrolyte. The least value was 5F/g for ($Mn_{0.8}Co_{0.2}$) due to a non-uniform crystalline image with a hairy surface that made it difficult for electrolytic ion movement (Muhammad Khalid, 2019).

Several metal-oxides like MnO2, RuO_2, TiO_2, NiO, ZnO, Fe_3O_4, MnO_2, MoO_3, Mn_3O_4, Co_3O_4, and $CoMoO_4$ (Mohmmad et al., 2018) among others have been used as possible electrode material in supercapacitors (Cao et al., 2015; X. Yu et al., 2014). When these active materials are added to the graphene structure in an appropriate quantity, they can exhibit an excellent electrode material performance. When added, the metal oxide nanoparticle acts as nano-spacers between the graphene layers to prevent it from restacking. Also, the free space between the 2-D graphene sheets creates a smooth horizontal way for the mobility of the electrolytic ions hence improving the energy storing capacity. The literature described the supercapacitor behavior of graphene-SnO_2 and graphene-ZnO composite materials (Y. Liu et al., 2017). They found that the electrochemical performance of graphene-ZnO composite was improved to a great extent in terms of capacitance value and reversibility when compared to pristine SnO_2 or ZnO

or graphene. The specific capacitance of 61 F/g and energy density of 4.8 Wh/kg was reported, which greater than that of graphene-SnO_2 samples. Graphene-MnO_2 composite with high MnO_2 content (78 wt.%) exhibited a specific capacitance of 310 F/g at a scan rate of 2 mV/s. The literature claims that hybridization of MnO_2 and graphene caused an increase in the specific surface area exhibiting a higher conductivity and that led to a high-performance rate (Y. Liu et al., 2017).

Besides, conventional symmetric supercapacitors, several studies have been carried out to exploit the potential of asymmetric supercapacitors devices based on metal oxide/graphene composites (Y. Liu et al., 2017). Fabrication of asymmetric supercapacitors aims to attain a higher energy density. The most crucial step when assembling is the choice of two such electrodes, that have the same working potential range and appropriate wettability in the same electrolyte. This allows the extension of the operating potential window along with the enhanced capacitance performance rate. In literature, a study established that an asymmetric supercapacitor assembled using MnO_2 nanoparticles as anode and graphene as cathode displayed a specific capacitance of 37 F/g and could operate up to a voltage range of 2.0 V with capacitance retention of 96% for 500 cycles. This displayed a much higher energy density of 25.2 Wh/kg and power density of 100 W/kg when compared to 4.9 Wh/kg of MnO_2/MnO_2 and 3.6 Wh/kg of graphene/ graphene-based symmetric supercapacitors (Y. Liu et al., 2017).

The planar SC was fabricated by using δ-MnO facial assembly set with reduced graphene oxide (RGO) flakes. The interactions caused due to morphologically and the synergic interaction with electrostatic effects was enhanced by the RGO and MnO_2 nanosheets integration. Synthesis of graphene aerogels (GA) has also been reported in the literature using a sol-gel method (C. Wang et al., 2014). The synthesized GA exhibited a good

specific surface area of 793 m^2/g, a high pore volume of 3 cm^3/g, and a high specific capacitance of 410 F/g. The effect of the 3D network of GA support and the structural advantages resulted in good stability with depletion of 5% in 50,000 cycles and capacity of 410 F/g. An outstanding electrical and mechanical property of 3D graphene foam has been reported using the CVD synthesis of graphene foam (GF) on nickel foam (NF). This was more followed by the $CoMoO_4$ (X. Yu et al., 2014) and MnO_2 (Cao et al., 2015) hydrothermal deposition. There was no need for any other metal current collector since graphene has good mechanical and support conductance. The specific capacitance of 144 F/g for GF-Ni (OH) and 439.7 F/g for GF-$CoMoO_4$ was reported with a power density of 44 W/kg and 900 W/kg respectively which describe its usage for stretchable and flexible SCs due to its structural property and superior electrochemical. Literature reported about the graphene nanocomposites employing an in-solution process (Cao et al., 2015) with the Co_3O_4 and Mn_3O_4. Using Hummer's method for synthesis of graphene oxide (GO) and the precursor solution was intermixed with the graphene oxide. The Mn_3O_4/Co_3O_4 composite was deposited onto the RGO using thermal and microwave to assist the treatment carried out. The cobalt oxide nanoparticle microwave-assisted intercalation was also proposed using graphene wrapping (R. Kumar et al., 2014).

Nanostructured carbon-based electrode materials are most widely used for electrochemical applications due to their good electrical property, low cost, chemical and thermal stability, and good reversible redox reaction feasibility. Though, these properties do not offer good energy density-high specific capacitance and stable cycle life. To overcome these defects, the nanostructured carbon-based materials are mostly combined with the metal oxides. Thus, the designing of an electrode with flexible carbon fiber foam (CFF) and MnO_2 has been employed as advanced research that contributes to the

electrochemical behavior during both the charging and discharging period. The choice of CFF as the current collector is due to its high corrosion resistance, easy fabrication, low cost,1D structure, and high electrical conductivity. MnO_2 had been recognized as a promising candidate for its simple synthesis process (Dubey & Guruviah, 2019).

A few researchers have successfully developed a solid-state highly flexible CFF/MnO_2-based electrode material for supercapacitor applications. Hydrothermal synthesis is one of the methods used to functionalize CFF with coral-like MnO_2 nanostructure for the improvement of the pseudocapacitive properties (Reddy et al., 2015). The specific capacitance of 467 F/g with 100% initial capacitance maintenance after 5000 cycles is attributed to the presence of the unique structure of the electrode which permitted fast ion diffusion. Also, observed an energy density of 20 Wh/kg and faster charge and discharge rates. Morphology of the thermally aged CFF/MnO_2 and CFF hybrids were examined after reaction at 175 °C. in the report, observations made by the FESEM images exposed the interaction between CFF and MnO_2 which was quite strong and the CFF acted as a good substrate. In addition to these, an energy density of 20 Wh/kg and power density of 0.175 kWh/kg was reported for the devices fabricated with CFF/MnO2 (Dubey & Guruviah, 2019).

Graphene and graphene oxide (G/GO) are used in SCs applications because they do not depend on the distribution of pores in the solid-state as compared to other carbon materials (Iro Zaharaddeen et al., 2016). If the theoretical SSA is fully utilized, graphene can produce a capacitance of 55F/g (Xuli Chen et al., 2017). When graphene is used as an electrode material, all major surface sheets are readily available for electrolyte interaction. The synthesis of GO by acid oxidation of graphite (Xuli Chen et al., 2017) followed by chemical reduction, provides an effective method for low-cost mass

production of reduced graphene oxide (RGO) that can directly be used as EDLC electrode materials. The traditional way of producing graphene is initiated by graphite using the oxidization method to form graphene oxide. This is achieved by Hummer's method or modified Hummer's methods and other methods as shown in Figure 2.4. for producing GO sheets, a complete exfoliation of graphite oxide can mechanically be carried out by sonication (Dubey & Guruviah, 2019).

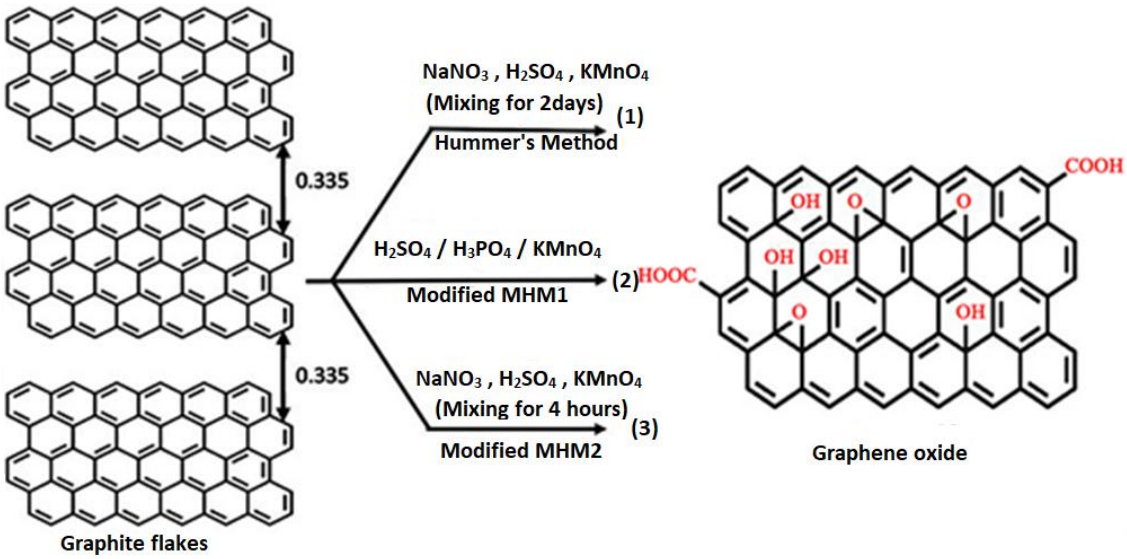

Figure 2.4: Graphene oxide synthesis by chemical oxidation method from graphite (Adetayo & Runsewe, 2019).

The chemical oxidation method produces graphene which starts with introducing functional groups like hydroxyl, carbonyl, and peroxyl between carbon layers of graphite. These functional groups weaken the binding van der Waal bonds between carbon layers to peel off layer by layer from graphite (Dubey & Guruviah, 2019). The resulting GO can be reduced to graphene by adding hydrazine solution into the GO solution. Large surface area graphene is highly desirable because it significantly reduces high inter-sheets contact resistance compared to smaller area graphene. The graphene sheets exhibit a drawback of easily forming restacks and irreversible agglomeration to their graphite structure which

makes determining intrinsic capacitance difficult. The graphene-based SCs are capable of operating up to a potential of 4.5V and an energy density of 85.6Wh/kg at room temperature and 136Wh/kg at 80^{o}C in the ionic liquid was a report in the literature (Xuli Chen et al., 2017).

The oxides of graphene work as an important alternative material to be used for nanocomposite formation. To improve the electrochemical properties of graphene-based electrodes, the materials have to be doped with chemicals having electron donors and acceptors. From the literature, a specific capacitance of 242F/g was reported by using N-doped-graphene oxide for SC with a capacitance of 320F/g was obtained from highly nitrogenated graphene oxide (D. Wang et al., 2014). The GO synthesized by modified hummer's method was experimented on a 2.5 to 7.5A/g and the highest current density of 7.5A/g produced energy density of 58.25 Wh/kg and power density of 13.12 kW/kg (Iro Zaharaddeen et al., 2016). The conventional graphene and RGO electrodes with electrolyte ion can only transfer charges between graphene sheets that inevitably leads to a much longer ion-transport path with their ions transferring through the graphene sheets. In literature, it was reported that holy-graphene sheets can allow ions to a path through the holes with limited transport path while keeping the electron-transport efficiency (Y. Xu et al., 2014). Doping graphene using hetero-atoms can improve the electrochemical/electrical properties of energy storage including other properties of energy storage (Y. Liu et al., 2016). Several works of literature have been reported with doping and improvement with GO as shown in Table 2.1.

Table 2.1: Graphene and GO nanomaterials in EDLCs

Electrode	Electrolyte	Specific capacitance (F/g)	Energy density (Wh/kg)	Power density (W/kg)	References
G – functionalized -OH & -COOH	0.075M hydroquinone & 1MH_2SO_4	3199 at 5mV/s	-	-	(G. Wang et al., 2014)
Hollow graphene	EMIMBF_4/AN	298 at 1A/g	53	1000	(Y. Xu et al., 2014)
N-doped graphene	1M $TEABF_4$	280 at 20A/g	48	800	(Y. Liu et al., 2016)
N/P doped RGO	6M KOH	165 at 0.1A/g	-	-	(Ke & J., 2016)
Graphene aerogel	3M KOH	4.76 at 0.4A/g	0.26	4080	(Zhu C, 2016)
Graphene aerogel	0.5M H_2SO_4	325 at 1A/g	45	7000	(Jung et al., 2015)
2D micro porous GO	EMMBF4	151.3 at 0.1A/g	42	10000	(Hao L, 2015)
N-doped GO	6M H_2SO_4	396.5 at 0.2A/g	-	-	(Jia, Y, & G, 2016)
Graphene / CNT	PVA/H_3PO_4	31.5 at 0.04A/g	-	-	(H. Sun et al., 2014)
Free standing graphene	1M Na_2SO_4	150.2 at 1A/g	-	-	(G. Sun et al., 2015)
RGO/Fe2O3	Organic solvent	855.2mAh/g at 0.02A/g	129.6	1870	(M. Li et al., 2016)
RGO/Cu	-	81.3	11.25	5000	(Purkait et al., 2018)
Metal oxide/ RGO	H_3PO_4/PVA	281.3F/cm^3	18.2 mWh/cm^3	76.4 mW/cm^3	(W Ma et al., 2016)
C-GO	6M KOH	329.5 at 0.5A/g	-	-	(Y. Song et al., 2016)

MnO2 CNT/GO	6M KOH	210 at 1mA/cm^2	24	10000	(Leea & B-H, 2016)
CoO/GO	2M KOH	889 at 2A/g	28.7	1600	(R. Wang et al., 2017)

2.5. Activated carbon (AC)

Recently, there is a significant increase in agricultural activities to support the growing population demand and sustainability. An increase in agricultural crop production leads to an increase in biomass as waste. These agricultural crop residues/wastes are left at the farms have slow degradation and therefore lead to waste management and often farmers resort to burning. Thus, the conversion and utilization of that biomass into value-added material is paramount. Biomass such as maize corn cobs, rice husks, coconut shells, sugarcane bagasse to mention but a few has been explored for the production of porous activated carbon for industrial application (Biswal et al., 2013; Xiufang Chen et al., 2017; A. Elmouwahidi et al., 2012; Adbelhahim Elmouwahidi et al., 2017; J. Hou et al., 2014; Mi et al., 2012b; Tian et al., 2015; L. Wei et al., 2011; T. Wei et al., 2016; Z. Zhu et al., 2015). The Activated Carbon (AC) with varying surface areas are abundantly being used for industrial application which includes energy storage materials, removal of toxic compounds, purification, and separation in liquids and gases, catalysts or catalysts support(Adrian et al., 2016; A. Elmouwahidi et al., 2012; Adbelhahim Elmouwahidi et al., 2017; Fraczek-szczypta et al., 2015; Lim et al., 2010; Rufford et al., 2010; Yakout & G. Sharaf, 2016), reduction in CO_2 (Shafeeyan et al., 2010) removal of dyes and odour (Yakout & G. Sharaf, 2016).

Zea Mays knew as Maize or corn is the most widely cultivated cereal grain food in Africa. The cultivation of maize is widespread particularly in the Eastern, Western, Southern, and central parts of Africa. This plays a big role in most homes as support for food and income-earning for the rural economy. The production yield per hectare (tons/hectare/year) of approximately 30 YPH by 2018, which was greater than the USA, China and Brazil combined at 22 tons/hectare/year (VIB, 2018). Normally, the maize corn cobs are treated as agricultural crop residue/waste as a result of harvesting where only the grains are taken for further processing and the cobs are disposed-off in the farm, power plant sites, and others are burnt to ashes. This causes environmental challenges such as pollution.

There are two major methods for conversion of biomass like corn cobs into AC which are; Chemical and physical activation (Adbelhahim Elmouwahidi et al., 2017; Yakout & G. Sharaf, 2016). The physical activation has mainly two (2) stages namely; carbonization of the carbonaceous material and activation at elevated temperatures in a suitable atmosphere of gases like Argon or Nitrogen (Lim et al., 2010). This process results in the removal of some volatiles, hence producing a wide range of pores which creates porous AC. This method has been adopted in industries for commercial production of micro-porous AC because of its environmental sustainability.

In the chemical activation method, the precursors (biomass) are impregnated with chemicals having dehydrating properties such as H_2SO_4, H_3PO_4, $ZnCl_2$, K_2CO_3, NaOH, KOH to mention but a few. These are used to carbonize at different conditions basing on the design of the experiments (Lim et al., 2010). Some chemicals are used to activate lignocellulosic materials which include H_3PO_4 and $ZnCl_2$. Strong bases like KOH and NaOH are used in the activation of coal precursors and chars (Lim et al., 2010; Yakout &

G. Sharaf, 2016). The main challenge of a chemical method with some chemicals like $ZnCl_2$ is the environmental contamination which includes corrosion and lack of chemical recovery methods. Impregnated KOH precursors yield large micro-porosity because it intercalates with the carbon matrix (Prahas et al., 2008). The chemical method provides several merits to the precursor which may include the use of single-stage activation, working at low-temperature ranges, short holding working time, higher porous structure, and high yield (Lim et al., 2010).

The chemical characterization of AC is mostly determined by the ability of the surface to obtain heteroatoms. This forms functional groups and delocalization around the structure which primarily identifies the acidic or basic character of the AC at the surface (El-sayed & Bandosz, 2004; Laszlo & Szucs, 2001). AC has reducing capability because of the functional groups of oxygen such as phenolic, lactone, carboxyl, and quinone (Manyala et al., 2016). Different carbonaceous electrode materials are used in supercapacitors (SC) because of high surface area, porosity, and surface functional groups. Materials such as AC (Yao et al., 2015), carbon composites (Yeon et al., 2017), metal carbide-derived carbon, Graphene and its derivatives, Carbon aerogels (Jae et al., 2014; Vlad et al., 2016) among others. The charge storage of electrochemical double-layer supercapacitors (EDLS) is based on interfacial layers formation of the electrode surfaces. This makes the surface area of materials for electrodes very important in SC application (Xiang et al., 2013; Yao et al., 2015). AC-derived materials are highly levelled to have higher porosity, high surface area, high chemical, and physical stability, and high packing density (Das et al., 2015; Lekakou et al., 2011). Commercially available ACs are synthesized from different biomass due to their low cost of production and environmental friendliness. The porous nature of AC material is advantageous in SC application with microporous and

microporous being more influential for charge transfer in the performance. The macropores also facilitate the transport zone with the structure of carbon materials. The high capacitance values are primarily due to the surface area of the material and the stability of electrolytes (Van et al., 2014). Liquid phase oxidation method of treatment is known in introducing oxygen and its functional groups onto the surface of activated carbon (AC) at lower temperatures of operation compared to other methods of gas phase (Shafeeyan et al., 2010).

AC is highly on-demand as materials for the fabrication of the SC electrodes. These have high specific surface area (SSA), low cost and availability make them widely preferred active materials for electrodes. In the synthesis, the carbonization process aids the production of amorphous carbon and the thermal chemical conversion of the precursors. The activation process leads to the manipulation of SSA. This is reached by partial controlled oxidation of carbon precursors gaining either by chemical or physical activation (Dubey & Guruviah, 2019). The theoretical SSA of AC is about $3000 m^2/g$ although literature reports a usable SSA range of 1000 to $2000 m^2/g$ (Purkait et al., 2018). The most commercially available have a working potential of 2.7V when employing AC as an electrode material and specific capacitance range of 100 to 120F/g (R. Wang et al., 2017) and a volumetric capacitance up to $660 F/cm^3$ (Dubey & Guruviah, 2019) and the specific capacitance of 300F/g (M. Li et al., 2016). These two processes result in activated carbon with theoretical surface area ($3000 m^2/g$) and pore size distribution in a wide range of macro-pores, mesopores, and micropores (>50–2 nm) (M Khalid et al., 2018). The micropores are in general considered to be inaccessible for electrolyte ions thus not capable of supporting an electrical double layer. The mesopores have maximum contribution towards capacitance in an electrical double layer capacitor followed by

micropores (Muhammad Khalid, 2019). EDLC and pseudocapacitance both are surface phenomena, thereby, activated carbon with a high surface area is the perfect candidate for application as electrode material (Najib & Erdem, 2019). Though, the experimental value of capacitance for activated carbon-based supercapacitor was found to be in the range 1 to10 $\mu F/cm^2$ which is lower than the theoretical calculations. This has been explained in detail by W. Li et al. (W. Li et al., 2016) and found that the surface area of the electrode material is not the only factor that determines the performance of the electrode. Several parameters need to be considered for calculating capacitance for instance; shape, structure, and size distribution of the pores along with the electrical conductivity and wettability of electrode in the particular electrolyte (M Khalid et al., 2018). This creates new phenomena for use of mesoporous carbon (pore size 2 to 50 nm) for supercapacitor applications, which contributes to easy ion-transport over the conventional activated carbon and hence, demonstrates high power capability (W. Li et al., 2016). (Y. Liu et al., 2017) synthesized mesoporous carbon by carbonizing a mixture of polyvinyl alcohol and inorganic salt and showed a specific capacitance of about 180 F/g in aqueous H_2SO_4 electrolyte. The performance of mesoporous carbons can be further enhanced by the controlled introduction of micropores. (Han et al., 2016) showed that a specific balance between mesopores to micropores ratio can tune the specific capacitance to 223 F/g in 6 M KOH electrolyte at 2 mV/s scan rate with 73% retention cyclability. This improved capacitance has been attributed to the presence of hierarchical porous structure of the electrode material that consists interconnected micropores and mesopores, having the high surface area of 2749 m^2/g, and large pore volume of 2.09 cm^3/g. The interconnected porous structure facilitates the easy movement if ions. The performance of mesoporous carbon can also be improved by its functionalization. The functionalized mesoporous carbon can then act as an efficient pseudocapacitor electrode in addition to EDLC.

Different functional groups like ─OH, ─COOH or ─C═O can be easily introduced by activating the mesoporous carbon using strong acids like nitric acid, sulfuric acid or ammonium persulfate. Jia et al. (Jia, Y, G, et al., 2016) pyrolyzed the mixture of milk powder and sodium hydroxide without any substrate resulting in the formation of N-doped mesoporous carbon which showed a high capacitance of 396.5 F/g at 0.2 A/g in the electrolyte solution of H_2SO_4 along with high stability in their capacitance of 95.9% for capacitance retention after 2000 cycles at 50 mV/s. (Jia, Y, & G, 2016) have also observed that the capacitance of mesoporous carbon increased from 117 to 295 F/g (10 mV/s scan rate) after its treatment with nitric acid.

(Dubey & Guruviah, 2019), obtained AC by carbonization of waste of fibreboards at 500^{o}C and activated with KOH at 800^{o}C varying the ratio of KOH/cake mass. This resulted in an SSA range of 1456 to 1647m^2/g giving a specific capacitance range of 212 to 223F/g. AC materials electrodes properties like low cost and electrical conductivity and hindered by the low effective SSA caused by randomly connected micropores with sizes less than 2nm which hardly accessible by electrolytic ions (Z. Yang et al., 2015). To address that challenge, the prepared mesoporous carbon of pore diameter ranging from 2 to 50nm with high SSA was used as an SC electrode. This was to facilitate a fast ion-transport pathway and high-power density. The AC material exhibited a specific capacitance of 180F/g in aqueous H_2SO_4 as electrolyte (Z. Yang et al., 2015). The volumetric specific capacitance, power density, and energy density of mesoporous AC electrodes could be influenced directly by content and population between micropores and mesopores are required for electrochemical energy storage efficiency (Xuli Chen et al., 2017).

2.5.1. Controlling of shape and size in mesoporous carbon

The control of the shape and size of the mesoporous carbon material can be done through different synthetic techniques. The material can be produced as an ordered mesoporous carbon with homogeneously balanced pores of regular size. This can facilitate ion-transportation and charge storage hence improving capacitance and rate capability. The literature reported highly ordered sizes of 2.8nm and 8nm which was synthesized by SBA-16 silica with mesostructured templates and polyfurfuryl alcohol as the source of carbon (W. Li et al., 2016). The two types of sized materials reported an SSA of 1880 and 1510m^2/g respectively and a specific capacitance of 205F/g for the 2.8nm diameter as the highest capacitance. The mesoporous carbon can also be manipulated to introduce micropores in the materials. (Jia, Y, & G, 2016) reported activation of mesoporous carbon with CO_2 at 950^{o}C which imparted micropores in the mesoporous carbon and improved the specific capacitance from 115F/g to 225F/g in 6M KOH. This improvement of the specific capacitance can be attributed to the formation of hierarchical pores with SSA of 2749m^2/g and balanced mesopores and micropores.

The synthesis of mesoporous carbon materials using carbonization of non-conventional materials such as biomass is being adopted more and more as shown in Table 2.2. (Jia, Y, G, et al., 2016) reported production of N-doped mesoporous carbon materials by a one-step pyrolysis method using a mixture of KOH and milk powder without any template. The produced materials exhibited an SSA of 2145.5m^2/g and pore volume of 1.25cm^3/g resulting in a specific capacitance of 396.5F/g at 0.2A/g in 6M H_2SO_4 giving capacitance retention of 95.9% after 2000 cycles at 50mV/s. the structure of pores and the shape of the mesoporous can be also further explored to improve the electrochemical performance. A composite of AC with graphene exhibited high SSA with improved

specific capacitance. (W Ma et al., 2016) reported a composite of graphene-AC porous materials with SSA of 3290m^2/g with the specific capacitance of 174F/g, the volumetric capacitance of 100F/cm^3 resulting in the energy density of 74Wh/kg and power density of 333kW/kg.

Table 2.2: Carbon-based EDLC as electrode materials

Electrode	**Electrolyte**	**Specific Capacitance (F/g)**	**Current density (A/g)**	**Retention cycles**	**References**
N-doped mesoporous carbon	-	288	0.1	25000	(JG Wang, Liu, H Sun, et al., 2018)
N-doped micro-mesoporous carbon	6M KOH	226	1.0	2000	(A. Chen et al., 2016)
N-doped mesoporous carbon	Ionic liquid	186	2.5	-	(D. Liu et al., 2016)
Layered N-doped mesoporous carbon	0.5M H_2SO_4	810	1.0	5000	(T. Lin et al., 2015)
	2M Li_2SO_4	710	1.0	5000	
N-doped mesoporous carbon	Ionic liquid	225	0.5	1000	(M. Xie et al., 2014)
Hierarchically N-doped mesoporous carbon	0.5M H_2SO_4	537	0.5	10000	(Han et al., 2016)

Incorporation of heteroatoms such as nitrogen, boron, phosphorous, and sulfur (N, B, P, and S) into the carbon network by replacing some carbon atoms offers a significant change in the electronic, electrical, and surface charges properties of the carbon materials. Doping of heteroatom in carbon materials can be done either by in situ preparation of

carbon or through post-treatment by heteroatom containing precursor (Mohmmad et al., 2018). In particular, nitrogen doping has gained more attention in a supercapacitor, because nitrogen doping not only improves the electrical conductivity and wettability but also contribute additional pseudocapacitance by enhancing the surface polarity and electron donor affinity of carbon. According to the studies made by Wang et al. (JG Wang, Liu, H Sun, et al., 2018), nitrogen doping facilitates the formation of well-defined mesopores and resulted in improved electrochemical performance. Lin et al. (T. Lin et al., 2015) developed N-doped mesoporous few-layer carbon with a large surface area of 1900 m^2/g for supercapacitor. It was reported that the as-developed few-layer carbon showed the highest ever specific capacitance of 810 F/g in a three-electrode cell and 710 F/g in a full cell at 1 A/g in 0.5M H_2SO_4 and 2M Li_2SO_4 electrolytes. The full cell device showed high stability with 50,000 repeating cycles between 0 to 1.2 V and demonstrated the highest specific energy of 23.0 Wh/kg while maintaining the specific power density of 18.5 kW/kg in 2M Li_2SO_4 electrolyte. Though the exact mechanism has not yet been confirmed it is evident that the pyrrolic N, pyridinic N, or quaternary N plays a crucial role in determining the ion flow towards the electrode, hence, influencing the capacitance of the electrode (A. Chen et al., 2016). Nitrogen and phosphorus dual doped mesoporous carbon was also prepared, which reveals a high specific capacitance of 220 F/g at a current density of 1 A/g with an excellent rate capability of 91% in a 6 M KOH aqueous electrolyte (JG Wang, Liu, H Sun, et al., 2018). This value of capacitance was found lower than nitrogen and sulfur or nitrogen and oxygen dual doped mesoporous carbon synthesized using polyhedral oligosilsesquioxanes, which showed an almost rectangular cyclic voltammogram curve in a wide potential window from −2 to +2 V in an ionic liquid electrolyte. These electrode materials showed a gravimetric and volumetric specific

capacitance of 163 F/g and 106 F cm^{-3} at a current density of 0.25 A/g (D. Liu et al., 2016). Another form of activated mesoporous carbon is carbon nanofibers. The ease

of preparation and highly mesoporous structure of these fibers exhibited excellent electrode material for electrochemical double-layer capacitors. (JG Wang, Liu, H Sun, et al., 2018) prepared polyacrylonitrile fibers followed by NaOH activation, and observed high specific capacitance of 371 F/g in the aqueous KOH (6 M), 213 F/g in non-aqueous $LiClO_4$ (1 M), and 188 F/g in ionic liquid electrolyte solutions. Mesoporous carbons have also been extensively studied in the form of composites with other active materials, including conductive polymers (polyaniline, poly-3-hexylthiophene) and metal oxides (Manganese oxide MnO_2, Ruthenium oxide RuO_2 (Mohmmad et al., 2018). In particular, pristine conducting polymers with their excellent electrochemical properties have displayed capacitance 10–100 times higher than EDLCs but they suffer from some limitations like poor stability and short lifetime. Thus, combining the properties of conducting polymers with mesoporous carbon can result in an electrode material with optimum properties. For instance, chemical polymerization of polyaniline onto an ordered bi-modal-mesoporous carbon resulted in the formation of PANI nanowires growing out of mesoporous carbon substrate has been reported by (Jiang et al., 2020). The subsequent composite exhibited a specific capacitance of 517 F/g in 1M H_2SO_4 electrolyte with a 91.5% retention rate after 1000 cycles. Chen et al. have presented a facile synthesis of highly porous N-doped carbon nanofibers coated with polypyrrole by carbonization which showed a specific capacitance of 202 F/g in aqueous KOH (6M) electrolyte at a current density of 1 A/g. It displayed a maximum power density of 90 kW/kg while maintaining high capacitance retention and cyclability. This kind of N-doped carbon

nanofiber-based composites exemplifies unconventional and practically potential candidates for a competent electrode material for supercapacitors (L Zhang et al., 2016)

2.6. Synthesis approach for electrode materials

The method of synthesis of electrode materials plays an important role in controlling the structures and properties of the materials. different synthesis methods are described briefly:

2.6.1. Sol-gel method

Sol-gel is a facile method to prepare materials with greater purity and homogeneity. The sol-gel method is so named, as in its micro-particles in the solution (sol) agglomerate and link together in regulated conditions to form an integrated network (gel). Two basic variations of the sol-gel method are the colloidal method and the polymeric or the alkoxide method, which are different from each other on the type of precursors used. In both methods, the precursor is mixed in a liquid (usually water is used for the colloidal method and alcohol for the polymeric method) and is then activated with the addition of an acid or a base. Then, as obtained activated precursor reacts forming a network, which develops with temperature and time maximally up to the container size (Poonam et al., 2019). Many TMOs have been prepared by this method. This process provides the advantage of preparing materials for different morphologies. The electrode material prepared by this process possesses high SSA with better electrochemical behavior which can also be controlled by temperature, change of surfactants, solvents, and reaction time. (L Zhang et al., 2016) have reported this method for the production of activated carbon fiber material (ACFM)-$Ni(OH)_2$ composite which exhibits the specific capacitance of appx 370–380 F/g. Also, the dependence of shape, structure, and volume of material on

the composition and concentration of the solution was established. (Poonam et al., 2019)have deposited $NiCo_2O_4$ films by a sol-gel method which exhibit the specific capacitance of 2157 F/g at a 0.133 mA/cm^2 current density and good cycling stability (96.5% specific capacitance retained after 10,000 cycles). $NiO/LaNiO_3$ electrode fabricated by spin-coating on $Pt/Ti/SiO_2/Si$ (100) substrate showed a specific capacitance of 2030 F/g at a 0.5 A/g and high stability (83% of the specific capacitance retention after 1000 cycles). This superior electrochemical response can be related to high porosity, well-connected network structures with reduced mass transfer resistance between electrolyte and ion which facilitates the electron hopping in nanoparticles.

2.6.2. Electro-polymerization / Electrodeposition

This is a common synthesis technique that provides precise regulation over the thickness of films and on the rate of polymerization. By suitable choice of deposition solution, nanostructured films with different mass loading and morphologies can be prepared by this method. This technique involves simple processing conditions and not many toxic chemicals are used in it. It is generally used for preparing CPs such as PANI, PEDOT, PPy, among others. (Poonam et al., 2019) have prepared MnO_2-PEDOT: PSS composite by a co-electrodeposition strategy which exhibits an areal specific capacitance of 1670mF/cm^2 at 0.5 mA/cm^2 and excellent mechanical robustness. Nanosized MnO_2 electrodes on Au nanowire stems are grown electrochemically by Chen et al. (Najib & Erdem, 2019) which exhibit high specific capacitance (1130 F/g at 2 mV/s), high energy density (15 Wh/kg at 50 A/g), high power density (20 kW/kg at 50 A/g) and long-term stability (90% of specific capacitance left after 5000 cycles). $ZnO@Ni_3S_2$ core-shell nanorods are formed by the electrodeposition method by (Xing et al., 2014) which exhibit a specific capacitance of 1529 F/g at 2 A/g and retain 42% of initial specific capacitance

after 2000 cycles. Stretchable CNT-PPy films are deposited by electrochemical deposition by Guo et al (Guo et al., 2016).

2.6.3. In-situ polymerization

In this process, monomers are dispersed into an aqueous solution using the sonication process. Then an oxidizing agent is mixed to initialize the polymerization in the aqueous solution and the sample is obtained by filtering the solution. Earlier this method yielded only irregular aggregates with a little portion of nanofibers, but with slight modification, nanoparticles, nanorods, and nanofibers were reported with better solution processability and better physical and chemical properties. A simple strategy for the growth of PEDOT structures on carbon fiber cloth (CFC) by in situ polymerization is reported (M. Rajesh et al., 2017). When a supercapacitor device is fabricated with these nanostructures, it exhibits a specific capacitance of 203 F/g at 5 mV/s, an energy density of 4.4 Wh/kg, and a power density of 40.25 kW/kg in 1M H_2SO_4 electrolyte. Also, it possesses 86% specific capacitance retention after 12,000 cycles. Wang et al. (R. Wang et al., 2016) have deposited PANI nanowires within the multi-walled carbon nanotubes (MWCNTs) by in situ electro-polymerization. The aligned MWCNTs provide support to the organic polymers along with providing a pathway for the transfer of charge. Also, confined MWCNT channels limit the structural changes in PANI chains while charging-discharging and enhance the lifetime of the structure. The films made with porous carbon encapsulated in MWCNTs showed a specific capacitance of 296 F/g at 1.6 A/g. Different π-conjugated sulfonate templates and additional assistance of graphene and MWCNTs are employed to enquire the polymerization behavior of PEDOT by Zhou et al. (H. Zhou et al., 2017). As prepared PEDOT: MWCNT composite reveals interconnected network

due to the π-π interaction of PEDOT with non-covalent functionalized MWCNT and exhibits a specific capacitance of 199 F/g at 0.5 A/g.

2.6.4. Direct coating

This technique is employed for the fabrication of those SC electrodes in which active material, in the form of a slurry, is applied directly on the substrate. Often, additives such as carbon black, polyvinylidene fluoride (PVDF), acetylene black, polytetrafluoroethylene (PTFE) are introduced as binders to provide maximum adhesion along with retaining electrical conductivity. The working electrode is fabricated with 90 wt% electrode materials (NiO) and 10 wt% PVA in mills water as a solvent and the slurry obtained is pasted on the Pt disc. Jana et al. (Jana et al., 2016) prepared supercapacitor electrode slurry by mixing nitric acid-treated carbon cloth with 10% PVDF and DMF (N, N-dimethyl formamide) and the prepared slurry is coated on a stainless-steel substrate. Du et al. (W. Du et al., 2014) synthesized supercapacitor electrode by coating the slurry formed by adding active material with acetylene black and PTFE onto Ni foam.

2.6.5. Chemical vapour deposition (CVD)

CVD technique is generally used where the porosity is very important. This process is performed under vapour phase, where the initial material is prepared in vapour form, flowed, and subjected to a high temperature (800 to1000 °C). The as-prepared structures have even morphology (Chee et al., 2016). Among various synthesis methods of graphene, for instance, mechanical cleavage of graphite, chemical exfoliation of graphite (in organic solvents), manufacturing of multi-layered graphene by arc discharge, reduction of graphene oxide (GO) synthesized from the oxidation of graphite, graphene synthesized by CVD provides better results owing to their large crystal domains,

monolayered structure and fewer defects in the sheets, which help enhance carrier mobility (Ke & Wang, 2016). Kalam et al. (Kalam et al., 2015) demonstrated that high-efficiency SCs with improved electrochemical characteristics can be fabricated by CVD-grown graphene hybridized with MWCNTs. (Lobiak et al., 2017) prepared hybrid carbon materials consisting of MWCNTs and graphitic layers, produced by CVD, over MgO assisted metal catalyst, such materials provide fast charge transport in the cell.

2.6.6. Vacuum filtration technique

This quick and proficient technique uses the simple concept of vacuum filtration to prepare nanocomposites from a physical combination of different materials. Generally, a mixture of materials is prepared followed by simple vacuum filtration and drying of the filtrate. In this method, the composition can be simply altered by varying the concentration or the weight percentage of each constituent in the mixture. Graphene suspension, developed by vacuum filtration deposition by Zhang et al.(H. Xu et al., 2015) for fabricating graphene-based Ni foam electrodes, shows a higher Ed and Pd along with good cycling performance. Xu et al. (L. Xu et al., 2017) have synthesized a nanocomposite of graphene/AC/PPy by vacuum filtration method. As prepared electrode exhibits the Cs of 178 F/g at 0.5 mA/cm^2 and retains 64.4% of Cs after 5000 charge/ discharge cycles. Y. Gao (Y. Gao, 2017) has used this technique to prepare graphene/ polymer electrode on Ni foam in which the vacuum pressure and its duration controls the distribution of graphene.

2.6.7. Hydrothermal/solvothermal method

The hydrothermal process can be ascribed as environment-friendly superheated aqueous solution dispensation. Also, this provides controlled diffusivity within a closed system.

The process has superiority over other techniques as it is ideal for preparing designer particulates (particles with high purity, crystallinity, quality, and controlled chemical and physical characteristics). Also, this is a low-temperature sintering process with a small energy requirement which is simple to implement and scale up (Poonam et al., 2019). Though, this process has lesser control over nanoparticle aggregation. The solvent properties (i.e., dielectric constant, solubility) change radically in the supercritical phase. Thus, the supercritical phase gives a favourable condition for particle formation owing to increased reaction rate and great supersaturation. If some other solvent is used instead of water, then the method is called solvothermal synthesis. A lot of SC electrodes have been fabricated using this process such as rod-like hollow $CoWO_4/Co_{1-x}S$ (Ge et al., 2018), Cobalt disulfide-reduced graphene oxide (CoS_2-rGO) (Venkateshalu et al., 2018), hexagonal $NiCo_2O_4$ nanoparticles (Poonam et al., 2018).

2.6.8. Co-precipitation method

This is a facile method for the large-scale production of powder samples. For precipitation to take place, the concentration of one solute should be more than the solubility limit and temperature should be high enough for fast separation into precipitates. Here, it is difficult to regulate the morphology of prepared samples due to the fast rate of precipitation. Various supercapacitor structures have been reported using this method such as $CoFe_2O_4$-magnetic nanoparticles with different precursors (Kennaz et al., 2018), $Ni_3(PO_4)_2$@GO composite (J. J. Li et al., 2015) which displays a specific capacitance of 1329.59 F/g at a 0.5 A/g and 88% of the Cs retention after 1000 cycles.

2.6.9. Dealloying method

The Dealloying method, also known as selective dissolution, is an easy, flexible and economical technique to produce nanoporous metallic materials (NPMs) with structures like core-shell, hollow core-shell, and porous nanoparticles (Poonam et al., 2019). In this method, the more active material is removed from a solution of binary metallic solid by electrolytic dissolution thus producing an interconnected porous structure. Such structures possess higher surface area, good mechanical and compression strength along with size-scale dependent elastic modulus. Much attention has been given to NPMs prepared by this method since the important work of (X. Li et al., 2014), and has become a very important method to produce NPMs in the last decade. They examined the fixed voltage dealloying of AgAu alloy particles in the size range of 2 to 6 nm and 20 to 55 nm. They demonstrated that only the core-shell structures (2 to 6 nm in diameter) evolved above the potential corresponding to Ag+/Ag equilibrium. CuS nanowire on nanoplate network with improved electrochemical performance has been prepared by Wang et al. (Z. Wang, Zhang, Zhang, et al., 2018) using an improved dealloying method at two contrasting reaction temperatures. Cu_2O has been synthesized by oxidation assisted dealloying method (R. Wang, Sui, Yang, et al., 2018). The free-dealloying method has been used for the synthesis of Cu-based metallic glasses in HF and HCl solutions (Z. Wang et al., 2015). Lu et al. (Z. Lu et al., 2018) reported a green and universal technique (vapour phase dealloying) for fabricating porous materials by using vapour pressure among constituent elements in an alloy, to selectively eliminate a component with high vapour pressure, for producing 3-dimensional bi-continuous open nano-porosity. With this technique, extensive elements can be fabricated with tuneable pore sizes along with full recovery of the evaporated component. Flexible electrodes of Co_3O_4 flakes and γ-

Fe_2O_3 nanoparticles have been prepared by oxidation-assisted dealloying method for the first time by Wang et al. (R. Wang, Sui, Huang, et al., 2018).

2.6.10. Other synthesis methods

Several other synthesis methods have been reported for SC electrodes. The microwave-assisted method has been used for the rapid synthesis of tin selenide (Ni et al., 2018). Nitrogen functionalized carbon nanofibers (N-CNFs) are prepared by carbonizing PPy-coated nanofibers (NFs), which in turn are obtained by 'electrospinning' and deacetylation of electrospun cellulose acetate NFs and PPy polymerization (J. Cai et al., 2015). An additive-free, cost-effective, and scalable 'successive ionic layer adsorption and reaction (SILAR) method' has been quoted to prepare Ni-Co binary hydroxide on RGO (Jana et al., 2016). The pulsed layer deposition method is used to fabricate NiO on graphene foam (H. Wang et al., 2014). Free-standing 3D porous RGO and PANI hybrid foam has been fabricated by 'dipping and dry method. Hierarchical porous carbon microtubes have been synthesized by carbonization along with KOH activation (L. Xie et al., 2016).

2.7. Concept of supercapacitor technology

Based on the charge accumulation process, a supercapacitor is mainly divided into a dual-layer capacitor and a pseudocapacitor. The dual-layer capacitor is a capacitive-type (non-Faradic) supercapacitor because when it is charged; there will be a combination of positive and negative charges at each electrode. The combinations are separated by the electrolyte. In the case of pseudocapacitor, the chemical reactions are occurred within the active materials of the electrodes according to Faraday's laws. Consequently, the amount

of the stored charge is related to the type of the active materials and the potential of the electrodes (Moftah & Shetiti, 2019).

2.7.1. Cell Construction

A supercapacitor is the same as a conventional capacitor; however, the former differs from the conventional capacitor in electrodes material which is based on carbon. It consists of two electrodes immersed in the electrolyte and separated by a separator (Moftah & Shetiti, 2019).

2.7.2. Electrode

The electrodes are made of conductive metal current collector quoted by activated carbon rough powder providing a large specific surface area and small distance of about 10 Armstrong. The carbon powder is pressurized to increase conductivity and decrease the contact resistance between the powder and the metal collector. Since the capacitance of any capacitor is proportional to the area and inversely proportional to the distance, the carbon powder provides the area of an electrode up to 3000 m^2/g and hence maximizing the number of electrolyte ions absorbed and so is the capacitance which increases linearly up to 250 F/g (Vlad et al., 2016)

2.7.3. Electrolyte

Supercapacitor electrolyte is a chemical liquid containing ions or a source of ions (charges). When applying a voltage to the electrodes the electrical potential draws the ions into the activated carbon so that positively charged ions will be attracted to the negative electrode and the negatively charged ions are attracted to the positive electrode. The accumulation of the ions on both electrodes will form double layers inside activated

carbon pores. The diameter of the ions and the size of activated carbon pores determine the double-layer phenomena and hence the capacitance. Because the activated carbon is an extremely pored material therefore, a very large number of ions can be absorbed into the electrodes of the capacitor resulting in high capacitance (Moftah & Shetiti, 2019).

Two types of electrolyte are used; aqueous and non-aqueous electrolyte (organic) which can classify the supercapacitor as following:

Aqueous electrolyte: Aqueous electrolyte based on sulphuric acid or potassium hydroxide. Their ions diameter is relatively small which allows higher ions absorption by the activated carbon pores and therefore, lower internal resistance. This leads to limiting the insulating ability of the electrolyte which on the other hand limits the cell voltage. The typical cell voltage is 1.23 V (Moftah & Shetiti, 2019).

Organic electrolyte: Non-aqueous electrolyte is quaternary salts dissolved in an organic solvent. Unlike the aqueous electrolyte, organic ions have a bigger diameter which limits the ions' penetration or absorption into the activated carbon pores. The internal resistance of organic electrolyte is a bit high compared to the aqueous electrolyte internal resistance resulting in providing a high voltage range of 3 to 3.5 V (Moftah & Shetiti, 2019). The type of electrolyte used in the supercapacitor may associate with determining the energy density and power density of the supercapacitor due to the role of the cell voltage range and the internal resistance. As stated, the aqueous electrolyte has a lower voltage range than the organic electrolyte. Equation (2.2) illustrates that the cell voltage determines the stored energy (Laheäär et al., 2015).

$$E = \frac{1}{2} C U^2 \tag{2.2}$$

Where E is the energy, C is the capacitance and U is the cell voltage.

In contrast, the organic electrolyte has higher internal resistance than the aqueous electrolyte by a factor of four as shown in Eqn (2.3) (Laheäär et al., 2015).

$$P = \frac{U^2}{4(ESR)} \tag{2.3}$$

Where P is the power and ESR is the internal resistance.

It can be seen from Eqn (2.2) and (2.3) that aqueous electrolyte has a lower energy density than the organic electrolyte due to its low voltage, but on the other hand, has higher power density than the organic electrolyte due to its low internal resistance.

2.7.4. Separator

A separator is a barrier used as a spacer between the electrodes to prevent electrodes short circuit. It blocks any electronic contact (short circuit) in the cell, but on the other hand, it allows ionic transfer between electrodes. The separator comes in a form of polymer, in case of organic electrolyte is used, and glass fiber or ceramic in case of aqueous electrolyte (Moftah & Shetiti, 2019).

2.8. Characteristics of supercapacitors

The supercapacitor has a series of characteristics that influence and determine its performance. These factors are the capacitance, rated voltage, power and energy densities, and finally its charge and discharge behaviors over time. Supercapacitors have the advantages of high-power density, safety, a broad range of operating temperatures, and superfast charge times. The charging time for a supercapacitor generally ranges from a few seconds to minutes, and the typical cycling life can reach 100,000 cycles with only a slight performance degradation. These aforementioned technological features allowed supercapacitors to become the next generation of energy storage devices. However, they

still have low energy densities. The energy density of standard supercapacitor devices is limited to 10's of Wh /kg. Thus, supercapacitors are presently only used as EV starters and cabin door switchers for airplanes, which require a high-power density and a short discharge time. The first advantage of using supercapacitors as EV power suppliers is their long cycling life, which is superior to the lifetime of LIBs, which is generally 2,000 times, or 5–6 years if the device is charged once daily. However, the lifetime of supercapacitors is much greater than ten years. Furthermore, supercapacitors have a rapid charging time of several minutes or less, which is much less than the time required to fill oil. For example, the bottleneck is the running distance (energy density), which should be at least 100 km for use in EVs. Thus, the energy density must also be greater than 100 W h/kg. In this case, the mileage goes to infinity with negligible charging times. EV mobility can be greatly enhanced using supercapacitors whose performance is competitive with LIBs.

2.8.1. Supercapacitor Capacitance

Due to its large surface area of the electrodes and to the very small distance, supercapacitors have a very large capacitance reaching thousands of Farads compared to the conventional capacitor whose capacitances range from 1 μF up to 1 F. The capacitance is determined from Eqn (2.4) (Laheäär et al., 2015).

$$C = \varepsilon \frac{A}{d} \; Farads \tag{2.4}$$

Where **ε** is the dielectric constant, A is the geometric area and d is the distance between the formed layers.

Considering Eqn (2.4), if the area is in the range of thousands of square meters and the distance of the range of nanometers, the capacitance, according to the equation, will be

in the range of the thousands of Farads. The capacitance is also determined by Eqn (2.5), as the capacitance can be defined as the ratio of the stored charge to the applied voltage (Laheäär et al., 2015).

$$P = \frac{Q}{V} \tag{2.5}$$

2.8.2. Supercapacitor Rated Voltage

In general, the supercapacitor has a lower rated voltage (1.23 to 3.5 V) due to the limit of breakdown potential of the electrolyte, however; the supercapacitor cells can be connected in series to form a module to meet the desired high voltage. Although this arrangement would provide a rated voltage to meet a certain required voltage, it affects the total capacitance of the module as the capacitance of several capacitors connected in series will reduce the total capacitance of the module and hence the stored charge. Equation (2.6) illustrates the reduction in over whole capacitance (Dubey & Guruviah, 2019).

$$\frac{1}{C_{Total}} = \frac{1}{C_1} + \frac{1}{C_2} + \frac{1}{C_3} + \cdots \frac{1}{C_n} \tag{2.6}$$

Where C_{Total} is the overall capacitance of the module and "n" is the number of capacitors connected in series. On the other hand, several supercapacitors can be arranged together so that achieving specific requirements in terms of capacitance, voltage, current, energy density, and power density. Consequently, there are three arrangement methods such as series, parallel, or a combination of them.

Commercially, the rated voltage is on the order of 2.5 to 2.7 V while the capacitance reaches a few thousand Farads. Due to their low voltage levels, supercapacitors need to be connected in series so that obtaining the required voltage levels, reaching a few

hundreds of volts. However, the total capacitance and stored energy reduce. The main disadvantage of this arrangement is that the total voltage over the whole series string of the supercapacitors maybe not be symmetrically shared between the individual supercapacitors based on the variations between their parameters. If the terminal voltage of any supercapacitor increases more than its rated voltage, this supercapacitor may be damaged. The solution to this problem is to equalize the total voltage between the different supercapacitors by using high-efficiency power electronics (Mathis et al., 2019). To increase the capacitance as well as the energy and power densities, the supercapacitors need to be connected in parallel. Also, the total current which can be delivered increases corresponding to the number of supercapacitors and vice versa. However, this current may be equally shared or not between the supercapacitors depending upon the percentage of the difference between their parameters. From the previous two methods, not all requirements are achieved because when the total voltage needs to be increased, the capacitance cannot be and vice versa. By connecting the supercapacitors in a series-parallel arrangement, the required capacitance and total voltage can be achieved but this arrangement needs an equalization circuit to be added (Moftah & Shetiti, 2019).

2.8.3. Supercapacitor Internal Resistance

The internal resistance of supercapacitor is represented by equivalent series resistance (ESR) and equivalent parallel resistances (EPR) are as follows (Mathis et al., 2019):

2.8.3.1. Equivalent series resistance (ESR)

The internal resistance of the supercapacitor is the sum of its component's resistivity such as electrodes, electrolyte, and any external circuit involved such as wire resistance as well as the ion size that is absorbed by pores. It is known as equivalent series resistance (ESR).

It determines the voltage during the discharge and the amount of power that can be delivered by the supercapacitor, the lower the ESR the higher power. This leads to the fact that supercapacitor efficiency is a function of these series resistances.

2.8.3.2. Equivalent parallel resistance (EPR)

Supercapacitor storage performance decays over time as it has a short–term energy performance. This is due to leakage current or self-discharge. This leakage current is modelled as a parallel resistor connected in parallel with the supercapacitor. It is called the Equivalent parallel resistance (EPR). It increases proportionally with temperature. Consequently, as the EPR increases the leakage decreases increasing long-term energy (Mathis et al., 2019).

2.8.4. Temperature

The supercapacitor performance remains unaffected over a wide range of temperatures. Unlike a lead-acid battery, there is no chemical reaction taking place in the charge and discharge process which gives the supercapacitor a lead of the lead-acid battery. The supercapacitor can operate without effect within a temperature range of +70 Co down to -20 Co. However, the conductivity of the organic electrolyte will be affected and hence limiting the performance of the supercapacitor (Moyo et al., 2018).

2.8.5. Supercapacitor Energy and Power Densities

Energy and power densities are factors that are shared between batteries, conventional capacitors, and supercapacitors. In the case of batteries, the ability to store energy is very high but the speed of delivering that energy is very poor, in other words, batteries have high energy density but low power density. However, in the case of a conventional

capacitor, the capability of delivering power is very high but the ability to store energy is very poor. This gap between the batteries and conventional capacitor energy and power densities are filled in by supercapacitor (Moftah & Shetiti, 2019).

2.8.6. Charging/Discharging Supercapacitor

A supercapacitor is the same as the conventional capacitor and unlike the battery when it comes to charge and discharge behaviors. It charges rapidly and exponentially and discharges in the same minor of charging over a short time (Jibrael et al., 2015). The charging time is only limited by the RC circuit. As the supercapacitor is made of several series RC circuits, therefore, the charging time is depending on the value of the RC circuit. Moreover, and unlike the batteries the charging and discharging cycle is considered unlimited as no chemical reaction taking place though out the process (Moftah & Shetiti, 2019).

2.9. Applications of supercapacitors

Supercapacitor found its way into many industrial aspects from power systems to standby and automotive systems both fossil and electric vehicles. It is also used in telecommunications and digital cameras. The following is a brief description of the supercapacitor used in some applications (Moftah & Shetiti, 2019):

Transmission lines: Due to variation in power demand a storage device becomes necessary. As matter of fact, a storage device is the heart of FACTs devices the supercapacitor is used in these FACTs devices to improve power transfer and enhance power quality and provide stability in voltage and frequency.

UPS: In this application, the supercapacitor is combined with the storage batteries to provide power over a short period of interruption so that the batteries are only delivering their energy over a long period of interruption which, consequently, extends the battery's life.

Telecommunications: The need for fast response backup systems during the lack of the main power source in this field is a very important issue to get high reliable operation and avoid interruption of the communication system. This requires a sort of backup batteries, UPS or other sorts of what it is called Hot Standby System, however, this system has an issue of power consumption which means high cost. However, a supercapacitor can act very fast as a cold standby unit and dissipate almost no energy.

Cold starting of diesel-fuelled engine: Diesel fuelled engines are quite hard to start-up in cold weather where the lubrication oil temperature drops below 0 degrees making an increase in the viscous friction which requires high cranking torque to start the engine. This cranking torque requires a high current from the lead-acid battery which also affects by the cold weather as its internal resistance increases as the temperature drops, which limited the discharge current and hence reduces the ability to sustain the cranking current during engine start. This issue is overcome by using a bank of a supercapacitor as it does not get affected by low temperature so that the cranking current surge is provided by the supercapacitor.

Hybrid electric vehicle: The hybrid electric vehicle operation involves transient power demand due to acceleration and deceleration which require storage devices with high power density along with high energy density. As the hybrid electric vehicle was driven by a bank of batteries, which are known for low power density and high energy density, the battery life will be affected, however, by combining the supercapacitor with the

battery, the transient current will be supplied by the supercapacitor resulting in battery life being extended (Moftah & Shetiti, 2019).

2.9.1. Advantages and Limitations of Supercapacitors

The advantages are as follows:

1. Unlike batteries, supercapacitors have virtually unlimited cycle life because they can be deep cycled up to a wide range of times, reaching thousands (about 500000 times).
2. Due to their low impedance compared to batteries, supercapacitors can enhance high pluses of energy without lifetime deterioration. Furthermore, within a very small period (a few seconds), fast charging can be achieved.
3. Supercapacitors have about 100 times higher specific power density than batteries.
4. If they are overcharged, nothing dangerous happens but the lifetime may affect them. Also, there is no need for an overcharge detection circuit because, within their rated voltage, it can be charged up to any voltage.
5. In terms of temperature, supercapacitors can be operated and stored in a range of (-40 to 70 Co) with relatively small changes to the parameters.
6. Maintenance-free, friendly to the environment, and completely pollution-free.
7. Explosion risk is minimal

2.9.2. The limitations are as follows:

a) The energy density is low and it is of an order of one-fifth to one-tenth the energy of batteries.

b) For batteries, supercapacitors have a high self-discharge rate.

c) The EDLC cells can withstand a low voltage of about 2.7 V. In the case of high voltage applications, several cells must be connected in series according to the amount of rated voltage required. However, they cannot be directly connected because the terminal voltage of each cell may differ from the other cells. Consequently, damage to cells that have terminal voltages higher than their voltage ratings. Mainly, this case is due to their capacitances are not the same causing supercapacitors with smaller capacitances to have higher terminal voltages.

d) Due to may not be possible to use the full stored energy depending upon the application, because, during discharging, the terminal voltage decreases exponentially.

REFERENCES

ADB, A. D. B. (2018). *Handbook on Battery Energy Storage System* (Issue December). https://www.adb.org/publications/battery-energy-storage-system-handbook

Adetayo, A., & Runsewe, D. (2019). Synthesis and Fabrication of Graphene and Graphene Oxide: A Review. *Open Journal of Composite Materials*, *09*(02), 207–229. https://doi.org/10.4236/ojcm.2019.92012

Adrian, B.-B., Maria, A.-F., Carmen, F.-G., & Vicente, G.-S. (2016). Activated carbon surface chemistry_ Changes upon impregnation with Al(III), Fe(III) and Zn(II)-metal oxide catalyst precursors from NO3- aqueous solutions. *Arabian Journal of Chemistry*, 14. https://doi.org/10.1016/j.arabjc.2016.02.018

Allagui, A., Freeborn, T. J., Elwakil, A. S., Fouda, M. E., Maundy, B. J., Radwan, A. G., Said, Z., & Abdelkareem, M. A. (2018). Review of fractional-order electrical characterization of supercapacitors _ Elsevier Enhanced Reader.pdf. *Journal of Power Sources*, *400*, 457–467. https://doi.org/10.1016/j.jpowsor.2018.08.047

Biswal, M., Banerjee, A., & Ogale, S. (2013). From dead leaves to high energy density supercapacitors. *Energy & Environmental Science*, 1–11. https://doi.org/10.1039/c3ee22325f

Borenstein, A., Hanna, O., Attias, R., Luski, S., Brousse, T., & Aurbach, D. (2017). Carbon-based composite materials for supercapacitor electrodes: A review. *Journal of Materials Chemistry A*, *5*(25), 12653–12672. https://doi.org/10.1039/c7ta00863e

C, E. (2020). *Enerize corporation*.

Cai, J., Niu, H., Li, Z., Du, Y., Cizek, P., Xie, Z., Xiong, H., & Lin, T. (2015). High-performance supercapacitor electrode materials from cellulose-derived carbon nanofibers. *ACS Appl. MaterInterfaces*, *7*, 14946–14953.

Cansiz', A. (2018). electromechanical energy conversion. *Compr. Energy Syst*, *4*(14), 598–635. https://doi.org/10.1016/B978-0-12-809597-3.00425-9.

Cao, X., B, Z., W, S., J, Y., & Z, F. (2015). Reduced graphene oxide- wrapped MoO3 composites prepared by using metal–organic frameworks as precursor for all-solid-state flexible supercapacitors. *Adv Mater*, *27*, 4695–4701. https://doi.org/10.1002/adma.201501310

Chee, W. K., Lim, H. N., Zainal, Z., Huang, N. M., Harrison, I., & Andou, Y. (2016). Flexible graphene-based supercapacitors: a review. *J. Phys. Chem. C*, *120*, 4153–4172.

Chemali, E., Preindl, M., Malysz, P., & Emad, A. (2016). Electrochemical and electrostatic energy storage and management systems for electric drive vehicles: state-of-the- Art review and future trends. *IEEE J. Emerg. Sel. Top. Power Electron*, *4*, 1117–1134. https://doi.org/10.1109/JESTPE.2016.2566583

Chen, A., Y, W., Q, L., Y, Y., Y, L., & Y, Z. (2016). Synthesis of nitrogen-doped micro-mesoporous carbon for supercapacitors. *Journal of the Electrochemical Society.*, *163*, A1959–A1964. https://doi.org/10.1149/2.0711609jes

Chen, Xiufang, Zhang, J., Zhang, B., Dong, S., Guo, X., Mu, X., & Fei, B. (2017). A novel hierarchical porous nitrogen-doped carbon derived from bamboo shoot for high performance supercapacitor. *Scientific Reports*, *7:7362*(April), 1–11. https://doi.org/10.1038/s41598-017-06730-x

Chen, Xuli, Paul, R., & Dai, L. (2017). Carbon-based supercapacitors for efficient energy storage. In *National Science Review* (Vol. 4, Issue 3). https://doi.org/10.1093/nsr/nwx009

Das, D., Samal, D. P., & Bc, M. (2015). Preparation of Activated Carbon from Green Coconut Shell and its Characterization. *Chemical Engineering & Process Technology*, *6*(5), 1–7. https://doi.org/10.4172/2157-7048.1000248

Du, W., Wang, Z., Zhu, Z., Hu, S., Zhu, X., Shi, Y., Pang, H., & Qian, X. (2014). Facile synthesis and superior electrochemical performances of CoNi2S4/graphene nanocomposite suitable for supercapacitor electrodes. *J. Mater. Chem. A*, *2*, 9613–9619.

Dubey, R., & Guruviah, V. (2019). Review of carbon-based electrode materials for supercapacitor energy storage. *Ionics*, *25*(4), 1419–1445. https://doi.org/10.1007/s11581-019-02874-0

El-sayed, Y., & Bandosz, T. J. (2004). Adsorption of valeric acid from aqueous solution onto activated carbons : role of surface basic sites. *Journal OfColloid and Interface Science*, *273*, 64–72. https://doi.org/10.1016/j.jcis.2003.10.006

Elmouwahidi, A., Zapata-Benabithe, Z., Carrasco-Marín, F., & Moreno-Castilla, C. (2012). Activated carbons from KOH-activation of argan (Arganiaspinosa) seed shells as supercapacitor electrodes. *Bioresource Technol*, *111*, 185–190.

Elmouwahidi, Adbelhahim, Esther, B.-G., Agustin, F. P.-C., Francisco, J. M.-H., & Francisco, C.-M. (2017). Activated carbons from KOH and H3PO4-activation of olive residues and its application as supercapacitor electrodes. *Electrochimica Acta*, *229*, 219–228. https://doi.org/10.1016/j.electacta.2017.01.152

Faisal, M., Hannan, M. A., Ker, P. J., Hussain, A., Mansor, M. Bin, & Blaabjerg, F. (2018). Review of energy storage system technologies in microgrid applications: Issues and challenges. *IEEE Access*, *6*, 35143–35164. https://doi.org/10.1109/ACCESS.2018.2841407

Fraczek-szczypta, A., Rabiej, S., Szparaga, G., Pabjanczyk-wlazlo, E., Krol, P., & Brzezinska, M. (2015). The structure and properties of the carbon non-wovens modi fi ed with bioactive nanoceramics for medical applications. *Materials Science and Engineering C*, *51*, 336–345. https://doi.org/10.1016/j.msec.2015.03.021

Ge, J., Wu, J., Dong, J., Jia, J., Ye, B., Jiang, S., Zeng, J., & Bao, Q. (2018). A high energy density asymmetric supercapacitor utilizing a nickel phosphate/graphene foam composite as the cathode and carbonized iron cations adsorbed onto polyaniline as the anode,. *Chem. Electro. Chem.*, *5*, 1–10.

Genc, R., Alas, M. O., Harputlu, E., Repp, S., Kremer, N., Castellano, M., Colak, S. G., Ocakoglu, K., & Erdem, E. (2017). No Title. *Sci. Rep*, *7*, 11222.

Guo, F. M., Xu, R. Q., Cui, X., Zhang, L., Wang, K. L., Yao, Y. W., & Wei, J. Q. (2016).

High performance of stretchable carbon nanotube-polypyrrole fiber supercapacitors under dynamic deformation and temperature variation. *J. Mater. Chem A*, *4*, 9311–9318.

Han, L., X, W., QC, Z., SM, X., KX, W., & JS, C. (2016). Nitrogen-doped carbon nets with micro/mesoporous structures as electrodes for highperformance supercapacitors. *Journal of Materials Chemistry A*, *4*, 16698–16705. https://doi.org/10.1039/C6TA05607E

Hao L, N. J. and L. B. et al. (2015). Structural evolution of 2D microporous covalent triazine-based framework toward the study of high-performance supercapacitors. *J Am Chem Soc*, *137*, 219–25.

Hou, J., Cao, C., Ma, X., Idrees, F., Xu, B., Hao, X., & Lin, W. (2014). From Rice Bran to High Energy Density Supercapacitors : A New Route to Control Porous Structure of 3D Carbon. *Scientific Reports*, *4*(7260), 1–6. https://doi.org/10.1038/srep07260

Iro Zaharaddeen, S., Subramani, C., & Dash, S. S. (2016). A brief review on electrode materials for supercapacitor. *International Journal of Electrochemical Science*, *11*(12), 10628–10643. https://doi.org/10.20964/2016.12.50

Jae, Y. L., Kim, G., Bang, Y., Yi, J., Gil, J., & Kyu, I. (2014). Activated carbon aerogel containing graphene as electrode material for supercapacitor. *Materials Research Bulletin*, *50*, 240–245. https://doi.org/10.1016/j.materresbull.2013.11.021

Jana, M., Saha, S., Samanta, P., Murmu, N. C., Kim, N. H., Kuila, T., & Lee, J. H. (2016). Growth of Ni-Co binary hydroxide on a reduced graphene oxide surface by a successive ionic layer adsorption and reaction (SILAR) method for high performance asymmetric supercapacitor electrodes. *J. Mater. Chem. A*, *4*, 2188–2197.

Jia, S., Y, W., & G, X. (2016). An efficient preparation of N-doped mesoporous carbon derived from milk powder for supercapacitors and fuel cells. *Electrochim Acta*, *196*, 527–34.

Jia, S., Y, W., G, X., S, Z., P, T., & J, Z. (2016). An efficient preparation of N-doped mesoporous carbon derived from milk powder for supercapacitors and fuel cells. *Electrochimica Acta*, *196*, 527–534. https://doi.org/10.1016/j. electacta.2016.02.196

Jiang, H., Zhang, Y., Pan, Z., Xu, L., Zheng, J., Gao, Z., Meng, C., Zhang, Y., Pan, Z., Xu, L., Zheng, J., Gao, Z., Hu, T., & Meng, C. (2020). Facile Hydrothermal Synthesis and Electrochemical Properties of (NH4)2V10O25·8H2O Nanobelts for High-Performance Aqueous Zinc Ion Batteries. *Electrochimica Acta*, *19*. https://doi.org/10.1016/ j.electacta.2019.135506

Jibrael, R. I., Mohammed, M. K. A., Roder, F., Braatz, R. D., Krewer, U., Sohail, M., Saleem, M., Ullah, S., Saeed, N., Afridi, A., Khan, M., Arif, M., Danner, T., Zhu, G., Hofmann, A. F., Latz, A., Chen, S. X., Tseng, K. J., Choi, S. S., … Hee, J. (2015). Graphene-based polymer nanocomposites. *Carbon*, *6*(1), 1–4. https://doi.org/10.4172/2157-7439.1000253

Jung, S., DL, M., & CT, L. (2015). Controlled porous structures of graphene aerogels and their effect on supercapacitor performance. *Nanoscale*, *7*, 4386–93.

Kalam, A. A., Park, S., Seo, Y., & Bae, J. (2015). High-efficiency supercapacitor electrodes of CVD-grown graphenes hybridized with multiwalled carbon nanotubes,. *Bull. Korean Chem*, *36*, 2111–2115.

Ke, Q., & J., W. (2016). Graphene-based materials for supercapacitor electrodes: a review. ; 2: *J Materiomics*, *2*, 37–54.

Ke, Q., & Wang, J. (2016). , Graphene-based materials for supercapacitor electrodes-a review,. *J. Materiomics*, *2*, 37–54.

Kennaz, H., Harat, A., Guellati, O., Momodu, D. Y., Barzegar, F., Dangbegnon, J. K., Manyala, N., & Guerioune, M. (2018). Synthesis and electrochemical investigation of spinel cobalt ferrite magnetic nanoparticles for supercapacitor application,. *J. Solid State Electrochem*, *22*, 835–847.

Khalid, M, Aguilera, R. ., Savkin, A. ., & Agelidis, V. G. (2018). On maximizing profit of wind-battery supported power station based on wind power and energy price forecasting. *Appl. Energy*, *211*, 764–773.

Khalid, Muhammad. (2019). A review on the selected applications of battery-supercapacitor hybrid energy storage systems for microgrids. *Energies*, *12*(23). https://doi.org/10.3390/en12234559

Koohi-Fayegh, S., & Rosen, M. A. (2020). A review of energy storage types, applications and recent developments. *Journal of Energy Storage*, *27*(July 2019), 101047. https://doi.org/10.1016/j.est.2019.101047

Kumar, R., HJ, K., S, P., A, S., & IK, O. (2014). Graphene wrapped and cobalt oxide-intercalated hybrid for extremely durable super-capacitor with ultra high energy and power densities. *Carbon*, *79*, 192–202. https://doi.org/10.1016/j.carbon.2014.07.059

Laheäär, A., Przygocki, P., Abbas, Q., & Béguin, F. (2015). Appropriate methods for evaluating the ef fi ciency and capacitive behavior of different types of supercapacitors. *Electrochemistry Communications*, *60*, 21–25. https://doi.org/10.1016/j.elecom.2015.07.022

Laszlo, K., & Szucs, A. (2001). Surface characterization of polyethyleneterephthalate (PET) based activated carbon and the effect of pH on its adsorption capacity from aqueous phenol and 2 , 3 , 4-trichlorophenol solutions. *Carbon*, *39*, 1945–1953. https://doi.org/10.1016/S0008-6223(01)00005-7

Leea, D., & B-H, K. (2016). MnO2 decorated on electrospun carbon nanofiber/graphene composites as supercapacitor electrode materials. *Synth Met*, *219*, :115–123. https://doi.org/10.1016/j. synthmet.2016.06.007

Lekakou, C., Moudam, O., Markoulidis, F., Andrews, T., Watts, J. F., & Reed, G. T. (2011). Carbon-Based Fibrous EDLC Capacitors and Supercapacitors. *Journal of Nanotechnology*, *409382*, 8. https://doi.org/10.1155/2011/409382

Li, J. J., Li, M. C., Kong, L. B., Wang, D., Hu, Y. M., Han, W., & Kang, L. (2015). Advanced asymmetric supercapacitors based on Ni3(PO4)2@GO and Fe2O3@GO electrodes with high specific capacitance and high energy density,. *RSC Adv*, *5*, 41721–41728.

Li, M., F, P., ESG, C., Y, L., Y, C., & J, X. (2016). Designed construction of ghraphene and iron oxide freestanding electrode with enhanced flexible energy storage performance. *ACS Appl Mater Interfaces*, *8*, 6972–6981. https://doi.org/10.1021/acsami. 5b10853

Li, W., J, L., & D, Z. (2016). *Mesoporous materials for energy conversion and storage devices. Nature Reviews Materials. 1*, 16023. https://doi.org/10.1038/ natrevmats.2016.23

Li, X., Chen, Q., McCue, I., Snyder, J., Crozier, P., Erlebacher, J., & Sieradzki, K. (2014). , Dealloying of noble-metal alloy nanoparticles, . *Nano Lett.*, *14*, 2569–2577.

Lim, W. C., Srinivasakannan, C., & Balasubramanian, N. (2010). Activation of palm shells by phosphoric acid impregnation for high yielding activated carbon. *Journal of Analytical and Applied Pyrolysis*, *88*, 181–186. https://doi.org/10.1016/j.jap.2010.04.004

Lin, T., IW, C., F, L., C, Y., H, B., & F, X. (2015). Nitrogen-doped mesoporous carbon of extraordinary capacitance for electrochemical energy storage. Science. *Science*, *350*, 1508–1513. https://doi.org/10.1126/ science.aab3798

Liu, D., C, Z., D, Q., H, T., Y, L., & BL, S. (2016). Highly efficient synthesis of ordered nitrogen-doped mesoporous carbons with tunable properties and its application in high performance supercapacitors. *Journal of Power Sources*, *321*, 143–154. https://doi.org/1016/j.jpowsour.2016.04.129

Liu, Y., K, S., & I, Z. (2017). Asymmetric supercapacitor, based on composite MnO2-graphene and N-doped activated carbon coated carbon nanotube electrodes. *Electrochimica Acta*, *233*, 142–150. https://doi.org/10.1016/j. electacta.2017.03.028

Liu, Y., Y, S., & L, S. (2016). Elemental superdoping of graphene and carbon nanotubes. *Nat Commun*, *7*, 10921.

Lobiak, E. V., Bulusheva, L. G., Fedorovskaya, E. O., Shubin, Y. V., Plyusnin, P. E., Lonchambon, P., Senkovskiy, B. V., Ismagilov, Z. R., Flahaut, E., & Okotrub, A. V. (2017). , Onestep chemical vapor deposition synthesis and supercapacitor performance of nitrogen- doped porous carbon-carbon nanotube hybrids, . *Beilstein J. Nanotechnol*, *8*, 2669–2679.

Lu, Z., Li, C., Han, J., Zhang, F., Liu, P., Wang, H., Wang, Z., Cheng, C., Chen, L., Hirata, A., Fujita, T., Erlebacher, J., & Chen, M. (2018). Three-dimensional bicontinuous nanoporous materials by vapor phase Dealloying, . *Nat. Commun*, *9*, 276.

M. Di Somma, et al. (2015). Operation optimization of a distributed energy system considering energy costs and exergy efficiency. *' Energy Convers. Manage*, *103*, 739–751.

Ma, W., S, C., S, Y., W, C., W, W., Y, C., & M, Z. (2016). Flexible all-solid-state asymmetric supercapacitor based on transition metal oxide nanorods/reduced graphene oxide hybrid fibers with high energy density. *Carbon*, *113*, 151e158. https://doi.org/10.1016/j.carbon.2016.11.051

Mahlia, T. M. I., Saktisahdan, T. J., Jannifar, A., Hasan, M. H., & Matseelar, H. S. C.

(2014). A review of available methods and development on energy storage; technology update. *Renew. Sustain. Energy Rev*, *33*, 532–545.

Manyala, N., Bello, A., Barzegar, F., Khaleed, A. A., Momodu, D. Y., & Dangbegnon, J. K. (2016). Coniferous pine biomass : A novel insight into sustainable carbon materials for supercapacitors electrode. *Materials Chemistry and Physics*, *182*, 139–147. https://doi.org/10.1016/j.matchemphys.2016.07.015

Mathis, T. S., Kurra, N., Wang, X., Pinto, D., & Simon, P. (2019). Energy Storage Data Reporting in Perspective — Guidelines for Interpreting the Performance of Electrochemical Energy Storage Systems. *Advanced Energy Materials*, *1902007*, 1–13. https://doi.org/10.1002/aenm.201902007

Mi, J., Wang, X., Fan, R., Qu, W., & Li, W. (2012). Coconut-Shell-Based Porous Carbons with a Tunable Micro / Mesopore Ratio for High-Performance Supercapacitors. *Energy&Fuels*, *26*, 5321–5329. https://doi.org/10.1021/ef3009234

Moftah, A., & Shetiti, A. Al. (2019). Review of Supercapacitor Technology. *International Journal of Computer Science and Electronics Engineering (IJCSEE) Volume 3, Issue 3 (2015) ISSN 2320–4028 (Online) Review*, *November*, 2–7.

Mohmmad, K., Bhardwaj, P., & Varela, H. (2018). Carbon-Based Composites for Supercapacitor. In *Science, Technology and Advanced Application of supercapacitors* (Issue tourism, p. 13). https://www.intechopen.com/books/advanced-biometric-technologies/liveness-detection-in-biometrics

Moyo, B., Momodu, D., Fasakin, O., Dangbegnon, J., & Manyala, N. (2018). materials Electrochemical analysis of nanoporous carbons derived from activation of polypyrrole for stable supercapacitors. *Energy Materials*, *53*, 5229–5241. https://doi.org/10.1007/s10853-017-1911-y

Najib, S., & Erdem, E. (2019). Current progress achieved in novel materials for supercapacitor electrodes: Mini review. *Nanoscale Advances*, *1*(8), 2817–2827. https://doi.org/10.1039/c9na00345b

Ni, D., Chen, Y., Yang, X., Liu, C., & Cai, K. (2018). Microwave-assisted synthesis method for rapid synthesis of tin selenide electrode material for supercapacitors. *J. Alloy Compd*, *737*, 623–629.

Ogunniyi, E. O., & Pienaar, H. C. V. Z. (2017). Overview of battery energy storage system advancement for renewable (photovoltaic) energy applications. *Proceedings of the 25th Conference on the Domestic Use of Energy, DUE 2017*, *October*, 233–239. https://doi.org/10.23919/DUE.2017.7931849

Poonam, K., Sharma, N., Singh, S. K., & Tripathi. (2018). Characterization of nickel cobalt oxide: a potential material for supercapacitor,. *Mater. Res. Express*. https://doi.org/10.1088/2053-1591/aae9c1

Poonam, Sharma, K., Arora, A., & Tripathi, S. K. (2019). Review of supercapacitors: Materials and devices. *Journal of Energy Storage*, *21*(January), 801–825. https://doi.org/10.1016/j.est.2019.01.010

Prahas, D., Kartika, Y., Indraswati, N., & Ismadji, S. (2008). Author ’ s personal copy

Activated carbon from jackfruit peel waste by H 3 PO 4 chemical activation : Pore structure and surface chemistry characterization. *Chemical Engineering Jounal*, *140*, 32–42. https://doi.org/10.1016/j.cej.2007.08.032

Purkait, T., G, S., D, K., M, S., & RS, D. (2018). No Title. *Sci Rep*, *8*, 640. https://doi.org/10.1038/s41598-017-18593-3

Rajesh, M., Raj, C. J., Manikandan, R., Kim, B. C., Park, S. Y., & Yu, K. H. (2017). A high performance PEDOT/PEDOT symmetric supercapacitor by facile in-situ hydrothermal polymerization of PEDOT nanostructures on flexible carbon fibre cloth electrodes. *Mater. Today*, *6*, 96–104.

Reddy, K., M, H., & VG, G. (2015). Hybrid nanostructures based on titanium dioxide for enhancedphotocatalysis. *Appl Catal A Gen*, *489:*, 1–16. https://doi.org/10.1016/j.apcata.2014.10.001

Rufford, T. E., Hulicova-Jurcakova, D., Khosla, K., Zhu, Z., & Lu, G. Q. (2010). Microstructure and electrochemical double-layer capacitance of carbon electrodes prepared by zinc chloride activation of sugar cane bagasse. *J. Power Sources*, *195*, 912–918.

Sandoval, D., Goffin, P., & Leibundgu, H. (2017). How low exergy buildings and distributed electricity storage can contribute to flexibility within the demand side. *Appl. Energy*, *187*, 116–127.

Shafeeyan, M. S., Wan, M. W. A., Houshmand, A., & Shamiri, A. (2010). A review on surface modification of activated carbon for carbon dioxide adsorption. *Journal of Analytical and Applied Pyrolysis*, *89*(2), 143–151. https://doi.org/10.1016/j.jaap.2010.07.006

Sonawane, G. H., Patil, S. P., & Sonawane, S. H. (2018). Nanocomposites and Its Applications. In *Applications of Nanomaterials* (pp. 1–22). https://doi.org/10.1016/b978-0-08-101971-9.00001-6

Song, Y., Z, L., K, G., & T, S. (2016). Hierarchically ordered mesoporous carbon/graphene composites as supercapacitor electrode materials. *Nanoscale*. https://doi.org/10.1039/C6NR04130B

Sun, G., X, Z., & R, L. (2015). Hybrid fibers made of molybdenum disulfide, reduced graphene oxide, and multi-walled carbon nanotubes for solid-state, flexible, asymmetric supercapacitors. *Angew Chem Int Ed*, *54*, 4651–6.

Sun, H., X, Y., & Deng J. (2014). Novel graphene/carbon nanotube composite fibers for efficient wire-shaped miniature energy devices. *Adv Mat*, *26*, 2868–73.

Tian, W., Gao, Q., Yanli Tan, a K. Y., Zhu, L., Yanga, C., & Zhang, H. (2015). Bio-inspired Beehive-like Hierarchical Nanoporous Carbon Derived from Bamboo-based Industrial Byproduct as High Performance Supercapacitor Electrode Material. *Materials Chemistry A*, 10. https://doi.org/10.1039/b000000x

Van, K. Le, Thuy, T., & Thi, L. (2014). Activated carbon derived from rice husk by NaOH activation and its application in supercapacitor. *Progress in Natural Science: Materials International*, *24*(3), 191–198. https://doi.org/10.1016/j.pnsc.2014.05.012

Venkateshalu, S., Rangappa, D., & Grace, A. N. (2018). Hydrothermal synthesis and

electrochemical properties of CoS2-reduced graphene oxide nanocomposite for supercapacitor application,. *Nt. J. Nanosci*, *17*, 760020–1760028.

VIB. (2018). Maize in Africa, facts series. In *International plant Biotechnology outreach*.

Vlad, A., Singh, N., Melinte, S., Gohy, J., & Ajayan, P. M. (2016). Carbon Redox-Polymer-Gel Hybrid Supercapacitors. *Scientific Reports*, *February*, 3–8. https://doi.org/10.1038/srep22194

Wang, C., HC, C., & SY, L. (2014). Manganese oxide/graphene aerogel composites as an outstanding supercapacitor electrodematerial. *Chem Eur J*, *20*, 517–523. https://doi.org/10.1002/chem. 201303483

Wang, D., Y, M., Y, Y., & B, P. (2014). A general approach for fabrication of nitrogen doped graphene sheets and its application in supercapacitors. *J Colloid Interface Sc*, *417*, 270–277. https://doi.org/10.1016/j.jcis.2013.11.021

Wang, G., R, L., & L, L. (2014). Improving the specific capacitance of carbon nanotubes-based supercapacitors by combining introducing functional groups on carbon nanotubes with using redox-active electrolyte. *Electrochim Acta*, *115*, 183– 8.

Wang, H., Yi, H., Chen, X., & Wang, X. (2014). Asymmetric supercapacitors based on nanoarchitectured nickel oxide/graphene foam and hierarchical porous nitrogen-doped carbon nanotubes with ultrahigh-rate performance, . *J. Mater. Chem A*, *2*, 3223–3230.

Wang, J., Liu, H., H Sun, W, H., H, W., & Liu X. (2018). One-pot synthesis of nitrogen-doped ordered mesoporous carbon spheres for highrate and long-cycle life supercapacitors. *Carbon*, *127*, 85–92. https://doi.org/10.1016/j. carbon.2017.10.084

Wang, R., M, H., Q, Z., Z, R., C, X., N, H., H, N., S, S., & J-M, L. (2017). Construction of 3D CoO quantum dots/graphene hydrogels as binder-free electrodes for ultra-high energy storage applications. *Electrochim Acta*, *686*(17), :31014–31019. https://doi.org/10.1016/j.electacta.2017.05.042

Wang, R., Sui, Y., Huang, S., Pu, Y., & Cao, P. (2018). , High-performance flexible all-solid-state asymmetric supercapacitors from nanostructured electrodes prepared by oxidation- assisted dealloying protocol. *Chem. Eng. J*, *331*, 527–535.

Wang, R., Sui, Y., Yang, F., Qi, J., Wei, F., He, Y., Meng, Q., & Sun, Z. (2018). Synthesis of Cu2O by oxidation-assisted dealloying method for flexible all-solid-state asymmetric supercapacitors. *J. Mater. Sci.: Mater. Electron*, *29*, 2080–2090.

Wang, R., Wu, Q., Zhang, X., Yang, Z., Gao, L., Ni, J., & Tsui, O. K. C. (2016). Flexible supercapacitors based on a polyaniline nanowire-infilled 10 nm-diameter carbon nanotube porous membrane by in situ electrochemical polymerization. *J. Mater. Chem. A*, *4*, 12602–12608.

Wang, Z., Liu, J., Qin, C., Yu, H., Xia, X., Wang, C., Zhang, Y., Hu, Q., & Zhao, W. (2015). Dealloying of Cu-based metallic glasses in acidic solutions: products and energy storage applications. *Nanomaterials*, *5*, 697–721.

Wang, Z., Zhang, X., Zhang, Y., Li, M., Qin, C., & Bakenov, Z. (2018). Chemical dealloying synthesis of CuS nanowire-on-nanoplate network as anode materials for Li-ion batteries,. *Metals*, *8*, 252.

Wei, L., Sevilla, M., Fuertes, A. B., Mokaya, R., & Yushin, G. (2011). Hydrothermal Carbonization of Abundant Renewable Natural Organic Chemicals for High-Performance Supercapacitor Electrodes. *Advanced Energy Materials*, *1*, 356–361. https://doi.org/10.1002/aenm.201100019

Wei, T., Zhang, Q., Wei, X., Gao, Y., & Li, H. (2016). A Facile and Low-Cost Route to Heteroatom Doped Porous Carbon Derived from Broussonetia Papyrifera Bark with Excellent Supercapacitance and CO 2 Capture Performance. *Scientific Reports*, *6:22646*(November 2015), 2–10. https://doi.org/10.1038/srep22646

Wong, L. A., Ramachandaramurthy, V. K., Taylor, P., Ekanayake, J. B., Walker, S. L., & Padmanaban, S. (2019). Review on the optimal placement, sizing and control of an energy storage system in the distribution network. *Journal of Energy Storage*, *21*(June 2018), 489–504. https://doi.org/10.1016/j.est.2018.12.015

Xian Jian, Shiyu Liu, Yuqi Gao, Wei Tian, Zhicheng Jiang, Xiangyun Xiao, Hui Tang, & Liangjun Yin. (2016). Carbon-Based Electrode Materials for Supercapacitor: Progress, Challenges and Prospective Solutions. *J. of Electrical Engineering*, *4*(2), 75–87. https://doi.org/10.17265/2328-2223/2016.02.004

Xiang, Y. C., Chen, C., Zhang, Z. J., & Xie, D. H. (2013). High performance porous carbon through hard–soft dual templates for supercapacitor electrodes. *Journal of Matrials Chemistry A*, *1*, 7379–7383. https://doi.org/10.1039/c3ta10841d

Xie, L., Sun, G., Su, F., Guo, X., Kong, Q., Li, X., Huang, X., Wan, L., Song, W., Li, K., Lv, C., & Chen, C. M. (2016). Hierarchical porous carbon microtubes derived from willow catkins for supercapacitor applications,. *J. Mater. ChemA*, *4*, 1637–1646.

Xie, M., Y, X., J, L., L, C., & X., G. (2014). Ordered nitrogen doped mesoporous carbon assembled under aqueous acidic conditions and its electrochemical capacitive properties. *Microporous and Mesoporous Materials.*, *197*, 237–243. https://doi.org/10.1016/j. micromeso.2014.06.024

Xing, Z., Chu, Q., Ren, X., Ge, C., Qusti, A. H., Asiri, A. M., -Youbi, A. A., & Sun, X. (2014). Ni3S2 coated ZnO array for high-performance supercapacitors. *J. Power Sources*, *245*, 463–467.

Xu, H., Yang, Q., Li, F. F., Tang, L., Gao, S., Jiang, B., Sekhar, C., Ray, C., Konios, D., Stylianakis, M. M., Stratakis, E., Kymakis, E., Lai, Q., Zhu, S., Luo, X., Zou, M., Huang, S., Wazir, A. H., Kundi, I. W., … De Leeuw, N. H. (2015). Will Advanced Lithium- Alloy Anodes Have a Chance in Lithium-Ion Batteries? *AIP*, *2*(032146), 200–247. https://doi.org/10.1016/j.jpowsour.2013.03.160

Xu, L., Jia, M., Li, Y., Zhang, S., & Jin, X. (2017). , Design and synthesis of graphene/activated carbon/polypyrrole flexible supercapacitor electrodes,. *RSC Adv.*, *7*, 31342–31351.

Xu, Y., Z, L., & X, Z. (2014). Holey graphene frameworks for highly efficient capacitive energy storage. *Nat Commun*, *5*, 4554.

Y. Gao. (2017). Graphene and polymer composites for supercapacitor applications: a review. *Nanoscale Res. Lett.*, *122*, 387–404.

Yakout, S. M., & G. Sharaf, E.-D. (2016). Characterization of activated carbon prepared

by phosphoric acid activation of olive stones. *Arabian Journal of Chemistry*, *9*, 1155–1162. https://doi.org/10.1016/j.arabjc.2011.12.002

Yang, Z., Ren, J., & Z, Z. (2015). Recent advancement of nanostructured carbon for energy applications. *Chem Rev*, *115*, 5159–223.

Yao, F., Pham, T., & Hee, Y. (2015). Carbon-Based Materials for Lithium-Ion Batteries , Electrochemical Capacitors , and Their Hybrid Devices. *Chempubsoc*, *8*, 2284–2311. https://doi.org/10.1002/cssc.201403490

Yeon, S., Kim, D., Lee, S., Nam, S., Park, S., So, Y., Shin, K., Jin, C., Park, Y., Kang, Y. C., So, J. Y., Park, Y., & Kang, Y. C. (2017). High microporosity of carbide-derived carbon prepared from a vacuum- treated precursor for energy storage devices. *Carbon*, *11870*. https://doi.org/10.1016/j.carbon.2017.03.063

Yu, X., B, L., & Z, X. (2014). Super long-life supercapacitors based on the construction of nanohoneycomb-like strongly coupled CoMoO(4)-3D graphene hybrid electrodes. *Adv Mater*, *26*, 1044– 1051.

Zhang, H., Baeyens, J., Cáceres, G., Degrève, J., & Lv, Y. (2016). Thermal energy storage: recent developments and practical aspects. *Prog. Energy Combust. Sci*, *53*, 1–40. https://doi.org/10.1016/J.PECS.2015.10.003

Zhang, L., Jiang, Y., L, W., C, Z., & S, L. (2016). Hierarchical porous carbon nanofibers as binder-free electrode for high-performance supercapacitor. *Electrochimica Acta*, *196*, 189–196. https://doi.org/10.1016/j. electacta.2016.02.050

Zhou, H., Liu, G., Liu, J., Wang, Y., Ai, Q., Huang, J., Yuan, Z., Tan, L., & Chen, Y. (2017). Effective network formation of PEDOT by in-situ polymerization using novel organic template and nanocomposite supercapacitorNo Title. *Electrochim. Acta*, *247*, 871–879.

Zhu C, L. T. and Q. F. et al. (2016). Supercapacitors based on three-dimensional hierarchical graphene aerogels with periodic macropores. *Nano Lett*, *16*, 3448–56.

Zhu, Z., Jiang, H., Guo, S., Cheng, Q., Hu, Y., & Li, C. (2015). Dual Tuning of Biomass-Derived Hierarchical Carbon Nanostructures for Supercapacitors : the Role of Balanced Meso / Microporosity and Graphene. *Scientific Reports*, *5:15936*(April), 1–9. https://doi.org/10.1038/srep15936

CHAPTER THREE

3.0. Synthesis and characterization of graphene oxide from locally mined graphite flakes and its supercapacitor applications

3.1. Introduction

The science of nanomaterials involves different steps which include synthesis of the starting materials, characterization, optimization, isolation exfoliation, and cleaning. In naturally occurring materials, carbon is the most abundant element in all organic substances in the universe. It occurs in many forms of different classes of different arrangements called allotropes of carbon with Africa as one of the continents with many mineral deposits like graphite among others. Its abundance makes it the main source for any form of carbon which includes carbon black, graphene oxide, graphene, nanotubes, onions, graphite, diamond to mention but a few (Paulchamy et al., 2015). Graphene oxide (GO) is in the category of graphite which can be processed by oxidation and mechanical methods. The graphene and its oxidized state have gained a lot of interest by both industrial applicability and academic research in fixing the earth's challenges and demand for materials. This is because of their interesting different properties which include mechanical, electrical among others (Eluyemi et al., 2016; Muhamad et al., 2016). Different materials are used in the process of synthesis of graphene oxide. Graphite flakes deposits which are present in Africa can be used as raw materials for the manufacture of materials such as Graphene oxide and other carbon materials like thermally expanded graphite used in fabrication for different application parts.

Graphene oxide (GO) can be synthesized chemically from graphite flakes. Graphene oxide in its structure contains different functional groups attached to the basal planes and

the sideways of the structure (W. Cai et al., 2008; W. Gao et al., 2009). Graphene oxide is sp^3 hybridized structure with layers of carbon. These are formed by the number of functional groups of oxygen (W. Gao et al., 2009; Zheng et al., 2014) which makes it's hydrophilic with interlayers expansion(Sekhar & Ray, 2015). GO also can dissolve in several organic solvents. This means it can be used in other materials like polymers and ceramics as a combination since it has a high surface area. The high surface area makes GO a suitable material for storage devices for energy like batteries and super-capacitors (Paulchamy et al., 2015). The current research study focuses on the synthesis and characterization of GO from locally mined graphite flakes comparing the hummer's with more two (2) modified Hummer's methods and its application for energy storage as supercapacitor electrode materials. The study starts with conversion of graphite flakes into GO using Hummer's method (HM) and modified Hummer's method (MHM) which are chemical oxidation processes that can be performed. This study is aiming at value addition of African raw materials application.

The application of materials for energy storage is for the assessment of the materials to solve the challenges faced by manufacturing industries. The graphite flakes were converted into graphene oxide with an application for energy storage as electrode materials for supercapacitors also known as Electric Double-layer Capacitors (EDLC). These can store energy and power to be delivered. The EDLC has a high capacity of producing high power compared to batteries with a mechanism of charge transfer through the structure of the material using electrolyte and a separator between the electrodes (Iro Zaharaddeen et al., 2016; Pope et al., 2013). EDLC has low weight, high cycle life, high power, low maintenance, and works at a different thermal range from as low as -40^{o}C to as high as 70^{o}C without affecting its efficiency and no fear for the explosion (Iro

Zaharaddeen et al., 2016). These devices can be used in systems where short cycle load is needed more frequently to mention in electric motor vehicles, mechanical systems with motors, washing machines, electric trains among others (Chang et al., 2019; Mittal & Kumar, 2011).

The performance of those materials greatly depends on electrical properties, surface area, pore-volume, stability, interaction with the electrolyte among others (Linfei Lai et al., 2012; Rajagopalan & Chung, 2014). GO is among the materials with different functional groups like COOH, CO, COC, OH which enhances the performance of the EDLC devices (Gomez et al., 2011; Linfei Lai et al., 2012; N. L. Yang et al., 2010). GO is one of the carbon materials which has tremendous properties when it comes to application for energy storage (Chang et al., 2019; Xin Li & Wei, 2013) with high stability and lightweight (Chang et al., 2019; Dong et al., 2017; Shu-bo Zhang et al., 2014). This gives high performance in the capacitive application of EDLC and other hybrid types (S. Chen et al., 2015; Kuila et al., 2012; Leng et al., 2013; Lobato et al., 2015; Wujun Ma et al., 2016; Zhai et al., 2011). The EDLC stores its charge with non-faradaic or by an electrostatic process where there is no charge transfer between electrolyte and electrode materials (Kiamahalleh et al., 2012). When the device is biased, the charge just accumulates at the surface of the electrode which causes charge attraction due to the potential difference resulting in diffusion of the electrolyte ions to go through the separator pores to another electrode enhance high power density (Iro Zaharaddeen et al., 2016).

GO has gained substantial research interest in the field of energy storage which includes supercapacitors, batteries, and hybrids. This is because of their superlative properties. The recent advancement in the use of graphene oxide for supercapacitors as symmetric and

asymmetric have high application. This makes them lead the next generation device for energy storage although there is still a challenge to have a low performance for energy density and storage capacity (Hota et al., 2020; Xiulun et al., 2020).

There is a great improvement in the performance of GO with asymmetric devices. Recently it has been reported that amorphous MoS_2 with reduced GO with the introduction of more sulphur sites increases the interaction of hydrogen ion from the electrolyte solution which increases the electrical conductivity, higher mechanical strength, and surface area of the system. These properties help to increase the performance storage capacity of the materials up to a specific capacitance of 460 F/g at a current density of 1A/g (Hota et al., 2020). Also, it has been reported that the decollated nanostructure of conductive skeletons of carbon materials with binary transition metal sulphides improves the specific capacitance. Tao Liu et al; 2019 (T. Liu et al., 2019), reported FeNiS/rGO with a promising high-performance specific capacitance of 2484 F/g at 1A/g.

Focusing on the effective performance of the supercapacitors without losing their power density and stability, metal-oxide materials have been explored for high capacitance and high performance. This is due to their exceptional mesoporous structure and surface area. Several non-noble metal oxides are used because they are environmentally friendly and inexpensive and these include Fe_2O_3, MnO_2, NiO among others. Xiulun Sun et al (Xiulun et al., 2020) synthesized α-Fe_2O_3 nanowires on a nickel form with $MgCl_2$ metal salt. The material exhibited excellent electrochemical performance with a specific capacitance of 1.57 F/cm^2 with a current density of 1mA/cm^2 with 98% specific capacitance retention (Xiulun et al., 2020).

3.2. Materials and methods

3.2.1. Chemicals and materials

Graphite flakes as locally supplied, sulphuric acid (98%), sodium nitrate (98%), Potassium permanganate (99%), Hydrogen peroxide (30%), and hydrochloric acid (35%) as supplied by Aldrich Sigma.

3.3. Conversion by oxidation of graphite flakes into Graphene Oxide (GO)

In the synthesis of GO from graphite flakes, Hummer's method (HM) and two modified Hummer's Methods (MHM) were used.

3.3.1. Hummer's Method (HM)

GO was synthesized through an oxidation process as that begun by the addition of 2.0g of graphite flakes into 2.0g $NaNO_3$ in a 500ml beaker. 50ml of concentrated H_2SO_4 was then added to the beaker under an ice bath with continuous stirring for 2 hours. After that time, 6.0g of $KMnO_4$ was added carefully to the above mixture at a slow rate to control the temperature to be below 15^oC. The mixture was removed from the ice bath and put on a hot plate with a magnetic stirrer at 35^oC and stirred for 2 days until pasty brownish colour formed. After 2 days, the mixture was slowly diluted with 100ml of distilled water and the reaction temperature was increased rapidly to 98^oC causing effervescence and the colour change to brown(Muhamad et al., 2016). The mixture was further diluted by the addition of 200ml of distilled water with continuous stirring. The dilute solution was finally treated with 10ml of hydrogen peroxide to stop the reaction which changed to a yellow solution with suspension. The sample was cleaned by rinsing and centrifuging

with 10% HCl then followed with Deionised water for several rounds. The sample was then filtered and finally dried in a vacuum at 40^{o}C to obtain the GO powder.

3.3.2. Modified Hummer's method one (MHM 1)

The GO was synthesized from graphite flakes using modified conditions from Hummer's method (Hidayah et al., 2017). 2.0g of graphite flakes were added to H_2SO_4/H_3PO_4 solution prepared by a volume ratio of 9:1 (180:20 ml). This was done under continuous stirring in the ice bath temperatures for 2 hours. Then 7.3g of $KMnO_4$ was slowly added to the mixture while keeping the temperature below 10^{o}C under continuous stirring for 2 days. After 2 days, 90ml of distilled water was slowly added to the mixture with rapid mixing and the mixture turned dark brown with suspensions. This was further treated with 7.0ml of H_2O_2 and 55ml of distilled water for the conversion of MnO_2 and residual permanganate into soluble $MnSO_4$. The mixture turned yellow colour with suspensions. The sample was cleaned 4 times with 150 ml of 3% warm HCl and DI water until pH 7.0 then filtered and dried under vacuum at 40^{o}C for 18 hours.

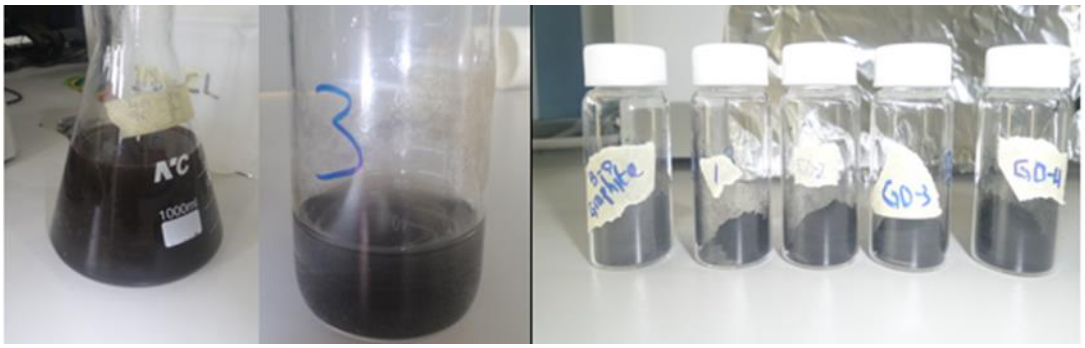

Figure 3.1: Images of sample preparation.

3.3.3. Modified Hummer's method two (MHM 2)

Another method of synthesis for the GO from graphite flakes (Muhamad et al., 2016) was used. 2.0g of graphite flakes and 2.0g of $NaNO_3$ were put in a 1000ml round-bottomed flask and mixed with 90ml of concentrated H_2SO_4 under an ice bath with constant stirring for 4 hours. After that time, 12.0g of $KMnO_4$ was slowly added with a controlled temperature below 10^oC. 184mls of distilled water was added to the mixture at constant stirring and the temperature was raised to 35^oC and kept at vigorous stirring for 4 hours. The mixture was then refluxed at 98^oC for 10 minutes, the temperature was changed to 30^oC for 10 minutes, the solution turned brown colour, then the temperature changed to 25^oC and maintained at that temperature for 2 hours. The solution was treated with 40.0mls of H_2O_2 which terminated the reaction and changed the solution to a bright yellow colour. 400ml of distilled water was added to the solution and stirred for one hour then left to settle for 4 hours, decanted off, and filtered. The resultant suspension was cleaned repeatedly with 10% HCl and distilled water under centrifugation until neutral. This was dried at 60^oC for 8 hours to get GO powder. The synthesis and preparation of GO are shown in Figure 3.1.

3.4. Electrode preparation and electrochemical measurements

The synthesized GO from HM, MHM1, and MHM2 were prepared as active materials for electrodes in the construction of the EDLCs. The active materials were mixed with carbon black and PVDF as a binder in a ratio of 8:1:1 and NMP as a solvent for the formation of the paste which was coated on the graphite foil with a 1.0 cm^2 covered area. The coated electrodes were dried in an oven at 70^oC for 15 hrs. The mass of coated material was

recorded after drying. The devices were assembled using the Swagelok system to have a symmetric device with 6M KOH as an electrolyte.

The electrochemical analysis technique for testing the device was done on a BCS BIO-LOGIC 805 system with the two (2) electrodes set up. Different testing techniques were carried out on the assembled devices to analyse their performance which included; cyclic voltammetry (CV), Galvanostatic charge-discharge (GCD), Electrochemical impedance spectroscopy (EIS), Stability by voltage holding/floating, and Self-discharge. The CV was carried out with the potential window of 1.0 V for different scan rates which included 5, 10, 20, 50, 70, 100, 200, and 500 mV/s. The GCD was performed with a potential window range from 0 to 1.0 V using different current densities to mention 0.25, 0.5, 1.0, 1.5, and 2.0 A/g. The EIS was performed from high to low-frequency range of 10 kHz to 10 MHz with a voltage of 10 mV. The voltage was varied from 10 mV to 20mV to check on the behavior of semi-circle and the curves at high frequency(Bello et al., 2017).

The stability test was performed by the technique of voltage holding or floating where the system sets 3 GCD cycles then the 4^{th} GCD charge cycle the voltage was kept at its maximum potential for 10hrs before performing another set of 3 GCD cycles. This was repeated until 130 hours. The self-discharge was performed after the stability study. This was carried out by charging the device to its maximum voltage using the 0.25 A/g current density. The charge was held at a maximum for 5 minutes before being left to undergo self-discharge in the open circuit (Barzegar et al., 2016; Bello et al., 2017).

3.5. Results and discussions

3.5.1. Characterization of materials

The graphite flakes and GO synthesized by different methods were characterized by ultra-violet- visible spectroscopy (UV-Vis - D-50 SPECORD 50 PLUS Analytikjena German), Fourier transform infrared spectroscopy (FTIR - BRUKER Optics Model TENSOR 27 Germany), Scanning Electron microscopy (SEM - EVO LS 10 SEM modal) with Energy Dispersive X-ray (EDAX-AMETEK), X-Ray Diffraction (XRD - RIGUKU Smart-lab Autosampler), Labram Micro Raman Spectrometer (Horiba Jobin Yvon model) and Electrochemical analysis techniques.

The absorption spectra were obtained with a UV-Vis as shown in figure 2. GO and graphite flakes samples were first dispersed differently in distilled water (0.5mg/ml) and sonicated for 30 minutes to increase the dispersion in water (Nicolosi et al., 2013). The graphite flakes and GO samples were put in the cuvette and scanned between 200 – 700nm wavelength as shown in Figure 3.2. The absorption peaks in the spectra (Figure 2) were observed at two different wavelengths. These two (2) specific kinds are feature characteristics that are used to identify GO from graphite flakes with one peak in the range of 320 to 360 nm as in figure 2a which appeared at a wavelength of 310nm. The first peak in GO that appears at around 230nm wavelength is a corresponding identifier of a π-π^* transition in aromatic C-C bond (Fentaw & Worku, 2017).

The position and abundance of each sample peak slightly changed between the GO samples for the different methods as shown in Figure 3.2(b, c, and d). The second peak shoulder which comes out of an approximate range of 280nm – 300nm corresponds to the

identification of n-π* transition of C=O bond (Eluyemi et al., 2016; Q. Lai et al., 2012; Muhamad et al., 2016).

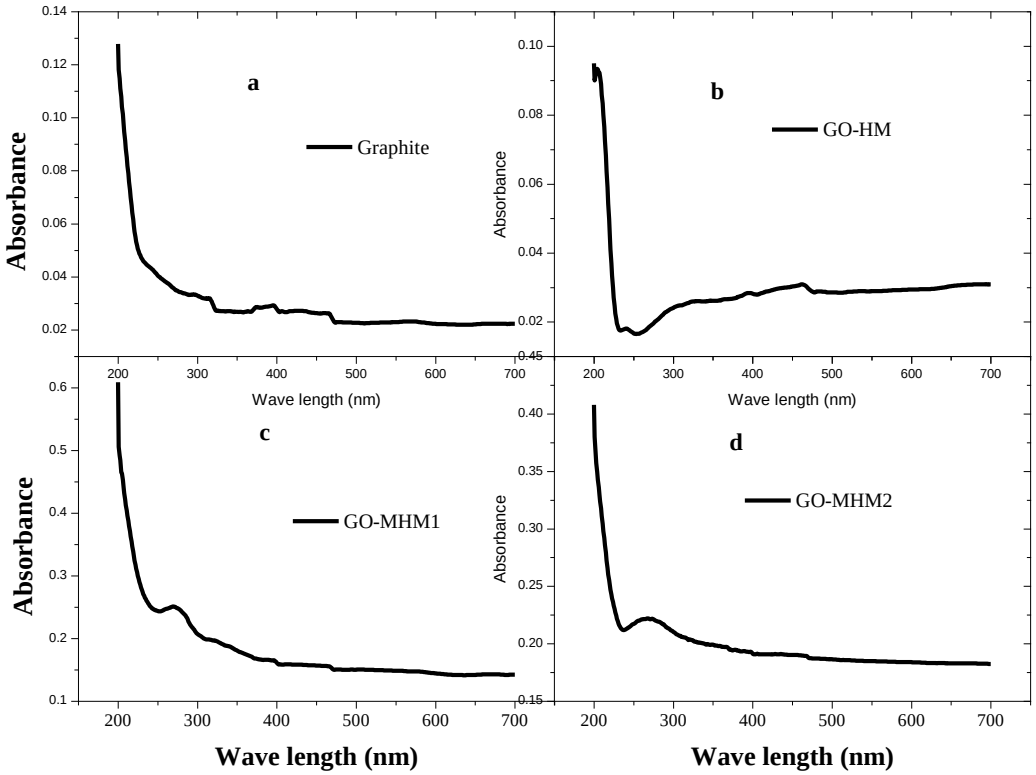

Figure 3.2: UV-Vis spectra of Graphite and synthesized GO.

To investigate the bond stretch interaction in the samples, an FTIR spectrometer was used. Figure 3.3 show different response at different wave number. In the fingerprint region (<1500 cm^{-1}) the sample materials depict the same peaks with stretch bonds like C-C, C-O, C=C, and C=O. The C-O showing the strongest peak followed by C=O at 1159 and 1576 cm^{-1} respectively. This is a sign of indication for the oxidation of GO materials. The diagnostic region showed bonding at different wavenumbers. The C=C stretching at 1461 cm^{-1} depicted in both GO-MHM2 and GO-HM, C=O stretching in all the GO samples at 1577cm^{-1} and 1728 cm^{-1} (COOH group) (Hidayah et al., 2017; Javed & Hussain, 2015;

Khalili, 2016; J. Song et al., 2014). GO-HM and GO-MHM2 samples shown a peak response at 2402 cm^{-1} which is an indication of a bond between GO and CO_2 which occurs at the temperature from 50 to 120^oC (Eigler et al., 2012; Nam et al., 2018; Pham et al., 2011). The C-H sp^3 stretching at 2770 cm^{-1} shown a weak response in the three (3) samples. The O-H/sp stretching was depicted in 3876 with a medium response with GO-HM and GO-MHM2 and weak response with GO-MHM1. The response of the C=O bond confirms an existing bond before in oxidation process (Bykkam et al., 2013; Huang et al., 2007; Sohail et al., 2017; Zaaba et al., 2017). This shows the absorptivity of GO for water molecules. The presence of hydrogen buckling bond orientation with carboxyl group tends to form a peak and valley with the edge interaction (Jibrael & Mohammed, 2016; X. Shen et al., 2014). The presentation of the functional groups such as C=O and C-O in the GO materials further confirms that the graphite flakes were oxidized to GO (J. Shen et al., 2011; J. Song et al., 2014; K. Zhou et al., 2011).

The scanning Electron Microscopy (SEM) was employed to provide the structure and morphology of graphite flakes and GO (Jibrael & Mohammed, 2016). Figure 3.4a shows the abundant carbon atoms on the surface of graphite flakes. Figure 3.4(b c and d) shows the particle morphology of the GO powder for the three (3) synthesized GO samples with their surfaces indicating the blend of carbon and oxygen (Jibrael et al., 2015). EDX analysis depends on the atomic mass of elements in the samples for detection. The lower the atomic mass, the lower the response. The peak size depends on the abundance of the element in the sample. For graphite flakes and GO, the main element is carbon as shown by its largest peak. The EDX generates an X-ray spectrum from the entire sample scanned areas using SEM images like in Figure 3.4. Using the Noran System Six (NSS) software,

the X-ray energy levels are associated with the individual elements in the sample and the orbital shell levels like K-shell that generated them.

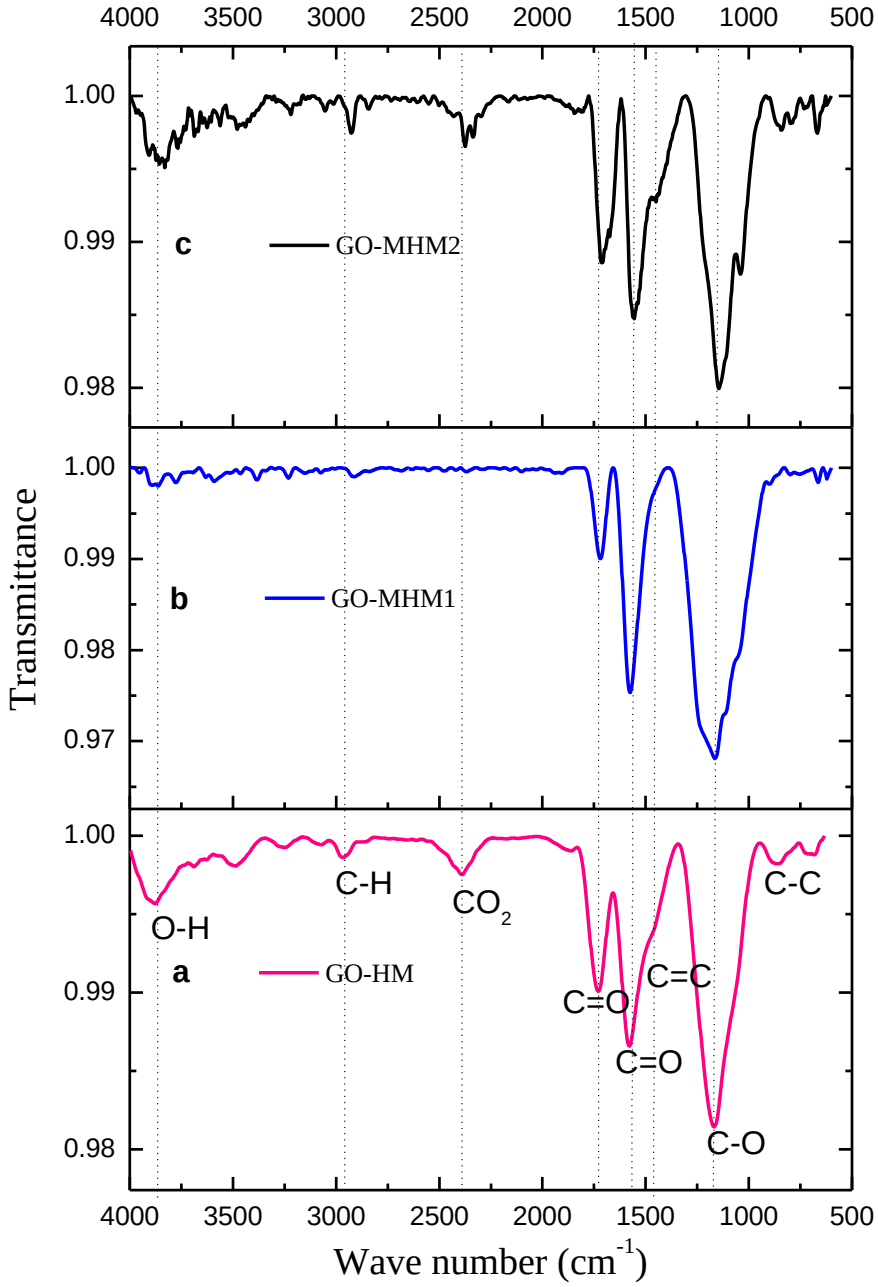

Figure 3.3: FTIR spectra of GO synthesized with HM, MHM1, and MHM2 methods.

The X-ray from the samples is generated by the inelastic interaction of the beam of electrons with the sample atoms. These characteristic X-rays from the samples are revealed as peaks imposed on the background of the continuum X-ray from the interaction of the electrons with the nucleus of the samples. The hole in the K-shell of the sample atom of the samples is created by an incident high energy electron and then loses energy to the ejected electron.

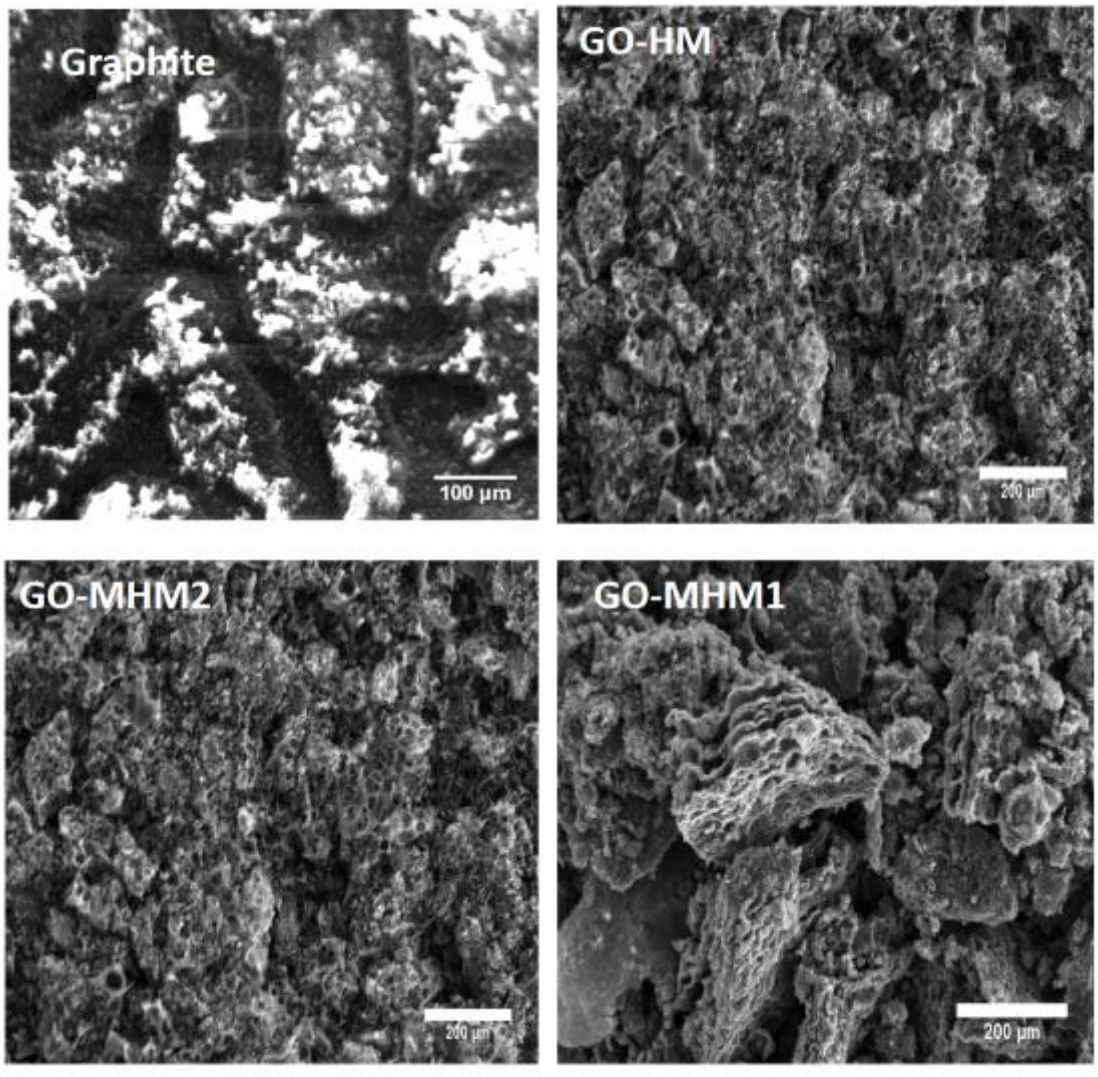

Figure 3.4: SEM micrographs of Graphite and synthesized GO.

The k-shell is then filled with an electron from the outer shell for the stability of the atom. The energy of the x-ray is related to the element atomic number from which the weight percentage is derived basing on the abundance of those atoms in the samples. From graph 1, the results show that the graphite flakes have a high number of C-atoms giving the weight percentage of 95.47% as in Table 1and Figure 3.5a. The concentration of oxygen is as low as 0.3% (Table 3.1 and Figure 3.5a) which means there is likely no oxidation in the sample of graphite.

The Energy Dispersive X-ray analyzer (EDX) spectra and elementally weight percentages were obtained for the graphite flakes and GO samples as shown in Figure 3.5 (a, b, c & d) and Table 3.1. The x-rays from the samples are generated by the inelastic interaction of the beam of electrons with the sample atoms. These characteristic x-rays from the samples are revealed as peaks (Figure 3.5) imposed on the background of the continuum x-rays from the interaction of the electrons with the nucleus of the samples. The lower the atomic mass, the lower the response, and the detector peak size depends on the abundance of the atoms of that element in the sample.

Table 3.1: EDX elemental weight percentage of graphite and synthesized GO

Sample	**Elemental weight percentage**											
	C	**O**	**Si**	**S**	**Cl**	**K**	**Ca**	**Mn**	**Fe**	**Mo**	**Al**	**C/O**
Graphite	95.47	0.3	1.02	-	-	-	-	-	-	3.09	0.11	318.2
GO-HM	44.59	2.08	6.09	9.78	1.38	2.02	3.78	-	30.29	-	-	21.4
GO-MHM2	48.2	2.41	-	30.24	1.12	2.55	6.18	9.31	-	-	-	20.0
GO-MHM1	56.02	6.73	-	29.09	3.35	4.8	-	-	-	-	-	8.3

When graphite flakes were oxidized with Hummer's method (HM), the weight percentage of carbon decreased to 44.59% (Table 3.1) which created an increase in the atomic percentage by 2.08%. This shows that the method introduced more oxygen in the graphite to form graphene oxide. The process introduced other atoms like sulphur, potassium, chlorine, calcium, and iron (Figure 3.5b). This is possibly due to incomplete reactions and poor cleaning method of GO. These elements may have come from the initial chemicals and reagents used in the process of oxidation. With the MHM2 Figure, 3.5d indicated the oxidation response equal to HM as seen with C/O in table 1 having the same ratio. The MHM 1 had an increase up to 6.73% with a C/O ratio of 8 (Table 3.1). This means the method shown a better oxidation completion compared to the rest hence reducing the oxidizing agent which in the removal of other elements like Manganese and Calcium (Table 3.1) showing the highest oxidation effect among all methods. In the process of oxidation, the reaction of Sulphur with carbon forming polysulphide hence reducing the interaction of oxygen with carbon (Drewniak et al., 2016).

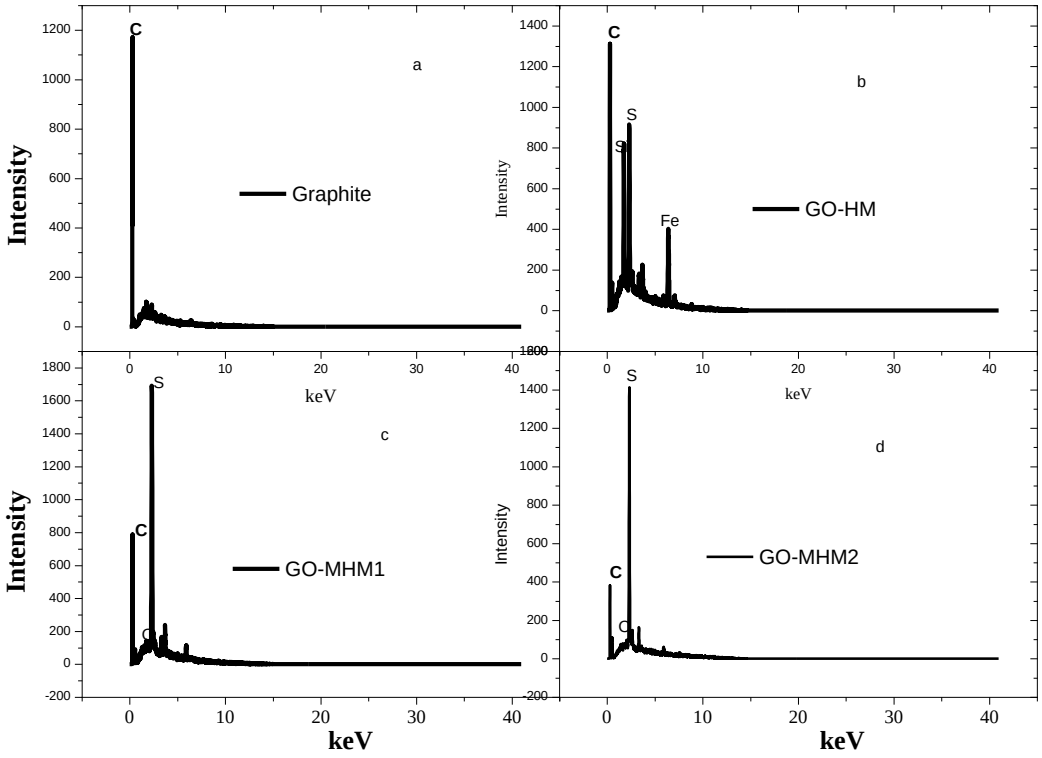

Figure 3.5: EDX spectra of Graphite and synthesized GO.

This may be so because MHM1 uses a high volume of concentrated acid combination than HM and MHM2 yet the weight of the graphite flakes remains the same in both methods. This also is because of the ability for sulphur to accept a pair of electrons donated by another atom. Also, when sulphur is in excess, can achieve a maximum covalence of six by expending to an excited state forming SP^3d^2 hybrid orbitals which limit oxygen's interaction since it only forms homo-nuclear diatomic molecules. Also, sulphur forms more oxides than its congeners.

Table 3.2: The current density, specific capacitance (F/g), specific energy (Wh/kg), specific Power (W/kg), and efficiency (%) of GO produced by HM, MHM1, and MHM2 using 6M KOH electrolyte and potential of 1.0 V.

Sample	**Current density (A/g)**	**Specific capacitance (C_s) (F/g)**	**Specific Energy (E) (Wh/kg)**	**Specific Power (P) (W/kg)**	**Efficiency (ɳ) (%)**
GO-HM	0.25	125.4	4.35	125	96.49
	0.5	133.16	4.62	250	98.72
	1	118.92	4.13	500	97.99
	1.5	112.5	3.91	750	97.81
	2	105.52	3.66	1000	95.30
GO-MHM1	0.25	192.49	6.68	125	92.74
	0.5	**211.2**	**7.33**	250	99.15
	1	195.4	6.78	500	100.95
	1.5	184.5	6.41	750	99.00
	2	176.72	6.14	1000	101.80
GO-MHM2	0.25	185.69	6.45	125	98.38
	0.5	204.94	7.12	250	99.45
	1	189.12	6.57	500	98.52
	1.5	183.48	6.37	750	99.93
	2	172.64	5.99	1000	97.12

The synthesized GO materials were analyzed by X-Ray Diffraction (XRD) technique with a Cu kα source and JCPDS-ICDD library database to determine the materials' average crystallite structural properties. Figure 3.6 shows the spectra of the GO materials indicating the formation of peaks at $2\Theta = 11^{o}$ with (001) plane, $2\Theta = 26.62^{o}$ with (002) plane, and another peak at $2\Theta = 43^{o}$ with (100) plane which appeared in all the three (3)

samples. The GO-MHM2 revealed another peak at 2Θ = 77° which is a reflection peak for the graphitic nature of the material. (J. Song et al., 2014)(Khalili, 2016). The peak at 2Θ =11° indicates that there was oxidation of the graphite to form graphene oxide in all samples. The samples showed other peaks at 2Θ = 26.62°, 43° and 77° which indicates that the graphite was not completely oxidized to GO hence remaining in the samples (J. Song et al., 2014)(Khalili, 2016)(Hidayah et al., 2017)(Javed & Hussain, 2015).

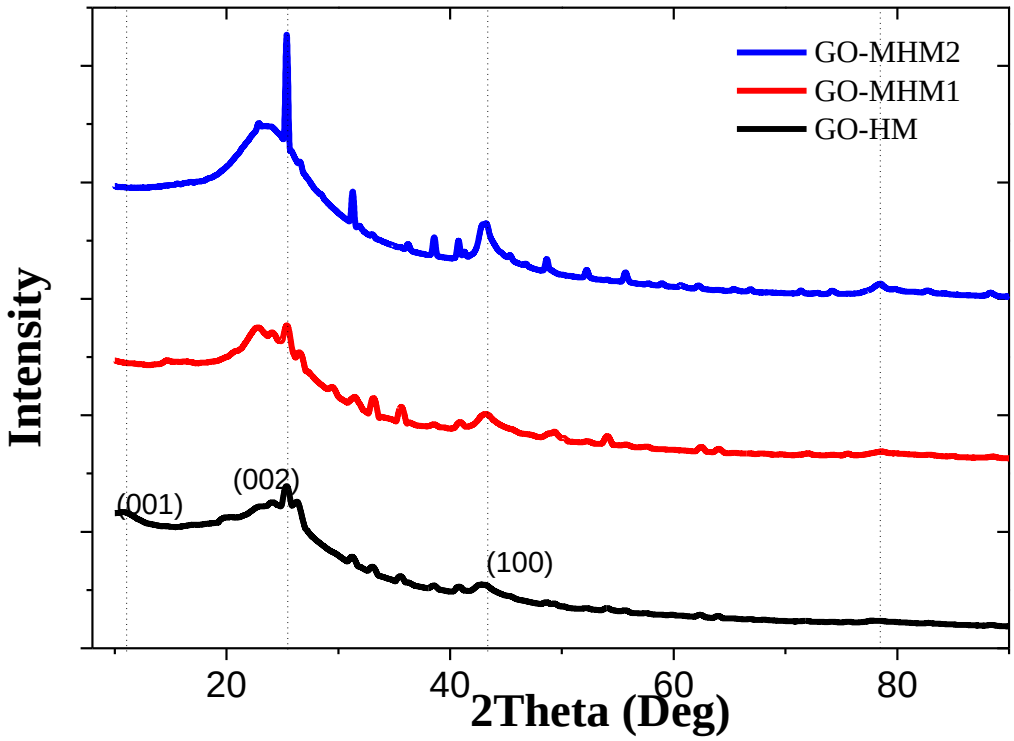

Figure 3.6: XRD spectra for GO materials.

The Raman spectroscopy was used to study the disorder and defects in the crystal structure. The disorder was determined by the intensity ratio between the disorder-induced D band and the Raman allowed G band as I_D/I_G. As graphite flakes are oxidized into GO, the G band peak broadens and the D band intensity increases substantially indicating the decrease in the size of the in-plane sp^2 sites possibly due to the oxidation process. The D band for the materials appeared at approximately 1364 cm^{-1} and the G

band at approximately 1600 cm^{-1} for GO-MHM2, GO-HM, GO-MHM1, and graphite flakes as shown in Figure 3.7. The D band is a result of the reduction of the sp^2 domain size which introduces vacancies, defects, and disorder due to the oxidation process. The G band is due to the plane vibration which is very responsive with the sp^2 sites as a result of C-C bond stretch (R. Gao et al., 2013; Krishnamoorthy et al., 2013; Perumbilavil et al., 2015). The I_D/I_G ratio for the materials was 1.25, 1.09. 1.07 and 0.4 for GO-MHM1, GO-MHM2, GO-HM, and graphite flakes respectively. The all the ratios are higher than that of graphite which indicates oxidation of the materials. GO-MHM1 shown the highest ratio indicating the higher oxidation process and this is in agreement with the EDX results where it showed the higher percentage of oxygen in the sample.

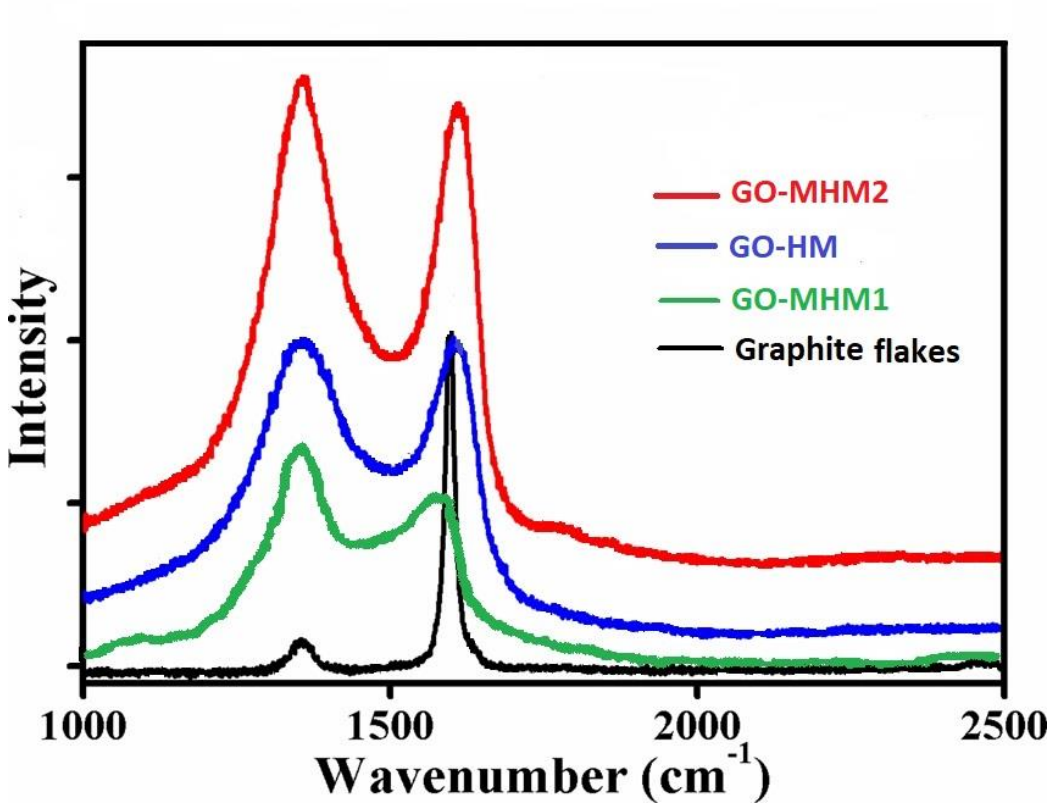

Figure 3.7: Raman spectra for GO-HM, GO-MHM1, GO-MHM2, and graphite flakes.

3.5.2. Electrochemical characterization of materials

The GCD curves of synthesized GO in 6M KOH electrolyte is shown in Figure 3.8 and Table 3.2. The specific capacitance (C_s) was calculated using equations 3.1 and 3.2. The capacitance (F) of the EDLC was evaluated using the discharge-time slope using equations (Barzegar et al., 2016; Laheäär et al., 2015; J. Xie et al., 2018).

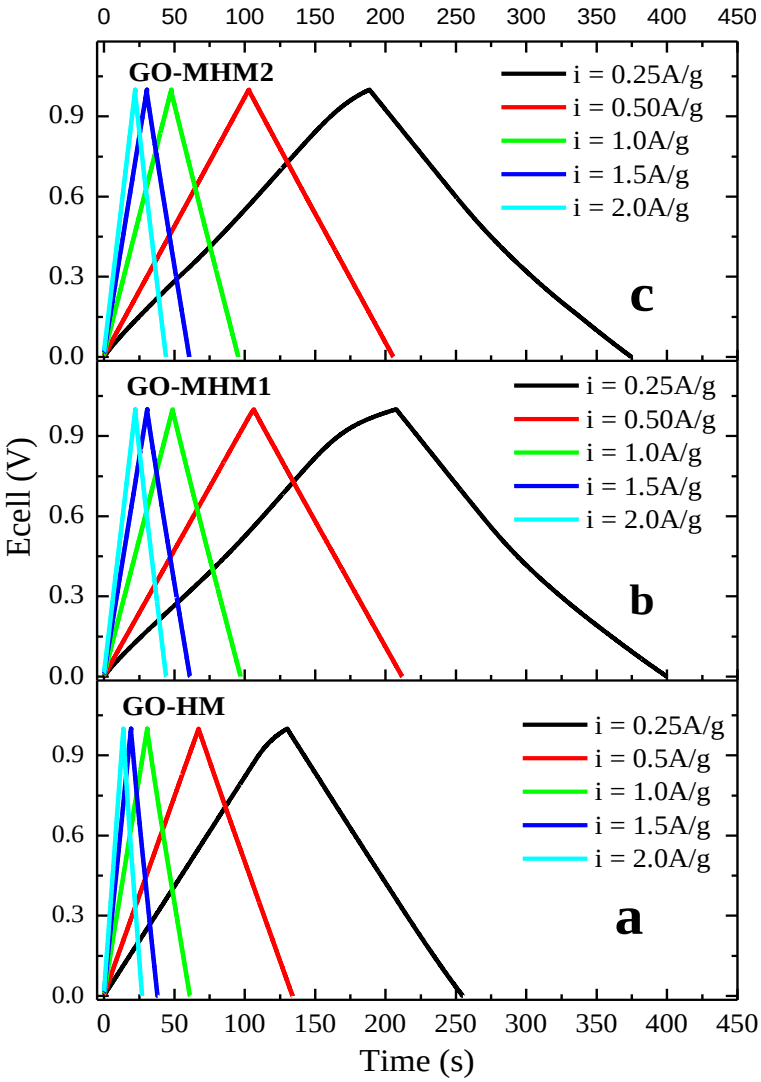

Figure 3.8: Galvanostatic Charge/Discharge of GO materials prepared with HM, MHM1, and MHM2 methods using 6M KOH as electrolyte at different current densities.

$$C = \frac{I\Delta t}{\Delta V} \tag{3.1}$$

The specific capacitance (F/g) for a single electrode using equation

$$C_s = \frac{2C}{0.5m_{el}} \tag{3.2}$$

Where I is the applied current (A)

Δt is the discharge time (s)

ΔV is the change in potential (V)

M_{el} is the total mass of electrode material

The specific energy (E), specific power (P), and the efficiency (η) was also evaluated using the following equations (Allagui et al., 2018; Barzegar et al., 2016; Laheäär et al., 2015);

$$E = \frac{CV_{max}^2}{2 \times 3.6m_{el}} \tag{3.3}$$

$$P = \frac{3600\ E}{\Delta t} \tag{3.4}$$

$$\eta_t = \frac{t_D}{t_C} \tag{3.5}$$

Where t_D is the discharge time (s), t_C is the charge time (s) and V_{max} is the maximum potential (V).

From Figure 3.8, the GO-MHM1 gave the highest specific capacitance (Cs) of 211.2 F/g at a current density of 0.5A/g as shown in Figure 3.8b and Table 3.2. The trend of the specific capacitance for all GO materials was reduced with an increased current density as shown in Table 3.2. The GO-MHM1 with C_s of 211.2 F/g gave specific energy of 7.33

Wh/kg as the highest with 250 W/kg of specific power and the efficiency of 99.15% (Table 3.2). GO-MHM2 in figure 8c with the C_s of 204.94 F/g at a current density of 0.5A/g as the highest for the material and the second-highest among the three (3) GO materials. The C_s of 204.94 F/g shown specific energy of 7.12 Wh/kg and specific power of 250 W/kg and an efficiency of 99.45%. The GO synthesized by HM shown the lowest C_s performance with 133.16 F/g at a current density of 0.5A/g having the highest performance for GO-HM material. The C_s of 133.16 F/g shown specific energy of 4.62 Wh/kg and specific power of 250 W/kg.

The C_s performance of the GO materials has a trend of GO-MHM1 > GO-MHM2 > GO-HM with a similar trend for the specific energy. This is because of the availability of oxygen functional groups on the surfaces of the material as depicted by EDX results in Table 3.1 with a C/O ratio of 8.3 for GO-MHM1, 20.0 for GO-MHM2, and 21.4 for GO-HM. The oxygen functional groups heighten the performance of the EDLC (Gomez et al., 2011; L. Lai et al., 2012). The specific power of all the GO materials gave the same performance with the same current density but increased with increased current densities with 2.0 A/g having the highest performance of 100 W/kg in all materials (Table 3.2). The efficiency of the devices was in the range of 92 to 101.8% which is the ideal performance of EDLC devices from porous carbon (Laheäär et al., 2015). The C_s of the samples are higher than the GO (Le et al., 2011) with a measurement between 132 F/g in the scan rate range of 0.5 to 0.01 V/s and showing the highest specific energy of 6.74 Wh/kg and specific power of 190 W/kg from fabricated inkjet printer graphene electrodes. The reduced GO (Nam et al., 2018) has a C_s of 85 F/g at 1.0 A/g which is also lower than the current study. The results from the current work showed a lower performance compared to the reduced GO (Chang et al., 2019) with C_s of 430 F/g, specific

energy of 8.96 Wh/kg, and the specific power of 100.42 W/kg at the scan rate of 4 mV/s. The Cyclic voltammogram (CV) of GO samples in the 6M KOH electrolyte at the scan rate of 5, 10, 20, 50, 70, 100, 200, and 500 mV/s are shown in Figure 3.8. The CV performance exhibited a symmetric and quasi-rectangular shape in all the samples. This shape indicates the performance of high double-layer capacitance (HDLC) (Ban et al., 2012; Hsieh et al., 2011).

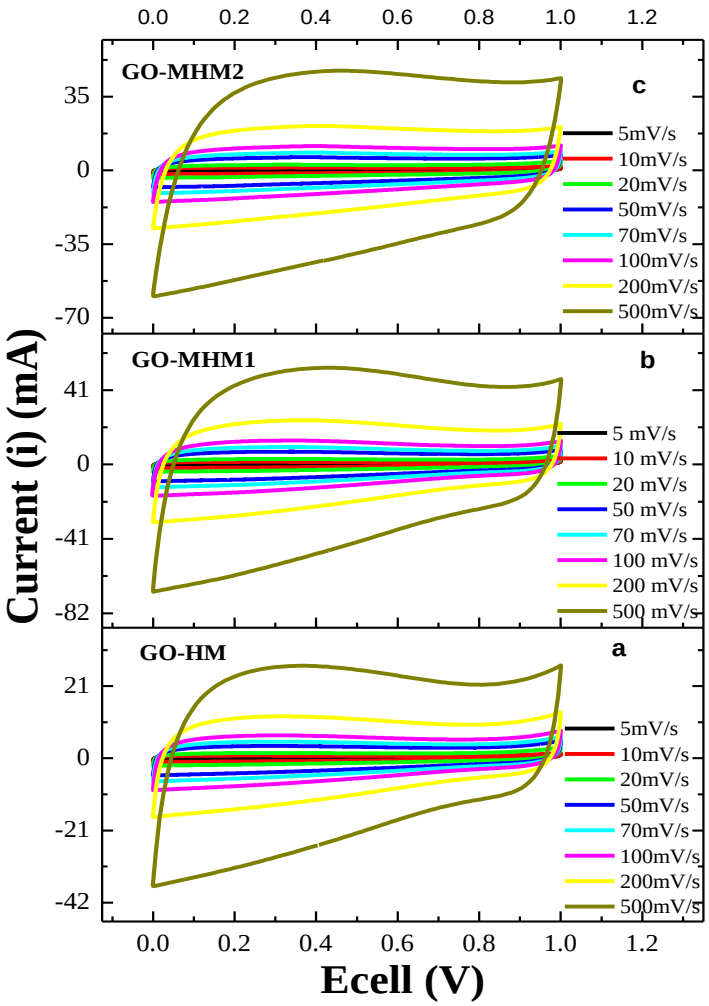

Figure 3.9: Cyclic voltammetry of GO materials prepared with HM, MHM1, and MHM2 using 6M KOH as electrolyte at different scan rates.

This is indicative of EDLC capacitive behavior and the shapes for all synthesized GO were maintained up to 500 mV/s (Figure 3.9). From Figure 3.9 (a and b), the shapes are similar to some small hump which indicate a little overcharging at high voltage (Mathis et al., 2019). Figure 3.8c shows the best quasi-rectangular shape with no hump even 500 mV/s for the GO-MHM2.

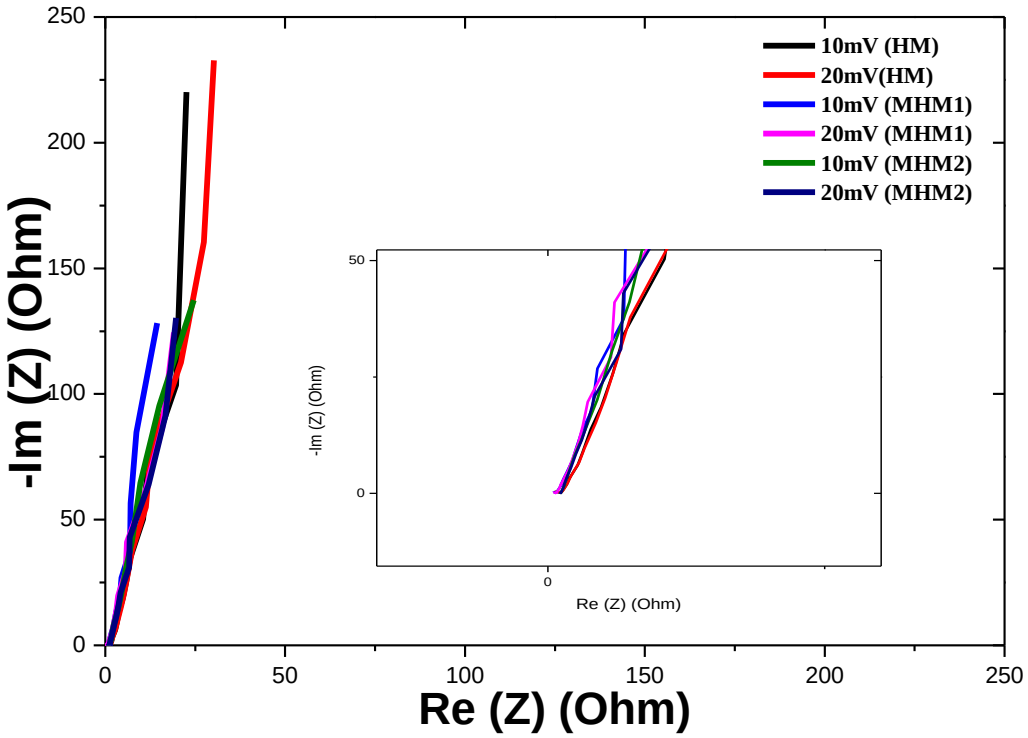

Figure 3.10: Nyquist EIS plot for GO materials at different voltages for the three methods used.

The transport charge characterization of the electrode material was further performed by electrochemical impedance spectroscopy (EIS) technique. This was carried out in the frequency range of 10 kHz to 10 mHz in the open potential circuit using 6M KOH as an electrolyte. The Nyquist plot of the results is shown in figure 10. The potential was varied from 10 mV to 20 mV to determine the charge transfer resistance (Mathis et al., 2019). Figure 10 shows the impedance plots with similar behavior in the high and low-frequency regime. The plots from the material shown no semi-circles in the frequency regime in the Nyquist plots (Figure 3.10 insert). This indicates a good capacitance and high electrical

conductivity of the GO electrode materials (L. Lai et al., 2012; Nam et al., 2018; Saha et al., 2016). The EIS shows approximately the same resistance (0.82 Ω) for all the GO synthesized materials with the real frequency axis. This indicates a very low series resistance in the assembled devices which included electrolyte, current collector, the surface of the materials, and the Swagelok used in all the GO (Linfei Lai et al., 2012; Mathis et al., 2019; J. Xie et al., 2018).

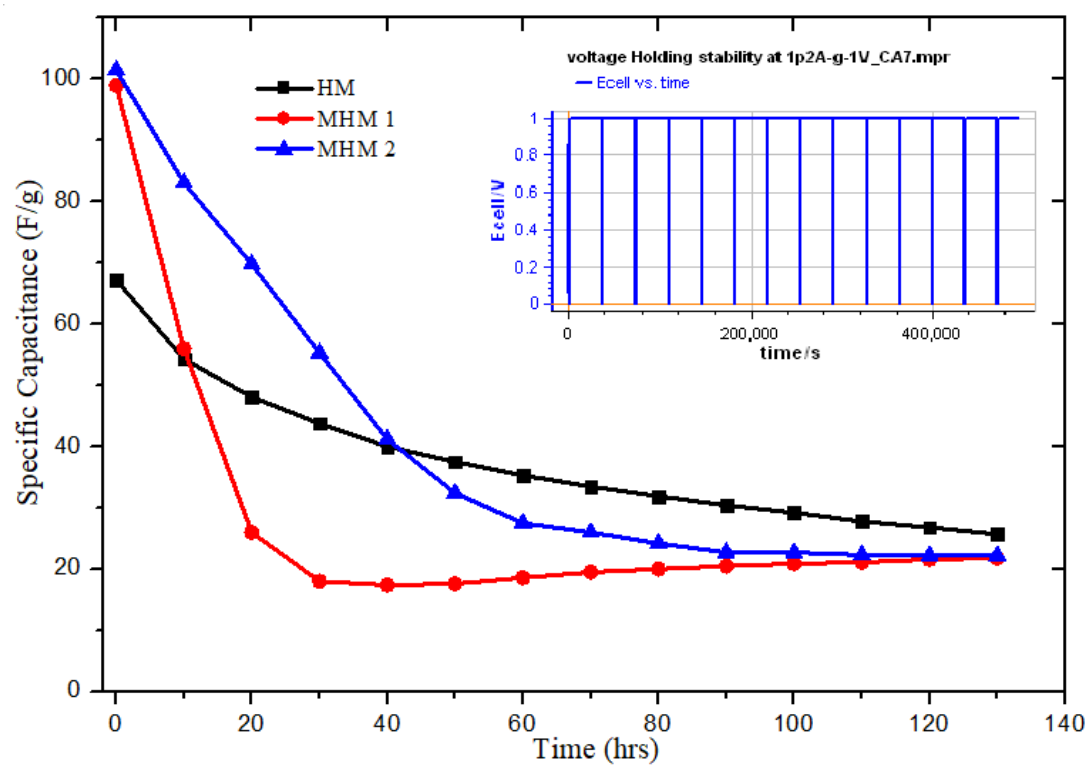

Figure 3.11: Voltage holding stability of GO materials prepared with HM, MHM 1, and MHM 2 methods and EC stability display in the insert.

The Nyquist plot shows the vertical curves from the high frequency to the low frequency of the imaginary axis. This is an indication of low internal resistance and high conductivity (Linfei Lai et al., 2012). The 45^{o} and 90^{o} angle line formation at a high-frequency regime concerning the real axis of the impedance indicate the behaviors of the charge storage capacitive mechanism for the EDLC materials. From figure 10, when there are no semi-circles in the high-frequency regime is a typical signature of supercapacitor

materials. This is because porous carbon electrode materials store their charge in the physical behavior without any charge transfer in the process (Mathis et al., 2019). To validate if there is any formation of the semi-circle at high potential. The EIS was carried out at different potentials and also to ascertain the charge transfer resistance. After performing the EIS at 10 and 20 mV, the curves showed no change at high-frequency regime but only a small deviation at a low frequency of the imaginary regime which indicates there was no charge transfer resistance but only small internal resistance causing a small deviation at the low-frequency regime of the imaginary axis as shown in figure 10 and its insert.

The stability of the assembled devices was carried out by voltage holding/floating methods as indicated in Figure 3.11 insert. Figure 3.11 shows the performance of the voltage holding for 130 hours. This is a new conventional cycling method that is a more realistic and reliable way for stability testing of supercapacitors (Barzegar et al., 2016; Bello et al., 2017). This method gives real stability to tough conditions like holding a charge at its maximum for 10 hours before the discharge cycle which causes degradation details that may occur in the electrochemical process of the device (Bello et al., 2017).

It can be seen from Figure 3.11 that performance decrease in the specific capacitance after 10hours and continued to decrease slowly until the end of 130 hours. The GO-MHM2 and GO-HM showed 17% capacitance fade after 10 hours and GO-MHM1 exhibited a 45% fade. The fading in GO-HM was more stable than other GO materials which kept a 50% loss at the end of 130 hours. The loss of capacitance of GO-MHM2 stabilized at a loss of 70% after 70 hours which further lowered to 80% at the end of 130 hours. At the end of 30 hours, GO-MHM1 lost up to 80% and was kept at that level until 130 hours. This indicates that there was high intercalation in the materials with an electrolyte

between 10 to 60 hours which may be due to the interaction of K^+ ions from the electrolyte at high potential. This may also be due to K^+ ion interaction with oxygen functional groups on the surface of the material causing faradic reactions as shown in Figure 3.12.

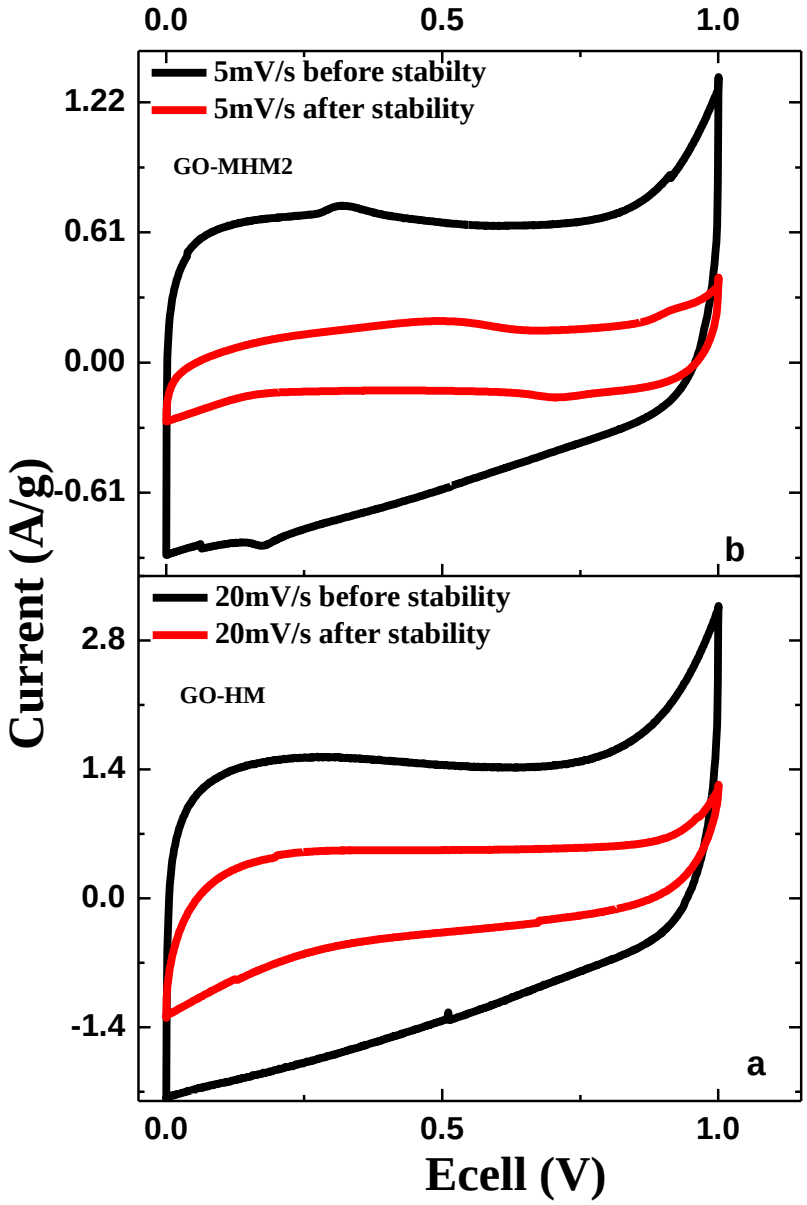

Figure 3.12: CV for the GO materials before and after the voltage holding stability test.

The faradaic reactions were revealed by the CVs carried out before and after stability as shown in Figure 3.12. Figure 3.12 show exponential peaks at a high voltage which may be due to dissociation of the electrolyte and interaction of the K^+ ions with the surface of the materials. There is also a reduction of the shape size in Figure 3.12 after stability which implies there is a loss of capacitance due to these mentioned factors. The high capacitance fade in the current work is similar to that performed on YP17/PTFE (Ruch et al., 2010) when comparing the voltage holding testing method with conventional cycling where they obtained a capacitance loss of 68% within 100 hours and 97% loss after 500 hours with voltage holding method yet conventional cycling shown 2% after 50,000 cycles which took approximately 800 hours.

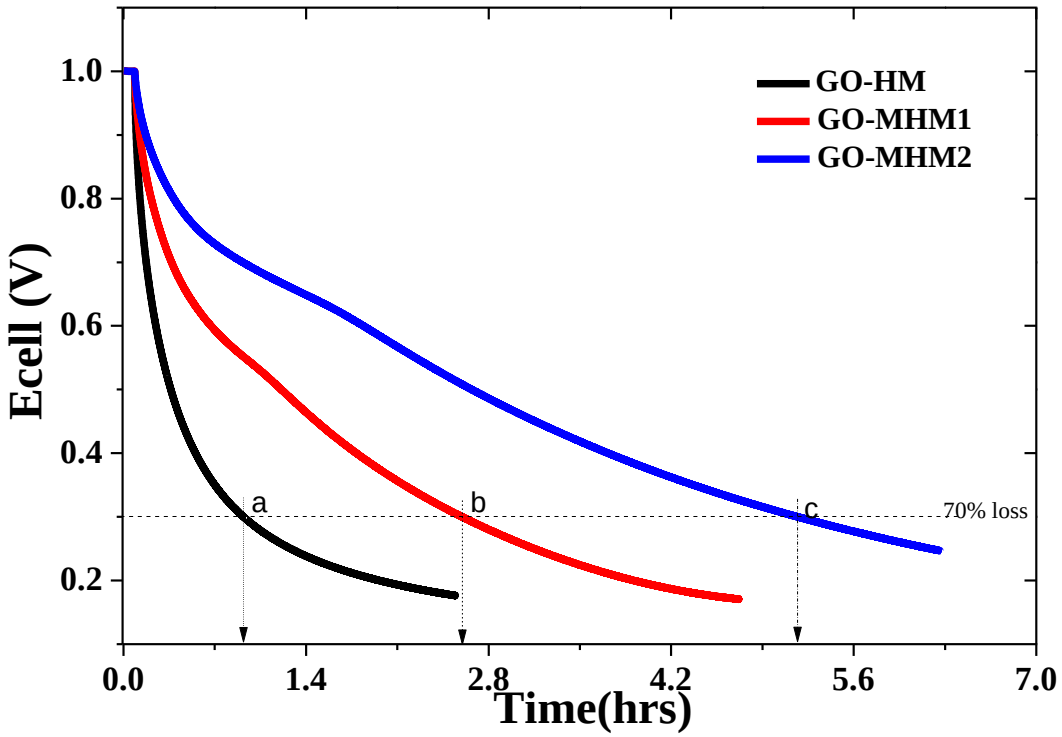

Figure 3.13: Self-discharge of GO materials after charging the device to 1V and holding for 5 minutes in an open circuit.

In comparing voltage holding with conventional cycling, (Weingarth et al., 2013) reported capacitance loss of 30% after 20 hours with voltage holding at 3.5 V which required 300 hours for conventional cycling to observe the same loss. (Weingarth et al., 2013) Concluded that voltage holding was more time-efficient than cycling test. The fact is that during voltage holding, the capacitor is subjected constantly to maximum potential for a long holding time keeping the dissociated ions in contact with the materials yet in conventional cycling, the capacitor is only exposed to the mutable potential (Barzegar et al., 2016; Weingarth et al., 2013).

Self-discharge is another important technique for the evaluation of the life of the supercapacitor. This was carried out after the voltage holding test on the same device. The devices were charged up to 1.0 V and hold for 5 minutes before they were left to self-discharge in an open circuit. Figure 3.13 shows the performance of the assembled devices from the GO synthesized materials. The GO-MHM2 shown a voltage loss of 70% after 5.2 hours (part c in Figure 3.3) showing to be a better performer than the other materials. GO-MHM1 lost 70% in less than 2.8 hours and GO-HM in less than 1.2 hours as shown in figure 13-part b and part a, respectively.

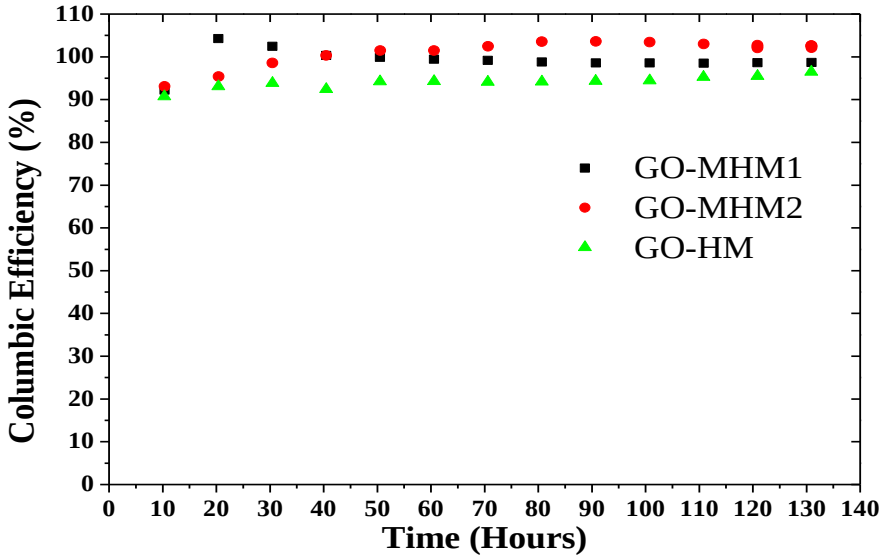

Figure 3.14: The plot of columbic efficiency % versing stability voltage holding time in hours

The columbic efficiency versus stability voltage holding time in hours shown in Figure 3.14 for the three synthesized materials. The stability test was carried out by voltage holding / floating with three (3) charge-discharge before holding the voltage at a maximum of 1.2V for 10 hours before another cycling round. Equation 3.5 was used to evaluate the columbic efficiency of the material with the discharge/charge time for each second cycle from the 3 cycles. The GO-MHM2 shown the highest retention of 102% followed by GO-MHM1 with 99.1% and GO-HM with the lowest retention of 96.5% which was maintained after performing the test for 130 hours.

Conclusion

The GO materials were synthesized successfully from graphite flakes using hummer's method and two other modified methods from Hummers with a change in some conditions and materials used. The materials were characterized with different techniques which included UV-Vis spectroscopy, FTIR, SEM-EDX, XRD, and electrochemical

analysis to check their applicability for energy storage in supercapacitors. The characterization techniques confirmed the existence of different functional groups which are key in GO. These include C-O, C=O, and main elements like carbon and oxygen. The presentation of the functional groups such as C=O and C-O in the GO materials further confirms that the graphite flakes were oxidized to GO. EC performance of the GO materials as supercapacitor electrode materials also confirmed the usefulness of the materials for EDLC device application. The electrochemical characterization performance of materials produced the highest specific capacitance of 211.2 F/g with a current density of 0.5 A/g and the specific energy of 7.33 Wh/kg from MHM1 sample.

REFERENCES

Allagui, A., Freeborn, T. J., Elwakil, A. S., Fouda, M. E., Maundy, B. J., Radwan, A. G., Said, Z., & Abdelkareem, M. A. (2018). Review of fractional-order electrical characterization of supercapacitors _ Elsevier Enhanced Reader.pdf. *Journal of Power Sources*, *400*, 457–467. https://doi.org/10.1016/j.jpowsor.2018.08.047

Ban, F. Y., Majid, S. R., Huang, N. M., & Lim, H. N. (2012). Graphene Oxide and Its Electrochemical Performance. *International Journal of Electrochemical Science*, *7*, 4345–4351.

Barzegar, F., Khaleed, A. A., Ugbo, F. U., Oyeniran, K. O., Momodu, D. Y., Bello, A., Dangbegnon, J. K., & Manyala, N. (2016). Cycling and floating performance of symmetric supercapacitor derived from coconut shell biomass. *AIP Advanced*, *6*(115306), 9. https://doi.org/10.1063/1.4967348

Bello, A., Barzegar, F., Madito, M. J., Momodu, D. Y., Khaleed, A. A., Olaniyan, O., Masikhwa, T. M., Masikhwa, Dangbegnon, J. K., & Manyala, N. (2017). Floating of PPY Derived Carbon Based Symmetric Supercapacitor in Alkaline Electrolyte. *E C S Society, The Electrochemical*, *75*(24), 1–12. https://doi.org/10.1149/07524.0001ecst

Bykkam, S., K, V. R., Ch, S. C., & Thunugunta, T. (2013). Synthesis and characterization of graphene oxide and its antimicrobial activity against klebseilla and staphylococus. *Inter Journal of Advanced Biotechnology and Research Journal of Advanced Biotechnology and Research*, *4*(1), 142–146.

Cai, W., Piner, R. D., Stadermann, F. J., Park, S., Shaibat, M. A., Ishii, Y., Yang, D., Velamakanni, A., Ani, S. J., Stoller, M., An, J., Chen, D., & Ruoff, R. S. (2008). Synthesis and Solid-state NMR structural Characterization of 13C-labeled Graphite oxide. *Science AAAS*, *321*(1815).

Chang, Y., Xia, S., Han, G., Zhou, H., Fu, D., Song, H., Xiao, Y., & Zhang, Y. (2019). Flexible supercapacitor electrode with high performance prepared from graphene oxide films assembled in the presence of p - phenylenediamine and urea. *Journal of Materials Science: Materials in Electronics*, *30*, 7216–7225. https://doi.org/10.1007/s10854-019-01000-0

Chen, S., Ma, W., Cheng, Y., Weng, Z., Sun, B., Wang, L., Chen, W., Li, F., Zhu, M., & Cheng, H.-M. (2015). Scalable non-liquid-crystal spinning of locaaly aligned graphene fibers for high-performance wearable supercapacitors. *Nano Energy*, *15*, 642–653.

Dong, L., Chen, Z., Lin, S., Wang, K., Ma, C., & Lu, H. (2017). reactivity-controlled preparation of ultralarge graphene oxide by chemical expansion of graphite. *Chemistry of Materials ACS*, *29*(2), 564–572.

Drewniak, S., Muzyka, R., Stolarczyk, A., Pustelny, T., Kotyczka-Moranska, M., & Setkiewicz, M. (2016). Studies of Reduced Graphene Oxide and Graphite oxide in

the Aspect of their possible application in Gas sensors. *Sensors MDPI*, *16*(103), 16.

Eigler, S., Dotzer, C., Hirsch, A., Enzelberger, M., & Müller, P. (2012). Formation and decomposition of CO2 intercalated graphene oxide. *Chemistry Materials*, *24*(7), 1276–1282.

Eluyemi, M. S., Eleruja, M. A., Adedeji, A. V, Olofinjana, B., Fasakin, O., & Akinwunmi, O. O. (2016). Synthesis and Characterization of Graphene Oxide and Reduced Graphene Oxide Thin Films Deposited by Spray Pyrolysis Method. *Graphene*, *5*(July), 143–154.

Fentaw, T., & Worku, D. (2017). Controlled synthesis , characterization and reduction of graphene oxide : A convenient method for large scale production. *Egyptian Journal of Basic and Applied Sciences*, *4*(1), 74–79. https://doi.org/10.1016/j.ejbas.2016.11.002

Gao, R., Hu, N., Yang, Z., Zhu, Q., Chai, J., Su, Y., Zhang, L., & Zhang, Y. (2013). Paper-like graphene-Ag composite films with enhanced mechanical and electrical properties. *Nanoscale Research Letters*, *8*(32), 2–9. http://www.nanoscalereslett.com/content/8/1/32

Gao, W., Alemany, L. B., Ci, L., & Ajayan, pulickel M. (2009). new insights into the structure and reduction of graphite oxide. *Nature Chemistry*, 6.

Gomez, H., Ram, M. K., Alvi, F., Villalba, P., Stefanakos, E., & Kumar, A. (2011). Graphene-Conducting Polymer Nanocomposite as Novel Electrode for Supercapacitors. *J. Power Sources*, *196*, 4102–4108.

Hidayah, N. M. S., Liu, W.-W., Lai, C.-W., Noriman, N. Z., Khe, C.-S., Hashim, U., & Lee, H. C. (2017). Comparison on graphite , graphene oxide and reduced graphene oxide : Synthesis and characterization. *Global Network for Innovative Technology*, *October*. https://doi.org/10.1063/1.5005764

Hota, P., Miah, M., Bose, S., Dinda, D., Ghorai, U. K., Su, Y., & Saha, S. K. (2020). Ultra-small amorphous MoS2 decorated reduced graphene oxide for supercapacitor application. *Journal of Materials Science & Technology*, *40*, 196–203. https://doi.org/10.1016/j.jmst.2019.08.032

Hsieh, C.-T., Hsu, S.-M., Lin, J.-Y., & Teng, H. (2011). Electrochemical capacitors based on graphene oxide sheets using different aqueous electrolytes. *The Journal of Physical Chemistry C*, *115*(25), 12367–12374.

Huang, J., Li, Q., Sun, D., Lu, Y., Su, Y., Yang, X., Wang, H., Wang, Y., Shao, W., He, N., Hong, J., & C Chen. (2007). Biosynthesis of silver and gold nanoparticles by novel sundried cinnamomum camphora leaf. *Nanotechnology*, *18*(10), 105104–105115.

Iro Zaharaddeen, S., Subramani, C., & Dash, S. S. (2016). A brief review on electrode materials for supercapacitor. *International Journal of Electrochemical Science*, *11*(12), 10628–10643. https://doi.org/10.20964/2016.12.50

Javed, S. I., & Hussain, Z. (2015). Covalently Functionalized Graphene Oxide – Characterization and Its Electrochemical Performance. *International Journal of Electrochemical Science*, *10*, 9475–9487.

Jibrael, R. I., & Mohammed, M. K. A. (2016). Production of graphene powder by electrochemical exfoliation of graphite electrodes immersed in aqueous solution. *Optik*, *127*, 6384–6389.

Jibrael, R. I., Mohammed, M. K. A., Roder, F., Braatz, R. D., Krewer, U., Sohail, M., Saleem, M., Ullah, S., Saeed, N., Afridi, A., Khan, M., Arif, M., Danner, T., Zhu, G., Hofmann, A. F., Latz, A., Chen, S. X., Tseng, K. J., Choi, S. S., … Hee, J. (2015). Graphene-based polymer nanocomposites. *Carbon*, *6*(1), 1–4. https://doi.org/10.4172/2157-7439.1000253

Khalili, D. (2016). Graphene oxide : a promising carbocatalyst for the regioselective thiocyanation of aromatic amines , phenols , anisols and enolizable ketones by hydrogen peroxide / KSCN in water. *New Journal of Chemistry*, 1–11.

Kiamahalleh, M. V., Zein, S. H. S., Najafpour, G., Sata, S. A., & Buniran, S. (2012). Multiwalled carbon nanotubes based nanocomposites for supercapacitors: a review of electrode materials. *Nano*, *7*(02), 1230002.

Krishnamoorthy, K., Veerapandian, M., Yun, K., & Kim, S. J. (2013). The chemical and structural analysis of graphene oxide with different degrees of oxidation. *Carbon*, *53*, 38–49. https://doi.org/10.1016/j.carbon.2012.10.013

Kuila, T., Bose, S., Mishra, A. K., Khanra, P., Kim, N. H., & Lee, J. H. (2012). Chemical functionalization of graphene and its applications. *Progress in Materials Science*, *57*(7), 1061–1105.

Laheäär, A., Przygocki, P., Abbas, Q., & Béguin, F. (2015). Appropriate methods for evaluating the ef fi ciency and capacitive behavior of different types of supercapacitors. *Electrochemistry Communications*, *60*, 21–25. https://doi.org/10.1016/j.elecom.2015.07.022

Lai, L., Yang, H., Wang, L., Teh, B. K., Zhong, J., Chou, H., Chen, L., Chen, W., Shen, Z., Ruoff, R. S., & Lin, J. (2012). Preparation of supercapacitor electrodes through selection of graphene surface functionalities. *ACS Nano*, *6*, 5941–5951.

Lai, Linfei, Yang, H., Wang, L., Teh, B. K., Zhong, J., Chou, H., Chen, L., Chen, W., Shen, Z., Ruoff, R. S., & Lin, J. (2012). Preparation of Supercapacitor Electrodes through Selection of Graphene Surface Functionalities. *ACS Catalysis*, *6*(7), 5941–5951. https://doi.org/10.1021/nn3008096

Lai, Q., Zhu, S., Luo, X., Zou, M., & Shuanghua Huang. (2012). Ultraviolet-visible spectroscopy of grphene oxides. *AIP*, *2*(032146), 5.

Le, L. T., Ervin, M. H., Qiu, H., Fuchs, B. E., & Lee, W. Y. (2011). Graphene supercapacitor electrodes fabricated by inkjet printing and thermal reduction of graphene oxide. *Electrochemistry Communications*, *13*, 355–358.

https://doi.org/10.1016/j.elecom.2011.01.023

Leng, K., Zhang, F., Zhang, L., Zhang, T., Wu, Y., Lu, Y., Huang, Y., & Chen, Y. (2013). Graphene-based Li-ion hybrid supercapacitors with ultrahigh performance. *Nano Research*, *6*(8), 581–592.

Li, X., & Wei, B. (2013). Supercapacitors based on nanostructured carbon. *Nano Energy*, *2*(2), 159–173.

Liu, T., Li, L., Zhang, L., Cheng, B., You, W., & Yu, J. (2019). 0D/2D (Fe0.5Ni0.5)S2/rGO nanocomposite with enhanced supercapacitor and lithium ion battery performance. *Journal of Power Sources*, *426*(April), 266–274. https://doi.org/10.1016/j.jpowsour.2019.04.053

Lobato, B., Vretenar, V., Kotrusz, P., Hulman, M., & Centeno, T. A. (2015). Reduced graphite oxide in supercapacitor electrodes. *Journal of Colloid and Interface Science*, *446*, 203–207.

Ma, W., Chen, S., Yang, S., Chen, W., Cheng, Y., Guo, Y., Peng, S., Ramakrishna, S., & Zhu, M. (2016). Hierachical MnO2 nanowire/graphene hybrid fibers with excellent electrochemical performance for flexible solid-state supercapacitors. *Journal of Power Sources*, *306*(481–488).

Mathis, T. S., Kurra, N., Wang, X., Pinto, D., & Simon, P. (2019). Energy Storage Data Reporting in Perspective — Guidelines for Interpreting the Performance of Electrochemical Energy Storage Systems. *Advanced Energy Materials*, *1902007*, 1–13. https://doi.org/10.1002/aenm.201902007

Mittal, A. K., & Kumar, M. J. (2011). Electrochemical Double-Layer Capacitors Featuring Carbon Nanotubes. *Encyclopedia of Nanoscience and Nanotechnology*, *13*(271), 263–271.

Muhamad, K. S. S. K., Mohamed, F., Radiman, S., Hamzah, A., Sarmani, S., Siong, K. K., Yasir, M. S., Rahman, I. A., & Rosli, N. R. A. M. (2016). Synthesis and characterization of exfoliated graphene oxide. *AIP*, *1784*, 040013–040015.

Nam, P. T., Khanh, N. Van, Thom, N. T., Phuong, N. T., Trang, N. Van, Xuyen, N. T., Thai, V. Q., Tuan, V. A., & Thanh, D. T. M. (2018). Synthesis of reduced graphene oxide for high-performance supercapacitor. *Vietnam Journal of Chemistry*, *56*(6), 778–785. https://doi.org/10.1002/vjch.201800087

Nicolosi, V., Chhowalla, M., Kanatzidis, M. G., Strano, M. S., & Cleman, J. N. (2013). Liquid Exfoliation of layered materials. *Science AAAS*, *340*, 1226419.

Paulchamy, B., Arthi, G., & Bd, L. (2015). A Simple Approach to Stepwise Synthesis of Graphene Oxide Nanomedicine & Nanotechnology. *Journal of Nanomedicine & Nanotechnology*, *6*(1), 1–4. https://doi.org/10.4172/2157-7439.1000253

Perumbilavil, S., Sankar, P., Thankamani, P. R., & Philip, R. (2015). White light Z-scan measurements of ultrafast optical nonlinearity in reduced graphene oxide nanosheets in the 400 – 700 nm region. *Applied Physics Letters*, *107*(051104), 7.

https://doi.org/10.1063/1.4928124

Pham, V. H., Cuong, T. V., Hur, S. H., Oh, E., Kim, E. J., Shin, E. W., & Chung, J. S. (2011). Chemical functionalization of graphene sheets by solvothermal reduction of a graphene oxide suspension in Nmethyl- 2-pyrrolidone. *Journal of Materials Chemistry*, *21*(3371–3377).

Pope, M. A., Korkut, S., Punckt, C., & Aksay, I. A. (2013). Supercapacitor electrodes produced through evaporative consolidation of graphene oxide-water-ionic liquid gels. *Journal of the Electrochemical Society*, *160*(10), A1653–A1660.

Rajagopalan, B., & Chung, J. S. (2014). Reduced chemically modified graphene oxide for supercapacitor electrode. *Nanoscale Research Letter*, *9*(1), 1–10.

Ruch, P. W., Cericola, D., Kötz, R., & Wokaun, A. (2010). Aging of electrochemical double layer capacitors with acetonitrile-based electrolyte at elevated voltages. *Electrochimica Acta*, *55*(15), 4412–4420. https://doi.org/10.1016/j.electacta.2010.02.064

Saha, U., Jaiswal, R., & Goswami, T. H. (2016). A facile bulk production of processable partially reduced graphene oxide as superior supercapacitor electrode material. *Electrochim Acta*, *196*, 386–404.

Sekhar, C., & Ray, C. (2015). Application and uses of Graphene oxide and Reduced graphene oxide. In *A volume of Micro and Nano Technologies* (pp. 39–55).

Shen, J., Shi, M., Yan, B., Ma, H., Li, N., & Ye, M. (2011). Ionic liquidassisted one-step hydrothermal synthesis of TiO2-reduced graphene oxide composites. *Nano Research*, *4*(8), 795–806.

Shen, X., Lin, X., Yousefi, N., Jia, J., & Kim, J.-K. (2014). Wrinkling in graphene sheets and graphene oxide papers. *Carbon*, *66*, 84–92.

Sohail, M., Saleem, M., Ullah, S., Saeed, N., Afridi, A., Khan, M., & Arif, M. (2017). Modified and improved Hummer's synthesis of graphene oxide for capacitors applications. *Modern Electronic Materials*, *3*(3), 110–116. https://doi.org/10.1016/j.moem.2017.07.002

Song, J., Wang, X., & Chang, C. (2014). Preparation and Characterization of Graphene Oxide. *Hindawi*, *2014*(276143), 6. https://doi.org/10.1155/2014/276143

Weingarth, D., Foelske-Schmitz, A., & Kötz, R. (2013). Cycle versus voltage hold e Which is the better stability test for electrochemical double layer capacitors ? *Journal of Power Sources*, *225*, 84–88. https://doi.org/10.1016/j.jpowsour.2012.10.019

Xie, J., Yang, P., Wang, Y., Qi, T., Lei, Y., & Li, C. M. (2018). Puzzles and confusions in supercapacitor and battery_ Theory and solutions. *Journal of Power Sources*, *401*, 213–223. https://doi.org/10.1016/j.jpowsour.2018.08.090

Xiulun, S., Xueying, S., Liu, X., Liu, R., Li, S., Shen, M., & Qiang Li. (2020). One-

dimentional Mg2+-induced α-Fe2O3 nanowires for high-performance supercapacitor. *Results in Materials*, *5*(100052), 6. https://doi.org/10.1016/j.rinma.2019.100052

Yang, N. L., Zhai, J., Wan, M. X., Wang, D., & Jiang, L. (2010). Layered Nanostructures of Polyaniline with Graphene Oxide as the Dopant and Template. *Synthetic Materials*, *160*, 1617–1622.

Zaaba, N. I., Foo, K. L., Hashim, U., Tan, S. J., Liu, W., & Voon, C. H. (2017). Synthesis of Graphene Oxide using Modified Hummers Method : Solvent Influence. *Procedia Engineering*, *184*, 469–477. https://doi.org/10.1016/j.proeng.2017.04.118

Zhai, Y., Dou, Y., Zhao, D., Fulvio, P. F., Mayes, R. T., & Dai, S. (2011). Carbon materials for chemical capacitive energy storage. *Advanced Materials*, *23*(42), 4828–4850.

Zhang, S., Yan, Y., Huo, Y., Yang, Y., Feng, J., & Chen, Y. (2014). Electrochemically reduced graphene oxide and its capacitance performance. *Materials Chemistry and Physics*, *148*(3), 903–908.

Zheng, Q., Li, Z., Yang, J., & Kim, J. (2014). graphene oxide-based transparent conductive films. *Progress in Materials Science*, *64*, 200–247.

Zhou, K., Zhu, Y., Yang, X., Jiang, X., & Li, C. (2011). Preparation of graphene-TiO2 composites with enhanced photocatalytic activity. *New Journal of Chemistry*, *35*(2), 353–359.

CHAPTER FOUR

4.0. Modified Activation process for Supercapacitor Electrode Materials from African Maize Cob

4.1. Introduction

Recent advances in energy storage technologies and the urgent need to satisfy the requirements of increasing energy demand due to the rapid increase in world population, the gradual consumption of fossil fuel depict an end to the era and alternate energy resources among which electrical energy storage devices is a viable option. This is because the green chemical synthesis route, coupled with the increasing demand not only overcome environmental concerns but also cost-effective methodologies can be developed for energy storage applications. Supercapacitors have low energy density (<10 $Whkg^{-1}$) compared to other storage devices such as batteries this has become a major setback and has limited their use in application such as cordless electric tools, hybrid electric vehicles, backup power sources, renewable energy systems, and industrial energy management (Hall et al., 2010). To overcome this problem, many research activities have focused on developing nanostructured active electrode materials with suitable surface area, porosity, and morphology to increase energy density without sacrificing their intrinsic high-power density and cycle life (L. L. Zhang et al., 2010). This can also be achieved by exploring electrolytes with large potential windows such as ionic or organic electrolytes. Depending on the charge storage mechanisms of the active materials used ECs can be generally classified into two types namely electric double-layer capacitors based on ion adsorption (EDLCs mainly carbonaceous material with a high surface area) and pseudocapacitors (including redox material such as transition metal oxides and

conducting polymers) (Tarimo et al., 2020a). Pseudocapacitors have been shown to exhibit much higher capacitance than the EDLCs and are either used to complement EDLCs to improve the power and energy densities (Nankya et al., 2020).

An electrode is considered a backbone of an electrical double layer capacitor because the overall performance and stability of the Supercapacitors depend upon the materials used as electrodes. A large variety of electrode materials is used in Supercapacitors; each material has its behavior to its performance and capacitance. For electrode fabrication materials that possess large specific surface area and pore volume like mesoporous and microporous materials are considered. Many attempts by several research groups to fabricate electrodes from different carbon sources have been explored (Dörfler et al., 2013; F. Gao et al., 2020). Despite all these efforts, activated carbon (AC) is still the choice material used in the industry due to its high specific surface area (SSA), low cost, good electrochemical performance, and stability (Zhai et al., 2011). Different carbonaceous electrode materials are used in supercapacitors (SC) because of high surface area, porosity, and surface functional groups. For example, carbon composites (Yeon et al., 2017), carbide-derived carbon (Y. Zhu et al., 2011), graphene and its derivatives (Y. Zhu et al., 2011), carbon aerogels (Jae et al., 2014; Vlad et al., 2016) among others. AC-derived material is highly levelled to have higher porosity, high surface area, high chemical, and physical stability, and high packing density (Das et al., 2015; Lekakou et al., 2011). Commercially available ACs are synthesized from different biomass due to their low cost of production and environmental friendliness. The porous nature of AC material is advantageous in SC application with microporous and microporous being more influential for charge transfer in the performance. The macropores also facilitate the transport zone with the structure of carbon materials. The

high capacitance values are primarily due to the surface area of the material and the stability of electrolytes (Van et al., 2014).

Biomass is a feasible and sustainable source of materials and alternative to fossil fuel in energy applications and presently provides ~14% of the total energy consumed and ~ 35% for cooking and heating in third world countries, especially Africa(Dhillon & von Wuehlisch, 2013). Bio-inspired materials as electrodes for supercapacitor has become attractive because biomass resources are readily available, abundant, naturally renewable, eco-friendly and meet the condition for green and sustainable carbon sources for the advancement of electrode materials for the next cohort of SCs (N. Liu et al., 2013; Liyuan Zhang et al., 2014). Toward the development of AC as electrodes for supercapacitor from biomass materials slow progress has been made so far. The conversion and utilization of this biomass into value-added material are paramount. Biomass such as maize corn cobs, rice husks, coconut shells, sugarcane bagasse to mention but a few have been explored for the production of porous activated carbon for industrial application (Biswal et al., 2013; Xiufang Chen et al., 2017; A. Elmouwahidi et al., 2012; Adbelhahim Elmouwahidi et al., 2017; J. Hou et al., 2014; Mi et al., 2012a; Tian et al., 2015; L. Wei et al., 2011; T. Wei et al., 2016; Z. Zhu et al., 2015). Activated carbon (AC) with varying surface areas are abundantly being used for industrial application which includes energy storage materials, removal of toxic compounds, purification, and separation in liquids and gases, catalysts or catalysts support(Adrian et al., 2016; Adbelhahim Elmouwahidi et al., 2017; Fraczek-szczypta et al., 2015; Yakout & G. Sharaf, 2016), CO_2 reduction (Shafeeyan et al., 2010) removal of dyes and odour (Yakout & G. Sharaf, 2016). Much other ecological biomass material including eggshell (Tang et al., 2014), wood sawdust (L. Wei et al., 2011), pistachio nutshells (J. Xu et al., 2014), cigarette filter (M. Lee et al., 2014),

sunflower seed shell (Xiao Li et al., 2011), and rice husk (Kumagai et al., 2013) have been investigated as possible carbon sources for SC applications. All these sources of carbon materials mentioned above are low cost, sustainable, and are not harmful to the environment.

Zea Mays, commonly known as maize or corn is the most widely cultivated cereal grain food worldwide. The cultivation of maize is widespread particularly in the Eastern, Western, Southern, and central parts of Africa. This plays a big role in most homes as support for food and income-earning for the rural economy. The production yield per hectare (YPH) (tons/hectare/year) was estimated at approximately 32 YPH by 2020 which is greater than the USA, China and Brazil combined at 30 tons/hectare/year (Shahbandeh, 2020). Normally, the maize corn cobs are treated as agricultural crop residue/waste as a result of harvesting where only the grains are taken for further processing. The cobs are disposed-off in the farm, power plant sites, and others are burnt to ashes. This causes environmental challenges such as pollution.

Many research effort on biomass have been reported, for example, Ding et al. reported a sodium ion capacitor with the cathode and anode based on peanut shell nanosheets carbon with a Specific Surface Area (SSA) of 2396 m^2/g and a specific capacity of 161 mAh g^{-1} at 0.1 A/g and 73 mAh/g at 25.6 A/g (Ding et al., 2015). The same research group reported hemp bast fibers which exhibited SSA of 2287 m^2/g and a specific capacitance (C_{SP}) of 106 F/g at 10 A/g in ionic liquids (Huanlei Wang et al., 2013). Seaweed was also pyrolyzed at different temperatures under a nitrogen atmosphere with an SSA of 1300 m^2/g, resulting in a high volumetric capacitance (Raymundo-Piñero et al., 2009). Dead leaves were pyrolyzed by Biswal et al. (Biswal et al., 2013) to produce carbon material exhibiting an SSA of 1230 m^2/g and a specific capacitance of 400 F/g in 1 M H_2SO_4

electrolyte. Human hair was explored as a source of carbon for SC and symmetric cell exhibited a C_{SP} of 340 F/g and 126 F/g both in the alkaline electrolyte (6 M KOH) and organic electrolyte (1 M $LiPF_6$ in EC/DEC), respectively at 1 A/g with excellent cycling ability (Qian et al., 2014). Carbon synthesized from corn-cob has been used as an electrode in Electrochemical Double Layer Capacitor (EDLC) by Ghosh et al (Ghosh et al., 2019). The material produced was pre-treated with 5% $ZnCl_2$ using Co as catalyst pyrolyzed at 700 ^oC and the device fabricated exhibited a Specific capacitance of 270 F/g at a scan rate of 5 mV/s. Similarly, corncob-derived carbon with hierarchical porosity was reported(S. Yang & Zhang, 2018). The carbon produced Inherited the special biogenetic textures of corncob benefiting from proper activation process, the carbon materials exhibited excellent electrical conductivity and high specific capacitance of 293 F/g at 1 A/g. Corn Cob Lignin-based Porous Carbon Modified Reduced Graphene Oxide Film was also reported For Flexible Supercapacitor Electrode (Cui et al., 2019). The assembled supercapacitor exhibited the advantages of flexible, lightweight, low price, and environment friendly, which can achieve a high specific capacitance of 324.5 mF/cm^2 at 0.2 mA/cm^2 and 91.8% capacitance retention after 1000 charging/discharging cycles. Moreover, a two-step method for the preparation of high-performance corncob-based activated carbons as supercapacitor electrodes were reported using ammonium chloride as a pore-forming additive followed by carbonization. The device fabricated had a good rate performance with a capacitance of 175 F/g at 0.5 A/g and good cycling stability after a 10 000 charges/discharge test (Q.-L. Wei et al., 2018).

Considering the limited amount of work in the use of corn cob and the fact that they are abundant and generally accessible for potential value addition as carbon materials. This present research uses the liquid-phase oxidation process and gas phase method for the

production of enhanced porous carbon at three (3) different temperatures for activation after treatment with concentrated sulphuric acid (concern H_2SO_4). The use of sulphuric acid has been shown to effectively hydrolyse and oxidize materials introducing a sufficient number of functional groups on the surface of carbon, which include carboxyl, lactone, phenolic, sulphur groups among others (Shafeeyan et al., 2010). These functional groups improve the efficiency of the non-faradaic and faradaic behavior in electron and charge transfer processes.

4.2. Experiments

4.2.1. Preparation of activated carbon

The Activated carbons (ACs) were prepared from maize cobs (AMC) as follows; the MC was obtained from farmland within the African University of Science and Technology (AUST) Abuja Nigeria. The MC was cleaned and sized (~3cm), then dried in an oven at 110^{o}C for 48 h. The dried samples were grounded and sieved to a fraction using a 1.0 mm sieve. The MC powder was functionalized by chemical treatment using 14% wt/v concentrated H_2SO_4. The functionalized MC was left to stand for 48 h in a fume hood, then washed with DI water until a pH 6.5 was achieved. The sample was then dried in an electric oven at 120^{o}C for 18 h. The dried sample was divided into three (3) portions. These portions were activated at three (3) different temperatures in a furnace under a nitrogen atmosphere with a flow rate of 300 mL/min with a ramped temperature of 3^{o}C/min and a holding time of 2 h. The 1st portion was activated at 600^{o}C and the sample was named AC-S-600, the 2^{nd,} and the 3rd portions were heated at 700^{o}C and 800^{o}C then named AC-S-700 and AC-S-800 respectively.

4.2.2. Characterization techniques for Activated Carbon (AC)

The thermogravimetric analysis (TGA) was executed on the AMC powder material and AC samples using the TGA-DSC analyzer (Jupiter STA449 F3 NTZSCH GmbH). The samples were heated in pure air at a flow rate of 10 cm^3/min from room temperature to 1000^oC with a ramped temperature of 10^oC/min with a run time of 1 h and 40 minutes using calcinated silica pan as reference material (Lijuan et al., 2017; Lim et al., 2010; Van et al., 2014). The morphological characterization of the samples was carried out with the Field Emission Scanning Electron Microscope (FESEM) GeminiSEM 500M/s Carl ZEISS-EDAX Z2 Analyser AMETEK). The crystal structure of the AC powder samples was examined by the X-Ray Diffraction (Riguku Smartlab Autosampler) using a Cu kα radiation with the JCPDS-ICDD database. The surface functional groups of AC samples were analyzed by Fourier Transformation InfraRed (FTIR) spectroscopy (Bruker Optik GmbH Vertex 70, Germany) and was scanned through a range of 600 – 4000 cm^{-1}. The Nitrogen Adsorption/desorption isotherms were determined based on the 350 ^oC automated adsorption instruments (11-2370. Gemini Miceomeritics USA). The AC samples were preheated at 90 ^oC (ramp 10 ^oC/min) and degassed at 300^oC in a vacuum with the holding time of 10 h. The Nitrogen adsorption isothermal was measured over (P/P_o) relative pressure and the BET surface area (S_{BET}) was calculated by BET (Brunauer-Emmett-Teller) equation with adsorption data (Van et al., 2014). The micropore volume (V_{mic}), microporous surface area (S_{mic}), and external surface area (S_{ext}) were obtained from the t-plot method (Van et al., 2014). The mesopore volume (V_{mes}) was acquired by BJH (Barrett-Joyner-Halenda) method (Ghosh et al., 2019; Van et al., 2014) and the total pore volume (V_{tot}) estimated from the sum of mesoporous volume

(V_{mes}) and microporous volume (V_{mic}). The mean pore radius r_{mp} was determined from the total pore volume and S_{BET} with some assumptions.

The surface chemistry of the AC samples was further examined by X-ray Photoelectron Spectroscopy (XPS) using spectra in the K-alpha Photoelectron spectrometer using omicron Nano Technology UK. This was used to determine the chemical and elemental composition of the sample surfaces and for the identification of oxygen functional groups with their binding energy (Adbelhahim Elmouwahidi et al., 2017; Shafeeyan et al., 2010) and Labram Micro Raman Spectrometer (Horiba Jobin Yvon model). Chemical titration Boehm method was used in further determination of oxygen functional groups as follows; 200mg of each AC sample was mixed in 25 mL of one of the four reactants of 0.1 M concentration [$NaHCO_3$, Na_2CO_3, NaOH or HCl]. The mixtures were sonicated for 24 hours, then filtered to remove the carbon. The excess of base and acid in the solution was titrated with 0.1 M HCl solution of 0.1 M NaOH. The number of acidic and basic sites were calculated on the basis that NaOH neutralizes carboxylic, phenolic, and lactonic groups, $NaHCO_3$ neutralizes only carboxylic, Na_2CO_3 neutralizes carboxylic and lactonic and HCl neutralizes all the basic sites (Schönherr et al., 2018).

4.2.3. Electrochemical preparation and electrochemical measurements

The working electrodes were fabricated with graphite foil as a current collector and AC as the active material. The active material constituted a mixture of AC, carbon black, and Polyvinylidene Difluoride (PVDF) in the ratio of 8:1:1 by weight, respectively (Manyala et al., 2016). This was mixed with the N-methyl-2 pyrrolidone solvent to make a paste and coated on the graphite foil. The coated electrodes were dried in an oven at a temperature of 70^{o}C for 15 h. The electrochemical (EC) analysis was carried by BIO-

LOGIC (BCS-805) workstation using a three-electrode set-up system with a saturated calomel electrode (SCE), coated material, and a platinum sheet electrode as a reference, working and counter electrodes, respectively. The following techniques; (i) Cyclic Voltammetry (CV) with electrode potential of 1.0 V for 6M KOH and 1.2 V for 1M Na_2SO_4 at different scan rates (5, 10, 20, 50, 70, 100 mV/s). (ii) The Galvanostatic Charge-Discharge (GCD) was performed at different current densities from 0.25, 0.5, 1.0, 1.5, to 2.0 A/g according to the total mass of the active electrodes in each device. (iii) Electrochemical Impedance Spectroscopy (EIS) was obtained from 10 kHz to 10 mHz at a voltage of 10 mV. (iv) Stability of the SC by voltage holding/floating of the GCD after every 3 cycles for 10 h at the maximum voltage until 100has described (Adbelhahim Elmouwahidi et al., 2017; Weingarth et al., 2013).

4.3. Results and Discussion

4.3.1. The characterization of activated carbon AC

The thermal degradation and stability of the raw material (MC) and AC samples was performed with thermogravimetric analysis (TGA-DSC) at a temperature range of 28 ^oC to 1000 ^oC as depicted in Table S1 and Figure S1 (Appendix 1) represents the mass fraction loss in percentage at different temperature range. The dried powder of MC was analyzed to determine the required activation temperature. The MC sample in Figure S1(Appendix 1) shows two main stages of weight loss with the first stage starting at approximately 28 ^oC up to 120 ^oC on the TGA graph. This was due to the physisorbed desorption of water/moisture from the powder and showed an endothermic effect in the DSC heat flow profile that ended at 120 ^oC (Lijuan et al., 2017). The second stage was observed between 200 – 350 ^oC (52.4%) which is due to the decomposition of organic

compounds and groups such as carboxyl, lactonic among others which are present at the surface of the material (Van et al., 2014). Table S1(Appendix 1) shows the highest mass loss at the second stage in MC up to 350^{o}C. This implies that 350^{o}C can serve as the best carbonization temperature for the material. The activation of AC materials was done starting from 600^{o}C where the MC material maintained a constant mass loss basing on the TGA-DSC profile (Figure S1). The ACs profile in Figure S1(Appendix 1) depicted a trend of mass fraction loss in the materials also with mainly two (2) stages of mass loss which was between 70 – 120^{o}C for the first stage and between 650 – 770^{o}C for the second stage. The first stage corresponds to the desorption of water molecules in the samples (Lijuan et al., 2017) which depicts an endothermic effect only in the AC-S-800 sample on the DSC profile. The second stage was due to the thermal degradation of organic compounds which corresponds to a weight loss range from 12 – 26% (Table S1) and may constitute loss of cellulose, hemicellulose, and lignin compounds which vaporize at that temperature range (Köseog˘lu & Akmil-Basar, 2015).

The DSC profile of AC-S-600 and AC-S-700 show a gradual increase in the heat flow (exothermic effect) throughout the samples indicating that the samples are hydrophobic and gain more heat energy as temperature increases. The AC-S-800 sample shows a different DSC profile with an endothermic effect at the first and second stages of the mass loss with a drastic effect at 950^{o}C until the end of the thermal analysis. This suggests that the AC-S-800 sample is highly microporous with high retention of gases and water molecules indicating low pore volume and low surface area was confirmed by BET results and the FESEM images. The mass loss increased with the increase in temperature of activation in the order of AC-S-800 > AC-S-700 > AC-S-600 (Table S1). The decomposition generally increases for biomass with the elevation of temperature. The

physical properties of the AC-S-600, AC-S-700, AC-S-800 AC samples were estimated by N_2 adsorption-desorption as shown in Table 4.1 and Figure 4.1. The technique revealed the BET surface area (SBET) of 253.6 m^2/g for AC-S-600, AC-S-700 with 105.23 m^2/g, and AC-S-800 with the lowest of 30.09 m^2/g. The pore volume of the samples varies from 0.0312 to 0.1463 cm^3/g with the increasing order of AC-S-800 < AC-S-700 < AC-S-600 as shown in Table 4.1.

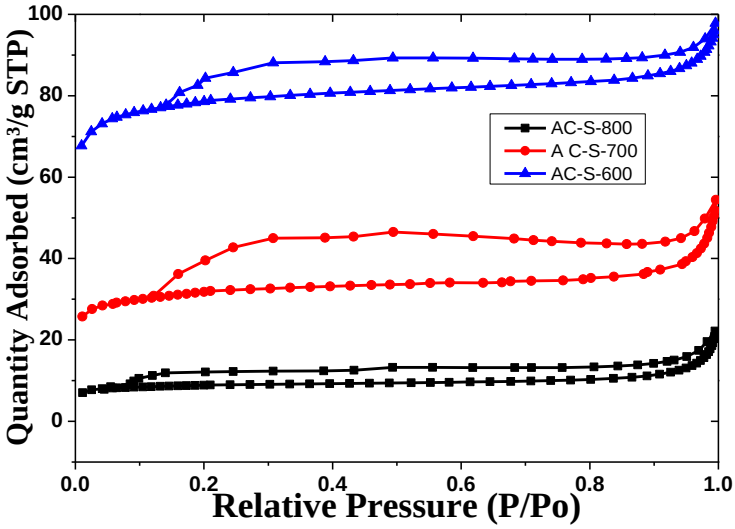

Figure 4.1: N_2 adsorption-desorption isotherm at 77K of Activated carbon samples.

The S_{BET} and pore volume decreased with an increase in the temperature used for each sample. The surface area decreases as the temperature increases, and a similar trend was observed by the micropore volume which decreases with increasing temperature. This indicates that H_2SO_4 acid-treated materials gave low physical properties and high chemical properties like oxidation and functionalization of the materials with an increase in temperature as detected by other techniques used in characterization (XPS, FTIR). This indicates that concentrated H_2SO_4 acid caused hydrolysis and oxidation reactions in the samples and the effect increased with the increase in the temperature. This effect leads to the blocking of the micropores and mesopores in the sample. When the temperature is

increased beyond 200°C, the H_2SO_4 acid-treated samples tend to generate polysulphates which are highly corrosive and oxidizing then functional groups form by crosslinking polycondensation (J. Li et al., 2019; Liou, 2010; Xiang et al., 2013). This leads to the formation of pore-form structures within the pores hence closing the micropores and creating oxygen functional groups and trapping of high concentration of oxygen in the structure. The isothermal curves with hysteresis loops are shown in Figure 1 depicted a type I and IV curves format of the isothermal classification by IUPAC. The shapes of the curves have some sharp rise which denotes the possible formation of micro and mesopores at 0.2 and 0.9 respectively showing an important uptake at those relative pressures (Van et al., 2014). The average pore distribution in all the samples implies that the materials can be used for storage applications. Using BJH analysis for pore size data, the average mean pore radius was estimated to be 0.577, 0.722, 1.04 nm with AC-S-600, AC-S-700, and AC-S-800 respectively using total pore volume and BET surface area. The pore size distribution for the samples in Figure S2(Appendix 1) shows a low range below 100nm (1000Å) of the diameter of pores which favours the materials for supercapacitor application.

Table 4.1: Physical properties of AC samples from N_2 adsorption at 350°C

Samples	S_{BET} (m^2/g)	S_{mic} (m^2/g)	S_{mic}/S_{BET} (%)	S_{ext} (m^2/g)	V_{mic} (cm^3/g)	V_{mes} (cm^3/g)	V_{tot} (cm^3/g)	V_{mic}/V_{tot} (%)	r_{mp} (µm)
AC-S-600	253.60	204.33	80.6	49.27	0.0998	0.0465	0.1463	68.2	5.77
AC-S-700	105.23	68.61	65.2	36.62	0.0330	0.0430	0.0760	43.4	7.22
AC-S-800	30.09	21.17	70.4	8.92	0.0098	0.0214	0.0312	31.4	10.4

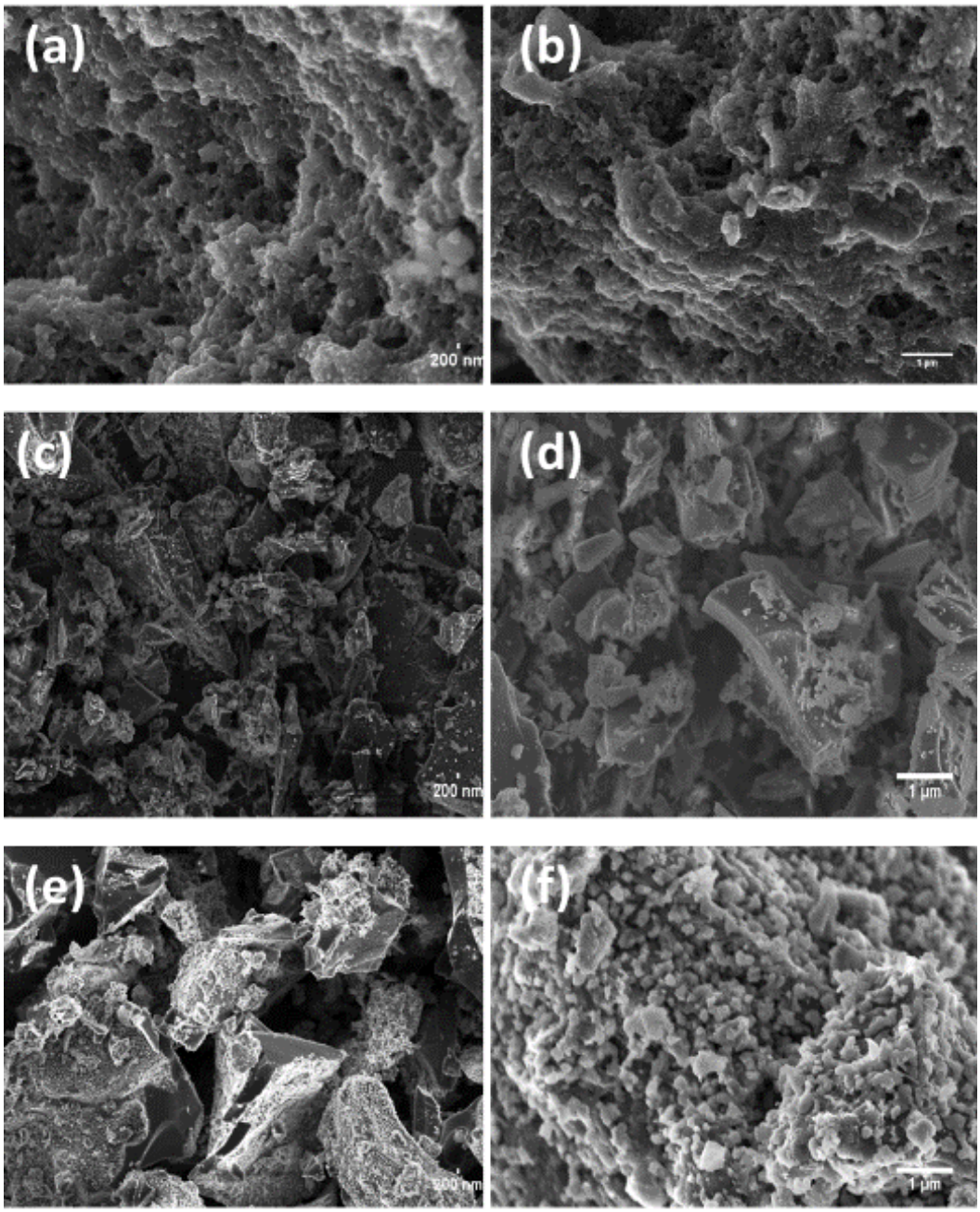

Figure 4.2: FESEM micrographs for AC-S samples taken at two different magnifications AC-S-600 at (a) 200nm, (b) 1µm, AC-S-700 at (c) 20µm, (d) 2µm, AC-S-800 at (e) 10µm, (f) 1µm.

The FESEM micrographs of AC-S-600, AC-S-700, and AC-S-800 in Figure 4.2 depicts the physical morphology of the activated carbon materials at different temperature activation. AC-S-600 shows a honeycomb structure with different pore sizes and shapes which is due to the removal of volatile compounds during carbonization and leads to the

creation of varying pore sizes. Figure 4.2a AC-S-700 presents a dense microstructure with smooth and fewer pores when compared to the others. The AC-S-800 sample revealed small pores in the microstructure which may have been due to high oxidation properties of H_2SO_4 and the recombination of oxides from decarboxylation reaction with other functional groups (Jiachuan Chen et al., 2017; Lijuan et al., 2017; S. Zhang & Pan, 2015). Similarly, the AC-S-800 sample depicted aggregated oxygen functional groups concentration on the surface as detected by the Boehm method. This was also confirmed by XRD and XPS data. Figure 4.3 (AC-S-800b) at a 1 µm scale displayed a highly oxidized surface with 0.420mmol/g of basic functional groups (Table S3, Appendix 1). The basic groups are more in this sample since acidic groups decompose at around 650^{o}C leaving the basic one which decomposes between 700 -980^{o}C (Van et al., 2014). Some of these basic groups are very beneficial for the performance of the supercapacitors as indicated further in the electrochemical results.

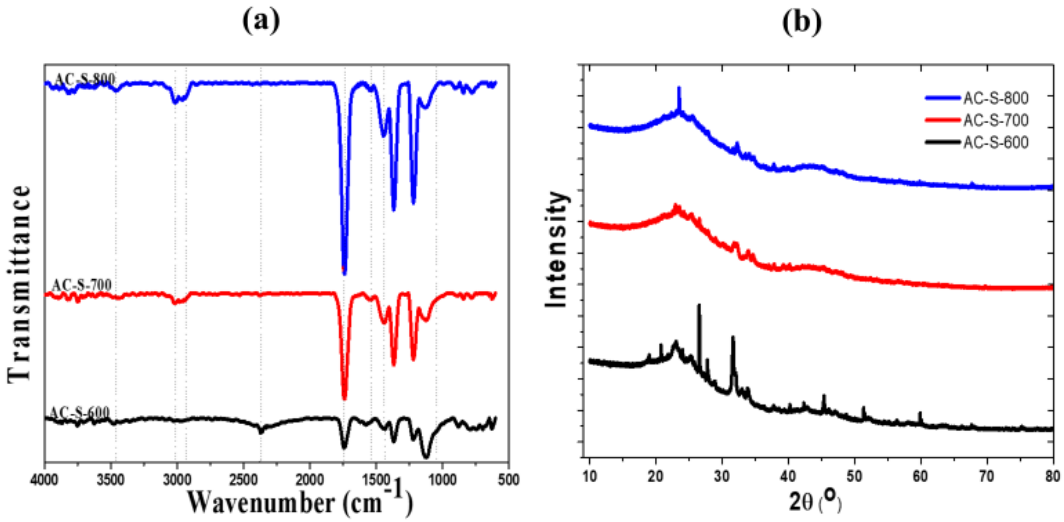

Figure 4.3: (a) FTIR spectra and (b) X-ray diffraction peaks for AC-S-600, AC-S-700, and AC-S-800 AC materials.

The FTIR spectra of the AC-S-600, AC-S-700, and AC-S-800 activated carbon samples are presented in Figure 4.3a with functionality/group assignments shown in Table S2(Appendix 1). All three (3) samples presented peaks at the same positions for each assignment for both regions. The fingerprint region from 1000 to 1500 cm^{-1} revealed the concentration of C-C, C-OH, C-O, C-N stretching, and aromatic compounds with strong and medium transmittance. The peaks at 1080 and 1220 cm^{-1} are the bond stretch composition for the structure of C-C and C-O bonds. Also, the diagnostic region revealed several groups in different positions as shown in Table S2(Appendix 1). These peak positions are in agreement with different activated carbon from different materials from the literature. Some of these materials include olive stones activated with phosphoric acid (H_3PO_4) (Yakout & G. Sharaf, 2016), cotton stalk activated with H_3PO_4 (Mohamad & Williams, 2012), hydrochar activated with H_3PO_4 (Jiachuan Chen et al., 2017), maize cobs treated with $ZnCl_2$ (Ketcha et al., 2012), Fox nuts activated with H_3PO_4 (A. Kumar & Jena, 2016), agricultural waste biomass activated with $ZnCl_2$ and K_2CO_3 (Köseoglu & Akmil-Basar, 2015), cotton stalk with H_3PO_4 and $ZnCl_2$ (Lijuan et al., 2017) and rice husks activated with NaOH (Van et al., 2014).

The XRD spectra of the samples are presented in Figure 4.3b. The materials show two broad peaks at a 2Θ range of 23 to 30º and 40 to 47º corresponding to the (002) and (100) crystal plane of graphite materials and it's reflected in all three samples. Generally, all the samples shown broaden peaks around 2Θ of 24º and 44º which indicates the typical peaks for amorphous carbon with non-crystalline material structures. (Ghosh et al., 2019; J. Li et al., 2019; Shi et al., 2019). The AC-S-600 sample revealed a high-intensity peak at 2Θ = 26.426 with a hexagonal crystal system of graphite with a d-spacing of 3.370 Å at (002) plane indicating graphitization. The second peak at 2Θ = 44.572º for amorphous carbon

at d_{101} = 2.031Å and another peak at 2Θ = 32.0° which was identified as oxygen with d-spacing of 2.795Å. This peak appeared in the same position for the other two samples as an indication of surface oxygen functional groups and was confirmed by Boehm's results in Table S4(Appendix 1). This means that the samples were oxidized by H_2SO_4 acid treatment which increased the oxygen and sulphur functional groups on the surfaces of the samples. The oxidation trend in the samples in the order of AC-S-800 > AC-S-700 > AC-S-600 as a result of an increase in temperature.

The AC-S-700 sample revealed disordered carbon peaks with the prominent one at 2Θ = 24.267° with the d-spacing of 3.664Å at (110) plane as hard carbon peak with another peak at 2Θ = 14.418° with (002) identifying its graphitic nature. The other carbon peak was revealed at 2Θ = 47.259° with (100) plane. The AC-S-800 sample had several peaks at a different position, graphite carbon peak at 2Θ = 26.426° with d-spacing of 3.37Å at (002) plane, another carbon peak at 2Θ = 41.266° with d-spacing of 2.19Å at (100) plane. They are a number of oxygen peaks indicating that the sample is highly oxidized; 2Θ = 31.999° with d_{011} = 2.795Å, 2Θ = 23.720° with d_{001} = 3.7748Å, 2Θ = 34.491° with d_{110} = 2.598Å as the prominent peaks. All the samples revealed some peaks of sulfur, sodium, and boron at positions of 23.3° (d_{220}=3.818Å), 31.0° (d_{101}=2.88Å), and 17.618 – 22.059° at (112) plane, respectively.

The surface chemistry functional groups in this study were determined by the Boehm titration method and the results are shown in Table S3(Appendix 1). This shows the acidity and basicity of the surface oxygen groups of the AC materials under study. It is assumed that bases neutralize all oxygen groups that are more acidic in that $NaHCO_3$ was used to deprotonate primarily carboxylic groups, Na_2CO_3 to neutralize lactonic groups and NaOH for deprotonation of phenolic groups. Also, HCl acid was used to protonate

all the basic groups (Schönherr et al., 2018). Table S3(Appendix 1) revealed the presence of both acidic and basic groups in the samples under study. The total basicity increases with an increase in activation temperature because their decomposition is between 700 to 1000^{o}C (Van et al., 2014) and the total acidity is constant through the samples. These functional groups can enhance the performance of supercapacitors (Van et al., 2014).

The XPS technique was further used to confirm the surface chemistry (their C1s, O1s, and S2p core levels of atoms.) of the material by determining the binding energy of the elemental composition and the chemical state of the material's surface (Moulder et al., 1992). This revealed the presence and interaction of different functional groups which include C-C (C-H), C-O, C=O, O-C=O, C-S among others as depicted in Table S5(Appendix 1) (Adrian et al., 2016; Adbelhahim Elmouwahidi et al., 2017; J. T.-H. Juan et al., 2016; Shafeeyan et al., 2010). The surface chemistry profile of the AC materials is summarized in Table 5 and Table S5(Appendix 1).

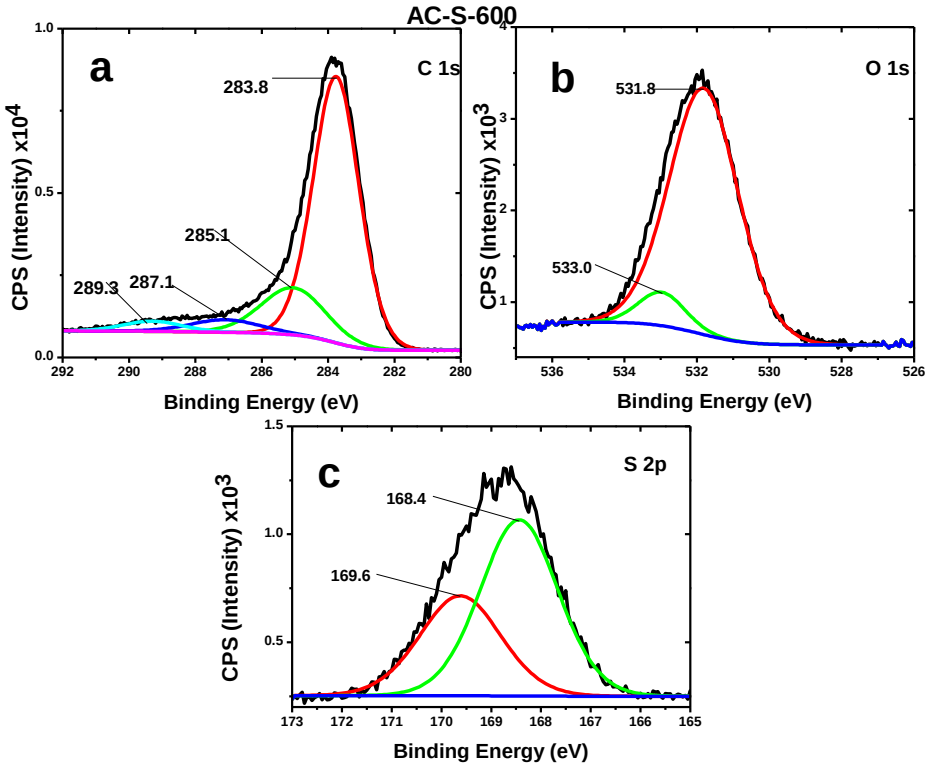

Figure 4.4: XPS deconvoluted spectra of AC-S-600 activated carbon material (a) C 1s Carbon atom at 283.7 eV, (b) O 1s Oxygen atom at 531.7 eV, (c) S 2p Sulphur atom at 168.7 eV.

The deconvoluted spectra as depicted in Figures 4.4 with the C1s, O1s, and S2p core level interaction in all the three (3) samples. From Table S4(Appendix 1), it was revealed that the carbon percentage is highest in AC-S-600 with 67.01% and oxygen with 22.59%. In all the samples, the percentage of oxygen detected is high with 31.70% in AC-S-800 samples implying that they are highly functionalized by oxidation. The trend of carbon composition is AC-S-600 > AC-S-700 > AC-S-800. In all the samples, there is approximately 2.6% sulfur was detected in the samples. This is because the treatment was done with concentrated H_2SO_4 acid which formed functional groups at the surfaces as shown in Table S5(Appendix 1). There is some percentage composition of sodium and boron in the samples, which may be due to micro-nutrients uptake of the maize plants from the soils, they were cultivated. The concentration of these elements is approximately the same implying that they came from the same source.

Table S5 (Appendix 1) shows convoluted spectra positions with their assignments and sample percentage content. This is in agreement with Boehm's analysis results in Table S3(Appendix 1) and FTIR results indicating the oxidation and formation of functional groups at the surface of the materials. The spectra from the deconvoluted peaks of samples in Figures 4.4 for AC-S-600 indicate the formation of bonds with different binding energy as assigned in Table S5(Appendix 1). These have the same binding energy response for C1s, O1s, and S2p for the three (3) samples with no single shift in the peaks as in Table S4(Appendix 1). This means that these are the main core atoms for the prepared AC materials. The convoluted C1s spectrum of AC-S-600 revealed peaks with the binding energy of 283.8eV having the highest area indicating C-C and C=O network of carbon.

This binding energy and assignments are in agreement with the literature (Adbelhahim Elmouwahidi et al., 2017). At the lower binding energy, the S2p spectrum was revealed in all the samples forming polysulphates groups of O-S=O, O-C-S among others which were caused by chemical activation with H_2SO_4 (G. Hasegawa, T. Deguchi, K. Kanamori, Y. Kobayashi, H. Kageyama, T. Abe, 2015). This is explained based on the fact that sulfur atoms may be attributed by carbon matrix at reduced states which are further stabilized by oxidation leading to the formation of stable S-functional groups. The increase in oxygen with an increase in temperature was due to the formation of polysulphates, which block the pores and trap the oxygen. This may reduce the conductivity but increases the functional groups on the material surface, which increases the functionality of the faradaic reactions.

The Raman spectra of the three AC-s materials are shown in Figure S3(Appendix 1). The samples show peaks at 1355cm^{-1} for the D-band and 1597cm^{-1} for G-band. These peaks indicate the disordered carbon and graphitic carbon for D-band and G-band respectively (Perumbilavil et al., 2015). The intensity ratio of I_D/I_G indicates the disordered carbon which is 1.035, 0.998, and 1.007 for AC-S-600, AC-S-700, and AC-S-800 respectively. These values of I_D/I_G present a good degree of graphitization of the produced materials.

4.3.2. The electrochemical characterization of activated carbon

The characterization of the materials as electrodes for supercapacitor application was evaluated by cyclic voltammetry (CV) curve and galvanostatic charge-discharge (CD) curves. By using three electrodes system the electrodes of the supercapacitor, the calculation was done based on the following equations(Bello et al., 2020; Kigozi, Koech, et al., 2020; Muniyandi Rajkumar et al., 2015; Tarimo et al., 2020a);

$$C_s = \frac{Idt}{m_{el}dV} \tag{4.1}$$

Where; C_s is the specific capacitance (F/g), I the discharge current (A), M_{el} the total mass of active materials (g), dV the change in discharge voltage (V), and dt the change in discharge time (s).

The results of the setups made from the AC (AC-S-600, AC-S-700, and AC-S-800) samples were analyzed with two different electrolytes namely: potassium oxide (6M KOH) and sodium sulphate (1M Na_2SO_4) and results. The corresponding Figures of the cyclic voltammetry (CV), galvanostatic charge-discharge (GCD), and Electrochemical Impedance Spectroscopy (EIS). Figures were generated and shown the work.

In the assessment of the cyclic voltammetry, the voltammograms from the two electrolytes were obtained using five different scan rates of 5, 10, 20, 50, 70, and 100 mV/s at a voltage window of 0 – 1.0V for 6M KOH and 0 -1.2V for 1M Na_2SO_4. All three (3) electrode materials, display rectangular and semi-rectangular shapes at different scan rates and with different voltage windows as shown in Figure 4.5(a – f). This is an Indication of Electrical Double Layer capacitor (EDLC) behaviors for all three electrodes. This means there was a low electrolyte diffusional restriction with the materials (Adbelhahim Elmouwahidi et al., 2017). The electrode maintains its rectangular shape with an increasing scan rate indicates excellent capacitive nature with a very quick response of the electrochemical interaction of the electrode materials as in Figures 4.5. This may be due to the easy transport mobility of the ions through the pores in the formation of the material under study (Liang et al., 2013) and further indicates that there was small resistance in the samples as electrode materials (Moyo et al., 2018). There is some exponential distortion in some quasi-rectangular shapes with higher scan rates as a

response to high polarization that indicates that there was some overcharging of the electrodes. This resulted in a parasitic side reaction which may have occurred with the electrode materials or the electrolyte (Mathis et al., 2019). Figure S4(Appendix 1) shows some small humps and exponential character which may have been attributed to the acidic groups (Table S3), the pseudo-faradaic interaction reaction with the different surface functional groups on the surfaces of the materials (Table S5). (Van et al., 2014). The slight difference in the shapes is due to the conductivity of different electrolytes in the study may be due to some resistances and capacitance nature of the double layer materials.

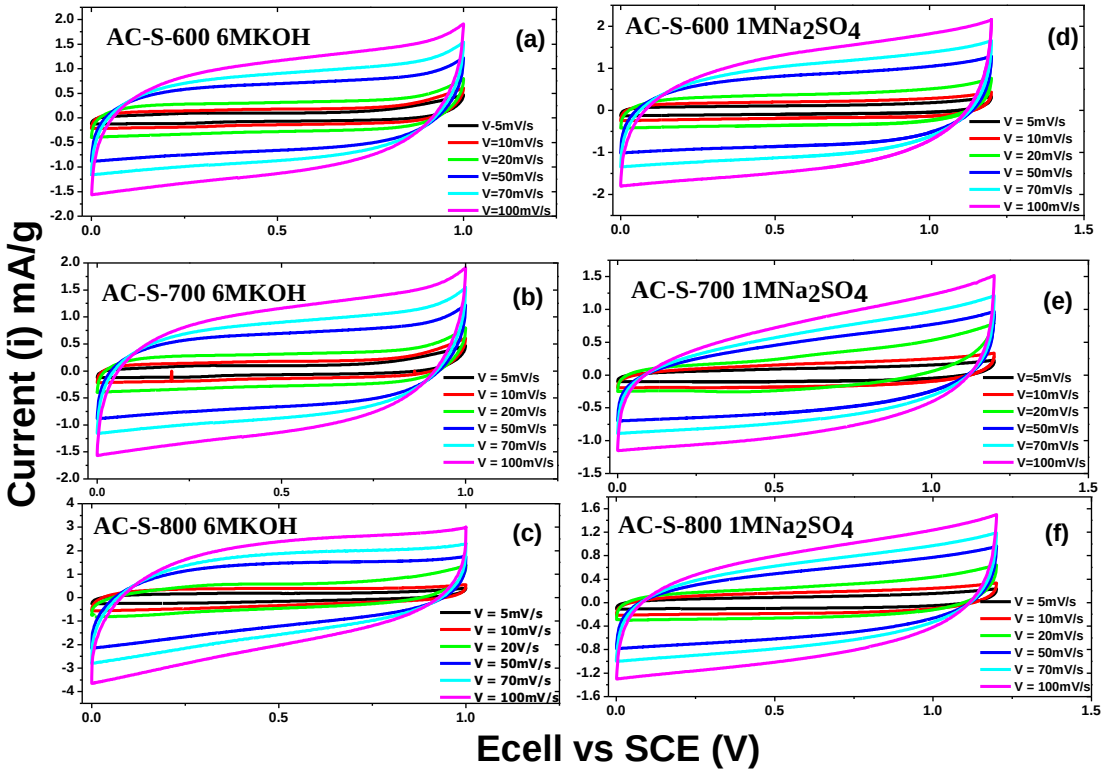

Figure 4.5: CV curves of AC-S-600, AC-S-700, and AC-S-800 Electrode materials at different scan rates with 6MKOH and 1M Na_2SO_4 as electrolytes.

The galvanostatic charge/discharge (GCD) of the electrodes was studied using the chronopotentiometry technique. The GCD from the different electrode materials is presented in Figures 4.6 at varying specific current and different potential windows for both electrolytes as mentioned earlier. The current density was varied from 0.25 to 2.0

A/g for all three electrodes. Triangular symmetric GCD was observed for all samples as shown in Figures 4.6 This symmetric behavior is a measure of ideal Electrical Double-Layer capacitor (EDLCs). The deviation from the ideal EDLC could be due to (i) current leakage limited by the poor assembly of the device to be tested, (ii) lack of adequate electronic conductivity arrangement or high series resistance, (iii) side reaction which occurs within the electrolyte or with the active electrode material (Mathis et al., 2019). As the current density increases, there is a slight distortion to the triangular shape using KOH electrolyte. This may be due to resistance in the system or limited diffusion of Potassium ions (K^+) into the pores of the active material at high current (Van et al., 2014). The samples behaved differently with 1 M Na_2SO_4 electrolyte possibly due to the smaller size of bare sodium ions (Na^+) which were able to diffuse through the porous carbon pores hence showing alteration in the discharge curves (Moyo et al., 2018).

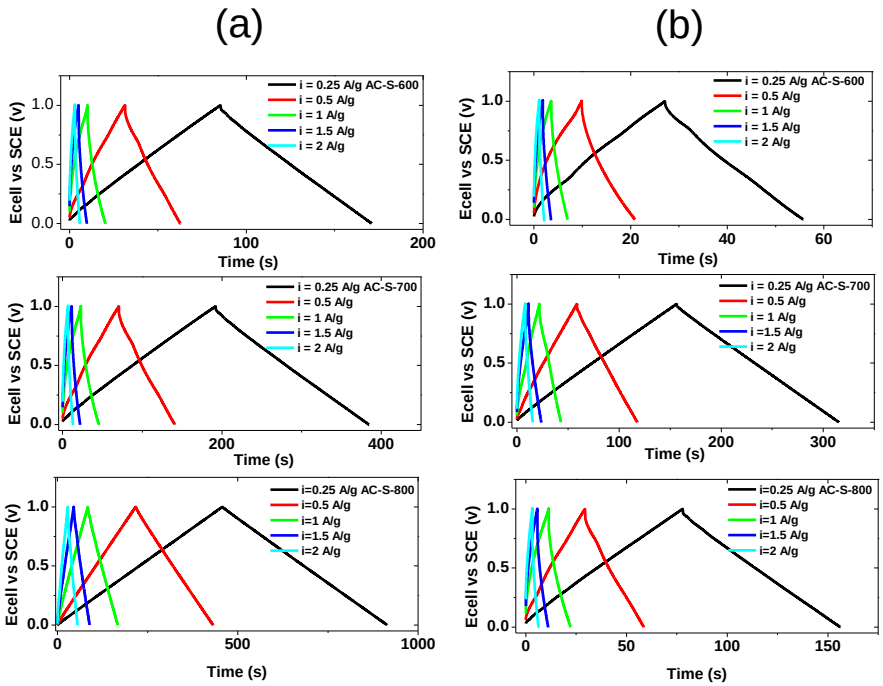

Figure 4.6: Galvanostatic charge-discharge curves for AC-S-600, AC-S-700, and AC-S-800 electrodes materials at different current densities with (a) 6M KOH and (b) 1M Na_2SO_4 as electrolytes.

The two electrolytes were used to compare the activities of the materials in the basic and neutral environment. The data in Figure 4.7 show the results of the activities of the materials during the Electrochemical (EC) analysis. The electrodes from the AC-S-600 in 6 M KOH electrolyte gave a specific capacitance of 85.25 F/g 0.25A/g while the same material in 1 M Na_2SO_4 electrolyte, gave a specific capacitance of 28.43 F/g at the same specific current. The AC-S-700 AC electrode in 6 M KOH gave 172.08 F/g at 0.25A/g, which is higher than AC-S-600 with the same electrolyte. The electrode fabricated from the AC-S-700 in 1 M Na_2SO_4 had a specific capacitance of 159.02 F/g at 0.25A/g. Furthermore, the AC-S-800 electrodes in 6M KOH electrolyte gave the highest specific capacitance of 456.4 F/g and 78.5 F/g at 0.25 A/g in 1M Na_2SO_4 electrolyte. From literature, it has been shown that the hydrated ion size (3.31 Å for K^+ and 3.58 Å for Na^+), and ionic conductivity (73.5 S cm^2 mol^{-1} for K^+ compared to 50.11 S cm^2 mol^{-1} for Na^+), play a crucial role in the electrochemical performance of carbon electrode materials (Zhong et al., 2015). Similarly, the ionic radius of the hydrated negatively charged anions contribute to the EDL behavior via electrosorption and the sizes are in the following order OH^- (3.00 Å) < NO_3^- (3.35 Å) < SO_4^{2-} (5.33 Å) (Zhong et al., 2015). Hence the alkaline electrolyte is expected to give the best electrochemical performance taking into account the micro and mesoporous texture of the carbon electrode that could easily accommodate the smaller size of K^+ and the electrosorption of the negative charge anions (OH^-), coupled with it better conductivity and ionic mobility (Bello et al., 2016). The acid-activation introduced sulphur in the electrode material. Sulphur is an active element for energy storage material with a theoretical capacity of 1672 $mAhg^{-1}$ and theoretical specific energy of 2600 $Whkg^{-1}$. This can improve the reaction completion for electrolyte ions to form sulphide ions. Also sulphur forms multiple strong coordinate bonds with carbon surfaces because of its low electronegativity (2.58). This is capable of forming more redox

active sites. This enhances the performance of the electrode. Sulphur also improves the stability, electrical and surface properties, and wettability of the electrode materials hence exhibiting high retention and high charge/discharge cycle stability (Tarimo et al., 2020a).

Nyquist plots of the electrode materials are shown in Figure 4.7 for the different electrolytes. For the electrode materials made from AC-S-800 material, the impedance data was collected at different potentials to ascertain the origin of the charge transfer resistance (R_{CT}) and interfacial resistance as shown in Figure S6(Appendix 1). The potential was varied from 5 to 20mV with both electrolytes as revealed in figure S16(a & b) (in supporting document). From Figure 4.7, the Nyquist plots for all the materials depicted different shapes, sizes of the semicircle, and Equivalent Series Resistance (ESR) at high-frequency regimes and almost the same behaviors at low-frequency regimes. This may be attributed to the presence of functional groups or other impurities (dopants) on the surface of the material and the current collector (Bello et al., 2017; Mathis et al., 2019). These may have caused less charge transfer resistance contributing to a less doom shaped arch curve (Figure 4.7). The ESR of the AC-S-600 electrode is approximated ~2.5Ω for both electrolytes (Figure 4.7 a & b). The ESR for AC-S-700 (Figure 4.7c & d) and AC-S-800 (Figure 4.7e & f) is estimated between 1 – 2.5Ω hence good performance. These values take into account the different factors, which include the internal resistance components of the cells and electrolytes. The AC-S-800 material with 6M KOH revealed no semicircle at high frequency (Figure 4.7e) with a 45^{o} line from ESR which indicates charge storage of a typical AC with functional groups on the surface and porous with no any charge transfer (Mathis et al., 2019).

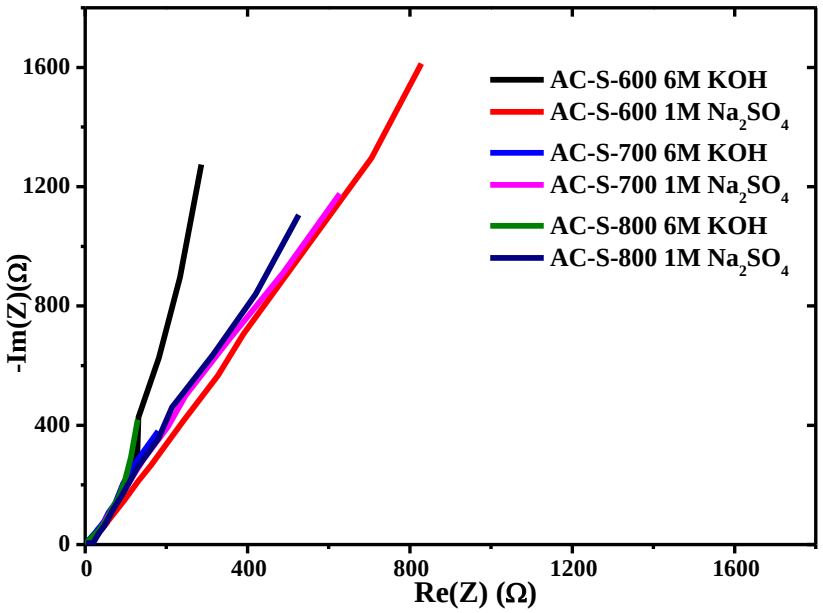

Figure 4.7: Electrochemical Impedance Spectroscopy (EIS) Nyquist plot for AC-S-600, AC-S-700, and AC-S-800 for two different electrolytes (6M KOH and 1M Na2SO4) at the potential of 10mV.

In the analysis of EIS data, the study revealed conductive material properties for electrode application by showing low ESR values meaning there was very low internal resistance within the material, current collector, electrolyte, and the cell components (Bello et al., 2017). In Figure S7(a & b) (Appendix 1) the potential was varied to examine the effect of charge transfer resistance (R_{CT}) or change in ESR. The response did not vary and never changed the impedance spectra at a lower frequency. This confirmed that there was no charge transfer resistance caused, only the interfacial impedance which occurs at constant R_{CT} (Mathis et al., 2019).

The stability of the cells was tested after CV, GCD, and EIS measurement by the floating test method as described in (Bello et al., 2017; Laheäär et al., 2015; Moyo et al., 2018; Ruch et al., 2010; Weingarth et al., 2013) which is called voltage holding or voltage floating or aging of the cell. In the current study the stability was set to have three (3) GCD then at the fourth charge maximum the voltage was held for 10 hours before the next 3 GCD and another holding. This was carried out for a total of 100 hours of holding

and the capacitance at every set was calculated using the second GCD cycle using 0.25A/g at a maximum potential window of 1.0 V for 6 M KOH electrolyte, and 1.2 V for 1 M Na_2SO_4 electrolyte. Figure S7 (b & c) (Appendix 1) shows the stability plots with capacitance as a function of floating/holding time. The capacitance for AC-S-600 with 6 M KOH showed some stability for the first 60 hours then dropped for 20 hours before stabilizing again (Figure S7b). This was almost the same case for the same material with the second electrolyte by dropping after 70 hours and never stabilized (Figure S7c).

The AC-S-700 and AC-S-800 materials revealed a more stable holding with both electrolytes and a little raise-drop with AC-S-700 with 6 M KOH at the beginning. The experiment was set to analyze the degradation effect of the active materials and the electrolyte by holding the cell at its maximum voltage of operation. In Figure S7(b & c) (Appendix 1), any raise in the capacitance after 40 hours may be due to an increase in more pore interaction as the electrolyte intercalate through the porous material. The drop in the capacitance from the lowest did not reach 20% since the degradation is considered between 20 – 30% losses of its capacitance (Weingarth et al., 2013). After 100 hours the cells still showed good performance hence no degradation (Lehtimäki et al., 2017).

The self-discharge of the cell was performed on the best cell with AC-S-800 using 6 M KOH. The cell was charged to a maximum of 1.0 V and held for 5 minutes before it was left at an open system of circuit potential to go through a self-discharge for hours as shown in Figure S7a (Appendix 1). The cell took more than twelve (12) hours to reach 30% loss and was examined for more than 16 hours and never reached half-maximum voltage loss compared to results in the literature (H. Li et al., 2012). This revealed good performance of the cell and the mechanism in the self-discharge is comparable with the Gibbs energy difference which occurs between charge and discharge states (Moyo et al., 2018) which

can explain the self-discharge phenomena. The voltage drop in the 4 hours is associated with the instability of the electrolyte which causes some degradation by the generation of gases since the electrolyte is near its ionic dissociation (Andreas HA, 2015; Oickle AM, 2013). This device exhibited stable electrochemical stability which can be used for standby applications.

Table 4.2: Performance of supercapacitors with different electrode materials from different biomass sources chemically treated with different impregnation from literature in comparison with this current study.

Electrode material	Chemical activation	Electrolyte used	Current Density (A/g)	Capacitance (F/g)	Ref
Corn cob	KOH	6M KOH	-	309.81	(Ghosh et al., 2019)
Banana stem	KOH	6M HOH	-	479.23	(Ghosh et al., 2019)
Olive residues	KOH/R	1M H_2SO_4	0.25	224	(Adbelhahim Elmouwahidi et al., 2017)
Olive residues	KOH/R	1M Na_2SO_4	0.25	193	(Adbelhahim Elmouwahidi et al., 2017)
Nanoporous carbon	K_2CO_3	2.5M KNO_3	0.5	140	(Moyo et al., 2018)
Rice husks	NaOH	0.5M K_2SO_4	1.0	198.4	(Van et al., 2014)
Coniferous pine biomass	KOH	1M Na_2SO_4	0.1	90	(Manyala et al., 2016)
Pinecone	KOH	3.5M KNO_3	0.5	300	(Momodu et al., 2019)
Hemp straw	KOH	6M KOH	1.0	244	(Shi et al., 2019)
Pinewood	H_3PO_4 / KOH	6M KOH	1.0	366	(J. Li et al., 2019)
AMC	H_2SO_4	6M KOH	0.25	456.4	This study
AMC	H_2SO_4	1M Na_2SO_4	0.25	159.02	This study

Conclusion

This research studied the value addition to corn cobs biomass towards AC materials for supercapacitors. The process of converting AMC biomass into AC material was achieved successfully by carbonization (functionalization) of the precursor with concentrated sulphuric acid and was activated in three (3) batches at different temperatures 600, 700, and 800^{o}C using a furnace in a nitrogen atmosphere. Acid functionalization indicated the addition of oxygen functional groups on the surface of the structure. The activated carbon materials were characterized and examined for physical and chemical properties including the application for supercapacitor electrode materials. The AC materials revealed low porous structures with S_{BET} between 30 – 254 m^2/g, a total pore volume of 0.0312 -0.1463 cm^3/g, and a mean pore radius of 5.77 – 10.4 µm. The materials were highly functionalized with oxygen groups on the surface with total acidity between 0.440 – 0.464 mmol/g, total basicity of 0.09 – 0.420 mmol/g, oxygen composition percentage of 22 – 32%. This greatly improved the performance of the GCD giving specific capacitance of 456.4 F/g at 0.25A/g with 6M KOH electrolyte and 159.02 F/g at 0.25 A/g with 1M Na_2SO_4 electrolyte. The results obtained demonstrate the adoption of the corn cobs as a promising material for supercapacitor applications.

REFERENCES

Adrian, B.-B., Maria, A.-F., Carmen, F.-G., & Vicente, G.-S. (2016). Activated carbon surface chemistry_ Changes upon impregnation with Al(III), Fe(III) and Zn(II)-metal oxide catalyst precursors from NO3- aqueous solutions. *Arabian Journal of Chemistry*, 14. https://doi.org/10.1016/j.arabjc.2016.02.018

Andreas HA. (2015). Self-discharge in electrochemical capacitors: a perspective article. *J Electrochem Soc*, *162*, A5047–A5053.

Bello, A., Barzegar, F., Madito, M. J., Momodu, D. Y., Khaleed, A. A., Masikhwa, T. M., Dangbegnon, J. K., & Manyala, N. (2016). Electrochemical performance of polypyrrole derived porous activated carbon-based symmetric supercapacitors in various electrolytes. *RSC Advances*, *6*(72). https://doi.org/10.1039/c6ra12690a

Bello, A., Barzegar, F., Madito, M. J., Momodu, D. Y., Khaleed, A. A., Olaniyan, O., Masikhwa, T. M., Masikhwa, Dangbegnon, J. K., & Manyala, N. (2017). Floating of PPY Derived Carbon Based Symmetric Supercapacitor in Alkaline Electrolyte. *E C S Society, The Electrochemical*, *75*(24), 1–12. https://doi.org/10.1149/07524.0001ecst

Bello, A., Sanni, D. M., Adeniji, S. A., Anye, V., Orisekeh, K., Kigozi, M., & Koech, R. (2020). Combustion synthesis of battery-type positive electrodes for robust aqueous hybrid supercapacitor. *Journal of Energy Storage*, *27*(December 2019), 101160. https://doi.org/10.1016/j.est.2019.101160

Biswal, M., Banerjee, A., & Ogale, S. (2013). From dead leaves to high energy density supercapacitors. *Energy & Environmental Science*, 1–11. https://doi.org/10.1039/c3ee22325f

Chen, J., Zhang, L., Yang, G., Wang, Q., Li, R., & Lucia, L. A. (2017). Preparation and Characterization of Activated Carbon from Hydrochar by Phosphoric Acid Activation and its Adsorption Performance in Prehydrolysis Liquor. *Bioresources*, *12*(3), 5928–5941.

Chen, X., Zhang, J., Zhang, B., Dong, S., Guo, X., Mu, X., & Fei, B. (2017). A novel hierarchical porous nitrogen-doped carbon derived from bamboo shoot for high performance supercapacitor. *Scientific Reports*, *7:7362*(April), 1–11. https://doi.org/10.1038/s41598-017-06730-x

Cui, L., Yang, Y., Cheng, C., Xu, L., Li, Y., Jia, M., Dun, X., & Jin, X. (2019). Corn Cob Lignin-based Porous Carbon Modified Reduced Graphene Oxide Film For Flexible Supercapacitor Electrode. *Journal of Wood Chemistry and Technology*, *39*(5), 343–359. https://doi.org/10.1080/02773813.2019.1623259

Das, D., Samal, D. P., & Bc, M. (2015). Preparation of Activated Carbon from Green Coconut Shell and its Characterization. *Chemical Engineering & Process Technology*, *6*(5), 1–7. https://doi.org/10.4172/2157-7048.1000248

Dhillon, R. S., & von Wuehlisch, G. (2013). Mitigation of global warming through renewable biomass. *Biomass and Bioenergy*, *48*, 75–89.

Ding, J., Wang, H., Li, Z., Cui, K., Karpuzov, D., Tan, X., Kohandehghan, A., & Mitlin, D. (2015). Peanut shell hybrid sodium ion capacitor with extreme energy--power rivals lithium ion capacitors. *Energy & Environmental Science*, *8*(3), 941–955.

Dörfler, S., Felhösi, I., Marek, T., Thieme, S., Althues, H., Nyikos, L., & Kaskel, S. (2013). High power supercap electrodes based on vertical aligned carbon nanotubes on aluminum. *Journal of Power Sources*, *227*, 218–228.

Elmouwahidi, A., Zapata-Benabithe, Z., Carrasco-Marín, F., & Moreno-Castilla, C. (2012). Activated carbons from KOH-activation of argan (Arganiaspinosa) seed shells as supercapacitor electrodes. *Bioresource Technol*, *111*, 185–190.

Elmouwahidi, Adbelhahim, Esther, B.-G., Agustin, F. P.-C., Francisco, J. M.-H., & Francisco, C.-M. (2017). Activated carbons from KOH and H3PO4-activation of olive residues and its application as supercapacitor electrodes. *Electrochimica Acta*, *229*, 219–228. https://doi.org/10.1016/j.electacta.2017.01.152

Fraczek-szczypta, A., Rabiej, S., Szparaga, G., Pabjanczyk-wlazlo, E., Krol, P., & Brzezinska, M. (2015). The structure and properties of the carbon non-wovens modi fi ed with bioactive nanoceramics for medical applications. *Materials Science and Engineering C*, *51*, 336–345. https://doi.org/10.1016/j.msec.2015.03.021

G. Hasegawa, T. Deguchi, K. Kanamori, Y. Kobayashi, H. Kageyama, T. Abe, K. N. (2015). High-Level Doping of Nitrogen, Phosphorus, and Sulfur into Activated Carbon Monoliths and Their Electrochemical Capacitances. *Chem. Mater*, *27*, 4703–4712.

Gao, F., Qin, S. H., Zang, Y. H., Gu, J. F., & Qu, J. Y. (2020). Highly efficient formation of Mn3O4-graphene oxide hybrid aerogels for use as the cathode material of high performance lithium ion batteries. *Xinxing Tan Cailiao/New Carbon Materials*, *35*(2), 121–130. https://doi.org/10.1016/S1872-5805(20)60479-6

Ghosh, S., Santhosh, R., Jeniffer, S., Raghavan, V., Jacob, G., Nanaji, K., Kollu, P., Jeong, S. K., & Grace, A. N. (2019). Natural biomass derived hard carbon and activated carbons as electrochemical supercapacitor electrodes. *Scientific Reports*, *9*(16315), 1–15. https://doi.org/10.1038/s41598-019-52006-x

Hall, P. J., Mirzaeian, M., Fletcher, S. I., Sillars, F. B., Rennie, A. J. R., Shitta-Bey, G. O., Wilson, G., Cruden, A., & Carter, R. (2010). Energy storage in electrochemical capacitors: designing functional materials to improve performance. *Energy & Environmental Science*, *3*(9), 1238–1251. https://doi.org/10.1039/c0ee00004c

Hou, J., Cao, C., Ma, X., Idrees, F., Xu, B., Hao, X., & Lin, W. (2014). From Rice Bran to High Energy Density Supercapacitors : A New Route to Control Porous Structure of 3D Carbon. *Scientific Reports*, *4*(7260), 1–6. https://doi.org/10.1038/srep07260

Jae, Y. L., Kim, G., Bang, Y., Yi, J., Gil, J., & Kyu, I. (2014). Activated carbon aerogel

containing graphene as electrode material for supercapacitor. *Materials Research Bulletin*, *50*, 240–245. https://doi.org/10.1016/j.materresbull.2013.11.021

Juan, J. T.-H., Rosas, J. M., Palomo, J., Valero-Romero, M. J., Rodríguez-Mirasol, J., & Cordero, T. (2016). Functionalization of activated carbons by HNO 3 treatment : In fl uence of phosphorus surface groups. *Carbon*, *101*, 409–419. https://doi.org/10.1016/j.carbon.2016.02.015

Ketcha, J. M., Dina, D. J. D., Ngomo, H. M., & Ndi, N. J. (2012). Preparation and Characterization of Activated Carbons Obtained from Maize Cobs by Zinc Chloride Activation. *American Chemical Science Journal*, *2*(4), 136–160.

Kigozi, M., Koech, R. K., Kingsley, O., Ojeaga, I., Tebandeke, E., Kasozi, G., & Onwualu, P. A. (2020). Synthesis and characterization of graphene oxide from locally mined graphite flakes and its supercapacitor applications _ Elsevier Enhanced Reader.pdf. *Results in Materials*, *100113*. https://doi.org/10.1016/j.rinma.2020.100113

Köseog˘lu, E., & Akmil-Bas?ar, C. (2015). Preparation, structural evaluation and adsorptive properties of activated carbon from agricultural waste biomass. *Advanced Powder Technology*, *26*, 811–818. https://doi.org/10.1016/j.apt.2015.02.006

Kumagai, S., Sato, M., & Tashima, D. (2013). Electrical double-layer capacitance of micro-and mesoporous activated carbon prepared from rice husk and beet sugar. *Electrochimica Acta*, *114*, 617–626.

Kumar, A., & Jena, H. M. (2016). Preparation and characterization of high surface area activated carbon from Fox nut (Euryale ferox) shell by chemical activation with H3PO4. *Results in Physics*, *6*, 651–658. https://doi.org/10.1016/j.rinp.2016.09.012

Laheäär, A., Przygocki, P., Abbas, Q., & Béguin, F. (2015). Appropriate methods for evaluating the ef fi ciency and capacitive behavior of different types of supercapacitors. *Electrochemistry Communications*, *60*, 21–25. https://doi.org/10.1016/j.elecom.2015.07.022

Lee, M., Kim, G.-P., Song, H. D., Park, S., & Yi, J. (2014). Preparation of energy storage material derived from a used cigarette filter for a supercapacitor electrode. *Nanotechnology*, *25*(34), 345601.

Lehtimäki, S., Railanmaa, A., Keskinen, J., Kujala, M., & Tuukkanen, S. (2017). Performance , stability and operation voltage optimization of screen-printed aqueous supercapacitors. *Scientific Reports*, *7*(46001), 1–9. https://doi.org/10.1038/srep46001

Lekakou, C., Moudam, O., Markoulidis, F., Andrews, T., Watts, J. F., & Reed, G. T. (2011). Carbon-Based Fibrous EDLC Capacitors and Supercapacitors. *Journal of Nanotechnology*, *409382*, 8. https://doi.org/10.1155/2011/409382

Li, H., Kang, Z., Liu, Y., & Lee, S.-T. (2012). Carbon nanodots: synthesis, properties and applications. *J. Mater. Chem*, *22*, 24230–24253.

Li, J., Han, K., Qi, J., Teng, Z., Li, M., & Wang, M. (2019). Biomass - derived 3D hierarchical porous carbon by two - step activation method for supercapacitor. *Journal of Materials Science: Materials in Electronics*, *30*, 19415–19425. https://doi.org/10.1007/s10854-019-02303-y

Li, X., Xing, W., Zhuo, S., Zhou, J., Li, F., Qiao, S.-Z., & Lu, G.-Q. (2011). Preparation of capacitor's electrode from sunflower seed shell. *Bioresource Technology*, *102*(2), 1118–1123.

Liang, Y., Liang, F., Zhong, H., Li, Z., Fu, R., & Wu, D. (2013). An advanced carbonaceous porous network for high-performance organic electrolyte supercapacitors. *J. Mater. Chem. A*, *1*, 7000–7005.

Lijuan, H., Peng, Y., Feng, W., Peng, S., JinJun, L., & Zizheng, L. (2017). Tubular activated carbons made from cotton stalk for dynamic adsorption of airborne toluene. *Journal of The Taiwan Institute of Chemical Engineers*, *80*, 399–405. https://doi.org/10.1016/j.jtice.2017.07.029

Lim, W. C., Srinivasakannan, C., & Balasubramanian, N. (2010). Activation of palm shells by phosphoric acid impregnation for high yielding activated carbon. *Journal of Analytical and Applied Pyrolysis*, *88*, 181–186. https://doi.org/10.1016/j.jap.2010.04.004

Liou, T. (2010). Development of mesoporous structure and high adsorption capacity of biomass-based activated carbon by phosphoric acid and zinc chloride activation. *Chemical Engineering Journal*, *158*, 129–142. https://doi.org/10.1016/j.cej.2009.12.016

Liu, N., Huo, K., McDowell, M. T., Zhao, J., & Cui, Y. (2013). Rice husks as a sustainable source of nanostructured silicon for high performance Li-ion battery anodes. *Scientific Reports*, *3*.

Manyala, N., Bello, A., Barzegar, F., Khaleed, A. A., Momodu, D. Y., & Dangbegnon, J. K. (2016). Coniferous pine biomass : A novel insight into sustainable carbon materials for supercapacitors electrode. *Materials Chemistry and Physics*, *182*, 139–147. https://doi.org/10.1016/j.matchemphys.2016.07.015

Mathis, T. S., Kurra, N., Wang, X., Pinto, D., & Simon, P. (2019). Energy Storage Data Reporting in Perspective — Guidelines for Interpreting the Performance of Electrochemical Energy Storage Systems. *Advanced Energy Materials*, *1902007*, 1–13. https://doi.org/10.1002/aenm.201902007

Mi, J., Wang, X.-R. R., Fan, R.-J. J., Qu, W.-H. H., & Li, W.-C. C. (2012). Coconut-shell-based porous carbons with a tunable micro/mesopore ratio for high-performance supercapacitors. *Energy & Fuels*, *26*(8), 5321–5329. https://doi.org/10.1021/ef3009234

Mohamad, A. N., & Williams, P. T. (2012). Pore characteristics of activated carbons from the phosphoric acid chemical activation of cotton stalks. *Biomass and Bioenergy*, *37*, 142–149. https://doi.org/10.1016/j.biombioe.2011.12.019

Momodu, D., Okafor, C., Manyala, N., Bello, A., & Zebazekana, M. G. (2019). Transformation of Plant Biomass Waste into Resourceful Activated Carbon Nanostructures for Mixed-Assembly Type Electrochemical Capacitors. *Waste and Biomass Valorization*, *10*, 1741–1753. https://doi.org/10.1007/s12649-017-0165-x

Moulder, J. F., Stickle, W. F., Sobol, P. E., & Bomben, K. D. (1992). *Handbook of X-ray Photoelectron Spectroscopy*. Perkin-Elmer Corporation, Physical Electronics Division.

Moyo, B., Momodu, D., Fasakin, O., Dangbegnon, J., & Manyala, N. (2018). materials Electrochemical analysis of nanoporous carbons derived from activation of polypyrrole for stable supercapacitors. *Energy Materials*, *53*, 5229–5241. https://doi.org/10.1007/s10853-017-1911-y

Muniyandi Rajkumar, Hsu, C.-T., Wu, T.-, Chen, M.-G., & Hu, C. (2015). Advanced materials for aquous supercapacitors in the asymmetric design. *Progress in Natural Science: Materials International*, *25*, 527–544. https://doi.org/10/1016/j.pnsc.2015.11.012

Nankya, R., Opar, D. O., Kim, M., Paek, S., & Jung, H. (2020). Synergetic effect of nitrogen and sulfur co-doping in mesoporous graphene for enhanced energy storage properties in supercapacitors and lithium-ion batteries. *Journal of Solid State Chemistry*, *289*(May), 121451. https://doi.org/10.1016/j.jssc.2020.121451

Oickle AM. (2013). *A systematic study of self-discharge mechanisms in carbon-based, aqueous electrolyte electrochemical capacitors*.

Perumbilavil, S., Sankar, P., Thankamani, P. R., & Philip, R. (2015). White light Z-scan measurements of ultrafast optical nonlinearity in reduced graphene oxide nanosheets in the 400 – 700 nm region. *Applied Physics Letters*, *107*(051104), 7. https://doi.org/10.1063/1.4928124

Qian, W., Sun, F., Xu, Y., Qiu, L., Liu, C., Wang, S., & Yan, F. (2014). Human hair-derived carbon flakes for electrochemical supercapacitors. *Energy & Environmental Science*, *7*(1), 379–386.

Raymundo-Piñero, E., Cadek, M., & Béguin, F. (2009). Tuning Carbon Materials for Supercapacitors by Direct Pyrolysis of Seaweeds. *Advanced Functional Materials*, *19*(7), 1032–1039. https://doi.org/10.1002/adfm.200801057

Ruch, P. W., Cericola, D., Kötz, R., & Wokaun, A. (2010). Aging of electrochemical double layer capacitors with acetonitrile-based electrolyte at elevated voltages. *Electrochimica Acta*, *55*(15), 4412–4420. https://doi.org/10.1016/j.electacta.2010.02.064

Schönherr, J., Buchheim, J. R., Scholz, P., & Adelhelm, P. (2018). Boehm Titration Revisited (Part I): Practical Aspects for Achieving a High Precision in Quantifying Oxygen-Containing Surface Groups on Carbon Materials. *Journal of Carbon Reserch*, *4*(21), 1–13. https://doi.org/10.3390/c4020021

Shafeeyan, M. S., Wan, M. W. A., Houshmand, A., & Shamiri, A. (2010). A review on surface modification of activated carbon for carbon dioxide adsorption. *Journal of Analytical and Applied Pyrolysis*, *89*(2), 143–151. https://doi.org/10.1016/j.jaap.2010.07.006

Shahbandeh, M. (2020, September 7). *Corn production worldwide 2019/2020, by country*. Statista. https://www.statista.com/statistics/254292/global-corn-production-by-country/ 15:07, 07/09/2020

Shi, G., Liu, C., Wang, G., Chen, X., Li, L., Jiang, X., Zhang, P., & Dong, Y. (2019). Preparation and electrochemical performance of electrospun biomass-based activated carbon nanofibers. *Ionics*, *25*, 1805–1812. https://doi.org/10.1007/s11581-018-2675-3

Tang, H., Gao, P., Liu, X., Zhu, H., & Bao, Z. (2014). Bio-derived calcite as a sustainable source for graphene as high-performance electrode material for energy storage. *Journal of Materials Chemistry A*, *2*(38), 15734–15739.

Tarimo, D. J., Oyedotun, K. O., Mirghni, A. A., Sylla, N. F., & Manyala, N. (2020). High energy and excellent stability asymmetric supercapacitor derived from sulphur-reduced graphene oxide/manganese dioxide composite and activated carbon from peanut shell. *Electrochimica Acta*, 136498. https://doi.org/10.1016/j.electacta.2020.136498

Tian, W., Gao, Q., Yanli Tan, a K. Y., Zhu, L., Yanga, C., & Zhang, H. (2015). Bio-inspired Beehive-like Hierarchical Nanoporous Carbon Derived from Bamboo-based Industrial Byproduct as High Performance Supercapacitor Electrode Material. *Materials Chemistry A*, 10. https://doi.org/10.1039/b000000x

Van, K. Le, Thuy, T., & Thi, L. (2014). Activated carbon derived from rice husk by NaOH activation and its application in supercapacitor. *Progress in Natural Science: Materials International*, *24*(3), 191–198. https://doi.org/10.1016/j.pnsc.2014.05.012

Vlad, A., Singh, N., Melinte, S., Gohy, J., & Ajayan, P. M. (2016). Carbon Redox-Polymer-Gel Hybrid Supercapacitors. *Scientific Reports*, *February*, 3–8. https://doi.org/10.1038/srep22194

Wang, H., Xu, Z., Kohandehghan, A., Li, Z., Cui, K., Tan, X., Stephenson, T. J., King'ondu, C. K., Holt, C. M. B., Olsen, B. C., Jin Kwon, T., Harfield, D., Anthony O., Anyia, A., & David, M. (2013). Interconnected carbon nanosheets derived from hemp for ultrafast supercapacitors with high energy. *ACS Nano*, *7*(6), 5131–5141.

Wei, L., Sevilla, M., Fuertes, A. B., Mokaya, R., & Yushin, G. (2011). Hydrothermal Carbonization of Abundant Renewable Natural Organic Chemicals for High-Performance Supercapacitor Electrodes. *Advanced Energy Materials*, *1*, 356–361. https://doi.org/10.1002/aenm.201100019

Wei, Q.-L., Chen, Z. M., Wang, X. F., Yang, X. M., & Wang, Z. C. (2018). A two-step method for the preparation of high performance corncob-based activated carbons as supercapacitor electrodes using ammonium chloride as a pore forming additive. *New*

Carbon Materials, *33*(5), 402–408. https://doi.org/10.1016/S1872-5805(18)60348-8

Wei, T., Zhang, Q., Wei, X., Gao, Y., & Li, H. (2016). A Facile and Low-Cost Route to Heteroatom Doped Porous Carbon Derived from Broussonetia Papyrifera Bark with Excellent Supercapacitance and CO 2 Capture Performance. *Scientific Reports*, *6:22646*(November 2015), 2–10. https://doi.org/10.1038/srep22646

Weingarth, D., Foelske-Schmitz, A., & Kötz, R. (2013). Cycle versus voltage hold e Which is the better stability test for electrochemical double layer capacitors ? *Journal of Power Sources*, *225*, 84–88. https://doi.org/10.1016/j.jpowsour.2012.10.019

Xiang, Y. C., Chen, C., Zhang, Z. J., & Xie, D. H. (2013). High performance porous carbon through hard–soft dual templates for supercapacitor electrodes. *Journal of Matrials Chemistry A*, *1*, 7379–7383. https://doi.org/10.1039/c3ta10841d

Xu, J., Gao, Q., Zhang, Y., Tan, Y., Tian, W., Zhu, L., & Jiang, L. (2014). Preparing two-dimensional microporous carbon from Pistachio nutshell with high areal capacitance as supercapacitor materials. *Scientific Reports*, *4*.

Yakout, S. M., & G. Sharaf, E.-D. (2016). Characterization of activated carbon prepared by phosphoric acid activation of olive stones. *Arabian Journal of Chemistry*, *9*, 1155–1162. https://doi.org/10.1016/j.arabjc.2011.12.002

Yang, S., & Zhang, K. (2018). Converting corncob to activated porous carbon for supercapacitor application. *Nanomaterials*, *8*(4), 1–10. https://doi.org/10.3390/nano8040181

Yeon, S., Kim, D., Lee, S., Nam, S., Park, S., So, Y., Shin, K., Jin, C., Park, Y., Kang, Y. C., So, J. Y., Park, Y., & Kang, Y. C. (2017). High microporosity of carbide-derived carbon prepared from a vacuum- treated precursor for energy storage devices. *Carbon*, *11870*. https://doi.org/10.1016/j.carbon.2017.03.063

Zhai, Y., Dou, Y., Zhao, D., Fulvio, P. F., Mayes, R. T., & Dai, S. (2011). Carbon materials for chemical capacitive energy storage. *Advanced Materials*, *23*(42), 4828–4850.

Zhang, L. L., Zhou, R., & Zhao, X. S. (2010). Graphene-based materials as supercapacitor electrodes. *Journal of Materials Chemistry*, *20*(29), 5983–5992. https://doi.org/10.1039/c000417k

Zhang, L., Wang, Y., Peng, B., Yu, W., Wang, H., Wang, T., Deng, B., Chai, L., Zhang, K., & Wang, J. (2014). Preparation of a macroscopic, robust carbon-fiber monolith from filamentous fungi and its application in Li--S batteries. *Green Chemistry*, *16*(8), 3926–3934.

Zhang, S., & Pan, N. (2015). Supercapacitors Performance Evaluation. *Adv. Energy Mater*, *5*, 1401401.

Zhong, C., Deng, Y., Hu, W., Qiao, J., Zhang, L., & Zhang, J. (2015). A review of

electrolyte materials and compositions for electrochemical supercapacitors. *Chemical Society Reviews*, *44*(21), 7484–7539. https://doi.org/10.1039/c5cs00303b

Zhu, Y., Murali, S., Stoller, M. D. M., Ganesh, K. J., Cai, W., Ferreira, P. J., Pirkle, A., Wallace, R. M., Cychosz, K. a, Thommes, M., Su, D., Stach, E. A., Ruoff, R. S., & others. (2011). Carbon-based supercapacitors produced by activation of graphene. *Science (New York, N.Y.)*, *332*(6037), 1537–1541. https://doi.org/10.1126/science.1200770

Zhu, Z., Jiang, H., Guo, S., Cheng, Q., Hu, Y., & Li, C. (2015). Dual Tuning of Biomass-Derived Hierarchical Carbon Nanostructures for Supercapacitors : the Role of Balanced Meso / Microporosity and Graphene. *Scientific Reports*, *5:15936*(April), 1–9. https://doi.org/10.1038/srep15936

CHAPTER FIVE

5.0. Porous carbon derived from *Zea mays* cobs as excellent electrodes for supercapacitor applications

5.1. Introduction

Technology evaluation globally has shown that there is a huge demand for energy consumption. This is due to the increasing population and the number of gadgets which are developed to simplify life. In generation Alpha, the interaction with artificial intelligence and automated voice becoming an integral part of normal systems, and is impacting health, life, and future generation. All these aspects require power to be renewable and sustainable. Renewable energy harvested from sources like solar/ hydro, wind, geothermal among others is not produced continuously because they are time and weather-dependent. To improve on these technologies, and become sustainable, energy storage accumulators such as supercapacitors and batteries are required (Kigozi, Koech, et al., 2020; Tarimo et al., 2020b). Supercapacitors (SCs) have attracted tremendous attention in today's energy storage research due to their excellent performance of high power density, high cycling stability, and quick charge/discharge process (Hsiao et al., 2020; Kigozi, Koech, et al., 2020; Murugesan Rajesh et al., 2020; Tarimo et al., 2020b).

Supercapacitors are categorized depending on their mechanism of energy storage which includes; (i) electrical chemical double-layer capacitor (EDLC) which store their energy by accumulation of charges in a Helmholtz double-layer interaction between electrolyte and electrode, (ii) pseudocapacitors with storage achieved by a reversible faradic redox reaction between electrolyte and electrodes (Kigozi, Koech, et al., 2020; Murugesan Rajesh et al., 2020; Tarimo et al., 2020b; Jiaqi Wang et al., 2020). (iii) hybrid

supercapacitors formation by coupling of different redox and EDLC materials (Muzaffar et al., 2019). The EDLC electrode materials (activated carbon (AC)) have unique properties including high volume/low density and large specific surface area which improves optimized porosity, wettability, high electrolytic ion adsorption, and excellent electrical conductivity (Murugesan Rajesh et al., 2020). Activated carbon (AC) is widely used as electrode material for supercapacitors, and obtained from the activation of biomass. This is because biomass is economically viable and abundant in nature (Murugesan Rajesh et al., 2020)(Hsiao et al., 2020)(Malothu et al., 2020). The AC materials are recently derived mainly from renewable and sustainable resources such as agricultural crop wastes, biomass, and domestic waste which are eco-friendly and renewable (Kigozi, Kali, et al., 2020; Malothu et al., 2020).

There is generally two main activation process which includes physical and chemical activation used for the synthesis of AC from biomass. Chemical activation is commonly used because of its low activation time, low temperatures, uniform pore size distribution, high yield, and controllable specific surface area compared to the physical process (Kigozi, Kali, et al., 2020). The chemical activation normally employs activation agents include potassium hydroxide (KOH), sulphuric acid (H_2SO_4), sodium hydroxide (NaOH), phosphorous acid (H_3PO_4), zinc chloride ($ZnCl_2$) among others which are extensively applied at different temperatures and different atmospheres (Jiaqi Wang et al., 2020)(Malothu et al., 2020). Several EDLC supercapacitors are reported using different AC from biomass and other materials which include African maize corn cob reported SSA of 254m^2/g exhibited a specific capacitance of 456 F/g at specific current of 0.25A/g(Kigozi, Kali, et al., 2020), waste tea reported SSA of 294.6 m^2/g with performance of specific capacitance of 199F/g at the current density of 0.5A/g, the SSA

of 1308 m2/g gave a specific capacitance of 140F/g at a current density of 0.1A/g (Inal & Aktas, 2020), rosewood and corn cob (X. Xie et al., 2020), banana peels (Nguyen et al., 2020), corn husk with SSA of 1370 m^2/g giving a specific capacitance of 127F/g obtained at 1A/g (Malothu et al., 2020), Pinecone was reported with SSA of 1169.31 m^2/g shown a performance of specific capacitance of 43F/g at 0.5A/g (Murugesan Rajesh et al., 2020), coconut shell exhibited SSA of 11614 m^2/g resulted in a high capacitance of 426F/g at 0.5A/g with electronic conductivity of 11.43S/cm (Y. Lin et al., 2020) Tongcao biomass was reported to have the SSA of 1425.2 m^2/g with gravimetric capacitance of 244.51F/g at a scan rate of 20mV/s (Hsiao et al., 2020), The nitrogen doped porous carbon (NPC)/mesophase pitch exhibited SSA of 503.8 m^2/g shown a specific capacitance of 232.2F/g at current density of 2A/g (M. Liu et al., 2020).

The EDLC charge is stored at the interface of the electrolyte/electrode system. This is primarily controlled by a high specific surface area (SSA) of the materials for the electrode to improve the electrochemical performance. When carrying out activation for biomass for carbon derived material for supercapacitor, the process needs to be good for improving SSA which can enhance the electrochemical storage performance. From the literature, higher SSA improves EDLC performance. This is because there is an optimization of pore structure, large mesopore volume, and tailored morphology are needed (Ashraf et al., 2018; Malothu et al., 2020).

To achieve the required porosity and morphology, different activation agents are employed as mentioned earlier but also the optimization of carbonization and activation temperature is necessary. The focus of this research work is to optimize the temperature for activation of *Zea mays* cob to improve porosity, morphology, and performance. The activation of this study used KOH which is the most common activating agent frequently

used for the different biomass activation processes. KOH gives better porosity and large SSA because of its comprehensive cation, the carbon lattice expansion by K^+ ion intercalation, its synergistic, and their chemical activation (H. Lu & Zhao, 2017; Murugesan Rajesh et al., 2020). The KOH activation proved to give excellent electrode materials which contribute to redox reaction with heteroatoms bonded on the surface of the material (Raj et al., 2018). Kigozi et al 2020 reported acid activation of maize cobs with SSA of 357 m^2/g using similar parameters. In this study, the *Zea mays* cobs derived porous activated carbon materials were synthesized by carbonization at 400^{o}C for 90 mins and KOH activation at different temperatures (600, 700, and 800^{o}C) using a ratio of 1:4 of the sample with KOH. The synthesized carbon materials were used to fabricate symmetric devices and tested in two and three-electrode configurations to evaluate the electrochemical performance.

5.2. Experiments

5.2.1. Materials

The *Zea mays* (maize) cobs were obtained from the nearby farms of the African University of Science and Technology (AUST) Abuja. The potassium hydroxide used (90% SDFCL), carbon black, PVDF, and NMP (99% Sigma-Aldrich)

5.2.2. Preparation of activated carbon

The Activated carbons nanostructure was prepared as follows; the *Zea Mays* cobs were gotten from farmers near the African University of Science and Technology (AUST) Abuja Nigeria. The cobs were cleaned and sized to approximately ~3cm. The sample was dried in an oven at 110^{o}C for 48 h then grounded and sieved to fraction using a 1.0mm sieve. The cobs sample powder was synthesized using two steps at elevated temperature.

First, carbonization of raw material from the *Zea mays* at 400^{o}C for 90min under the nitrogen atmosphere. Thereafter, the sample was divided into three (3) portions. These portions were mixed with KOH as the activating agent in a mass ratio of 1:4. These portions were activated using three (3) different temperatures on different days in a furnace under a nitrogen atmosphere with a flow rate of 300mL/min with a ramped temperature of 3^{o}C/min and a holding time of 2 h. The first (1st) portion was activated at 600^{o}C and the sample was named ANN6, the second (2nd), and the third (3rd) portions were heated at 700^{o}C and 800^{o}C then named ANN7, and ANN8 respectively.

5.2.3. Material Characterization

The morphological and elemental composition of the samples was examined by the Field Emission Scanning Electron Microscope ((FESEM) Gemini-SEM 500M/s Carl ZEISS-EDAX Z2 Analyser AMETEK) Bangalore, India. X-Ray Diffraction (XRD) patterns were obtained by Rigaku Smart lab Autosampler XRD (RIGAKU Corp., Tokyo, Japan) equipped with a Cu kα radiation (wavelength λ = 1.54 Å) and the JCPDS-ICDD database. The thermogravimetric analysis (TGA) of the samples was executed using a TGA-DSC analyzer (Jupiter STA449 F3 NTZSCH GmbH) Selb, Germany. The samples were heated in pure air at a flow rate of 10 cm^{3}/min from room temperature to 1000^{o}C at a ramped temperature of 10^{o}C/min with a run time of 100 minutes using calcinated silica pan as reference material (Lim et al., 2010)(Van et al., 2014)(Lijuan et al., 2017). The surface chemistry and functional groups of AC samples were examined by Fourier Transformation InfraRed (FTIR) spectroscopy (Bruker Optik GmbH Vertex 70, Ettlingen, Germany) scanned from 600 to 4000 cm^{-1}. The X-ray Photoelectron Spectroscopy (XPS) method with spectra in the K-alpha Photoelectron spectrometer using omicron Nano Technology London, UK. (Adbelhahim Elmouwahidi et al., 2017;

Shafeeyan et al., 2010). The Nitrogen Adsorption and desorption isotherms of the activated samples were obtained using a 77K automated adsorption instrument (11-2370. Gemini Miceomeritics, Atlanta, GA, USA). The AC samples were degassed at 300^{o}C in a vacuum for 10 h (Kigozi, Kali, et al., 2020).

5.2.4. Electrochemical characterization

The two and three-electrode systems configuration measurements were employed using BIO-LOGIC (BCS-805) workstation operating on the BT-Lab software. The working electrodes were prepared by mixing the active materials 80%, carbon black 10%, and 10% binder (poly Vinylidene). In the mixture, a few drops of 1-methyl-2-pyrrolidine (NMP) was added to form a uniform paste that was coated on a graphite foil as the current collector for the electrodes. The coated electrodes were dried in an electric oven at 70^{o}C for 15h. The electrochemical measurements including galvanostatic charge-discharge (GCD), cyclic voltammetry (CV), electrochemical impedance spectroscopy (EIS), stability, and self-discharge were examined using 6M KOH aqueous electrolyte. In the three-electrode configuration system, the as-prepared materials were used as working electrode, Ag/AgCl as a reference electrode, and Pt as the counter electrode. The CV and GCD were carried out using a potential range from 0 to 1.0V. The two-electrode measurement was carried out with two working electrodes with similar mass load separated by cellulose filter paper assembled in a Swagelok symmetrical setup with 6M KOH aqueous solution. The CV and GCD properties were investigated between 0 to 1.0V potential and the EIS test was performed in the frequency range of 10kHz to 10MHz at 10mV. The stability of the device was carried out with the floating technique (voltage holding) as described in (Adbelhahim Elmouwahidi et al., 2017; Kigozi, Kali, et al., 2020), and the self-discharge was performed by charging the device to a maximum

voltage the held for 5 minutes then left to self-discharge to determine the percentage voltage loss with time as described by (Barzegar et al., 2016; Bello et al., 2017; Moyo et al., 2018).

The Specific capacitance (c_{sp} F/g) with three-electrode was calculated using GCD equation (5.1), (Kigozi, Koech, et al., 2020; M. Liu et al., 2020; Malothu et al., 2020; Murugesan Rajesh et al., 2020).

$$C_{sp} = \frac{I\Delta t}{m\Delta V} \tag{5.1}$$

Where; **I** is the discharge current (A), Δ**t** is the discharge time (s), Δ**V** is the applied potential window (V) and **m** is the coated mass of the active materials (g). The specific capacitance of a single electrode in the two-electrode symmetric setup was calculated using equation (5.2) (Kigozi, Koech, et al., 2020; H. Wei et al., 2019).

$$C = 4\frac{I\Delta t}{M\Delta V} \tag{5.2}$$

Where; C is the capacitance (F/g), I/M is the specific current (A/g), Δt is the discharge time (s) and ΔV is the potential window (V). The energy density (**E**, Wh/kg) and power density (**P**, W/kg) of the symmetric device supercapacitor was calculated using the following equations.

$$E = \frac{C(\Delta V)^2}{28.8} \tag{5.3}$$

$$P = 3600\frac{E}{\Delta t} \tag{5.4}$$

5.3. Results and discussion

5.3.1. Morphology and structural characterization

The morphology of the three activated carbon materials was analyzed by FESEM/EDS as stated earlier and the results are shown in Figure 5.1. The AC samples exhibited irregular sheets with apparent porosities. This implies that the morphology could be from the volatile organics and swell expansion as reported by Xie et al (X. Xie et al., 2020) and Wang et al (Jiaqi Wang et al., 2020). The three-carbon samples exhibited rough surfaces with excellent porosity creating a perfect interface for diffusion and intercalation of the electrolytic ions during the charge-discharge process of the EDLC electrodes. The visible surface porous structure of the samples varied with the varying temperature. ANN6 (Figure 5.1a) exhibited huge irregular pores similar to a honeycomb structure which is comparable to that of ANN7 as shown in Figure 5.1b. However, the ANN8 (Figure 5.1c) show densely packed structure when compared with the ANN6 and ANN7 which we refer to as better in-depth porosity. The EDS (Energy dispersive spectroscopy) and the elemental mapping of all three (3) samples confirm the presence of carbon materials with 75 – 99%wt in the activation with KOH. This creates high porosity with the high surface area due to redox reactions and the evolution of volatile organics as gases hence increasing the porosity (C. H. Wang et al., 2016). The EDS of ANN6 shown 99.48% carbon with some silica and sulphur as other elements. The ANN7 exhibited 89.47% carbon with silica and calcium as the other elements. ANN8 sample exhibited 75.22% carbon as shown in Table 5.1 and the spectra in Figure 5.1. The higher value of silica in ANN8 is due to increased temperature of activation leading to the formation of silica groups.

Table 5.1: EDS elemental composition for ANN6, ANN7, and ANN8 AC samples

Sample	C	Si	S	Ca
ANN6	99.48	0.48	0.04	-
ANN7	89.47	7.91	-	2.62
ANN8	75.22	18.43	-	6.35

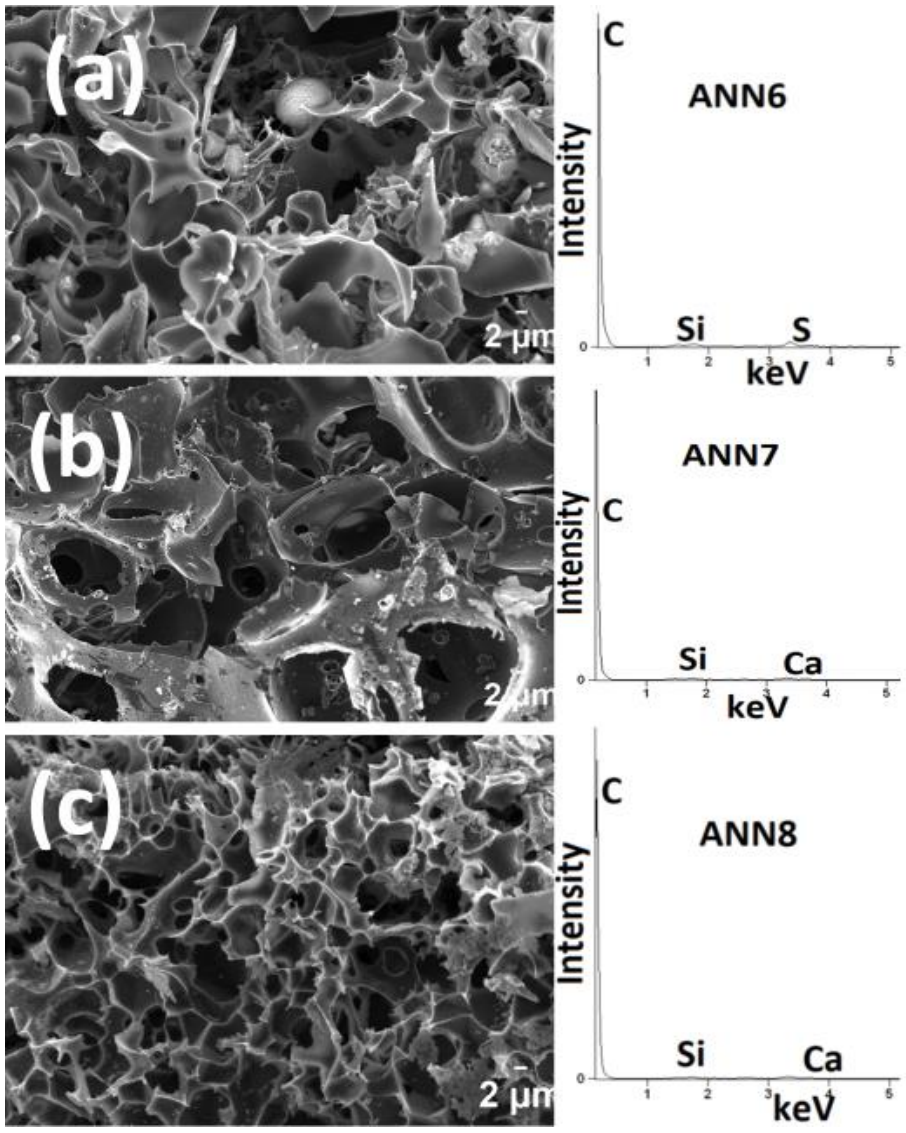

Figure 5.1: FESEM/EDX morphology and compositions for (a) ANN6, (b) ANN7, the and (c) ANN8 samples.

The XRD pattern of the activated carbon was carried out to confirm the phase composition as shown in Figure 5.2a. The spectra exhibited common strong broad peaks at $2\theta = 23.3^{o}$ and 43.1^{o} corresponding to (002) and (100) lattice planes for all the samples respectively (Y. Lin et al., 2020; Qiu et al., 2017; Sudhan et al., 2017; J. Yang et al., 2020). The peak formation at $2\theta = 23.2^{o}$ with a plane of (002) indicates a graphitic structure and amorphous morphological phase in the derived activated carbon materials (Zequine et al., 2016). The degree of graphitization is closely related to the conductivity of the carbon materials (Ji et al., 2019). The JCPDS card no. 41-1487 shown the profile of ANN6 and ANN7 at $2\theta = 23$ and $40 – 43^{o}$ with a d-spacing of 4.435 – 4.456Å and 2.214 – 2.228Å, respectively. The shift in the 2θ value of ANN8 towards large angles at high-temperature sample leads to the change in the d-spacing at $2\theta = 26.4^{o}$ and 43.09^{o} to 3.380Å and 2.108Å respectively. This is also visible in their morphology where ANN8 is different from the other two. In all the 3 samples, the d -spacing at $2\theta = 23^{o}$ is greater than 3.35Å (for graphite) indicates the formation of hard carbon (Kigozi, Kali, et al., 2020). The decrease in d-spacing causing a decrease in non-crystallinity as shown in Figure 5.1 between ANN6, ANN7, and ANN8 morphology variation (Malothu et al., 2020).

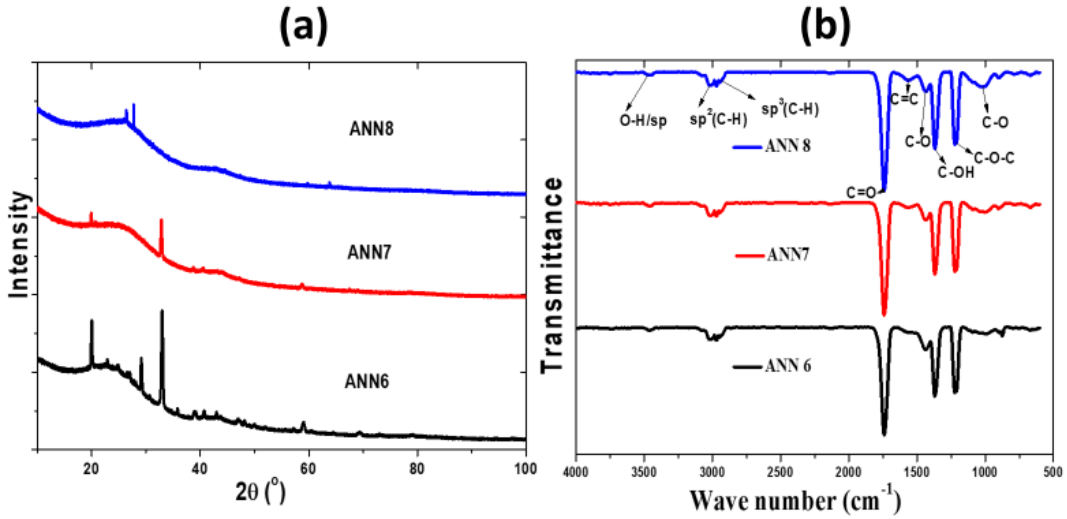

Figure 5.2: (a) XRD spectra, (b) FTIR spectra for ANN6, ANN7, and ANN8 activated carbon.

The FTIR spectra of derived activated carbon are shown in Figure 5.2b. The samples were scanned from 4000 to 600cm^{-1}. The fingerprint region (1500 – 600) indicated three main strong peaks of C-OH, C-O-C, C-H, C-N, and C-O for the skeleton of the materials. Also, the diagnostic region (4000 – 1500 cm^{-1}) exhibited the main vibration at 1737cm^{-1} for the 3 samples as the strongest peak. This can be attributed to the frequency vibration of the C=O stretching in the structure of lactone, carboxyl, or quinone groups stretching in aromatic which are more intense in the activated carbon. Other characteristic peaks present include sp^3(C-H), sp^2(C-H) stretching vibration (2990 to 3050 cm^{-1}), and O-H/sp stretching vibration (3450cm^{-1}). The vibration stretching between 2990 – 3050 cm^{-1} is attributed to C-H stretch and out of plane bending vibration. The fingerprint region exhibited bending vibration of C-H or C-N which indicates the reaction of dehydrogenation. This is accelerated with the increase in temperature of activation. The functional groups' information and frequency vibrations are consistent with the literature (Kigozi, Koech, et al., 2020; M. Liu et al., 2020; H. Zhao et al., 2017).

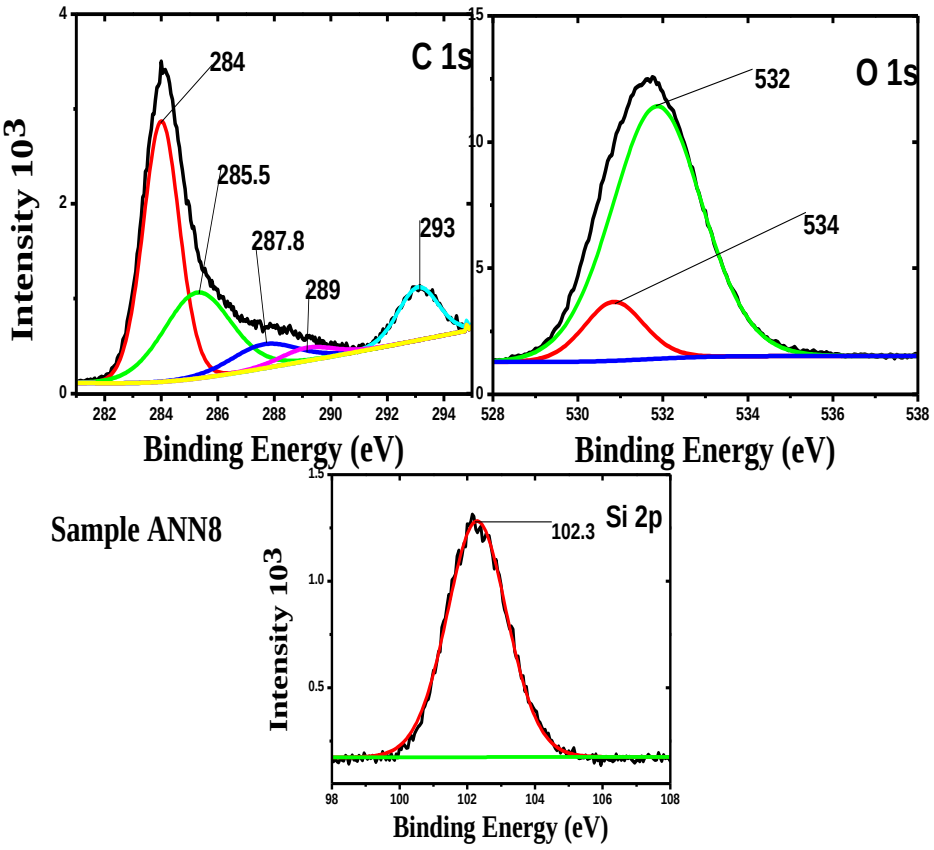

Figure 5.3: XPS deconvoluted spectra for ANN8 activated sample.

The composition and functional groups of the samples were further examined by the XPS technique as shown in Figure 5.3 with their binding energy and assignment of C1s, O1s, and Si2p. The samples exhibited no significant difference in their positions and shapes for different temperature treatments. The deconvolution of the C1s for sample ANN8 in Figure 5.3, ANN7 and ANN6 spectra Figure 1S (Appendix 2) was observed in five-carbon states as follows; C-C and sp^2 at 284ev, C-O, C-N at 285.5ev, C-C at 287.8ev, O-C=O, C=O at 289ev. The Si2p exhibited one peak at 102ev which indicates Si-O and the O1s shown two oxygen states of C=O at 532ev and C-O at 534ev. The spectra states are consistent with the different literature as reported (Wenxin Chen et al., 2016; Bei Liu et al., 2017; Nguyen et al., 2020; Murugesan Rajesh et al., 2020). The denoted functional groups of O=C, C-O-H, C-O-C among others are common structures of phenolic, ester, quinine, lactonic, carboxyl group from the surface of the materials. Table 5.2 shows the

atomic percentages from XPS analyses. This depicted a considerable decrease in carbon and oxygen percentage which is attributed to an increase in temperature that caused an increase in the silica percentage at a higher temperature of activation (Inal & Aktas, 2020; Peng et al., 2018).

Table 5.2: Atomic percentages as obtained from XPS analysis

Sample	Atomic concentration (%)		
	C 1s	**O 1s**	**Si 2p**
ANN8	51.86	37.68	10.46
ANN7	75.66	24.08	5.26
ANN6	83.46	14.48	2.05

The thermogravimetric analysis (TGA/DSC) was carried out to confirm the degradation and purity of the ANN6, ANN7, and ANN8 samples materials. The TGA/DSC data collected by heating the three samples to 1000^{o}C under a pure airflow as shown in Figure 4a and the TGA data in Table 5.3.

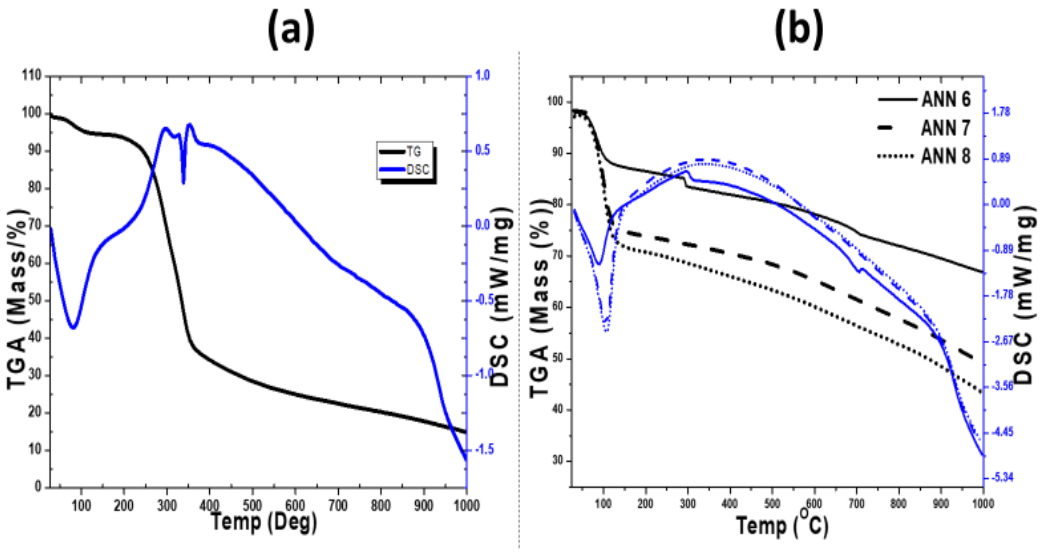

Figure 5.4: TGA/DSC profile (a) Zea mays cobs and (b) activated carbon ANN6, ANN7, and ANN8.

The TGA data collected on the raw material *Zea mays* cobs shown in figure 4a exhibited two decomposition distinct stages; the 1st stage is at a range of 210 to 260°C and the 2nd stage between 350 to 370°C. the heat flow through the raw material exhibited exothermal and endothermal flow. The first endothermic phase at 100°C and the second at 360°C after which the heat flow was uniform throughout up to 1000°C with the highest exothermal phase at 352°C with 0.70mW/mg. The material decomposition was up to 85% mass loss at 1000°C. ANN6 sample material (Figure 5.4b) exhibited three decomposition stages; the 1st and 2nd between 45 to 114°C and the third stage at 286 to 298°C and the mass loss as shown in Table 5.3. The heat flow through ANN6 exhibited endothermic and exothermic flow (Figure 5.4b). The ANN7 and ANN8 sample materials exhibited two distinct similar decomposition stages. These are consistent with that of ANN6 for the first and second stages. Stage one and stage two decomposition may be due to organic volatile materials and moisture which was trapped after activation processes. The heat flow through the three materials exhibited the same trend with endothermic at 106°C and peak exothermic at around 351°C and 0.91mW/mg.

Table 5.3: TGA/DSC material decomposition of the raw material and activated carbon samples

Decomposition stages	**Mass fraction (%) lost at different stages**			
	Raw material	**ANN6**	**ANN7**	**ANN8**
I	10.4	2.1	2.5	2.5
II	63	10.9	23.7	26.1
III		16.4	-	-
At 1000°C	15.3	67.1	49.3	43.8

To determine the porosity and the specific surface area (SSA) of the *Zea mays* derived activated carbon, the BET measurement was performed on the materials as shown in

Figure 5.5. The N_2 adsorption-desorption isotherm was performed to calculate the pore volume and specific surface area as shown in Table 5.4 for the three samples. The isotherms of the samples show type I isotherm with micropores, and the hysteresis loop is mainly caused by the mesoporous structure (X. Xie et al., 2020). The hysteresis loop at a relative pressure from 0.4 to 0.9P/Po in the adsorption-desorption isotherms mainly because of the presence of mesopores with the formation of interparticle condensation of N_2 at >0.9P/Po. The calculated SSA for ANN8 exhibited the highest value of 1443.94m^2/g with a total pore volume of 0.7915cm^3/g. The samples ANN7 and ANN6 exhibited the SSA of 972.65 and 461.36m^2/g with a total pore volume of 0.5310 and 0.2464cm^3/the respectively as shown in Table 5.4. Figure 5.5b exhibited a pore size distribution of the three samples with an average mean pore diameter of 6.39, 7.71, and 7.91nm for ANN6, ANN7, and ANN8, respectively (M. Liu et al., 2020). The high surface area and averagely smaller pores result in suitability for electrode materials for energy storage systems as its morphology can induce fast charge transfer which also contributes to an EDLC formation of surface interfaces for the electrode surfaces and electrolyte ions (Murugesan Rajesh et al., 2020)(M. Liu et al., 2020)(Hsiao et al., 2020).

Table 5.4: The pore characteristics of ANN6, ANN7, and ANN8 activated carbon samples

Sample	**S_{BET} (m^2/g)**	**S_{mic} (m^2/g)**	**S_{mic}/S_{BET} (%)**	**S_{ext} (m^2/g)**	**V_{micro} (cm^3/g)**	**V_{meso} (cm^3/g)**	**V_{total} (cm^3/g)**	**V_{mic}/V_{tot} (%)**
ANN6	461.36	385.66	83.6	75.71	0.1889	0.05749	0.2464	76.7
ANN7	972.65	689.28	70.87	460.76	0.3628	0.1682	0.5310	68.3
ANN8	1443.94	1000.89	69.30	383.05	0.5167	0.27485	0.7915	65.3

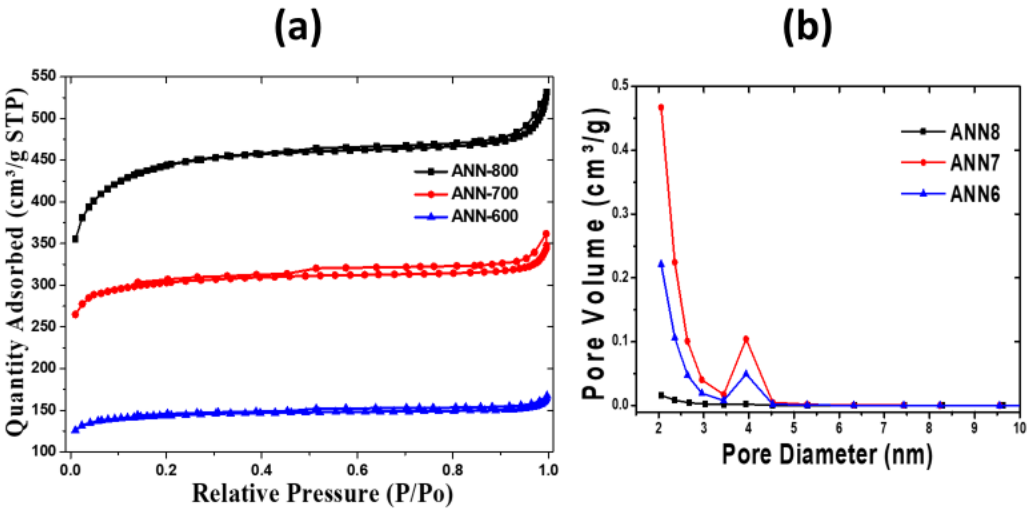

Figure 5.5: (a) N_2 adsorption-desorption isotherms and (b) Pore size distribution of the activated carbon samples.

5.3.2. Electrochemical characterization of materials

The performance of as-prepared electrode materials was first tested in the three-electrode system using 6M KOH as the electrolyte. The CV curves for ANN6, ANN7, and ANN8 at a scan rate of 10mV/s is shown in Figure 5.6a. Sample ANN7 exhibited a slight discharge hump near 0.8V due to some redox pseudo-capacitance of the functional groups. All the CV curves exhibited a quasi-rectangular-like shape throughout the scanning range showing the good performance of EDLC (Ji et al., 2019)(Y. Chen et al., 2019). The GCD curves for all the materials as shown in Figure 5.6b indicated an isosceles triangular shape for the GCD profile carried at 0.25A/g. This confirmed the dominant EDLC behavior for the electrode material. Using the discharge time at different current densities, the specific capacitance was determined using equation one for the three samples as shown in Figure 5.6c. The highest specific capacitance of ANN6, ANN7, and ANN8 are 537.27F/g at 0.5A/g, 517.47F/g at 0.5A/g, and 389.73.73F/g at 0.25A/g

respectively. The other GCD plot for the samples exhibited the same V-shape at different current density as shown in Figure S2 (Appendix 2).

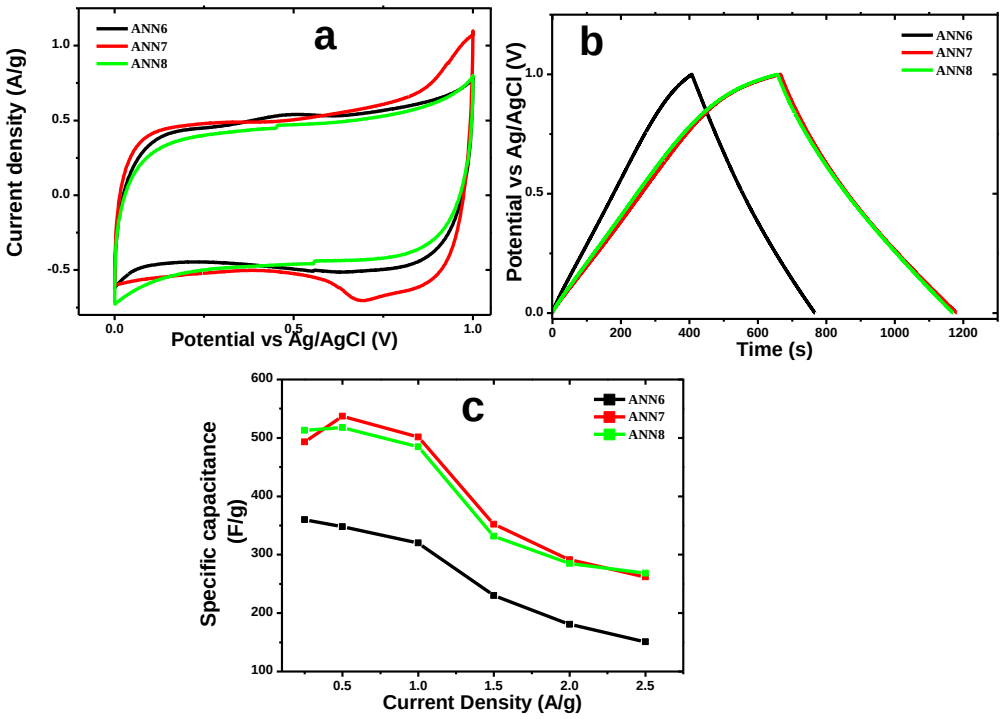

Figure 5.6: (a) CVs at a scan rate of 10mV/s, (b) GCD carried at a current density of 0.25A/g, (c) specific capacitance with different current densities of ANN6, ANN7, and ANN8 activated carbon samples.

The samples exhibited a good specific surface area that matches performance. The performance is also influenced by the possible interaction of electrolyte ions and good porous surfaces of the materials and the heteroatomic function groups on the surface wettability. The sheet-like structure of the materials as shown in Figure 5.1 exposes the active sites for complete interface interaction for electrode surfaces and electrolyte ions. The results are comparable with the results reported in the literature (D. Juan et al., 2020; R. Li et al., 2020; M. Liu et al., 2020; Lokhande et al., 2019).

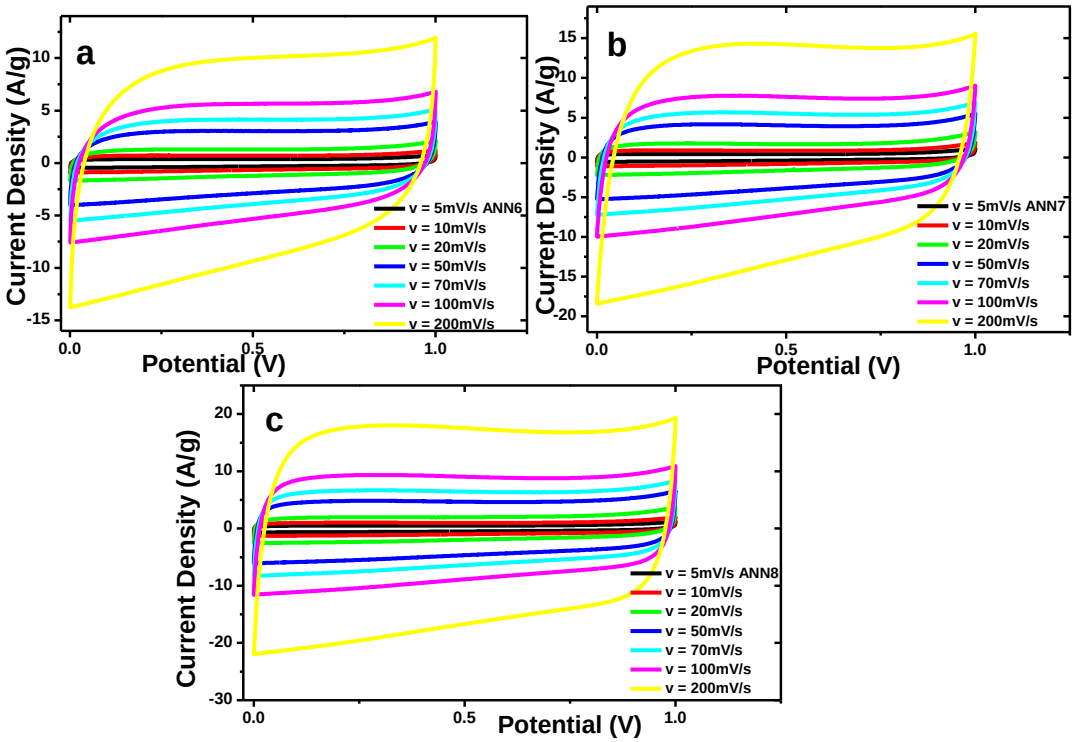

Figure 5.7: CV curves for (a) ANN6, (b) ANN7, and (c) ANN8 carbon samples at different scan rates.

To evaluate objectively the electrochemical (EC) properties of the synthesized materials which include specific capacitance, energy density, power density, and stability were determined. The as-prepared materials were evaluated with the two-electrode configuration system. The CV was carried out at different scanning rates from 5mV/s to 200mV/s with a potential range from 0 to 1.0V exhibiting quasi-rectangular shapes as shown in Figure 5.7. The GCD of the materials was evaluated at different current densities from 0.25 to 2.5A/g depicting V-shapes as shown in Figure 5.8. The CV and GCD curves evaluated in the two-electrode system shown no significant changes in shapes compared to those for the three-electrode system as shown in Figure 5.6(a & b). The CV for the as-prepared electrode materials in Figure 5.7 all show similar quasi-rectangular shapes. The ANN6 (Figure 5.7a) exhibited a redox reaction at the lower and upper potentials. This

behavior was also depicted in the ANN7 sample (Figure 5.7b) but with fewer redox peaks. This may be due to the reversible redox reaction between the functional groups mainly originating from quinone or carbonyl (R) functional groups with the electrolyte as illustrated in the equation below;

$$R - C_X - O \; + \; H^+ \; + \; e^- \quad \leftrightarrow \quad R - C_X - OH$$

The ANN8 sample exhibited quasi-rectangular shapes without causing the faradaic process. This may be to the uniform porosity in the ANN8 sample as shown in Figure 5.1(ANN8) which is different from others. All the sample materials showed identical shapes at even higher rates of 200mV/s without distorting the shapes by indicating the high stability of the materials. This also implies that the materials have excellent charge-discharge character (J. Liu et al., 2016; Zequine et al., 2016). The exhibited symmetrical rectangular shapes indicated better performance than most reported results in the literature (Y. Chen et al., 2019; Ji et al., 2019; D. Juan et al., 2020; Nguyen et al., 2020). The CVs after stability exhibited less or no exponential for the faradaic process indicating no pseudo-capacitance after holding the electrode materials at the high potential for a total of 130h as shown in Figure S3(a-f) (Appendix 2) at a scan rate of 5mV/s.

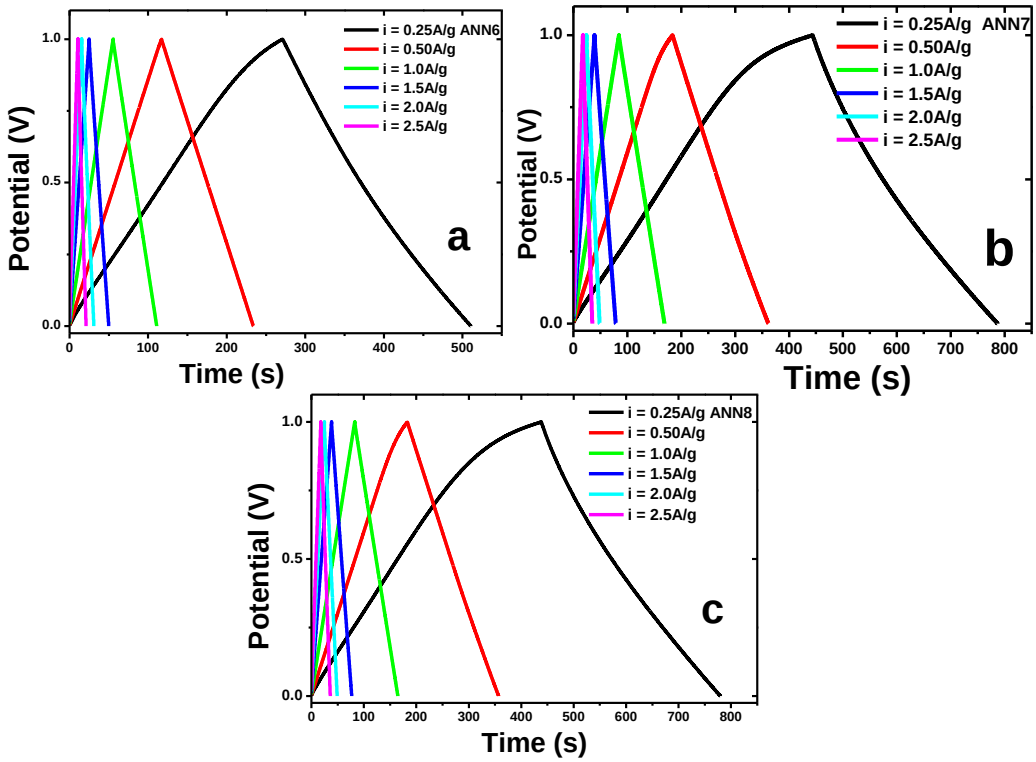

Figure 5.8: GCD curves for (a) ANN6, (b) ANN7, and (c) ANN8 carbon samples at different current densities.

The GCD at different specific current was carried out to examine the specific capacitance performance of the materials with the two-electrode system configuration. The GCD curves exhibited almost symmetrical triangular V-shapes indicating a typical character for good EDLC properties as shown in Figure 5.8. This indicates a no faradaic process in the materials which usually leads to poor stability performance. The GCD features correspond very well with the CV performance in Figure 5.7. There was consistency in the charge-discharge character for the three-electrode system (Figure 5.6b) and the two-electrode configuration. The electrochemical (EC) evaluation for specific capacitance was estimated by equation (5.2) for ANN6, ANN7, and ANN8 materials considering the mass loading of the two electrodes as total mass (Kigozi, Koech, et al., 2020; Murugesan Rajesh et al., 2020). There was a variation in the calculated specific capacitance values

of the devices as shown in Figure S4a (Appendix 2) with the applied current densities. The ANN7 sample material exhibited a maximum specific capacitance of 358.66F/g at 0.5A/g. The specific capacitance of the assembled devices decreased with the increasing current densities for all sample materials (Figure S4a Appendix 2). this mainly due to limited electrolyte ion transfer and limited interaction at the interface of the electrode at higher current density (Raj et al., 2017). The ANN8 exhibited a maximum specific capacitance of 347.76F/g at 0.5A/g current density. Also, ANN6 presented its highest specific capacitance of 241.28F/g 0.25A/g current density.

The energy density and the power density of the assembled devices were calculated according to equations (5.3) and (5.4) respectively as presented in the Ragone plot shown in Figure S4b (Appendix 2) for all the sample materials. The device assembled from ANN7 presented the highest energy density of 12.45 Wh/kg for a current density of 0.5A/g with a corresponding power density of 250 W/kg. This result is comparable and even higher than the symmetric assembled EDLC supercapacitors (SCs) reported in the literature (Hsiao et al., 2020; Inal & Aktas, 2020; Malothu et al., 2020; Murugesan Rajesh et al., 2020). The ANN6 sample material exhibited an energy density of 8.38 Wh/kg for a power density of 125 W/kg at a current density of 0.25A/g. The ANN8 sample material also presented an energy density of 12.08 Wh/kg with a corresponding power density of 250 W/kg at 0.5A/g current density. The energy density is approximately the same as that of the ANN7 sample which can further be tested for commercial application of different supercapacitors.

The electrochemical impedance spectroscopy (EIS) was performed on all sample materials to determine the resistive behavior of the electrode materials for supercapacitor application. The EIS was determined in the frequency range from 10 kHz to 10 mHz at a

potential of 10mV. The Nyquist plot of the sample materials is shown in Figure 5.9 with the zoomed at high frequency in the insert and Figure S5 (Appendix 2) to expose the semicircle. The small semicircles at the real axis indicate low charge transfer resistance (R_{CT}) at the sample interface hence leading to high electrochemical performance (Kigozi, Koech, et al., 2020). The ANN7 sample material shown an R_{CT} of 2.5Ω as the highest resistance with ANN6 and ANN8 exhibiting an R_{CT} of 1.1 and 1.3Ω respectively. The vertical behavior at low frequency with the imaginary axis indicates low diffusion of the ion into the pores of the electrode materials shown in Figure 5.9. This suggests high cycling stability and the ideal capacitive performance of the materials. The sample materials were also tested at 20mV to check the behavior of the plots at higher potential as shown in Figure S5 (Appendix 2). This suggested a similar behavior at high frequency with a small variation at a lower frequency. This indicates that at higher potential, there is a slight ion diffusion into the sample pores.

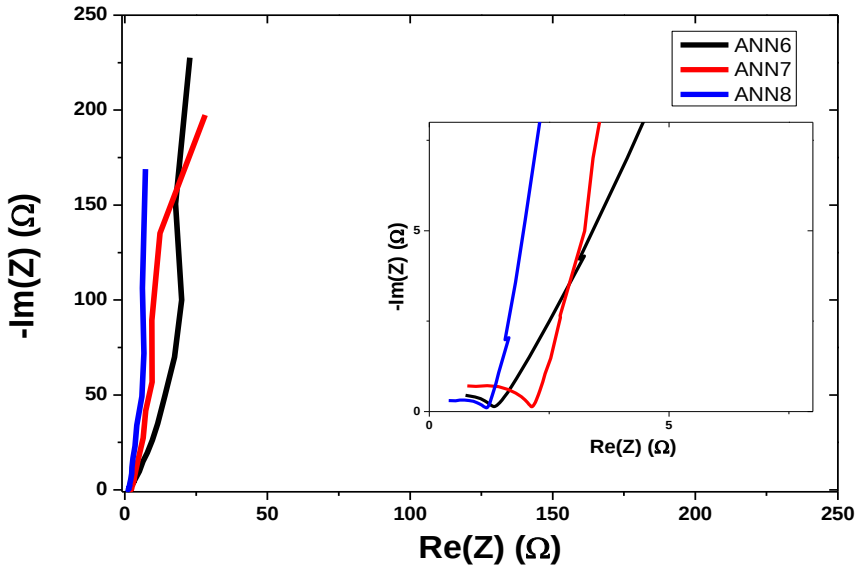

Figure 5.9: Figure EIS for ANN6, ANN7, and ANN8 activated carbon scanned at 10mV, Insert is the zoomed high frequency.

The stability test of the as-prepared devices was evaluated using the voltage holding / floating method. The three sample materials exhibited almost no degradation for the electrochemical performance of the devices showing uniform behavior as shown in Figure S7 (Appendix 2). The stability was carried out by holding the assembled device at a maximum potential of 1.0V for 10h after every three charge-discharge cycles repeated for 130h at 0.5A/g. The capacitance of the assembled devices remained almost constant throughout 130h with no main decrease with increased time and cycling. This indicates that there was uniform wettability throughout the electrode/electrolyte ion interaction and there were no trapped ions in the pores of the large porosity of the as-prepared electrode material (Tarimo et al., 2020b). The SCs showed excellent stability with 99% retention of the initial specific capacitance value even after 130h holding. This excellent stability of the assembled devices is attributed to the existence of the microporous nature of the prepared sample material that keeps the uniform wettability and easy access of electrolytic ion movement. The self-discharge test was carried out on the assembled devices after voltage holding to determine the life span. In the test, the device was fully charged to a maximum potential of 1.0V at 0.5A/g then hold for 5 min before undergoing a self-discharge in an open circuit. Figure S8 (Appendix 2) exhibited an immediate drop for ANN6 sample material and lost 70% of the potential within 20 min. ANN7 and ANN8 shown a linear drop of potential losing 70% approximately after 4h and 3 h respectively. The potential drop may be due to the decomposition of water used in the electrolyte at higher potential since ionic strength depends on the electrolyte and the water splitting requires a minimum potential difference of approximately 1.23V.

Conclusion

The *Zea mays* (maize) cobs derived porous carbon (ANN) was successfully optimized at different temperatures using KOH as the activation agent with a ratio of 1:4 under the nitrogen atmosphere. The activated porous carbon exhibited a remarkable increase in specific surface area, high porosity at increasing temperature. The sample materials showed optimum surface functional groups of oxygen base and resulted in excellent electrochemical performance and excellent stability for the supercapacitor application. The samples exhibited 99% stability for more than 130h of repeated maximum voltage holding. The symmetric assembled device of ANN7 with 5M KOH electrolyte in a two-electrode configuration system shown a maximum specific capacitance of 358.66F/g with an energy density of 12.45 Wh/kg at 0.5A/g and capacitance retention of 99% for 130h of repeated voltage floating. This research showed that an increase in temperature of activation of activated carbon from biomass has notable improvement in the electrochemical performance of supercapacitors. Also, the activated carbon from *Zea mays* cobs with an appropriate activation agent can give better-performing electrode materials for various supercapacitor applications using 700^{o}C as optimum temperature.

Supplementary information (Appendix 2)

REFERENCES

Ashraf, C. M., Anilkumar, K. M., Jinisha, B., Manoj, M., Pradeep, V. S., & Jayalekshmi, S. (2018). Acid washed, steam Activated, coconut shell derived carbon for high power supercapacitor applications. *J. Electrochem. Soc*, *165*, A900–A909. https://doi.org/10.1149/2.0491805jes

Barzegar, F., Khaleed, A. A., Ugbo, F. U., Oyeniran, K. O., Momodu, D. Y., Bello, A., Dangbegnon, J. K., & Manyala, N. (2016). Cycling and floating performance of symmetric supercapacitor derived from coconut shell biomass. *AIP Advanced*, *6*(115306), 9. https://doi.org/10.1063/1.4967348

Bello, A., Barzegar, F., Madito, M. J., Momodu, D. Y., Khaleed, A. A., Olaniyan, O., Masikhwa, T. M., Masikhwa, Dangbegnon, J. K., & Manyala, N. (2017). Floating of PPY Derived Carbon Based Symmetric Supercapacitor in Alkaline Electrolyte. *E C S Society, The Electrochemical*, *75*(24), 1–12. https://doi.org/10.1149/07524.0001ecst

Chen, W., Hu, C., Yang, Y., Cui, J., & Liu, Y. (2016). Rapid synthesis of carbon dots by hydrothermal treatment of lignin. *Materials*, *9*(3). https://doi.org/10.3390/ma9030184

Chen, Y., Jing, C., Fu, X., Shen, M., Li, K., Liu, X., Yao, C., Zhang, Y., Yao, K. X., Jing, C., Fu, X., Shen, M., Li, K., Liu, X., Zhang, Y., & Yao, K. X. (2019). Synthesis of porous NiCoS nanosheets with Al leaching on ordered mesoporous carbon for high-performance supercapacitors. *Chemical Engineering Jounal*. https://doi.org/10.1016/j.cej.2019.123367

Elmouwahidi, A., Esther, B.-G., Agustin, F. P.-C., Francisco, J. M.-H., & Francisco, C.-M. (2017). Activated carbons from KOH and H3PO4-activation of olive residues and its application as supercapacitor electrodes. *Electrochimica Acta*, *229*, 219–228. https://doi.org/10.1016/j.electacta.2017.01.152

Hsiao, C., Lee, C., & Tai, N. (2020). Biomass-derived three-dimensional carbon framework for a flexible fibrous supercapacitor and its application as a wearable smart textile. *RSC Advances*, *10*, 6960–6972. https://doi.org/10.1039/c9ra07441d

Inal, I. I. G., & Aktas, Z. (2020). Applied Surface Science Enhancing the performance of activated carbon based scalable supercapacitors by heat treatment. *Applied Surface Science*, *514*(January), 145895. https://doi.org/10.1016/j.apsusc.2020.145895

Ji, L., Wang, B., Yu, Y., Wang, N., Zhao, J., Wang, B., Yu, Y., Wang, N., & Zhao, J. (2019). N, S co-doped biomass derived carbon with sheet-like microstructures for supercapacitors. *Electrochemica Acta*, *19*. https://doi.org/10.1016/j.electacta.2019.135348

Juan, D., Zhang, Y., Wu, H., Hou, S., & Chen, A. (2020). N-doped hollow mesoporous carbon spheres by improved dissolution-capture for supercapacitors. *Carbon*, *156*, 523–528. https://doi.org/10.1016/j.carbon.2019.09.091

Kigozi, M., Kali, R., Bello, A., Padya, B., Kalu-uka, G. M., Wasswa, J., Jain, P. K., Onwualu, P. A., & Dzade, N. Y. (2020). Modified Activation Process for Supercapacitor Electrode Materials from African Maize Cob. *Materials*, *13*(5412), 1–21. https://doi.org/10.3390/ma13235412

Kigozi, M., Koech, R. K., Kingsley, O., Ojeaga, I., Tebandeke, E., Kasozi, G., & Onwualu, P. A. (2020). Synthesis and characterization of graphene oxide from locally mined graphite flakes and its supercapacitor applications _ Elsevier Enhanced Reader.pdf. *Results in Materials*, *100113*. https://doi.org/10.1016/j.rinma.2020.100113

Li, R., Zhou, Y., Li, W., Zhu, J., & Huang, W. (2020). Structure Engineering in Biomass-Derived Carbon Materials for Electrochemical Energy Storage. *Research AAAS*, *2020*(8685436), 27. https://doi.org/10.34133/2020/8685436

Lijuan, H., Peng, Y., Feng, W., Peng, S., JinJun, L., & Zizheng, L. (2017). Tubular activated carbons made from cotton stalk for dynamic adsorption of airborne toluene. *Journal of The Taiwan Institute of Chemical Engineers*, *80*, 399–405. https://doi.org/10.1016/j.jtice.2017.07.029

Lim, W. C., Srinivasakannan, C., & Balasubramanian, N. (2010). Activation of palm shells by phosphoric acid impregnation for high yielding activated carbon. *Journal of Analytical and Applied Pyrolysis*, *88*, 181–186. https://doi.org/10.1016/j.jap.2010.04.004

Lin, Y., Chen, Z., Yu, C., & Zhong, W. (2020). Electrochimica Acta Facile synthesis of high nitrogen-doped content , mesopore-dominated biomass-derived hierarchical porous graphitic carbon for high performance supercapacitors. *Electrochem. Soc. 148 (2001) A149.*, *334*, 135615. https://doi.org/10.1016/j.electacta.2020.135615

Liu, B., Liu, Y., Chen, H., Yang, M., & Li, H. (2017). Oxygen and nitrogen co-doped porous carbon nanosheets derived from Perilla frutescens for high volumetric performance supercapacitors. *Journal of Power Sources*, *341*, 309–317. https://doi.org/10.1016/j.jpowsour.2016.12.022

Liu, J., Deng, Y., Li, X., & Wang, L. (2016). Promising Nitrogen-Rich Porous Carbons Derived from One-Step Calcium Chloride Activation of Biomass-Based Waste for High Performance Supercapacitors. *ACS Sustainable Chemistry and Engineering*, *4*(1), 177–187. https://doi.org/10.1021/acssuschemeng.5b00926

Liu, M., Li, W., Ruan, S., & Fei, Y. (2020). N - doped Hierarchical Mesoporous Carbon from Mesophase Pitch and Polypyrrole for Supercapacitors. *Energy and Fuels*, *34*, 5044–5052. https://doi.org/10.1021/acs.energyfuels.0c00176

Lokhande, P. E., Chavan, U. S., & Pandey, A. (2019). *Materials and Fabrication Methods for Electrochemical Supercapacitors : Overview* (Issue 0123456789).

Lu, H., & Zhao, X. (2017). Biomass-derived carbon electrode materials for supercapacitors. *Sustainable Energy Fuels*, *1*, 1265–1281. https://doi.org/10.1039/C7SE00099E

Malothu, R. U., Nanaji, K., Narasinga, T. R., & Suresh, A. D. (2020). Corn husk derived activated carbon with enhanced electrochemical performance for high-voltage supercapacitors. *Journal of Power Sources*, *471*(December 2019), 228387. https://doi.org/10.1016/j.jpowsour.2020.228387

Moyo, B., Momodu, D., Fasakin, O., Dangbegnon, J., & Manyala, N. (2018). materials Electrochemical analysis of nanoporous carbons derived from activation of polypyrrole for stable supercapacitors. *Energy Materials*, *53*, 5229–5241. https://doi.org/10.1007/s10853-017-1911-y

Muzaffar, A., Ahamed, M. B., Deshmukh, K., & Thirumalai, J. (2019). A review on recent advances in hybrid supercapacitors: Design, fabrication and applications. *Renewable and Sustainable Energy Reviews*, *101*(July 2018), 123–145. https://doi.org/10.1016/j.rser.2018.10.026

Nguyen, T. N., Le, P. A., & Phung, V. B. T. (2020). Facile green synthesis of carbon quantum dots and biomass-derived activated carbon from banana peels : synthesis and investigation. *Biomass Conversion and Biorenery*. https://doi.org/10.1007/s13399-020-00839-2

Peng, L., Liang, Y., Dong, H., Hu, H., Zhao, X., Cai, Y., Xiao, Y., Liu, Y., & Zheng, M. (2018). Super-hierarchical porous carbons derived from mixed biomass wastes by a stepwise removal strategy for high-performance supercapacitors. *Journal of Power Sources*, *377*(December 2017), 151–160. https://doi.org/10.1016/j.jpowsour.2017.12.012

Qiu, X., Wang, L., Zhu, H., Guan, Y., & Zhang, Q. (2017). Lightweight and efficient microwave absorbing materials based on walnut shell-derived nano-porous carbon. *Nanoscale*, *9*(22), 7408–7418. https://doi.org/10.1039/c7nr02628e

Raj, C. J., Rajesh, M., Manikandan, R., Sim, J. Y., Yu, K. H., Park, S. Y., Song, J. H., & Kim, B. C. (2017). Two-Dimensional Planar Supercapacitor Based on Zinc Oxide/Manganese Oxide Core/Shell Nano-architecture. *Electrochimica Acta*, *247*, 949–957. https://doi.org/10.1016/j.electacta.2017.07.009

Raj, C. J., Rajesh, M., Manikandan, R., Yu, K. H., Anusha, J. R., Ahn, J. H., Kim, D. W., Park, S. Y., & Kim, B. C. (2018). High electrochemical capacitor performance of oxygen and nitrogen enriched activated carbon derived from the pyrolysis and activation of squid gladius chitin. *Journal of Power Sources*, *386*(December 2017), 66–76. https://doi.org/10.1016/j.jpowsour.2018.03.038

Rajesh, M., Manikandan, R., Kim, B. C., Park, S., Cho, W.-J., Yu, K. H., & Raj, C. J. (2020). Pinecone biomass-derived activated carbon : the potential electrode material for the development of symmetric and asymmetric supercapacitors. *Energy Research*, *March*, 1–15. https://doi.org/10.1002/er.5548

Shafeeyan, M. S., Wan, M. W. A., Houshmand, A., & Shamiri, A. (2010). A review on surface modification of activated carbon for carbon dioxide adsorption. *Journal of Analytical and Applied Pyrolysis*, *89*(2), 143–151. https://doi.org/10.1016/j.jaap.2010.07.006

Sudhan, N., Subramani, K., Karnan, M., Ilayaraja, N., & Sathish, M. (2017). Biomass-derived activated porous carbon from rice straw for a high-energy symmetric supercapacitor in aqueous and nonaqueous electrolytes. *Energy and Fuels*, *31*(1), 977–985. https://doi.org/10.1021/acs.energyfuels.6b01829

Tarimo, D. J., Oyedotun, K. O., Mirghni, A. A., Sylla, N. F., & Manyala, N. (2020). High energy and excellent stability asymmetric supercapacitor derived from sulphur-reduced graphene oxide/manganese dioxide composite and activated carbon from peanut shell. *Electrochimica Acta*, *353*. https://doi.org/10.1016/j.electacta.2020.136498

Van, K. Le, Thuy, T., & Thi, L. (2014). Activated carbon derived from rice husk by NaOH activation and its application in supercapacitor. *Progress in Natural Science: Materials International*, *24*(3), 191–198. https://doi.org/10.1016/j.pnsc.2014.05.012

Wang, C. H., Wen, W. C., Hsu, H. C., & Yao, B. Y. (2016). High-capacitance KOH-activated nitrogen-containing porous carbon material from waste coffee grounds in supercapacitor. *Advanced Powder Technology*, *27*(4), 1387–1395. https://doi.org/10.1016/j.apt.2016.04.033

Wang, J., Li, Q., Peng, C., Shu, N., Niu, L., & Zhu, Y. (2020). To increase electrochemical performance of electrode material by attaching activated carbon particles on reduced graphene oxide sheets for supercapacitor. *Journal of Power Sources*, *450*(December 2019), 227611. https://doi.org/10.1016/j.jpowsour.2019.227611

Wei, H., Wang, H., Li, A., Li, H., Cui, D., Dong, M., Lin, J., Fan, J., Zhang, J., Hou, H., Shi, Y., Zhou, D., Guo, Z., Wang, H., Li, A., Li, H., Cui, D., Dong, M., Lin, J., … Guo, Z. (2019). Advanced porous hierarchical activated carbon derived from agricultural wastes toward high performance supercapacitors. *Alloys and Compounds*. https://doi.org/10.1016/j.jallcom.2019.153111

Xie, X., Wu, D., Wu, H., Hou, C., Sun, X., Zhang, Y., Yu, R., Zhang, S., Wang, B., & Du, W. (2020). Dielectric parameters of activated carbon derived from rosewood and corncob. *J Mater Scie: Mater Electron*, 8. https://doi.org/10.1007/s10854-020-04358-8

Yang, J., Xiang, F., Guo, H., Wang, L., & Niu, X. (2020). Honeycomb-like porous carbon with N and S dual-doping as metal- free catalyst for the oxygen reduction reaction. *Carbon*, *156*, 514–522. https://doi.org/10.1016/j.carbon.2019.09.087

Zequine, C., Ranaweera, C. K., Wang, Z., Singh, S., Tripathi, P., Srivastava, O. N., Gupta, B. K., Ramasamy, K., Kahol, P. K., Dvornic, P. R., & Gupta, R. K. (2016). High per formance and flexible supercapacitors based on carbonized bamboo fibers for wide temperature applications. *Scientific Reports*, *6*(August), 1–10. https://doi.org/10.1038/srep31704

Zhao, H., Lu, X., Wang, Y., Sun, B., Wu, X., & Lu, H. (2017). Effects of additives on sucrose-derived activated carbon microspheres synthesized by hydrothermal carbonization. *Journal of Materials Science*, *52*(18), 10787–10799.

https://doi.org/10.1007/s10853-017-1258-4

CHAPTER SIX

6.0. Hydrothermal synthesis of metal oxide composite cathode materials for high energy application: $NaFe_2O_3$-GO composite

6.1. Introduction

Up to date, energy storage and high energy is still the main concern in the use of electronic devices. Several electronic gadgets have been developed to simplify day-to-day life but there is still a challenge for high energy storage and excellent stability. As the technology of energy harvest and generation advances, also the high energy storage needs to improve at the same rate. The cathode materials have a huge role to play in the advancement of high energy density storage devices. Several methods have been employed to obtain different materials composition for high energy. Among those various methods, the hydrothermal synthesis method is considered more effective because of its ease of operation, simplicity of design among others. Some methods tried like Sol-gel (Nankya et al., 2020), solid-state (Fang et al., 2006; B. Zhang et al., 2007) and co-precipitation (J. Feng et al., 2013; Gu et al., 2014) methods suffer in several drawbacks which include high costs, poor composition, control of morphology, low purity additions like milling calcination among other challenges. Hydrothermal synthesis is one of the common methods used for the synthesis of highly performing materials for cathode high energy application.

Hydrothermal synthesis (HS) is a method of material synthesis of composites that depends on the solubility of the starting materials in hot water at high temperature and high pressure. HS method mainly is categorized as crystal growth/synthesis of material under high pressure and high temperature in the presence of aqueous or non-aqueous

solvents. The solvent is used to recrystallize and dissolve the substances which are insoluble under normal conditions (Byrappa, 2005; Byrappa & Yoshimura, 2001). HS methods have moderate cost, excellent composition control, very good control of morphology with high purity, and no additional steps.

HS is usually carried at low temperatures and a long operation time is required to obtain crystalline materials. When HS is performed at near or supercritical water conditions gives a promising property of the materials due to the properties of the solvents at high temperatures. The starting materials are usually insoluble under normal pressure and temperature. The temperature conditions of the crystal formation are predetermined by the ionic solubility which ranges between 250 to 350^{o}C. This method is a heterogeneous reaction process that involves inorganic materials and an aqueous / non-aqueous system (Hayashi & Hakuta, 2010). HS is used in both super liquiphobic and superhydrophobic coating of materials. The method produces crystalline materials with roughness on the surface because of high temperature and high pressure.

The advantageous side of the HS method is the ability to form an unstable crystalline phase at the melting point. Also, the method is good for the production of a large crystal with a controlled composition (Sonawane et al., 2018). The HS method can be carried out in two conditions (i) Conventional conditions, (ii) Supercritical water conditions. The aqueous solution I heated below 374^{o}C at 218atm, its conversion, and when it's above it's supercritical as shown in figure 3. The supercritical water condition is advantageous for multi-metal oxide composite. This enhances the reaction 1000 times more than the conventional HS condition. HS supercritical gives low dielectric constant and high crystalline products. This is due to the change of properties like dielectric constant, solubility among others under supercritical conditions. The dielectric constant of water

decreases with a decrease in pressure and an increase in temperature. The low dielectric constant enhances the reaction towards partial formation (Hakuta et al., 2003). The particle size formation from the HS method is dependent on the solubility of the metal oxide and the rate of hydrolysis. The subcritical and supercritical systems can be varied to achieve a controlled solvent field in nucleation and crystallization for the particle formation. The HS can be carried out in a batch or flow reaction system. The hydrothermal crystal growth leads to material production of fine to ultra-fine crystals and bulk single crystals. The metal oxide composite from HS has several advantages which include homogeneity and high purity product, metastable compounds, crystal symmetry, lower sintering temperature, narrow particle size distribution, single-step synthesis, simple equipment, low energy processing, wide chemical composition range, dense powder nanoparticle with a low range size distribution, low solubility particles, polymorphic growth of particle modification and short/fast reaction period (Byrappa & Yoshimura, 2013; Wu et al., 2020). HS can obtain small and uniform particle sizes which are an influence to improved electrochemical performance (Wu et al., 2020). The representative sample which was prepared with the HS batch system is shown in comparison with the literature. The hydrothermal synthesis method is simple in implementing and scale-up production. This allows the control of particle size and improvement of the properties but can cause some nano aggregation of nanoparticles.

The objective of this chapter is to provide a new and improved way to enhance the properties of different materials for cathode high energy density, discharge capacity, and different operating conditions. The chapter further focuses on the stability of imparting materials by increasing the performance even after prolonged storage. Also provides an electrochemical performance material synthesized by the hydrothermal method. This

introduces the field of hydrothermal materials synthesis and demonstrates the understanding of the effect of solution thermodynamics of the aqueous medium for hydrothermal nanocomposite processes.

6.2. Hydrothermal Synthesis (HS) apparatus

The HS process requires a pressure vessel that can contain a highly corrosive solvent at high pressure and high temperature. The autoclave apparatus must be able to operate routinely at extended temperature-pressure conditions. The autoclaves used are also called pressure vessels, reactors, autoclaves, or high-pressure bomb reactors. The HS apparatus should have the following properties;

i. Easy to assemble and dissemble
ii. Innerness to bases, acids, and redox agents
iii. Lined well to bear high temperature and high pressure for a longer period
iv. Well-sealed and leak-proof that can handle high temperature and high pressure
v. Baffle volume which can contain the required temperature gradient

The apparatus is designed from different materials such as stainless steel, different alloys, thick glass, thick quartz among other materials that can fulfill the properties of resisting high temperature, and high-pressure routine operations. Most of the autoclaves are lined with an inert material and resist routine operations like Teflon, borosilicate glass among others (Nostrand, 2006).

6.3. Hydrothermal synthesis (HS) of metal oxide composite

6.3.1. Batch hydrothermal reaction system

This can be carried under conventional HS conditions or sub/supercritical conditions of aqueous or non-aqueous solvents. In the batch reaction system, Generally, the desired metal oxide is dissolved in the solvent (preferably deionized water). This is mixed with the preferred cation then the resultant solution is treated to achieve the required pH by use of a base/acid. Sonication/stirring is done to form a uniform solution. The resultant solution is transferred into an autoclave reactor with a liner (figure 6.1). The reactor is placed in the heating system (Oven/furnace) with a set temperature for the desired time. After the reactor is cooled, the particles collected and washed with deionized water then dried.

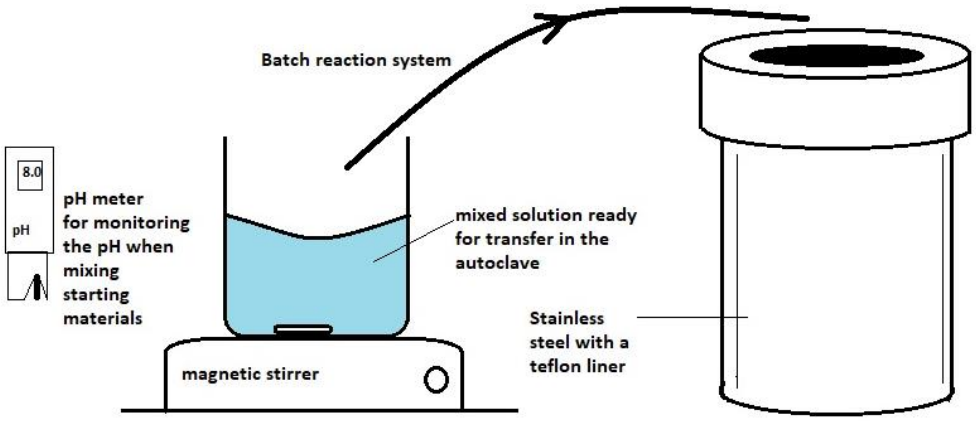

Figure 6.1: Set up a batch reaction system arrangement.

Some processes require precursors which are synthesized first using HS, then the target cation is blended mechanically followed by drying at high temperature for long hours for stable composite. The change in temperature gradually under normal HS (i.e. 100 to 140^{o}C) helps to increase the particle size from 2-4 to 7-8µm and makes the particle size uniform (Cheng et al., 2016).

In a batch system, several key parameters have to be considered for robustness and reproducibility of the materials, these include;

i. The pH of the reaction solution for the phase formation
ii. The size of the cation for the composite combination interface for structure determination
iii. The choice of the solvent which may be aqueous or non-aqueous for the required phase
iv. The required time for the completion of the reaction phase
v. The operation temperature is required for targeted phase formation

The use of different conditions and materials results in the production phase with different properties like morphology, structure, and different physiochemical properties. The preparation of different materials composite under batch reactor systems are described in Table 6.1 below. Table 6.1 shows the phase product, starting materials, conditions of synthesis, and the product particle size.

Table 6.1: Phase product synthesis using batch hydrothermal reaction systems

Phase product	**Starting materials**	**Operation conditions**	**Particle size (nm)**	**Reference**
$LiNi_{0.2}Mn_{1.5}O_4$	LiOH, Na_2CO_3, $NiCl_2$, $MnSO_4$	100-180^oC, 12h	8000	(Cheng et al., 2016)
$V_2O_5/Ni_{1/3}Co_{1/2}Mn_{1/3}O_2$	$CoSO_4.7H_2O$, $NiSO_2.6H_2O$, $MnSO_4.H_2O$, $NaCO_3$, SDBS	170^oC, 12h	0.2 – 1.4	(M. Yuan et al., 2019)
Mn_3O_4-NG	GO, $(CH_3COO)_2Mn$ hydrazine	180^oC, 12h	-	(Park et al., 2014)
VO_2-CNT-G	NH_4VO_3, GO, HCOOH	180^oC, 48h	100	(Nethravathi et al., 2012)

$NH_4V_3O_8$-CNT	NH_4VO_3, CNT	180°C, 48h	0.5 – 0.8	(L. X. Yuan et al., 2011)
$LiMnPO_4$	$Na_2S.9H_2O$, $MnSO_4.H_2O$, $Li_2SO_4.H_2O$, $NH_4H_2PO_4$	200°C, 10h	100	(Pan et al., 2013)
$LiFePO_4$	$FeSO_4.7H_2O$, H_3PO_4, LiOH, $C_{19}H_{42}BrN$	120°C, 5h	90-100	(Qin et al., 2010) (Meligrana et al., 2006)
$(NH_4)_2V_6O_{16}$	NH_4VO_3, HCOOH	120°C, 48h	170	(Jiang et al., 2020)
N-GO-Fe_2O_3	RGO, Fe_2O_3, $C_3N_3(NH_2)_3$	180°C, 12h	50 - 100	(Pu et al., 2018)
$Mn_3(PO_4)_2$	$MnCl_2.4H_2O$, KH_2PO_4, $CO(NH_2)_2$	120°C, 1h	47600	(Katkar et al., 2020)
Mn_3O_4-GO	$MnCl_2$, GO	180°C, 10h	-	(F. Gao et al., 2020)
Fe_3O_4-Sucrose	$FeCl_3$, NH_3. H_2O, sucrose	18O°C, 48h	16	(X. Sun et al., 2009)
NVOPF@TiO_{2-x}	NH_4VO_3, NaF, $NaH_2PO_4{\cdot}2H_2O$	170°C,8h	5.5	(P. Du et al., 2020)
$Na_3V_2O_{2x}(PO_4)_2F_{3-2X}$(MWCNT)	MNWCNT, VO_5F, Na_3V_2PO4	18O°C 8h	1500	(P. R. Kumar et al., 2015)
$K_2Ti_6O_{13}$	$Ti(OC_3H_7)_4$ KOH	350-450°C 48h	12.5-20.1	(Yahya et al., 2001)
$Mg_{3.5}H_2(PO_4)_3$	$M_gCl_2{\cdot}6H_2O$, $K_4P_2O_7$, HCl	400°C, 2h	20-500	(Assaaoudi et al., 2008)
$CuAlO_2$	$Cu(NO_3)_2{\cdot}3H_2O$, $Al(NO_3)_3{\cdot}9H_2O$, HCOOH, NaOH	400°C, 0.5h	5000	(Sato, Sue, Tsumatori, et al., 2008)
$Y_3Al_5O_{12}$(YAG/E_U)	$Y(NO_3)_3{\cdot}6H_2O$, $Al(NO_3)_3{\cdot}9H_2O$ $Eu(NO_3)_3{\cdot}6H_2O$, KOH	400°C, 2h	3000	(Yoon et al., 2006)

$KTiNbO_5$	$Ti(OCH_3H_7)_4$, Nb_2O_5,KOH	350°C, 20h	3000	(Sue et al., 2006)
$CoFe_2O_4$	$Co(NO_3)_2 \cdot 6H_2O$, $Fe(NO_3)_3.9H_2O$ LiOH, KOH, NaOH	390°C, 5h	5	(D. Zhao et al., 2006)
Zn_2SiO_4/Mn	$Zn(NO_3)_2$, SiO_2, KOH, $Mn(NO_3)_2$	4OO, ½ h	2000	(Takesue et al., 2007)(Takesue et al., 2010)
Li $Ni_{0.8}$ $Co_{0.15}Al_{0.05}O_2$ nanosphere	$NiSO_4 \cdot 6H_2O$, $CoSO_4 \cdot 7H_2O$, $Al_2(SO_4)_3 \cdot 16H_2O$, SiO_2HNS	120°C,10h	20	(Wu et al., 2020)
$LiFePO_4$	PEG, Li_2CO_3, $FeC_2O_4.2H_2O$, $NH_4H_2PO_4$	500°C, 12h	-	(Y. Zhang et al., 2012)
α-Zn_2SiO_4/Mn^{2+}	Mn^{2+} ion, $ZnSO_4$, SiO_4	400°C, 281atm, 1h	2000 - 9000	(Takesue et al., 2007)

To improve the properties of the metal oxide composite, some synthesizes include organic surfactant compounds. These dispersing agents are possibly used to modify the structure of the crystallites of the materials. The starting materials are mixed in a stoichiometric ratio to form a solution. Some materials perform better in composite due to the poor properties of these individual materials. Metal oxides like iron oxide have poor conductivity and degradation at high current and high charge transfer resistance in the materials. The composite of iron oxide and graphene combination is synthesized to overcome the poor conductivity challenge (Jibrael et al., 2015; Pu et al., 2018; X. Wang et al., 2014). The preparation of $LiFePO_4$ with the HS method tends to give plank shapes mainly. These shapes have disadvantages in the physicochemical properties of the material which results in low energy density. The HS preparation of $LiFePO_4$ involves the use of organic surfactants to avoid the formation of plank shapes. Wang et al (Y.

Zhang et al., 2012) synthesized $LiFePO_4$ using PEG as a carbon source rheological phase reaction as shown in table 1 under the Argon atmosphere. This resulted in uniform particles with a discharge capacity of 162mAh/g. Xu et al (H. Xu et al., 2015) also prepared $LiFePO_4$ using $C_6H_8O_6$ as a reducing agent at 500^oC. This resulted in a capacity of 167mAh/g at a 0.1C rate and was found to be higher than Wang et al (Y. Wang et al., 2015). This means that the synthesis of $LiFePO_4$ with the HS method gives a good material structure at higher temperatures in a combination of reducing agents to avoid the formation of plank shapes with doping as another way to improve the electronic conductivity and electrochemical properties of the materials (Y. Zhang et al., 2012).

The Batch system is the commonest HS technique for high crystalline powder /composites and synthesis of a large single particle. The batch system has a challenge of the long period needed for heating up to the required temperature and cooling down steps required for a given reactor volume. Centrally to batch, the flow reaction system is the upcoming promising technique for the synthesis of nanosized metal oxide composite particles. The flow rection system has rapid heating and cooling controls which takes a shorter time than batch when using continuous operation conditions

6.3.2. Flow hydrothermal reaction system

This is the continuous synthesis of nanoparticles under temperature and high pressure. This is the advancement of hydrothermal technology to deal with reaction at a higher temperature and higher pressure near or above a critical point. The nanoparticle materials using supercritical fluids like supercritical CO_2 or supercritical water as solvent/fluid for the reaction system. In the flow hydrothermal synthesis, the starting materials are prepared by dissolution in water of equimolar concentration. These solutions are pumped

in a mixer at a stoichiometric flow rate. The transformation is done at different pressures and temperatures close to critical or at supercritical conditions as shown in Figure 6.2.

The supercritical hydrothermal operation with water as a solvent is known to be highly suitable for nanoparticles synthesis which includes metal oxide composite. The HS under supercritical condition through a flow reactor, the aqueous metal salt solutions as starting materials are first prepared then fed into solution containers ready for pumping. The system also contains a steam/distilled water pressurized electric heating furnace to heat above the required reaction point. These are fed in the reactor under rapid heating and high pressure resulting in a short contact time. The solution leaves the reaction point and is rapidly quenched with the cooling system then sent to the filtration system to separate the particles. Also, the pressure after the reaction is regulated by backpressure controllers. The fine synthesized particles are collected in the effluent. The supercritical hydrothermal flow reaction system has several advantages which include; synthesis of required nanoparticle sizes, shapes, and composition in the shortest residence time (Byrappa & Yoshimura, 2013).

Table 6.2: Phase product synthesis using flow hydrothermal reaction systems

Phase Product	**Starting materials**	**Operation conditions**	**Av particle size (nm)**	**Reference**
$LiCoO_2$	$LiNO_3$, $CoSO_4$	382 – 387^oC, 226 – 230atm, 1 – 10ml/min	500	(Anikeev, 2010)
CeO_2	$Ce(NO_3)_3$	373 – 391^oC, 260atm, water flow rate 1 - 10ml/min, reactant flow 2 -3ml/min	≈100	(Anikeev, 2010)

Ga_2O_3	$Ga(NO_3)_3{\cdot}8H_2O$	365 – 384°C, 235atm, water flow rate 1 - 10ml/min, reactant flow 2ml/min	2 - 5	(Anikeev, 2010)
$LiMn_2O_4$	$Mn(NO_3)_2{\cdot}6H_2O$, $LiNO_3$, LiOH	400 – 420°C, 296atm, 10 – 40s	≈ 100	(J. H. Lee & Ham, 2006)
Tetragonal/Cubic/ $BaTiO_3$	TiO_2, EtOH, $Ba(OH)_2$	330 – 400°C, 158 – 296atm, 2 – 3min	10-100	(Elissalde et al., 2005; Reverón, C. Aymonier, et al., 2005; Reverón, Elissalde, et al., 2005)
$CoFeO_4$	$Fe(NO_3)_3$, NaOH, $CO(NO_3)_2$	202 – 402°C, 247atm, 11 – 23s	13 - 23	(Cote et al., 2003)
$Ca_{0.8}Sr_{0.2}Ti_xFe_xO_3$	$Sr(NO_3)_3$, $Fe(NO_3)_3$, $Ca(NO_3)_2$, TiO_2 sol	300 – 400°C, 296atm, 10s	20 - 30	(J. Lu et al., 2008)
$Y_{2.7}Tb_{0.3}Al_5O_{12}$	KOH, $Tb(NO_3)_3$, $Y(NO_3)_3$, $Al(NO_3)_3$	400°C, 296atm	14 - 152	(Hakuta et al., 2003)
Cubic $(Y, Eu)_2Al_5O_{15}$	$Y(NO_3)_3$, $Al(NO_3)_3$, $Eu(NO_3)_3$, KOH	400°C, 276atm	≈ 100	(In et al., 2007)
Y-AlOOHY-Al_2O_3	$Al(NO_3)_3$, KOH	400°C, 296 – 395atm	20	(Sato, Sue, Akiyama, et al., 2008)
Rhombohedra / Cubic / Tetragonal $(Ni, Cu, Zn)Fe_2O_4$	KOH, $Cu(NO_3)_2$ $Zn(NO_3)_2$, $Ni(NO_3)_4$ $Fe(NO_3)_3$	400°C, 296atm	22	(Sato, Sue, Suzuki, et al., 2008)

Cubic Ba ZrO_3	$ZrO(NO_3)_2$, $Ba(OH)_2$, NaOH, $Ba(NO_3)_2$ $Ba(CH_3\ CO_2)_2$	450 -485°C, 296atm	≈100	(Aimable et al., 2008)
Hexagonal / cubic $Ni(OH)_2Co_xNi_{1-x}(OH)_2$, $NiCo_2O_4$	$Co(NO_3)_2$, $Ni(NO_3)_2$, $Ni(CH_3CO_2)_2$, H_2O_2, KOH	90 – 310°C, 238atm	≈100	(Boldrin et al., 2007)
Cubic $Y_2Al_5O_{12}$	Al(ACAC), Y-acetate, $Al(NO_3)_3$, $Y(NO_3)_3$	260 – 385°C, 237atm	≈150	(Cabanas et al., 2007)
Cubic/Tetragonal $Ce_xZr_{1-x}O_2$	NH_4OH, $ZrO(NO_3)_2$, $ZrO(NO_3)_2$	374 – 400°C, 218 – 296atm	7 -16	(J. . Kim et al., 2007)

The flow reaction system (Figure 6.2) has two main additional features to that of the batch reaction system, these include; (i) Immediate change in the reaction medium dielectric constant leading to the high-density formation of homogeneous nucleation (ii) the reaction taking a very short time (less than a minute) that can overturn growth of crystals and aggregation, hence continuous and rapid synthesis of single particle-sized metal oxide composite with definite shape and relatively medium size distribution formation. The formation of particle size and crystallinity is based mainly on the metal oxide composite solubility and their supersaturation. The trend of some metal oxide solubility determines the particle formation (Anikeev, 2010). For example, as the solubility decreases, the conversion increases in the order ZrO_2 > Fe_2O_3AlOOH/Al_2O_3 > NiO > CuO. The solubility is generally dependent on the precipitation rate. The coloration between supersaturation and average particle size is generally known in the theory of nucleation tradition that the increasing supersaturation tends to decrease the particle size. The

supersaturation beyond the factor of 10^4 was found to be enough for the formation of a particle under 10nm. Low supersaturation causes slower precipitation which becomes a good condition for intermediate products to be stable (Hayashi & Hakuta, 2010).

The use of KOH in some composition tends to cause a decrease in particle size and may be attributed to the solubility decrease. When the supersaturation is high, it causes a large driving force for precipitation. This prevents the occlusion of water molecules in the precipitates (Sue et al., 2006). The reaction operation condition to mention is; solvents, time, temperature, pressure, and others play an important role in the synthesis of the metal oxide composite particles.

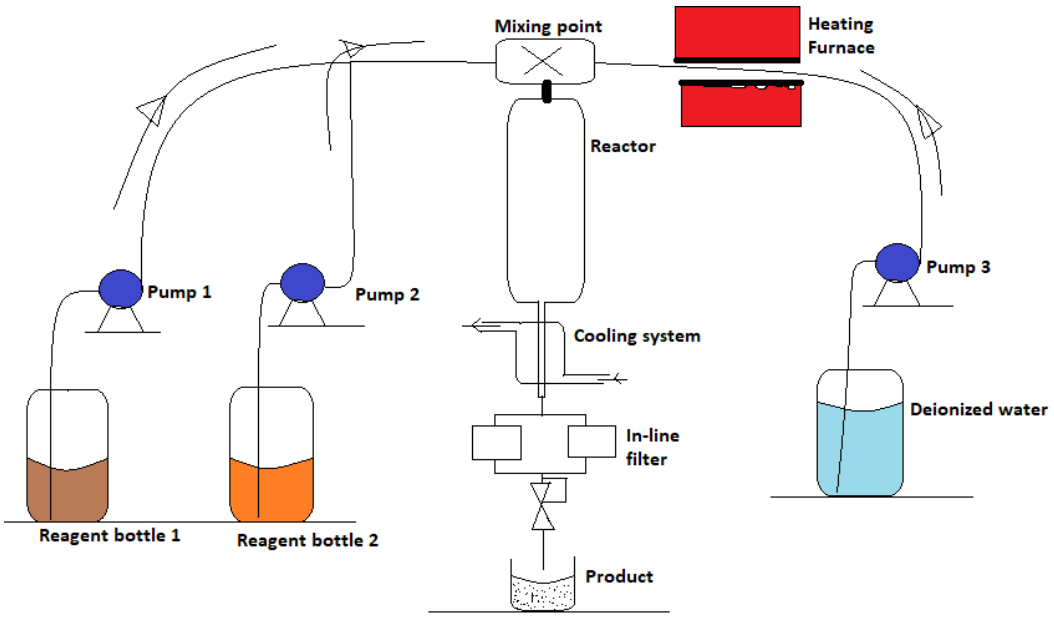

Figure 6.2: Flow chart for the flow reaction system (from (Byrappa & Yoshimura, 2013) with modification)

6.4. Metal oxide composite cathode materials for high energy density storage

Most of the cathode materials used are highly soluble in an aqueous electrolyte which causes a reduction in capacity after storage (Takeuchi & Randolph A. Leising, 1996). Most of the cathode materials have challenges of low electron conductivity and ion diffusivity (X. Yang et al., 2018). To handle the challenges, doping can be used to improve the rapid mobility of the lithium-ion through heteroatoms. The challenge can also be overcome by the coating of materials with active compounds (T. Chen et al., 2018)(BS Liu et al., 2018). Using metal oxide composite can help to reduce the solubility of the cathode materials at a high energy density state(W. Liu et al., 2018). The metal oxide composite like Fe_2O_3-Graphene provides high gravimetric energy density and high voltage capacity delivery as shown in the representative results. This makes metal oxide composite stable for cathode electrode materials at increased energy density. The stable cathode composite materials are prepared by reaction and chemical addition using different metal oxides and other compositions (Z. Liu et al., 2018)(JC Chen et al., 2019). The materials produced by HS have improved electrochemical behavior with increasing energy density, reduced delay in voltage, and discharge capacity when using high rates of application at high temperatures. These materials also give high utility and reliability for long storage in the electrochemical application. This provides high current capacities and high open-circuit voltage (Takeuchi & Randolph A. Leising, 1996).

When the target cations are small in size like Na^+, Li^+, NH_4^+, Ag^+ ions among others, are used in the matrix for the metal oxide composite, these cations can go through the open structure to allow the tunnels to be readily mobile and permits the intercalation within the matrix. The metal oxide composites supported on different precursors have special

interest due to their morphology dispersity and surface metal concentration. These lead to the mobility and intercalation of the electrolyte.

Research and fabrication of high cathode materials for high energy density is the way to promote other devices like Na-battery large scale application. More effort has been directed towards the fabrication of high energy density materials using specific materials to mention; rGO-MnO_2 (Kong et al., 2014), $MnCo_2O_4$ (Shanbhag et al., 2017), G-Mn_3O_4 (F. Gao et al., 2020), RGO-Mn_3O_4 (H et al., 2010), $Mn(CH_3COO)_2$-GO (L et al., 2012), $MnSO_4$-GO (G et al., 2016). Others exploring different materials like layered transition metal oxide (C.-Y. Yu et al., 2015), polyanion $NaV_2O_{2x}(PO_4)_2F_{3-2x}$ ($0 \leq X \leq 1$) (W. Li et al., 2018). Also, metal phosphates are widely involved in high energy density materials for lithium-ion batteries and other energy applications. The use of Ni in a composite can improve the capacity of the material (XR Li et al., 2018), cobalt is another element mainly for the stabilization of layered structural materials (P. Hou et al., 2017; HH Zhang et al., 2016) reported stability of LNCA ($LiNi_{0.8}Co_{0.15}Al_{0.05}O_2$) by changing the aluminium concentration at the interface of electrolyte/electrode interaction. The combination of cobalt and aluminium-doped composite is used to improve the oxidation and reduction process of Ni^{2+} which promotes the cycling stability of the material (Y. Kim & D, 2012; Natarajan et al., 2018) A combination of different metals and metal oxides is advantageous for ternary synergistic effects. LNCA composite is one of the materials considered as a promising cathode nanoparticle for high energy for lithium battery applications (T. Chen et al., 2018; Mukherjee et al., 2018; Zheng JC, Yang Z, He ZJ, Tong H, Yu WJ, 2018). LNCA has a theoretical specific capacity of 279mAh/g (Wu et al., 2020). Also, graphene can be used in the composite as adsorbent, photo-sensitizer, photo-stabilizer, or conductive support which help to improve the property material due

to the special functions and properties like photocatalyst, and cocatalyst in the nanocomposites

6.5. Solvents under hydrothermal synthesis (HS)

Water as a liquid in its normal temperature and pressure conditions is a strong universal polar solvent. This makes water a very virtuous solvent for inorganic salts like metallic salts and complexes but a very poor solvent for organic compounds. When the conditions are changed, like high temperature (374°C) and high pressure (218atm), which converts water to supercritical having a single-phase between liquid and vapor as shown in Figure 6.3. This collapses the polarity property of water to be as low as non-polar turning the solubility to be suitable for organic compounds and composite.

Hydrothermal synthesis can be performed under the aqueous or non-aqueous system. The properties of solvents change with the change in pressure and temperature which makes the reaction process change. The density of water and other properties change when the pressure and temperature are varied as shown in Table 6.3. The supercritical water as shown in Figure 6.3, gives a favourable condition for the reaction towards the particle formation. The synthesis under supercritical water also reduces the concentration of the alkaline in the process of particle growth. This supercritical reaction due to its properties like dielectric constant, viscosity, and solubility with several compounds. When the compounds are soluble in a supercritical solvent, the properties of those materials change drastically. Hiromichi et al (Hayashi & Hakuta, 2010) prepared $KNbO_3$ powder using supercritical water with a low concentration of KOH and Potassium niobite. The structure of the prepared $KNbO_3$ had rhombohedral and orthorhombic structural materials. This powder showed a promising application in non-linear optical devices. Goh *et al* (Goh et

al., 2002) prepared $KTaO_3$ crystals under supercritical conditions. The materials exhibited a morphology of $KTaO_3$ crystals in rectangular shapes with different particle sizes ranging from 10 – 100nm. These $KTaO_3$ can also be achieved on the $SrTiO_3$ substrate under supercritical conditions. When using supercritical conditions for metal oxide composite, it reduces the processing energy of the synthesis of a highly crystalline structure. The α-Zn_2SiO_4/Mn^{2+} are among particles that can be synthesized under supercritical conditions as in Table 6.1. This can be used to replace the commercial process of Mn-doped zinc silicate phosphate which requires a high temperature above 1000^oC and a long time to produce the required regular shapes (Takesue et al., 2007, 2008, 2010). The supercritical conditions can also be used to produce dense Zn_2SiO_4 particles in a short time because of the reaction medium which occurs at a higher pressure than the normal HS.

Table 6.3: The properties of water at different temperature and pressure (adapted from (Loppinet-Serani et al., 2010)

Properties	**Ambient water**	**Supercritical water**	**Superheated steam**
Temperature (^oC)	25	450	450
Pressure (atm)	1.0	272	13.6
Dielectric constant	78	1.8	1.0
Viscosity (Pa.s)	$8.90x10^{-4}$	$2.98x10^{-4}$	$2.65x10^{-7}$
Effective diffusion coefficient (cm^2/s)	$7.74x10^{-6}$	$7.67x10^{-4}$	$1.79x10^{-3}$
Density (g/cm^3)	0.998	0.128	0.00419
Solubility of O_2 (mg/l)	8	infinity	infinity

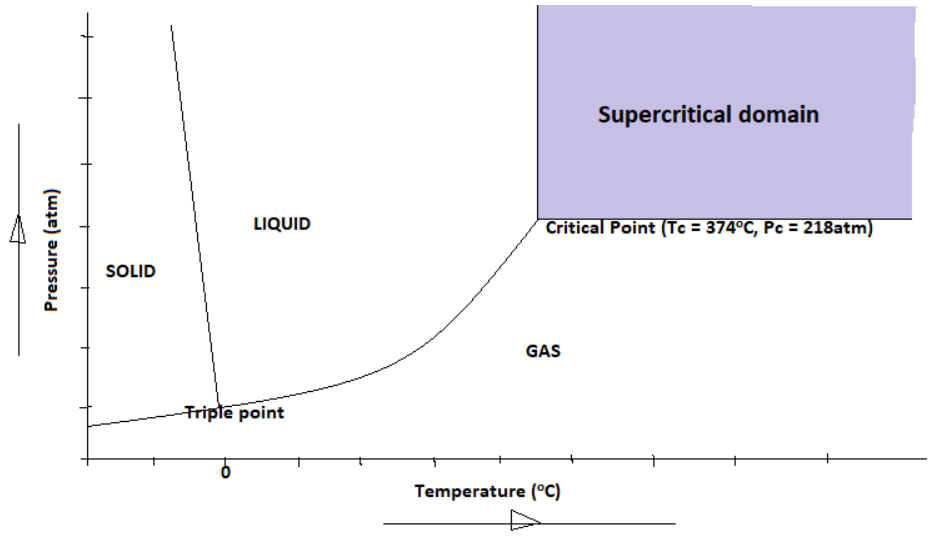

Figure 6.3: Illustration of Pressure-temperature phase diagram of pure water showing supercritical domain (from (Loppinet-Serani et al., 2010) with modifications).

6.6. Hydrothermal synthesis of $NaFe_2O_3$-GO

6.6.1. Experiment

In the synthesis of $NaFe_2O_3$-GO, the GO was synthesized by modified Hummer's method from graphite flakes as used by Kigozi et al (Kigozi, Koech, et al., 2020) 2.0 g of graphite flakes was added to a mixture of sulphuric acid and phosphoric acid (H_2SO_4/H_3PO_4) solution prepared by a volume ratio of 9:1 (180:20 ml) incessant stirring in the ice bath for 2 h. Then 7.3 g of potassium permanganate ($KMnO_4$) was slowly added to the mixture while keeping the temperature below 10°C under unremitting stirring for 2 days. After 2 days, 90 ml of distilled water was slowly introduced to the mixture with rapid stirring and the mixture changed dark brown with suspensions, 7.0 ml of hydrogen peroxide (H_2O_2) and 55 ml of distilled water was introduced for the conversion of manganese oxide (MnO_2) and residual permanganate into soluble manganese sulphate ($MnSO_4$). The mixture changed to yellow colour with particle suspensions. The material was cleaned

several times with 150 ml of 3% warm hydrochloric acid (HCl) and deionized water until pH 7.0 then filtered and dried using a vacuum oven at 40^{o}C for 18h.

The $NaFe_2O_3$-GO was synthesized by a batch hydrothermal method with starting materials which included ferric nitrate ($Fe(NO_3)_3$), sodium hydroxide (NaOH), and graphite oxide. The starting was dissolved in 100ml of deionized water, mixed, and sonicated for 30 minutes. The solution was transferred into a stainless-steel autoclave with a Teflon liner. The reactor was heated in an oven at 180^{o}C for 24hours. This followed natural cooling. The material was filtered, washed, and dried at 80^{o}C for 15h. The resultant sample was named $NaFe_2O_3$-GO. The sample was tested for energy storage applications for sodium battery applications (Wu et al., 2020).

6.6.2. Characterization and testing of $NaFe_2O_3$-GO

The material was characterized by FESEM/EDX, XRD, and electrochemical systems. The morphological characterization of the samples was done with the Field Emission Scanning Electron Microscope (FESEM) 9GeminiSEM 500M/s Carl ZEISS-EDAX Z2 Analyser AMETEK). The crystal structure of the powder sample was carried out by the X-Ray Diffraction (Riguku Smartlab Autosampler) by the use of a Cu kα radiation with the JCPDS-ICDD library database. The electrochemical analysis technique for testing the device was done on a BCS BIO-LOGIC 805 system with a half-cell electrode set up. Different techniques were used to analyse the performance with cyclic voltammetry (CV) and galvanostatic charge-discharge (GCD).

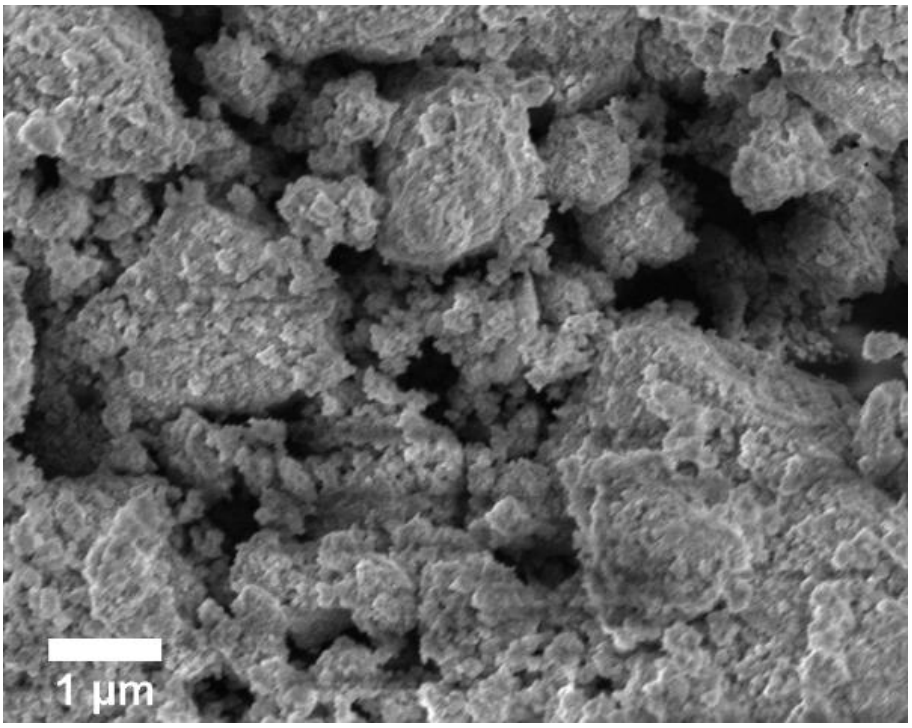

Figure 6.4: FESEM morphology for $NaFe_2O_3$-GO.

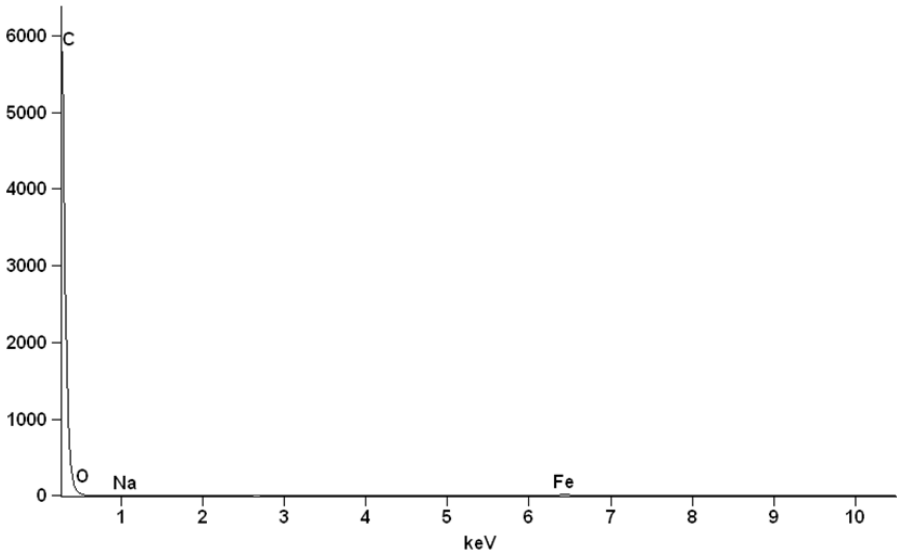

Figure 6.5: EDX profile for the $NaFe_2O_3$-GO.

The $NaFe_2O_3$-GO nanocomposite characterization with FESEM showed the morphology of particles as in Figure 6.4. The $NaFe_2O_3$-GO nanocomposite particles exhibited a compact particle with somewhat large surface areas. The surface of $NaFe_2O_3$-GO was

heavily covered with sodium and iron oxide particles. These enhance the reduction-oxidation reactions for the cathode material in the application of energy storage. The EDX was used to observe the distribution of elements in the sample as shown in Figure 6.5. This revealed a high composition of carbon and oxygen which is the main supporting structure from graphite oxide (GO). This contains sp^2 and some sp^3 hybridized carbon that give unique electrical and mechanical properties. GO have several functional groups that are involved in the reaction with an electrolyte which includes carbonyl, hydroxyl, and carboxyl which is a smart material in a composite (Y. Feng et al., 2011; Geim & Novoselov, 2007; McAllister et al., 2007).

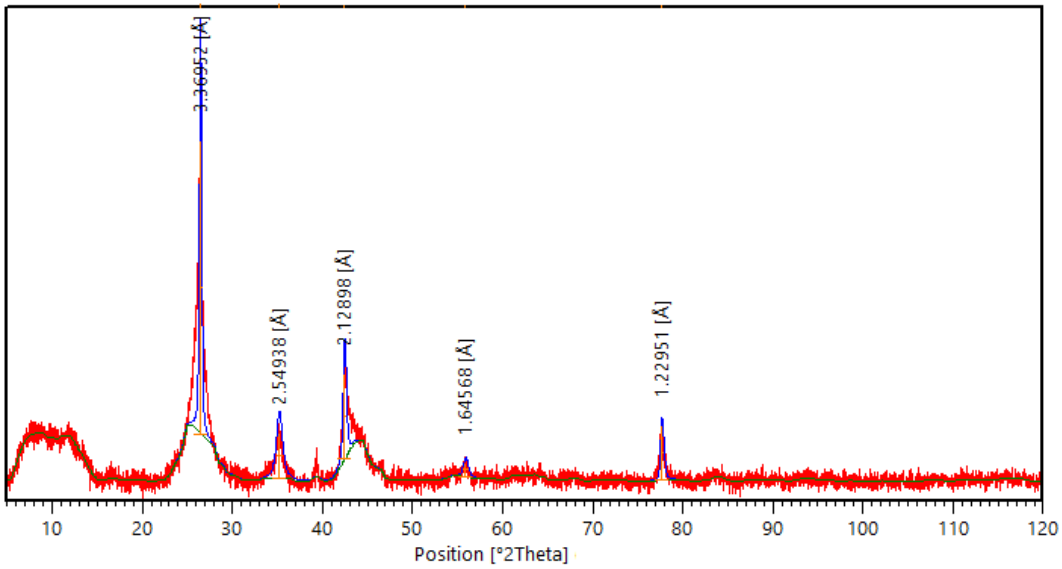

Figure 6.6: XRD profile for $NaFe_2O_3$-GO.

The crystalline structure of $NaFe_2O_3$-GO was investigated by XRD and the pattern is shown in Figure 6.6. Different strong and intense peaks are observed at different 2Theta (2Θ) positions which include; 2Θ = 10º which is assigned to the non-functionalized crystallinity of GO (Eda et al., 2008)(W. Chen et al., 2010)(Kigozi, Koech, et al., 2020), peaks at 2Θ=25º (3.36Å) and 43º (d=2.13Å) a suggestion for exfoliation of GO (Kigozi, Koech, et al., 2020), a peak at 2Θ=35º with d=2.55Å, for sodium, a peak at 2Θ=56º with

d=1.65Å and 2Θ=78° with d=1.23Å as some of the assignment for Fe_2O_3. The particle sizes were measured by Scherrer's equation with a range of 8.5 to 17.3nm.

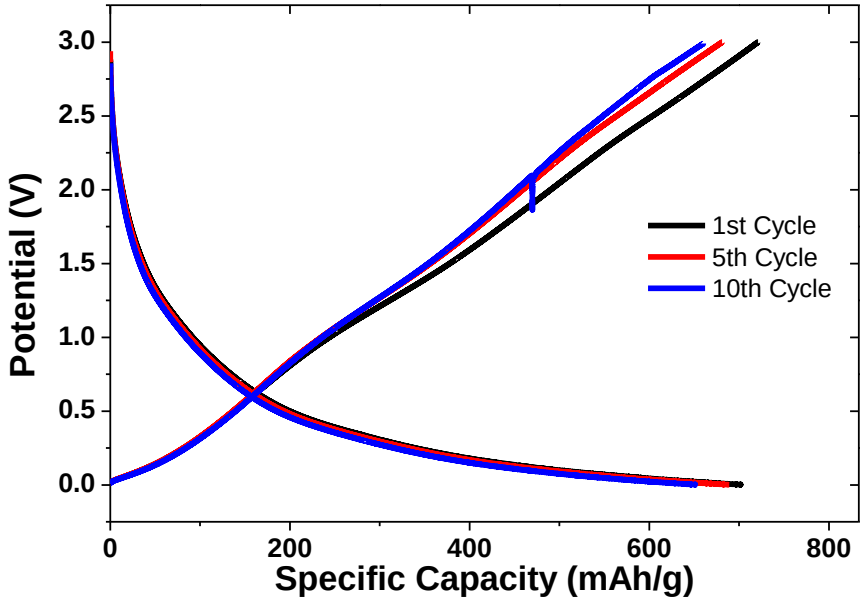

Figure 6.7: GCD profile for $NaFe_2O_3$-GO.

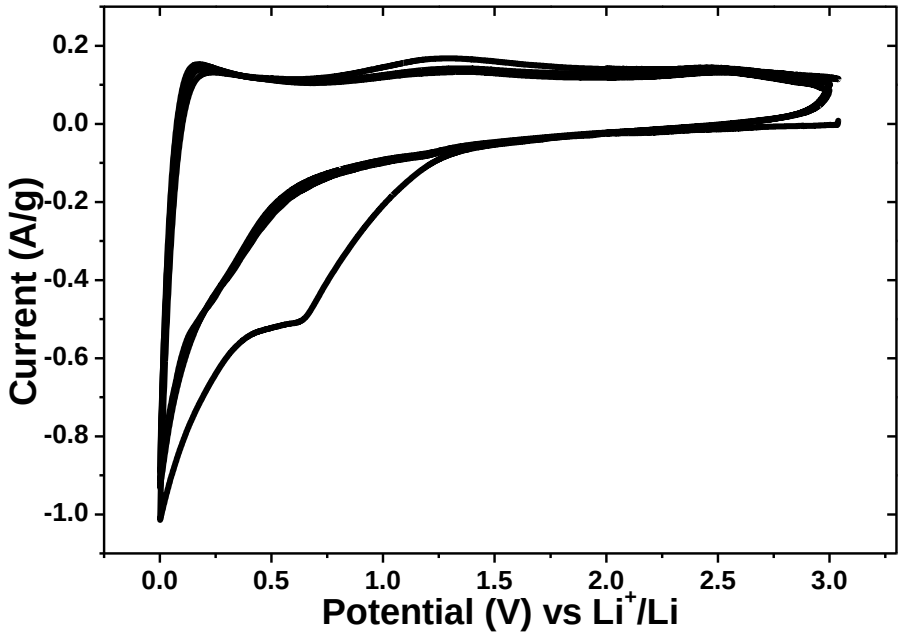

Figure 6.8: CV profile for $NaFe_2O_3$-GO.

The performance of $NaFe_2O_3$-GO nanocomposite for sodium-ion cathode material using half-cell battery was explored in a voltage range of 0.01 to 3.0V. The galvanostatic charge-discharge (GCD) was carried out with 50mAh/g. the GCD profile depicted slopes with the discharge curve from 20.5 to 0.01V in the first cycle and the performance was maintained up to the 10^{th} cycle as shown in Figure 6.7. This is a description caused by the electrolyte decomposition and the formation of a solid electrolyte interface (SEI) with a reduction. The performance of the discharge capacity was approximated to be 720mAh/g. the material composite showed a close performance throughout the cycles of the 5^{th} to 10^{th} cycle and remaining very stable. This means that the material has good electrochemical performance reversibility with good cycling performance.

The cyclic voltammetry profile of the material composite was performed at a potential range from 0.01 to 3.0V at a scan rate of 10mV/s as shown in Figure 6.8. The reduction process is shown two (2) reduction peaks in the first cathodic process at 0.75 and 0.06V. this indicates a reaction of the electrolyte with the carbon and the oxides causing decomposition of the electrolyte. In the proceeding cycles, the peaks shifted to 0.5V which may be due to electrode polarization caused by the interaction of the electrolyte with the material. The material showed similar performance to what was reported by (F. Gao et al., 2020) with the discharge capacity of 1524mAh/g with the start cycle.

The applicability of the metal oxide composite depends on the interaction of the metal and oxygen functionality that is present in the material matrix. This may degenerate in the material properties of the composite in electrical properties, carrier mobility, and the thermo-mechanical stability of the carbon/metal-based materials (Dreyer et al., 2010). Several non-metal elements have been introduced in different composites which include the GO layer to improve the electrochemical application (Ekimov et al., 2004).

6.7. The future of the hydrothermal synthesis method

The batch HS system method is one of the shared and easy synthesis methods to use in research work. The technology is used in the construction of the industrial process for large scale production and possible because supercritical conditions can be reached in reaction to massive production. The monitoring of phase formation in the system is still a challenge to help in the elucidation of nanoparticle formation. The system needs to be equipped with in-situ technology for the monitoring of the phase formation. The flow system is still uncommon in most research laboratories which makes it hard to know most of their challenges. There are challenges of material selection for fabrication which causes fatigue and fracture in the designs, face blockage, corrosion, and massive production. These causes contamination and limitation in production. The flow hydrothermal system requires fabrication materials that are highly resistant to corrosion.

Conclusions

In a search for materials for high energy density applications for batteries, different innovative nanocomposites are being investigated. This chapter highlights the use of the hydrothermal synthesis method for the uniform synthesis of metal oxide composite particles with good properties for cathode materials for high energy application. These metal oxide composites from hydrothermal methods have been demonstrated to be one of the most auspicious cathode materials for high energy density for battery application. There is a wide range of metal oxide composites synthesized for battery application. The hydrothermal synthesis of nanocomposites gains different properties to improve different challenges in the battery's applications like charge mobility, stability, degradation among others. Even though recent researches have shown significant progress in the use of a

hydrothermal method for cathode materials or high energy density, there are still some challenges for more research to explore. The use of different metal oxide matrix composites enhances high energy density, particle size, morphology, and other properties. Nevertheless, studies all over the world are rapidly making progress in the direction of the development of novel nanocomposites for high energy density and high cycling stability for batteries and hybrid. Using a hydrothermal synthesis of $NaFe_2O_3$-GO we managed to report a discharge capacity of 720mAh/g in a half-cell of sodium-ion battery application.

REFERENCES

Aimable, A., Xin, B., Millot, N., & Aymes, D. (2008). Continuous hydrothermal synthesis of nanometric BaZrO3 in supercritical water. *J. Solid State Chem*, *181*, 183–189.

Anikeev, V. I. (2010). Hydrothermal Synthesis of metal oxide nanoparticles. *Materials*, *3*(7), 3794–3817. https://doi.org/10.3390/ma3073794

Assaaoudi, H., Fang, Z., Butler, I. S., & Kozinski, J. A. (2008). Synthesis of erbium hydroxide microflowers and nanostructures in subcritical water. *Nanotechnology*, *19*, 185606.

Boldrin, P., Hebb, A. K., Chaudhry, A. A., Otley, L., Thiebaut, B., Bishop, P., & Darr, J. . (2007). Direct syntheses of nanosized NiCo2O4 spinel and related compounds via continuous hydrothermal synthesis methods. *Ind. Eng. Chem. Res*, *46*, 4830–4838.

Byrappa, K. (2005). Hydrothermal Processing. In *Kirk-Othmer Encyclopedia of Chemical Technology* (pp. 1–14). https://doi.org/10.1002/0471238961.0825041804012319.a01.pub2

Byrappa, K., & Yoshimura, M. (2001). *Handbook of Hydrothermal Technology*. Park Ridge N J.

Byrappa, K., & Yoshimura, M. (2013). *Handbook of Hydrothermal Technology* (2nd ed.). Elsevier inc.

Cabanas, A., Li, J., Blood, P., Chudoba, T., Lojkowski, W., Poliakoff, M., & Lester, E. (2007). Synthesis of nanoparticulate yttrium aluminum garnet in supercritical water-ethanol mixtures. *J. Supercrit. Fluid*, *40*, 284–292.

Chen, J., L, Z., D, J., XB, J., YM, W., QL, H., XF, X., Y, O., LM, P., WP, T., & T, L. (2019). LiNi0.8- Co0.15Al0.05O2 cathodes exhibiting improved capacity retention and thermal stability due to a lithium iron phosphate coating. *Electrochim Acta*, *312*, 179–187.

Chen, T., X, L., H, W., XX, Y., L, W., BW, D., WJ, G., & MZ, Q. (2018). The effect of gradient boracic polyaniondoping on structure, morphology, and cycling performance of Ni-rich LiNi0.8Co0.15Al0.05O2 cathode material. *J Power Sources*, *374*, 1–11.

Chen, W., Yan, L., & Bangal, P. (2010). Preparation of graphene by the rapid and mild thermal reduction of graphene oxide induced by microwaves. *Carbon*, *48*, 1146–1152.

Cheng, J., Li, X., Wang, Z., & Guo, H. (2016). Hydrothermal synthesis of LiNi0.5Mn1.5O4 sphere and its performance as High-Voltage Cathode Material for Lithium Ion Batteries. *Ceramics International*, *42*, 3715–3719. https://doi.org/10.1016/j.ceramint.2015.11.031

Cote, L. J., Teja, A. S., Wilkinson, A. P., & Zhang, Z. . (2003). Continuous hydrothermal synthesis of CoFe2O4 nanoparticles. *Fluid Phase Equilibria*, *210*, 307–317.

Dreyer, D., Park, S., Bielawaski, C., & Ruoff, R. (2010). The chemistry of graphene oxide. *Chem. Soc. Rev*, *39*, 228–240.

Du, P., Li, T., Jiang, X., Wang, D., & Zheng, X. (2020). Improving the electrochemical performance of Na3V2O2(PO4)2F cathode by using a defect-containing TiO2-x coating for sodium ion batteries. *Journal of Alloys and Compounds*, *814*, 1–10. https://doi.org/10.1016/j.jallcom.2019.152270

Eda, G., Fanchini, G., & Chhowalla, M. (2008). Large-area ultrathin films of reduced graphene oxide as a transparent and flexible electronic material. *Nat. Nanotech*, *3*, 270–274.

Ekimov, E., Sidorov, V., Bauer, E., Mel'nik, N., Curro, N., Thompson, J., & Stishov, S. (2004). Superconductivity in diamond. *Nature*, *428*, 542–545.

Elissalde, C., Reverón, H., Aymonier, C., Michau, D., Cansell, F., & Maglione, M. (2005). The ferroelectric transition temperature as an intrinsic probe for sinterednanocrystalline BaTiO3 synthesized under supercritical conditions. *Nanotechnology*, *16*, 797–802.

Fang, H.-S., Wang, Z.-X., Li, X.-H., Guo, H.-J., & Peng, W.-J. (2006). Low temperature synthesis of LiNi0.5Mn1.5O4 spinel. *Mater. Lett*, *60*, 1273–1275.

Feng, J., Huang, Z., Guo, C., Chernova, N. A., Upreti, S., & Whittingham, M. S. (2013). An organic coprecipitation route to synthesize high voltage LiNi0.5Mn1.5O4. *ACS Appl. Mater. Interfaces*, *5*, 10227–10232.

Feng, Y., Huang, S., Kang, K., & Al, E. (2011). Preparation and characterization of graphene and few-layer graphene. *New Carbon Materials*, *26*(1), 26–30.

G, W. J., D, J., R, Z., & Al., E. (2016). Highly flexible graphene/Mn3O4 nanocomposite nembrane as advanced anodes for Li-Ion batteries. *ACS Nano*, *10*(6), 6227–6234.

Gao, F., Qin, S. H., Zang, Y. H., Gu, J. F., & Qu, J. Y. (2020). Highly efficient formation of Mn3O4-graphene oxide hybrid aerogels for use as the cathode material of high performance lithium ion batteries. *Xinxing Tan Cailiao/New Carbon Materials*, *35*(2), 121–130. https://doi.org/10.1016/S1872-5805(20)60479-6

Geim, A., & Novoselov, K. (2007). The rise of graphene. *Nat. Mater*, *6*, 183–191.

Goh, G. K. L., Haile, S. M., Levi, C. G., & Lange, F. F. (2002). Hydrothermal synthesis of perovskite and pyrochlore powders of potassium tantalate. *J. Mater. Res*, *17*, 3168–3174.

Gu, Y.-J., Zang, Q.-F., Liu, H.-Q., Ding, J.-X., Wang, Y.-M., Wang, H.-F., Zhang, J., & Wei, W.-G. (2014). Characterization and electrochemical properties of LiNi0.5Mn1.5O4 prepared by a carbonate co-precipitation method. *Int. J. Electrochem. Sci*, *9*, 7712–7724.

H, W., F, C. L., Y, Y., & Al, E. (2010). Mn3O4-graphene hybrid as a high-capacity anode material for lithium ion batteries. *J Am Chem Soc*, *132*, 13978–13980.

Hakuta, Y., Haganuma, T., Sue, K., Adschiri, T., & Arai, K. (2003). Continuous production of phosphor YAG:Tb nanoparticles by hydrothermal synthesis in supercritical water. *Mater. Res. Bull*, *38*, 1257–1265.

Hayashi, H., & Hakuta, Y. (2010). Hydrothermal Synthesis of metal oxide nanoparticles in supercritical water. *Materials*, *3*(7), 3794–3817. https://doi.org/10.3390/ma3073794

Hou, P., HZ, Z., XL, D., XJ, X., & LQ, Z. (2017). Stabilizing the electrode/electrolyte interface of LiNi0.8- Co0.15Al0.05O2 through tailoring aluminum distribution in microspheres as long-life, high-rate, and safe cathode for lithium-ion batteries. *ACS Appl Mater Interfaces*, *9*(35), 29643–29653.

In, J. H., Lee, H. C., Yoon, M. J., Lee, K. K., Lee, J. W., & Lee, C. H. (2007). Syntesis of nano-sized YAG: Eu3+ phosphor in continuous supercritical water system. *J. Supercrit. Fluid*, *40*, 389–396.

Jiang, H., Zhang, Y., Pan, Z., Xu, L., Zheng, J., Gao, Z., Meng, C., Zhang, Y., Pan, Z., Xu, L., Zheng, J., Gao, Z., Hu, T., & Meng, C. (2020). Facile Hydrothermal Synthesis and Electrochemical Properties of (NH4)2V10O25·8H2O Nanobelts for High-Performance Aqueous Zinc Ion Batteries. *Electrochimica Acta*, *19*. https://doi.org/10.1016/ j.electacta.2019.135506

Jibrael, R. I., Mohammed, M. K. A., Roder, F., Braatz, R. D., Krewer, U., Sohail, M., Saleem, M., Ullah, S., Saeed, N., Afridi, A., Khan, M., Arif, M., Danner, T., Zhu, G., Hofmann, A. F., Latz, A., Chen, S. X., Tseng, K. J., Choi, S. S., … Hee, J. (2015). Graphene-based polymer nanocomposites. *Carbon*, *6*(1), 1–4. https://doi.org/10.4172/2157-7439.1000253

Katkar, P. K., Marje, S. J., Pujari, S. S., Khalate, S. A., Deshmukh, P. R., & Patil, U. M. (2020). Single-pot hydrothermal synthesis of manganese phosphate microrods as a cathode material for highly stable flexible solid-state symmetric supercapacitors. *Synthetic Metals*, *267*(February). https://doi.org/10.1016/j.synthmet.2020.116446

Kigozi, M., Koech, R. K., Kingsley, O., Ojeaga, I., Tebandeke, E., Kasozi, G., & Onwualu, P. A. (2020). Synthesis and characterization of graphene oxide from locally mined graphite flakes and its supercapacitor applications _ Elsevier Enhanced Reader.pdf. *Results in Materials*, *100113*. https://doi.org/10.1016/j.rinma.2020.100113

Kim, J. ., Myeong, W. ., & Ihm, S. K. (2007). Characteristics in oxygen strage capacity of ceria-zirconia mixed oxides prepared by continuous hydrothermal synthesis in supercritical water. *Appl. Catal. B-Environ*, *71*, 57–63.

Kim, Y., & D, K. (2012). Synthesis of high-density nickel cobalt aluminum hydroxide by continuous coprecipitation method. *ACS Appl Mater Interfaces*, *4*(2), 586–589.

Kong, L. B., Lu, C., Liu, M. C., Luo, Y. C., Kang, L., Li, X. H., & Walsh, F. C. (2014). The specific capacitance of sol-gel synthesized spinel MnCo2O4 in an alkaline electrolyte. *Electrochim. Acta*, *115*, 22–27.

Kumar, P. R., Jung, Y. H., Lim, C. H., & Kim, D. K. (2015). Na3V2O2x(PO4)2F3-2x: A stable and high-voltage cathode material for aqueous sodium-ion batteries with high energy density. *Journal of Materials Chemistry A*, *3*(12), 6271–6275. https://doi.org/10.1039/c5ta00980d

L, L., Z, G., A, D., & Al., E. (2012). Rapid microwave-assisted synthesis of Mn3O4-graphene nanocomposite and its lithium storage properties. *J Mater Chem*, *22*(8), 3600–3605.

Lee, J. H., & Ham, J. Y. (2006). Synthesis of manganese oxide particles in supercritical water. *Korean J. Chem. Eng*, *23*, 714–719.

Li, W., Zhang, F., Xiang, X., & Zhang, X. (2018). Nickel-substituted copper hexacyanoferrate as a superior cathode for aqueous sodium-ion batteries. *ChemElectroChem*, *5*, 350–354.

Li, X., X, X., Q, L., JL, W., HG, X., & H, P. (2018). Metal (M = Co, Ni) phosphate based materials for high-performance supercapacitors. *Inorg Chem Front*, *5*(1), 11–28.

Liu, B., XL, S., SH, Z., FD, Y., Y, X., Y, Z., YX, Z., & ZB, W. (2018). Investigation on electrochemical performance of LiNi0.8Co0.15Al0.05O2 coated by heterogeneous layer of TiO2. *J Alloys Compd*, *739*, 961–971.

Liu, W., HH, G., ML, Q., JY, D., L, X., S, Y., & TL, H. (2018). Effect of voltage range and BiPO4 coating on the electrochemical properties of LiNi0.8Co-0.15Al0.05O2. *ChemistrySelect*, *3*(26), 7660–7666.

Liu, Z., Z, W., TZ, L., PP, D., P, G., & YM, Z. (2018). Modification of LiNi0.8Co0.15Al0.05O2 using nanoscale carbon coating. *J Alloys Compd*, *763*, 701–710.

Loppinet-Serani, A., Aymonier, C., & Cansell, F. (2010). Supercritical water for environmental technologies. *Journal of Chemical Technology & Biotechnology*, *85*(5), 583–589.

Lu, J., Hakuta, Y., Hayashi, H., Ohashi, T., Nagase, T., Hoshi, Y., Sato, K., Nishioka, M., T., I., & Hamakawa, S. (2008). Preparation of Ca0.8Sr0.2Ti1-xFexO3-x (x = 0.1–0.3) nanoparticles using a flow supercritical reaction system. *J. Supercrit. Fluid*, *46*, 77–82.

McAllister, M., Li, J., Adamson, D., Schniepp, H., Abdala, A., Liu, J., Herrera-Alonso, M., Milius, D., Car, R., Rrud'homme, R., & Aksay, I. (2007). Single sheet functionalized graphene by graphite. *Chem. Mate*, *19*, 4396–4404.

Meligrana, G., Gerbaldi, C., Tuel, A., Bodoardo, S., & Penazzi, N. (2006). Hydrothermal synthesis of high surface LiFePO4 powders as cathode for Li-ion cells. *Journal of Power Sources*, *160*(1), 516–522. https://doi.org/10.1016/j.jpowsour.2005.12.067

Mukherjee, P., NV, F., N, P., J, C., LFJ, P., GG, A., & F, C. (2018). Surface structural and chemical evolution of layered LiNi0.8Co0.15Al0.050O2 (NCA) under high voltage and elevated temperature conditions. *Chem Mater*, *23*, 8431–8445.

Nankya, R., Opar, D. O., Kim, M., Paek, S., & Jung, H. (2020). Synergetic effect of nitrogen and sulfur co-doping in mesoporous graphene for enhanced energy storage properties in supercapacitors and lithium-ion batteries. *Journal of Solid State Chemistry*, *289*(May), 121451. https://doi.org/10.1016/j.jssc.2020.121451

Natarajan, S., SB, M., V, S., P, H., & R, G. (2018). Infrared spectroscopy signatures of aluminum segregation and partial oxygen substitution by sulfur in LiNi0.8Co0.15Al0.05O2. *ACS Appl Energy Mate*, *1*(6), 2536–2545.

Nethravathi, C., Viswanath, B., Michael, J., & Rajamath, M. (2012). Hydrothermal synthesis of a monoclinic VO 2 nanotube-graphene hybrid for use as cathode material in lithium ion batteries. *Carbon*, *50*(13), 4839–4846. https://doi.org/10.1016/j.carbon.2012.06.010

Nostrand, V. (2006). *Hydrothermal Processing*. Science Encyclopedia John Wiley and Sons.

Pan, X. L., Xu, C. Y., Hong, D., Fang, H. T., & Zhen, L. (2013). Hydrothermal synthesis of well-dispersed LiMnPO4 plates for lithium ion batteries cathode. *Electrochimica Acta*, *87*, 303–308. https://doi.org/10.1016/j.electacta.2012.09.106

Park, S. K., Jin, A., Yu, S. H., Ha, J., Jang, B., Bong, S., Woo, S., Sung, Y. E., & Piao, Y. (2014). In situ hydrothermal synthesis of Mn3O4 nanoparticles on nitrogen-doped graphene as high-performance anode materials for lithium ion batteries. *Electrochimica Acta*, *120*, 452–459. https://doi.org/10.1016/j.electacta.2013.12.018

Pu, N. W., Chen, C. Y., Qiu, H. X., Liu, Y. M., Song, C. H., Lin, M. H., & Ger, M. Der. (2018). Hydrothermal synthesis of N-doped graphene/Fe2O3 nanocomposite for supercapacitors. *International Journal of Electrochemical Science*, *13*(7), 6812–6823. https://doi.org/10.20964/2018.07.16

Qin, X., Wang, X., Xiang, H., Xie, J., Li, J., & Zhou, Y. (2010). Mechanism for hydrothermal synthesis of LiFePO4 platelets as cathode material for lithium-ion batteries. *Journal of Physical Chemistry C*, *114*(39), 16806–16812. https://doi.org/10.1021/jp104466e

Reverón, H., C. Aymonier, H., Loppinet-Serani, A., Elissalde, C., Maglione, M., & Cansell, F. (2005). Single-step synthesis of well-crystallized and pure barium titanate nanoparticles in supercritical fluids. *Nanotechnology*, *16*, 1137–1143.

Reverón, H., Elissalde, C., Aymonier, C., Bidault, O., Maglione, M., & Cansell, F. (2005). Supercritical fluid route for synthesizing crystalline barium strontium titanate nanoparticles. *J. Nanosci. Nanotechnol.*, *5*, 1741–1745.

Sato, T., Sue, K., Akiyama, Y., Shibata, K., Kawasaki, S. I., Tanaka, S., Saitoh, K., Kawai-Nakamura, A., Aida, K., & Hiaki, T. (2008). Effect of pH on hydrothermal

synthesis of gamma-Al2O3 nanoparticles at 673 K. *Chem. Lett*, *37*, 242–243.

Sato, T., Sue, K., Suzuki, W., Suzuki, M., Matsui, K., Hakuta, Y., Hayashi, H., Arai, K., Kawasaki, S. I., Kawai-Nakamura, A., & Hiaki, T. (2008). Rapid and continuous production of ferrite nanoparticles by hydrothermal synthesis at 673 K and 30 MPa. *Ind Eng. Chem. Res*, *47*, 1855–1860.

Sato, T., Sue, K., Tsumatori, H., Suzuki, M., Tanaka, S., Kawai-Nakamura, A., Saitoh, K., Aida, K., & Hiaki, T. (2008). Hydrothermal synthesis of CuAlO2 with the delafossite structure in supercritical water. *J. Supercrit. Fluid*, *46*, 173–177.

Shanbhag, D., Bindu, K., Aarathy, A. R., Ramesh, M., Sreejesh, M., & Nagaraja, H. S. (2017). Hydrothermally synthesized reduced graphene oxide and Sn doped manganese dioxide nanocomposites for supercapacitors and dopamine sensors. *Mater. Today*, *4*, 66–74. https://doi.org/10.1016/j.mtener.2017.03.006

Sonawane, G. H., Patil, S. P., & Sonawane, S. H. (2018). Nanocomposites and Its Applications. In *Applications of Nanomaterials* (pp. 1–22). https://doi.org/10.1016/b978-0-08-101971-9.00001-6

Sue, K., Suzuki, M., Arai, K., Ohashi, T., Ura, H., Matsui, K., Hakuta, Y., Hayashi, H., Watanabe, M., & Hiaki, T. (2006). Size-controlled synthesis of metal oxide nanoparticles with a flow-through supercritical water method. *Green Chem*, *8*, 634–638.

Sun, X., Zheng, C., Zhang, F., Yang, Y., Wu, G., Yu, A., & Guan, N. (2009). Size-controlled synthesis of magnetite (Fe3O4) nanoparticles coated with glucose and gluconic acid from a single Fe(III) precursor by a sucrose bifunctional hydrothermal method. *Journal of Physical Chemistry C*, *113*(36), 16002–16008. https://doi.org/10.1021/jp9038682

Takesue, M., Shimoyama, K., S, H., Y, H., H, S., & R.L, J. (2007). Phase formation of Mn-doped zinc silicate in water at high-temperatures and high-pressures. *J. Supercrit. Fluid.*, *43*, 214–221.

Takesue, M., Suino, A., Hakuta, Y., Hayashi, H., & Smith, R.L, J. (2010). Crystalisation trigger of Mn-doped zinc silicate in supercritical water via Zn, Mn, Si sources and complex agent ethylenediamine tetraaceticacid. *Master Chem. Phys.*, *121*, 330–334.

Takesue, M., Suino, A., Hakuta, Y., Hayashi, H., & Smith, R. . (2008). Formation mechanism and luminescence appearance of Mn-doped zinc silicate particles synthesized in super critical water. *J. Solid State Chem*, *181*, 1307–1313.

Takeuchi, E. S., & Randolph A. Leising. (1996). *PROCESS FOR MAKING A METAL OXIDE COMPOSITE CATHODE MATERIAL FOR HIGH ENERGY DENSITY BATTERIES*.

Wang, X., Zhang, Z., Qu, Y., Lai, Y., Li, J., Zhang, Z., Qu, Y., Lai, Y., & Li, J. (2014). Nitrogen-doped graphene/sulfur composite as cathode material for high capacity lithium-sulfur batteries. *Journal of Power Sources*, *14*.

https://doi.org/10.1016/j.jpowsour.2014.01.093.This

Wang, Y., Wei, H., Lu, Y., Wei, S., Wujcik, E. K., & Guo, Z. (2015). Multifunctional Carbon Nanostructures for Advanced Energy Storage Applications. *Nanomaterials*, *5*, 755–777. https://doi.org/10.3390/nano5020755

Wu, X., Lu, J., Han, Y., Wu, H., Bu, L., Xie, J., Qian, C., Li, H., Diao, G., & Chen, M. (2020). Template-assisted synthesis of LiNi0.8Co0.15Al0.05O2 hollow nanospheres as cathode material for lithium ion batteries. *Journal of Materials Science*, *55*(22), 9493–9503. https://doi.org/10.1007/s10853-020-04627-1

Xu, H., Yang, Q., Li, F. F., Tang, L., Gao, S., Jiang, B., Sekhar, C., Ray, C., Konios, D., Stylianakis, M. M., Stratakis, E., Kymakis, E., Lai, Q., Zhu, S., Luo, X., Zou, M., Huang, S., Wazir, A. H., Kundi, I. W., … De Leeuw, N. H. (2015). Will Advanced Lithium- Alloy Anodes Have a Chance in Lithium-Ion Batteries? *AIP*, *2*(032146), 200–247. https://doi.org/10.1016/j.jpowsour.2013.03.160

Yahya, R. ., Hayashi, H., Nagase, T., T, E., Onodera, Y., & N, S. (2001). Hydrothermal synthesis of potassium hexatitanates under subcritical and supercritical water conditions and its application in photocatalysts. *Chem Mater*, *13*, 842–847.

Yang, X., JW, C., QF, Z., WQ, T., LD, X., YH, L., MQ, X., QM, H., GZ, C., & WS, L. (2018). Mechanism of cycling degradation and strategy to stabilize a nickel-rich cathode. *J Mater Chem A*, *6*(33), 16149–16163.

Yoon, M. ., In, J. H., Lee, H. C., & Lee, C. . (2006). Comparison of YAG:Eu phosphor synthesized by supercritical water and solid-state methods in a batch reactor. *Korean J. Chem. Eng*, *23*, 842–846.

Yu, C.-Y., Park, J.-S., Jung, H.-G., Chung, K.-Y., Aurbach, D., Sun, Y.-K., & Myung, S.-T. (2015). NaCrO2 cathode for high-rate sodium-ion batteries. *Energy Environ. Sci*, *8*, 2019–2026.

Yuan, L. X., Wang, Z. H., Zhang, W. X., Hu, X. L., Chen, J. T., Huang, Y. H., & Goodenough, J. B. (2011). Development and challenges of LiFePO4 cathode material for lithium-ion batteries. *Energy and Environmental Science*, *4*(2), 269–284. https://doi.org/10.1039/c0ee00029a

Yuan, M., Li, Y., Chen, Q., Chen, C., Liu, X., Zeng, W., Wang, R., & Xiao, S. (2019). Surfactant-assisted hydrothermal synthesis of V2O5 coated LiNi1/3Co1/3Mn1/3O2 with ideal electrochemical performance. *Electrochimica Acta*, *323*(134822), 2934–2939. https://doi.org/10.1039/c2cp23363k

Zhang, B., Wang, Z. –., & Guo, H. –. (2007). Effect of annealing treatment on electrochemical property of LiNi0.5Mn1.5O4 spinel,. *Trans. Nonferr. Met. Soc*, *17*, 287–290.

Zhang, H., B, G., JN, G., Y, L., C, M., J, Z., TY, W., & CJ, C. (2016). One-step synthesis of nickel cobalt sulphides particles: tuning the composition for high performance supercapacitors. *RSC Adv*, *6*(64), 58916–58924.

Zhang, Y., Huo, Q. Y., Du, P. P., Wang, L. Z., Zhang, A. Q., Song, Y. H., Lv, Y., & Li, G. Y. (2012). Advances in new cathode material LiFePO 4 for lithium-ion batteries. *Synthetic Metals*, *162*(13–14), 1315–1326. https://doi.org/10.1016/j.synthmet.2012.04.025

Zhao, D., Han, E., Wu, X., & Guan, H. (2006). Hydrothermal synthesis of ceria nanoparticles supported on carbon nanotubes in supercritical water. *Mater. Lett*, *60*, 3544–3547.

Zheng JC, Yang Z, He ZJ, Tong H, Yu WJ, Z. J. (2018). In situ formed LiNi0.8Co0.15Al0.05O2@Li4SiO4 composite cathode material with high rate capability and long cycling stability for lithium-ion batteries. *Nano Energy*, *58*, 613–621.

CONCLUSION AND RECOMMENDATIONS

Carbon materials have now made a revolution in the world of materials' application. We now look at the conversion and technology for surface engineering and manipulation with variability of functional materials and nanoporous structure for the application. In these aforementioned studies, a wide range of carbon nanomaterials with numerous dimensions and unique morphological structure designs have been synthesized and successfully examined in energy storage device fabrication technologies. The integration of heteroatoms into the carbon network provided a new class of carbon materials with exceptional properties unmatched with parental carbon materials. Compositing carbon nanomaterials with metal oxides exhibited increased discharge capacity for battery application with excellent cycling life stability. In this study, we have thoroughly conferred the highly performing properties of carbon-based materials basing on supercapacitors and batteries. The potential of carbon nanomaterials and their composites for supercapacitors is in resolving the predicted of clean energy storage mitigation. Several materials, methods, and technologies have been used in finding a solution for an energy storing device with high capacitance along with high energy/power density. No doubt, carbon materials are potential candidates for supercapacitor electrode materials but they need a supporting active material to enhance their performance. Nevertheless, an increase in specific capacitance value, power density, and energy density in certain cases gives hope that if the research continues in the right direction of carbon material-based supercapacitor application. This can bring a new revolution in the electronic world.

For application in supercapacitors, improving the efficiency of the electrode materials is the most important for obtaining high performance. Porous carbon with suitable architectures is reliable for improved electrochemical capacitors. This study looked at

optimized the Zea mays (maize) cobs and graphene oxide as a potential abundant precursor for the production of porous carbon supercapacitors and batteries applications. The materials exhibited excellent performance and low cost of production. The physical and chemical characterization of the synthesized materials was carried out with different techniques in determining different properties including structure, morphology, chemical composition, and electrochemical performance. The chemical results revealed surface structure with oxygen-based functional groups and structural characterization revealed a BET specific surface area of 1443.94 m^2/g with a pore volume of 0.7915cm^3/g as the material with the highest porosity. Symmetric devices based on the produced materials delivered a specific capacitance of 358.7F/g with an energy density of 12.45 Wh/kg and a corresponding power density of 250 W/kg at 0.5A/g from KOH activation. The as-prepared electrodes exhibited excellent stability with the capacitance retention of 99% at the maximum potential for a repeated 10 h to a total of 130 h. these materials can be used as commercialized materials for energy storage.

Globally, several electronic devices have been developed to streamline day-to-day life but are still, challenged with high energy storage and excellent stability. This work concluded with some advantages, and some faced challenges for the oxidation, activation, and hydrothermal synthesis of materials with high energy efficiency applications. Activation and Hydrothermal methods are some of the commonest and relatively easy methods with need attention for young researchers. These methods can be used for the commercial production of energy storage materials that are environmentally friendly and low cost to reduce the challenges for energy storage materials. I am confident that the information presented in this study would certainly help in the research and development of carbon nanomaterials-based supercapacitors and batteries with low production and

high performance for application. This solves the challenge of high-cost materials for fabrication and high retention of devices.

The challenges faced and how were overcome in the research are highlighted below;

Lack of policies to guide on how to collect raw materials from one African country to the other. This also included the faster ways to access them in the mines. I bought the samples like graphite from the nearby market as a normal commodity and was not registered to avoid any policy bleach.

There was a challenge of accessing some facilities and equipment. this included equipment for sample preparation and characterization of the materials. The school started out sourcing and initiated collaborations with different institution that hosted me for the research work, to mention; International Advanced Research Center for New materials and metallurgy (ARCI) Hyderabad India.

There was limited access to the latest literature since most of the articles are not open access and the hard copy texts books are not up to date. I managed to network with students from countries and institutions with unlimited access to articles for the latest information. I later discovered that when you share a challenge in a research team, you can get the solution faster and easier.

CONTRIBUTION TO KNOWLEDGE

In Africa, there is a lot of potential materials that are taken as waste which include agricultural waste, domestic waste and industrial wastes. The research study was divided into two projects to explore the options for value addition.

Project 1;

Suitability of agricultural crop residue biomass as raw materials for energy storage systems. The novelty was on maize corn cobs conversion into mesoporous activated carbon as materials for electrodes for supercapacitors. The study shown that maize corn cobs are green sustainable materials which can be used in production of commercial mesoporous activated carbon. The study looked at the optimization of the activation agents and temperature to improve the properties of the materials. The results proved that when using potassium hydroxide as the activation agent at a temperature of 700^{o}C, you get a high performing carbon base material with specific capacitance of 358F/g with energy density of 12Whkg.

Project 2;

Value addition to locally mined graphite flakes as electrode materials for supercapacitors and batteries application. This mined graphite flakes are sold in local markets for use as fuel for cooking in the homes. The work looked at converting the materials into electrode materials for energy storage systems. The conversion process employed are acid oxidation and hydrothermal method to convert graphite flakes into graphene oxide and composite of graphene oxide. The improvement in the material's properties is the knowledge contribution which resulted in discharge capacity of 720mAh/g.

Appendices

Appendex 1

Modified Activation process for Supercapacitor Electrode Materials from African Maize Cob

List of Tables

Table S1: The mass fraction loss of raw material powder of maize corn cobs, AC-S-600, AC-S-700, and AC-S-800 activated carbon materials at the different temperature range.

Temperature range (ºC)	**Mass fraction loss (%)**			
	Before activation	**After activation**		
	Raw material	AC-S-600	AC-S-700	AC-S-800
28 - 120	5.0	5.0	10.5	8.0
120 – 200	2.6	2.5	2.4	2.0
200 – 350	52.4	0.5	1.8	1.2
350 – 600	14.5	6.0	5.3	4.4
600 – 1000	10.5	26.2	12.9	11.9
Total loss	85	59.8	67.1	72.5

Table S2: FTIR peaks assignment for functionality/groups on AC surfaces for AC-S-600, AC-S-700, and AC-S-800 materials

Wavenumber (cm^{-1})	Functionality/groups	Transmittance strength
1000 - 1500	C-OH stretching	Strong/medium
	C-O stretching (ethers)	
	C-N	
	Nitro groups	
	Aromatic compound	
1540	Quinones (Carboxylic acid)	weak
1743	C=O stretching (Carboxylic acid, Lactones, carbonyl groups)	Strong
2369	Methyl and methylene groups	Weak
2932 - 3000	C-H stretching (CH_3-, -CH_2-, carboxylic acid)	Weak
3459 - 4000	O-H overtones (carboxylic acid/phenolic group)	Weak

Table S3: Boehm Acidic and Basic surface characterization of the activated carbon materials

AC Sample	Acidic Functional groups			Total Acidity (mmol/g)	Total Basicity (mmol/g)
	Carboxylic (mmol/g)	Lactonic (mmol/g)	Phenolic (mmol/g)		
AC-S-600	0.250	0.168	0.022	0.440	0.090
AC-S-700	0.244	0.02	0.20	0.464	0.118
AC-S-800	0.112	0.100	0.230	0.442	0.420

Table S4: XPS mass surface concentration of activated carbon material's composition (%), binding energy position and their Full Width at Half Maximum intensity (FWHM)

AC Samples	Elementals peaks	Composition (%)	Position (eV)	FWHM (eV)
AC-S-600	C_{1s}	67.01	283.7	1.903
	O_{1s}	22.59	531.7	2.636
	S_{2p}	2.60	168.7	2.618
	B_{1s}	5.38	191.7	2.272
	Na_{1s}	2.42	1071.7	2.148
AC-S-700	C_{1s}	56.97	283.7	2.515
	O_{1s}	29.90	532.7	2.746
	S_{2p}	2.12	169.7	2.413
	B_{1s}	5.97	192.7	1.968
	Na_{1s}	5.04	1071.7	2.485
AC-S-800	C_{1s}	56.45	283.7	2.294
	O_{1s}	31.70	531.7	2.700
	S_{2p}	2.71	168.7	2.759
	B_{1s}	4.09	192.7	2.469
	Na_{1s}	5.05	1071.7	2.360

Table S5: XPS spectra of AC-S-600, AC-S-700, and AC-S-800 activated materials, Binding Energy, Functional group assignment and their relative chemical bonding contents

Peaks	Binding Energy (eV)	Functional group assignments	Samples % content		
			AC-S-600	AC-S-700	AC-S-800
O_{1s}	530.8 - 531.1	C=O, O_2, -O-, O-CH_2C-*	-	-	8.55
	531.6 - 531.8	C=O, O_2, S=O, O-C_6H_5NH*,	91.61	-	74.82
	532.2 - 533.0	C-O, -O- (C-O-S)	8.39	100	11.43
	535.8 - 535.9	C-O, O_2	-	-	5.20
C_{1s}	283.7 - 283.9	-C-C-, C=O,	73.22	-	69.74
	284.1 - 284.6	-C-C-, C=O, C-O-S	-	39.44	-
	284.7 - 285.4	C-C, C-H, C_g C=C-C*	18.06	28.39	20.57
	285.5 - 288.6	C-O, C=O, O-C=O, C-O-C, S=C=S*	5.17	23.48	-
	288.7 - 289.7	O=C=S (OC*S)*	3.55	8.69	9.69
S_{2p}	168.4 - 168.9	C-O-S, O=S=O*	62.82	59.07	86.01
	169.6 - 170.1	S=O, O=S=O*	37.18	40.93	13.99

*https://srdata.nist.gov/xps/ElmComposition.aspx was also used for assigning groups

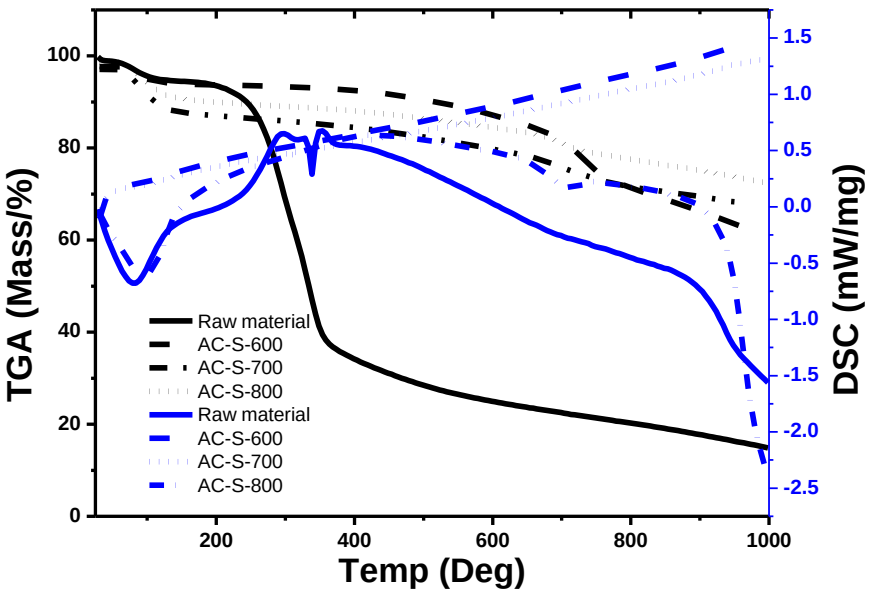

Figure S1: TGA-DSC analysis profile of AMC dried powder materials, AC-S-600, AC-S-700, and AC-S-800 activated carbons

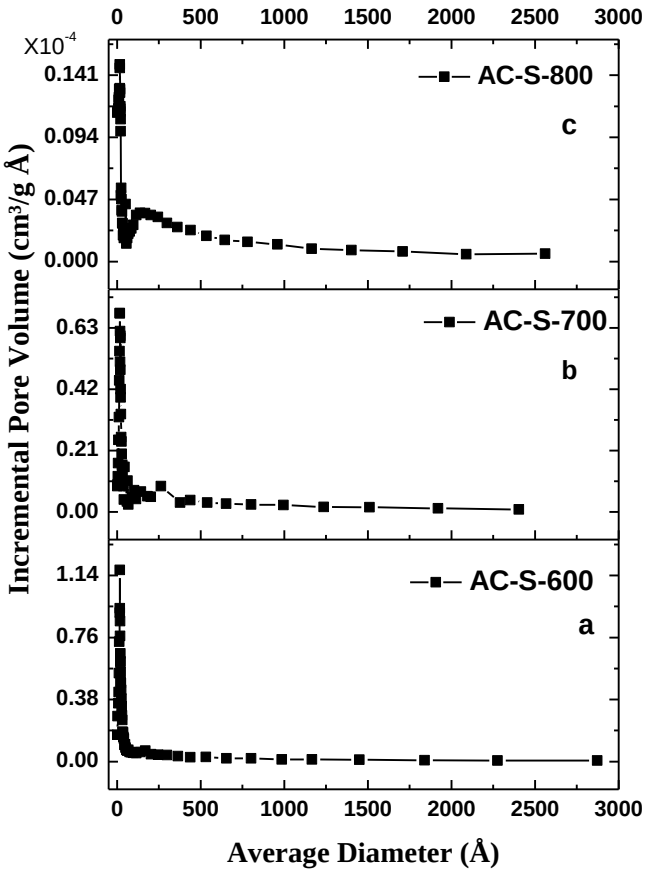

Figure S2: Pole size distribution for the activated carbon material samples

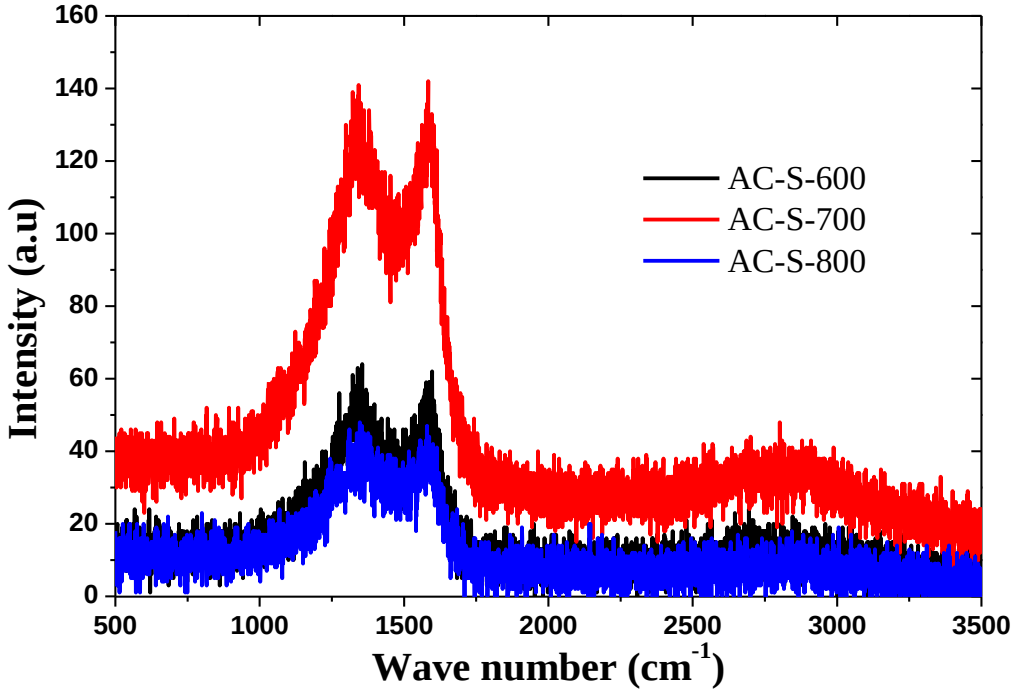

Figure S3: Raman spectra for the AC-S activated materials

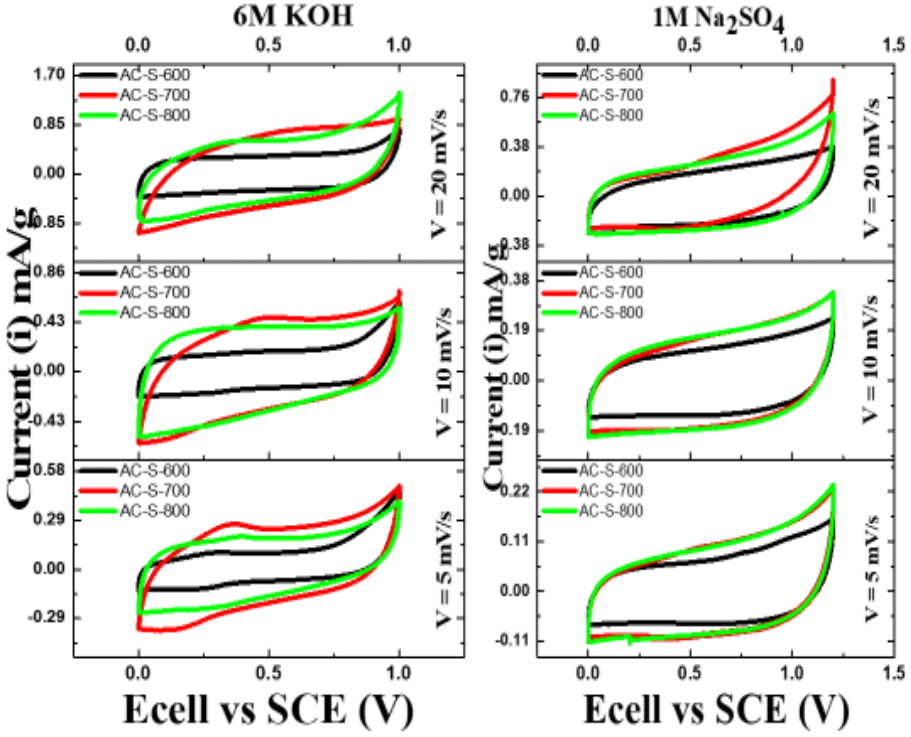

Figure S4: Combined CV curves of AC-S-Activated carbon samples at scan rates 5, 10 and 20 mV/s with 6M KOH and 1M Na_2SO_4 electrolyte.

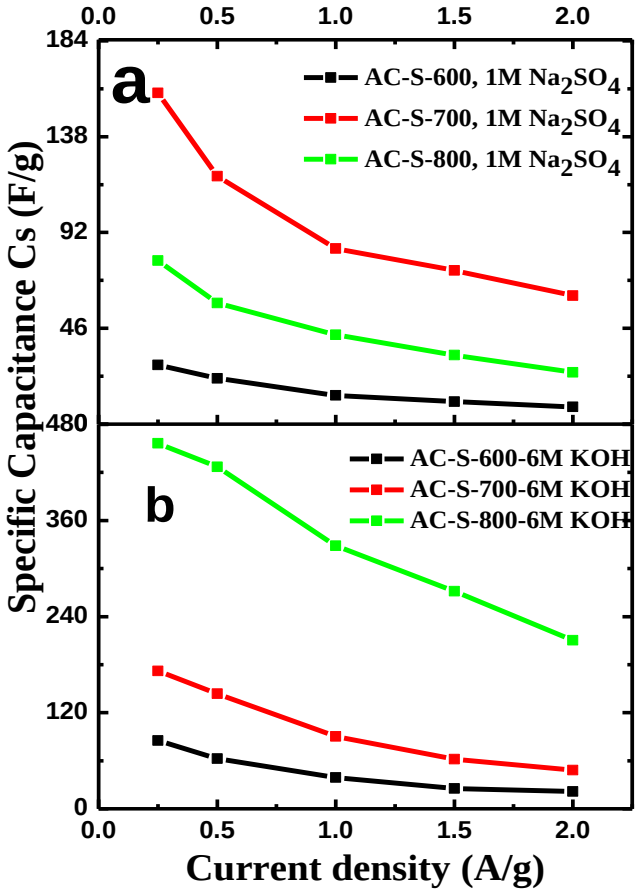

Figure S5: specific Capacitance (F/g) with current density (A/g) curves plot for AC-S-600, AC-S-700, and AC-S-800 for two different electrolytes (6M KOH and 1M Na2SO4)

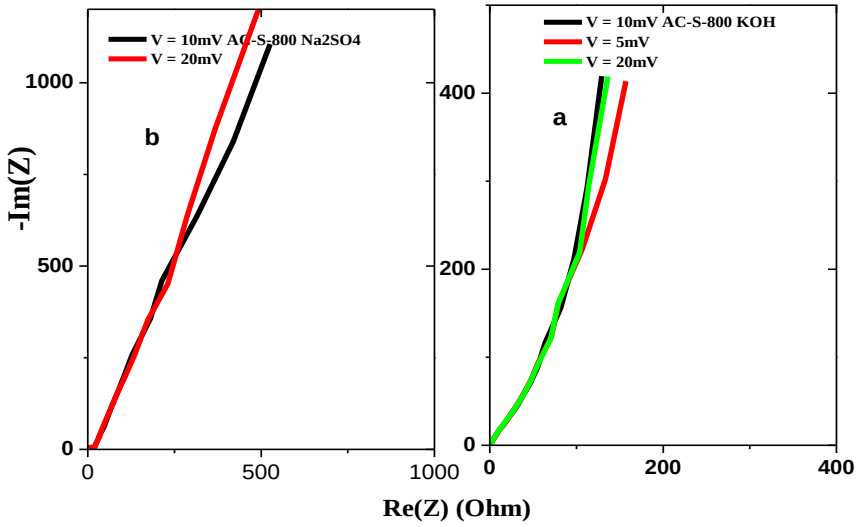

Figure S6: EIS Nyquist plots for AC-S-800 electrode material at different potentials using different electrolytes (a) 6M KOH at 5mV, 10mV and 20mV, (b)1M Na2SO4 at 10mV and 20mV.

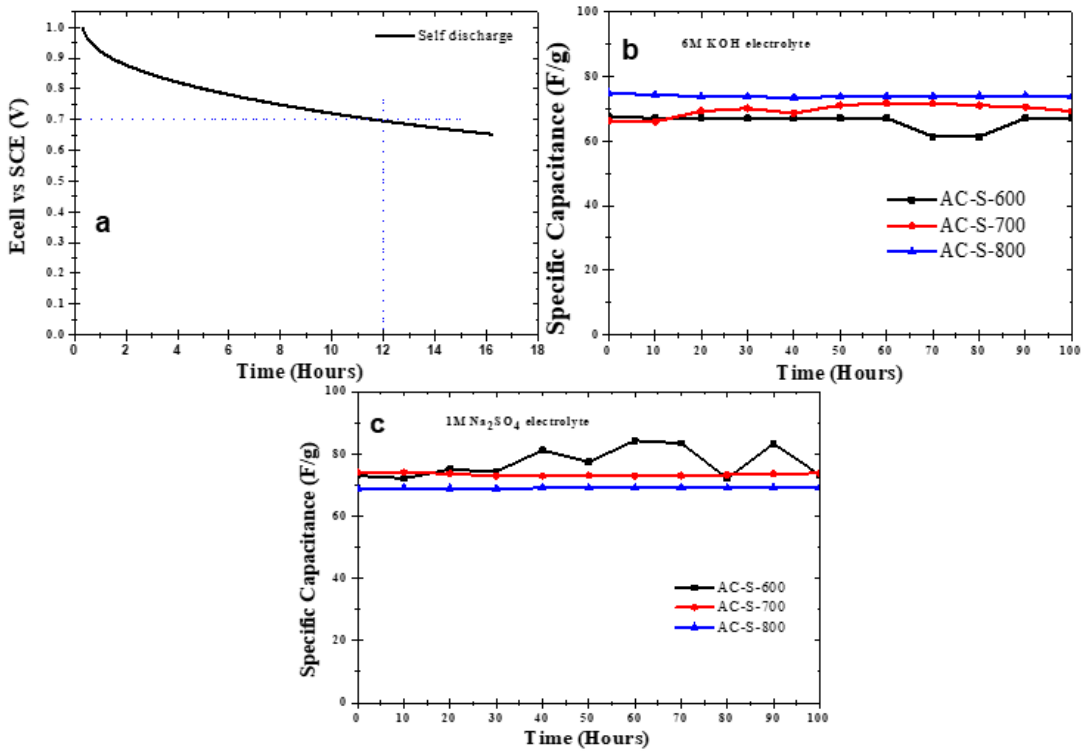

Figure S7: (a) The self-discharge of the device with the highest capacitance assembled with AC-S-800 with 6M KOH after charging to 1.0V, **(b)** Voltage holding stability capacitances of AC-S-600, AC-S-700, and AC-S-800 with 6M KOH electrolyte at the current density of 1.0.A/g for 100 hours, (**c**) stability of AC-S-600, AC-S-700, and AC-S-800 with 1M Na_2SO_4 electrolyte at the current density of 1.0 A/g with 3 charges/discharge cycles and charge hold for 10 hours then repeated for 100 hours

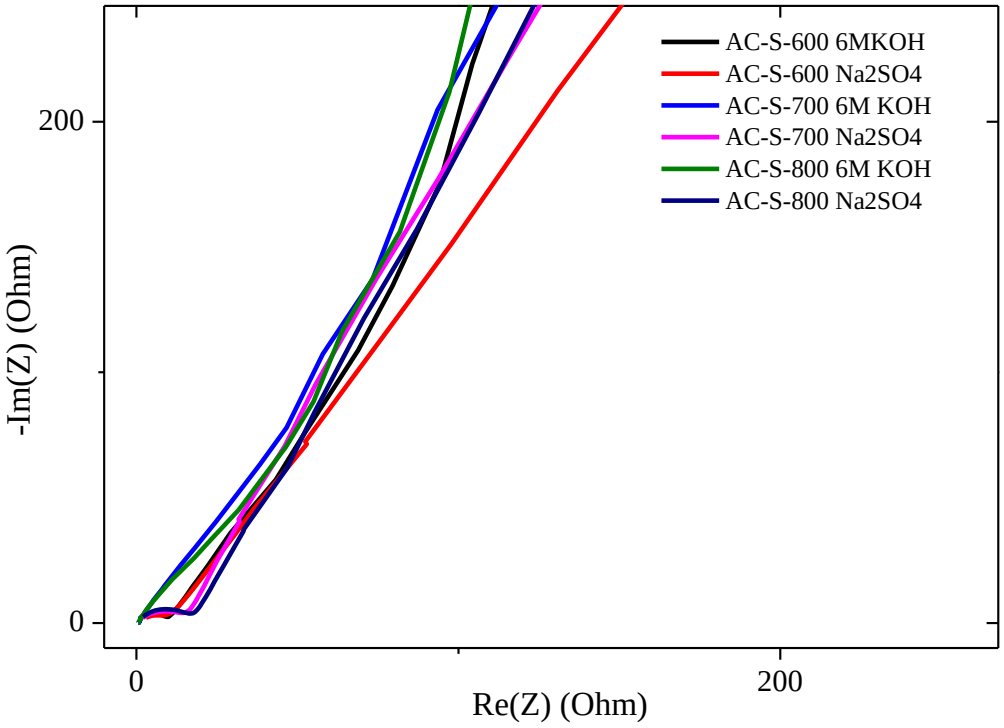

Figure S8: Electrochemical Impedance Spectroscopy (EIS) Nyquist plot for AC-S-600, AC-S-700, and AC-S-800 for two different electrolytes (6M KOH and 1M Na_2SO_4) at the potential of 10mV at low frequency.

APPENDIX 2

Zea mays cobs derived porous carbon for high energy and excellent stability for supercapacitor applications

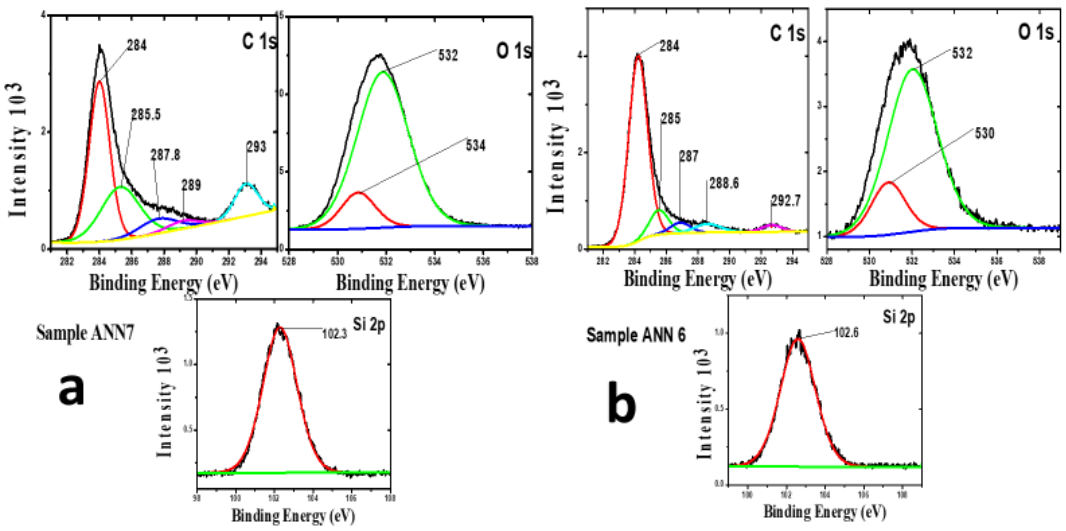

Figure S1: XPS deconvoluted spectra for (a) (ANN7) and (b) ANN6 activated samples

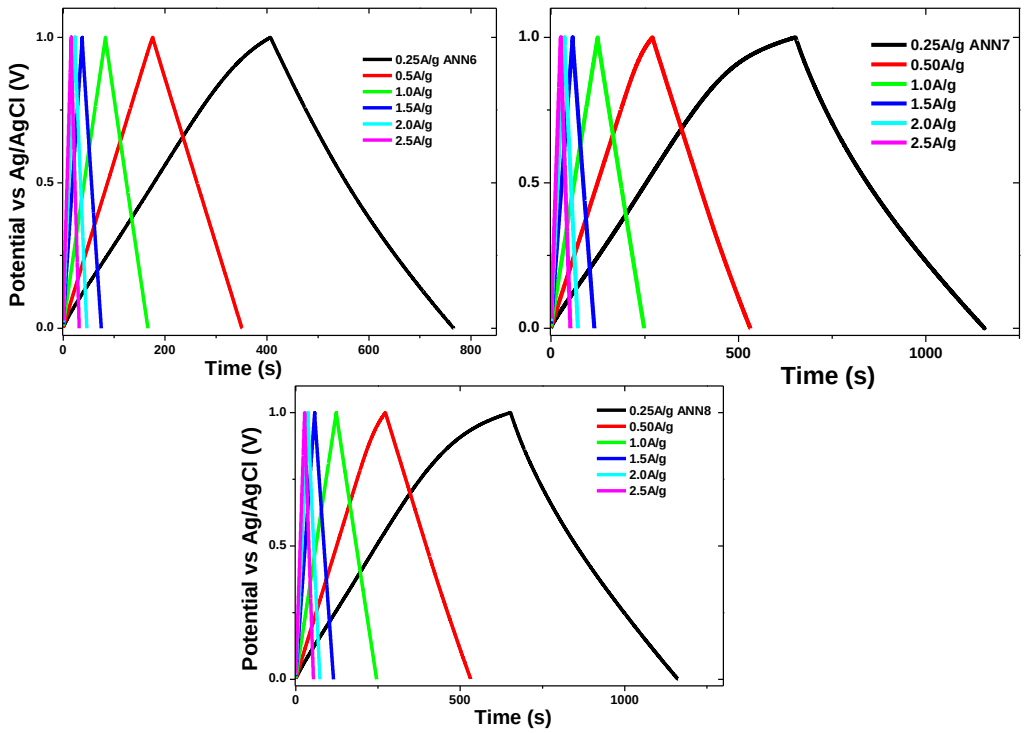

Figure S2: GCD for 3 electrode system for ANN6, ANN7 and ANN8 activated samples at different current density.

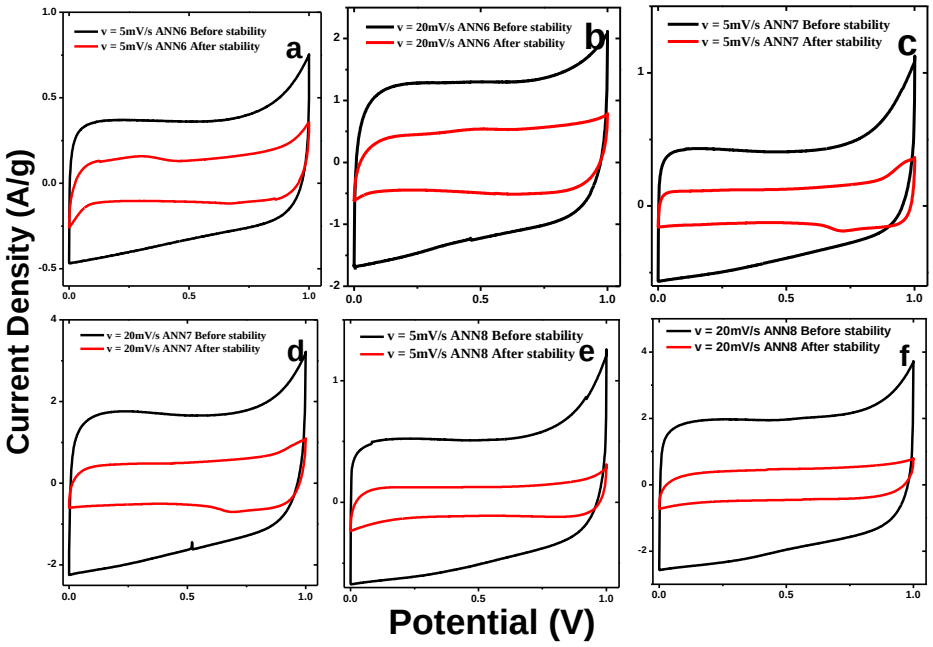

Figure S3: CV scanned at 5mV/s before and after stability test

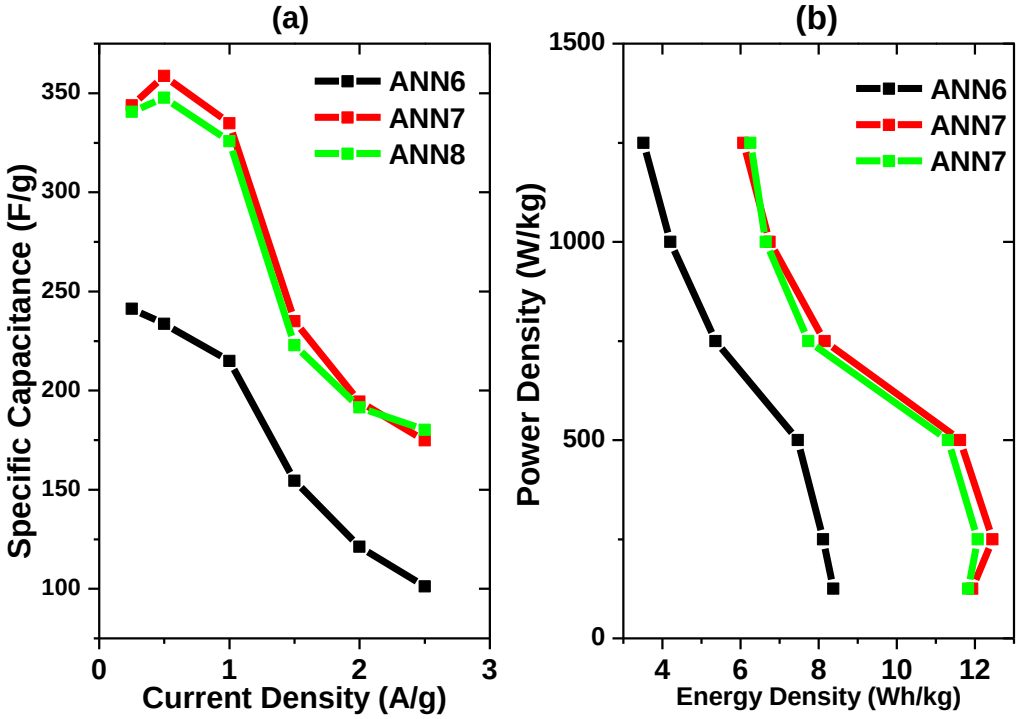

Figure S4: (a) specific capacitance at different current density, (b) the Ragone plots for ANN6, ANN7 and ANN8 based supercapacitors.

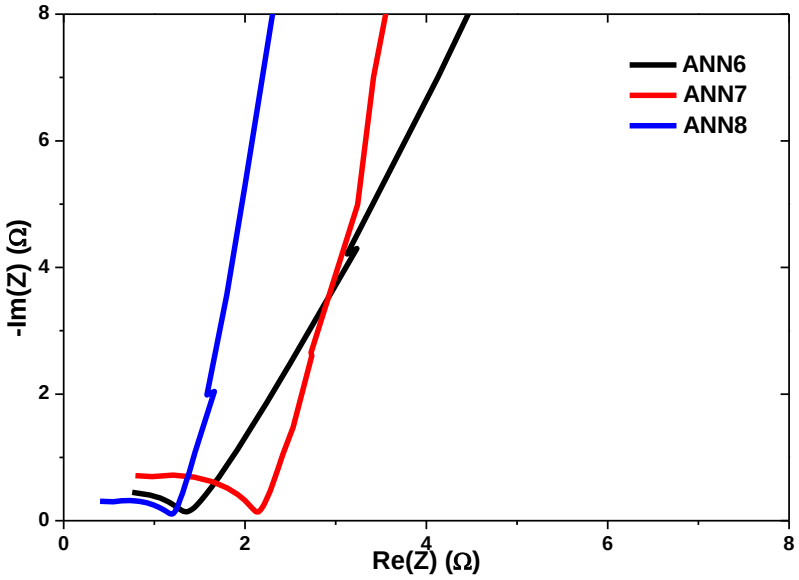

Figure S5: EIS for zoomed high frequency for ANN6, ANN7, and ANN8 activated carbon scanned at 10mV

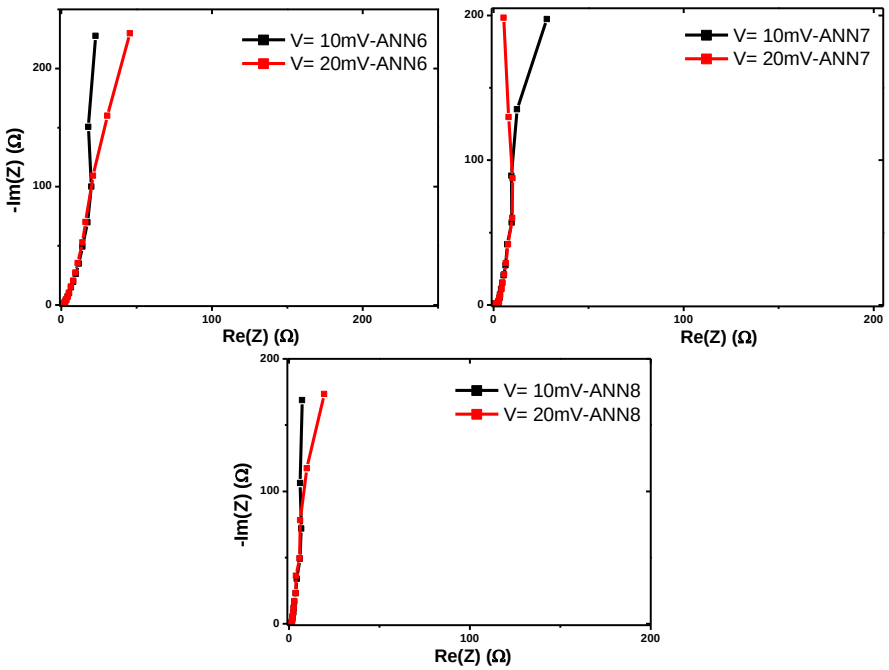

Figure S6: EIS scanned at different potential 10mV and 20mV

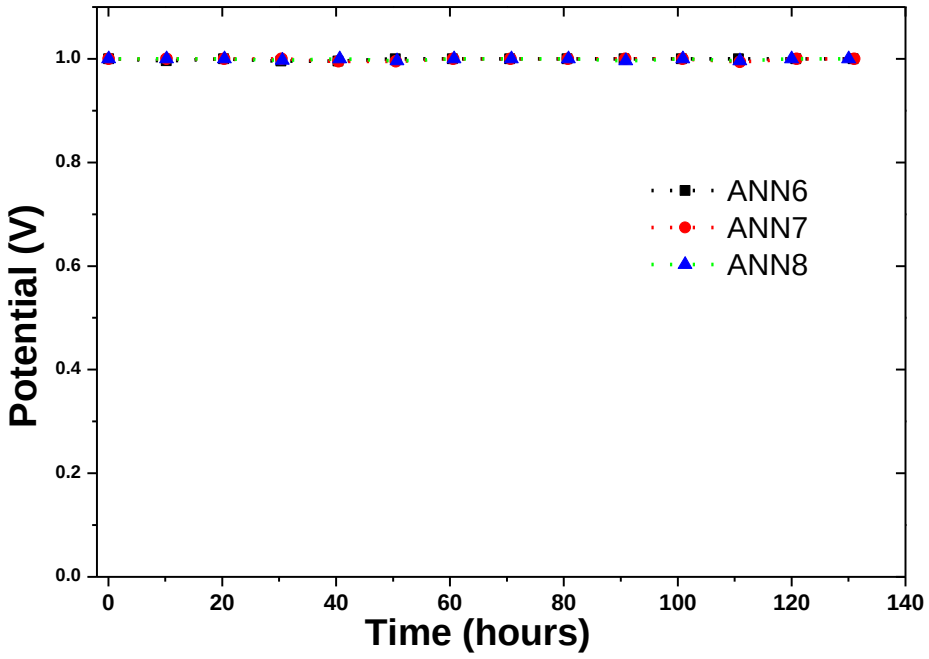

Figure S7: Stability by voltage holding at maximum potential for 10hours before discharge

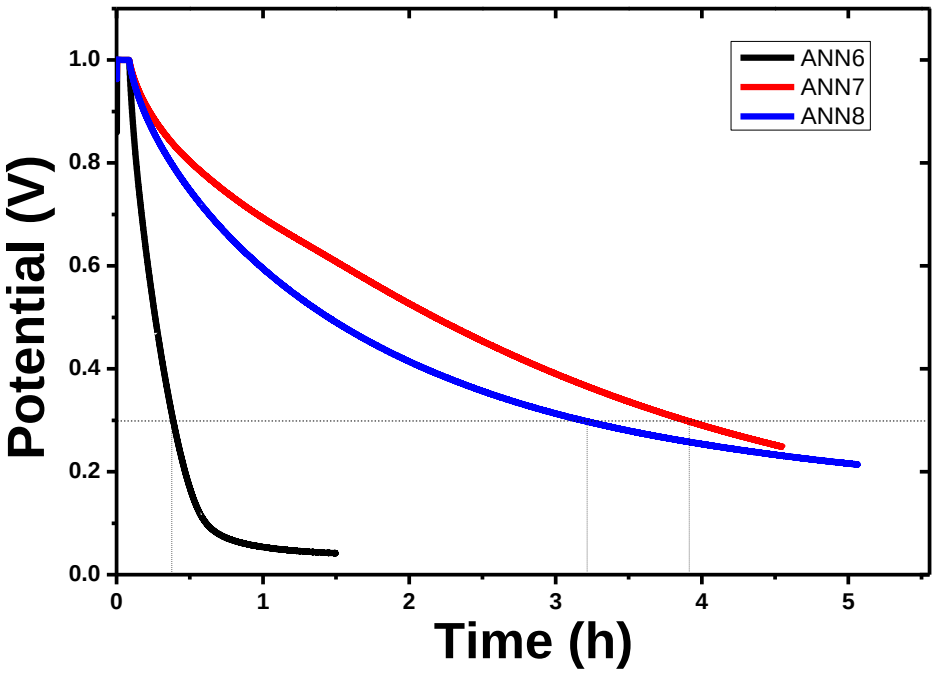

Figure S8: Self-discharge of devices from 1.0V after stability test.